2022

ALPINE SHRUB TUNDRA WATER STORAGE AND RUNOFF DYNAMICS IN THE MACKENZIE MOUNTAINS, SAHTÚ TERRITORY, NT

Geoffrey Kershaw
kers7130@mylaurier.ca

ALPINE SHRUB TUNDRA WATER STORAGE AND RUNOFF DYNAMICS IN THE MACKENZIE MOUNTAINS, SAHTÚ TERRITORY, NT

By:

Geoffrey George Leslie Kershaw

Bachelor of Science, University of Alberta, 2010

Master of Environmental Studies, Dalhousie University, 2013

DISSERTATION

Submitted to the Department of Geography and Environmental Studies

In partial fulfillment of the requirements for Doctor of Philosophy in Geography

Wilfrid Laurier University

Abstract

Alpine regions receive large volumes of precipitation and are important to local and regional water balances, particularly during baseflow periods of winter cold and summer drought when the larger basin area is frozen and/or water limited. Alpine headwaters in western Canada are expected to warm and receive more precipitation during the coming decades, with implications for groundwater recharge and streamflow generation within these systems and the regional river networks to which they contribute. Throughout the North, thawing peat plateaus and other ice-rich permafrost features are resulting in an increased extent of thermokarst and wetland land cover. This transition places infrastructure and water resources at risk as the structural integrity and reliable flow paths previously maintained by the frozen soils become compromised. Alpine systems are particularly susceptible to hydrological change due to the amplification of climate warming with both latitude and elevation. The inherent spatial heterogeneity of these same systems makes attempts to quantify the impacts of climate change on current and future basin water balance even more challenging, yet few field studies of alpine hydrology have been conducted in northern Canada. Specifically, no hydrological field studies have previously occurred within alpine shrub tundra terrain overlapping the Taiga Cordilleran Ecozone and/or the Mackenzie River basin.

The objective of this dissertation is to characterize the spatial and temporal variability in hydrological processes controlling the water balance of an alpine shrub tundra basin. Chapter Two presents five cover classes that are hydrologically distinct based on physiographic, surface, and subsurface characteristics. Glaciofluvial uplands are isolated from the channel network, routing all inputs to aquifer recharge. Peat plateaus have ice-rich permafrost at depth, resulting in limited storage and efficient subsurface runoff to neighbouring fens. Fen and riparian swamp

cover classes both act as primary contributors to the channel network, although some fen areas may be isolated thermokarst features. These thermokarst features lose water via taliks recharging aquifers and/or evaporative loss from surface ponds. In the context of climate change, permafrost thaw will result in the replacement of peat plateaus with fens, such that both storage capacity and groundwater connections will expand. A conceptual model presents the basin storage compartments and expected flow paths linking the cover classes to each other and the larger area beyond the topographical extent of the study basin.

Chapter Three utilizes the land cover classification established in Chapter Two to investigate temporal differences in 2019 open water season basin water balance. During the freshet, a large volume of snowmelt was received, and storage capacity was limited by shallow frost tables and bedfast ice. As a result, runoff generation was highly efficient and streamflow volumes large. The exception to this is the glaciofluvial upland, which channeled all snowmelt to aquifer recharge. As the freshet transitioned to summer, small magnitude rain events began to occur, and evapotranspiration became the primary means of basin water loss. Furthermore, groundwater exchange became more important to the basin water balance, with groundwater discharge from springs in the headwaters sustaining streamflow and channel bed infiltration becoming more prominent as bedfast ice and channel banks thawed. As the summer progressed, cumulative storage, streamflow, and evapotranspiration rates declined as groundwater discharge became the primary input and groundwater recharge the primary output. As climate change continues, a greater proportion of precipitation will be received as rain and the open water season will extend, resulting in a greater proportion of total annual basin outputs occurring via aquifer recharge, although shrubification and permafrost thaw may result in greater influence of evapotranspiration.

Chapter Four assesses the basin runoff response following discrete precipitation events and utilizes stable isotope analysis to establish seasonally distinct source water contributions, evaporative influence, and subsurface flow paths during the 2019 open water season. The large volume of snowmelt received during the freshet caused peak streamflow rates, but only 8 % of total freshet discharge was isotopically designated as event water at the main basin outlet. In comparison, the maximum daily and total freshet event water fraction was reduced at the headwater subbasin outlet, where spring sources of groundwater discharge were more influential on streamflow. During the summer months, headwater subbasin streamflow was volumetrically and isotopically unresponsive to rain events and groundwater discharge continued to dominate. At the main outlet, early summer runoff response volumes and event water contributions following precipitation events were greatly reduced, in part due to the smaller magnitude of rain input volumes compared to snowmelt, but also due to the increase in fen storage capacity. By the late summer, the frost table also reached the mineral substrates at depth in the riparian swamp, extending the flow path for rain received by this cover class. As a result, late summer streamflow following rain was composed of even less event water and the hydrograph response was characterized by a lower peak and extended recession limb compared to the early summer event.

This dissertation greatly enhances our understanding of the hydrological role alpine tundra plays in sustaining regional river systems via both surface streamflow and aquifer recharge. These findings provide the model structure and parameter values necessary for future hydrological modelling efforts that seek to better represent the contribution of these headwater subbasins to larger regional river systems under current and future climatic conditions.

Dedication

To Mackenzie, Selwyn, and Mount Fred Andrew - the monarchs of my head and heart.

Acknowledgements

First and foremost, I would like to thank Dr. Bill Quinton for being there at the start of this PhD journey. Without Bill, this work never would have begun, and I am indebted to him for taking a chance on me, providing the tools necessary, and giving me the freedom to lose myself deep in the mountains year after year after year. Bill, I appreciate your trust and none of this would have been achieved if not for your support. I would also like to thank the Garfield Weston Foundation, the Natural Sciences and Engineering Research Council, the Ontario Graduate Scholarship Program, the Northern Scientific Training Program, and Wilfrid Laurier University for their generous financial assistance.

Secondly, I would like to thank my supervisors Dr. Mike English and Dr. Brent Wolfe for seeing me through to the end of my program. Mike, you stepped in when I was floundering, tossing the kisby ring of your buoyant outlook on life and research, and reaffirmed what started me with this project – a love of the subject and the journey of learning. Brent, I was nowhere in your plans until I suddenly was, and from the moment you accepted me as your student, you have been unflaggingly positive and supportive, often offering assistance before I even had a chance to ask for it. I can not think of a better supervisor pairing than you both.

Thirdly, I would like to thank all those I met in the field, including Robby Dick and Ryan Connon for their help and companionship during the 2017 field season, and Dr. Steve Mamet for letting me continue to help with the Mackenzie Mountain Earthwatch program year after year. I also want to acknowledge the Sahtú Dene and Kaska Dena peoples tending to the good earth up there; Derek Reddies, Norm Steriah, Robertson Dick, the Double D-Dorthys, Janyce, Fred Andrew Jr, Dot Andrew, Leon Andrew, Famous Amos, Gordon Peter, and of course, the barreling Barichello's

(Barb, Norm, and Josh) who are the beating heart of Dechen Lá Lodge, ever welcoming and warm in spirit.

Finally, I'd like to thank my family. Caroline, you took a chance on love, tossed all warning aside, and jumped into that fixed wing with me in April 2019. We're still flying today my dear and darling! To my mother Linda and father Peter, where to begin. Dad, you spent two months in isolation with me for this project's inaugural 2018 spring field season. Not only was that a tremendous gift of your time, but there is not one other person in the world I could trust to share the professional challenges and personal intimacies of that experience. Outside the confines of this project, you both brought me up to love and appreciate the natural world, and you did it in this same special place every summer of my younger years, living in the same base camp and drinking the same stream waters that would come to be the focal point of this study. For all your love and support throughout my life, professional and otherwise, I am eternally grateful.

Statement of Originality

I declare that all material presented in this dissertation is original and the result of my own research. This dissertation has not been submitted, in part or in whole, for a degree at this or any other university. All ideas taken from other sources have been cited appropriately, crediting the authors' original published work.

Table of Contents

List of Figures

List of Tables

1. General introduction

Alpine regions are hydrologically vital for the role they play as water storage reservoirs and stream headwaters that generate larger amounts of runoff than the lowland areas where human populations largely reside. The orographic effect of mountain ranges displaces air masses sourced from lower elevations upward, producing precipitation as temperature falls and vapor condenses (Smith, 2008; Viviroli *et al.*, 2010) and resulting in greater precipitation with increasing elevation (Dingman, 1981; Granger, 1998; Viviroli *et al.*, 2010; Knowles *et al.*, 2015; Asong *et al.*, 2020). This orographic precipitation recharges aquifers that maintain winter baseflow (Jacques and Sauchyn, 2009; Walvoord and Kurylyk, 2016) while glacier melt and near-surface soil drainage can sustain rivers during summer drought when lowland areas are dry (Geris *et al.*, 2015; Van Loon and Laaha, 2015; Van Tiel *et al.*, 2018). This reliable water source from the alpine regions is vital for supporting irrigation systems and agriculture accounting for an estimated 20-40 % of world food production (Viviroli *et al.*, 2010; Qin *et al.*, 2020).

The water resources of alpine headwaters are at risk as climate change creates warmer temperatures and uncertainty in future precipitation phase and volumes received (Beniston, 2003; Hock *et al.*, 2019; Qin *et al.*, 2020). Alpine headwaters in northern Canada are expected to receive more precipitation during the coming decades (Stadnyk and Déry, 2021), yet total annual contributions to lowland regions may decline globally due to the continued depletion of glaciers and late lying snowpacks (Bailey *et al.*, 1997; Meier *et al.*, 2003; Stewart, 2009; Viviroli *et al.*, 2010; IPCC, 2013; Hock *et al.*, 2019; Qin *et al.*, 2020). While alpine hydrology often focuses on glacier mass balance, the hydrological response of the exposed and increasingly vegetated valleys at lower elevations is of growing importance (IPCC, 2013). Furthermore, climate warming is anticipated to be most extreme at high elevations and latitudes (Beniston, 2003;

Pepin *et al.*, 2015; Wang *et al.*, 2016) highlighting the study of northern alpine hydrology as a priority research topic for policy makers, hydrological modellers, water resource managers, and the downstream ecosystems and societies directly impacted by these changes.

1.1 Alpine hydrology

Northern alpine systems have undergone substantial geophysical, biological, and hydrological change following deglaciation and this transition is currently being accelerated by climate change (Pepin *et al.*, 2015; Wang *et al.*, 2016). As the thermal regime of discontinuous permafrost landscapes continues to warm, pronounced changes in the hydrological mechanisms responsible for the timing and extent of water storage and runoff response to precipitation events are occurring (Rouse, 2000).

1.1.1 Soils, substrates, and permafrost terrain

More than 50 % of northern hemisphere soils experience seasonal freeze-thaw, and of those, 24 % are underlain by permafrost (Zhang *et al.*, 2003). Permafrost plays an important hydrological role as it inhibits infiltration and results in rapid runoff production via shallow suprapermafrost soils (Walvoord *et al.*, 2012; Hayashi, 2013). Conversely, where permafrost is absent, taliks allow for vertical groundwater recharge, resulting in longer travel times before water returns to surface (Woo *et al.*, 2008b; Walvoord *et al.*, 2012). This aquifer recharge is particularly efficient when sorted glaciofluvial outwash deposits with high hydraulic conductivity are present, as is commonly found in recently deglaciated landscapes (Muir *et al.*, 2011; Kurylyk and Hayashi, 2017). Such deposits route inputs to aquifer recharge along flow paths isolated from and/or diverging from headwater streamflow (Carey and Quinton, 2004; Walvoord *et al.*, 2012).

Seasonally, active layer development above a permafrost body can also affect runoff production. Typically, the freshet period is characterized by shorter flow paths and greater runoff efficiency than the summer months due to an elevated frost table limiting storage availability (Carey and Quinton, 2004, 2005). Furthermore, infiltrating water during the early freshet can refreeze near-surface, with ice filled pores further reducing storage capacity and resulting in greater runoff via near-surface porous organic soils (Roulet and Woo, 1986; Quinton and Marsh, 1999; Carey *et al.*, 2013) and/or overland flow (Woo, 1986).

Mean annual ground temperatures are warming throughout northern Canada, with some of the most rapid warming trends occurring in alpine tundra areas with permafrost (Smith *et al.*, 2019). Twenty eight percent of global permafrost is located in mountain regions (Hock *et al.*, 2019) and due to its impeding effect on percolation into deeper groundwater reservoirs (Carey and Woo, 1999; Walvoord *et al.*, 2012), the loss of permafrost is anticipated to dampen annual peak flows and increase baseflow during the fall and winter as a greater proportion of basin inputs are routed to aquifer recharge instead of surface runoff (Walvoord *et al.*, 2012; Woo, 2012; Lamontagne-Hallé *et al.*, 2018). This is consistent with a spatial shift in groundwater discharge locations farther downslope (Lamontagne-Hallé *et al.*, 2018) and temporal trends of increasing baseflow observed in northern Canada (Jacques and Sauchyn, 2009; Connon *et al.*, 2014) and elsewhere (Hock *et al.*, 2019). As such, the distribution of permafrost is a vital hydrological characteristic that should be considered in models of current and future regional water balance.

1.1.2 Vegetation and topography

The distribution and density of vegetation in tundra settings is known to influence the local hydrology, including winter snow accumulation, summer thaw depth, and evapotranspiration losses from plants and near-surface soils (Wilcox *et al.*, 2019; Wallace and Baltzer, 2020). As the

climate continues to warm and the growing season extends, tree species have responded with increasing stand densities and expanding treelines farther upslope (Danby and Hik, 2007; Myers-Smith *et al.*, 2011) and shrubification has been observed throughout the North (Sturm *et al.*, 2001; McGuire *et al.*, 2006; Mekonnen *et al.*, 2021). This climate-driven increase in vascular plant abundance (Myers-Smith *et al.*, 2011, 2015; Elmendorf *et al.*, 2012) may result in greater evapotranspiration (ET) (Swann *et al.*, 2010; Wallace and Baltzer, 2020), but the net influence of greater ET on runoff production and streamflow from northern basins is uncertain given the dependence of ET on water availability (Cable *et al.*, 2014; Hoylman *et al.*, 2019).

While plant communities are important to local scale hydrology, in mountainous terrain with sparse vegetation, topography is generally recognized as more influential and also highly variable (Marsh *et al.*, 2020). Specifically, hydrological models often require slope, aspect, and elevation assigned as part of thermal and mass balance computations (de Jong *et al.*, 2005; Rasouli *et al.*, 2014; Craig *et al.*, 2020; Marsh *et al.*, 2020) used to estimate hydrological processes and variables important to cold climate systems, including the distribution of permafrost (Cable *et al.*, 2016), snow depth (Pomeroy *et al.*, 1998; Essery and Pomeroy, 2004), and snowmelt (Ménard *et al.*, 2014). As such, both topographic and surface characteristics must be represented in conceptual and numerical representations of alpine tundra basins and the regional river systems which they sustain.

1.2 Research objectives

Few hydrological study basins have been established and maintained in the circumpolar north (Laudon *et al.*, 2017) and those that exist tend to be located in lower elevation areas where the logistics of access and maintenance are more cost effective. Water resource management

decisions require an improved understanding of alpine hydrology as a necessary precursor for more accurate models of regional water balance and prediction of how these systems will adapt and modify their primary storage compartments and flow paths as climate conditions continue to change. Alpine shrub tundra areas represent a significant portion of the Taiga Cordillera Ecozone and are important to the water balance of larger northern river systems, including the Mackenzie River; yet no field-based studies have been conducted to obtain fundamental knowledge of hydrological processes occurring in these alpine areas. This work is necessary to support predictive hydrological modelling with better representations of land cover characteristics and hydrological processes occurring within this terrain. In response to this research need, the three primary objectives for this dissertation are as follows:

1. Establish the alpine shrub tundra cover classes that are present within the study basin, the hydrological characteristics unique to each, and the hydrological function they have in isolation and collectively.

2. Use the land cover classification to guide a water balance assessment of the study basin and describe seasonal differences in primary inputs, outputs, and hydrological processes active during the 2019 open water season.

3. Assess and compare runoff generating hydrological processes during freshet snowmelt and summer rain events of 2019, including changes in contributing area storage, streamflow volumes, and source water contributions using water isotope tracers.

The findings of each Chapter are examined in the context of a changing climate and commentary is provided on the potential implications of long-term trends in precipitation

regime, air temperature, and land cover assemblage on alpine shrub tundra water balance and runoff generating processes.

1.3 Study region

The Mackenzie River Basin (MRB) encompasses 20 % of Canada's land mass (1.8 million km^2) and generates greater annual discharge than any other river in Canada (Woo *et al.*, 2008b). Much of the moisture moving inland from the Pacific Ocean precipitates out in the Selwyn Mountains before reaching the Mackenzie Mountains (Woo *et al.*, 2008b), but the mountainous sub-basins of the MRB still receive more precipitation per unit area than the central and eastern lowland portions, with an estimated 60 % of total MRB discharge sourced from 40 % of the area along the western divide where the mountainous subbasins are located (Woo and Thorne, 2003).

The Taiga Cordillera Ecozone is a largely mountainous region in northern Canada covering 260,000 km^2 between 60.7 °N and 68.5 °N. It overlaps a large portion of the Mackenzie Mountain range and covers 8.2 % of the MRB along its northwestern divide. Much of the Taiga Cordillera is covered by grass and/or shrub tundra (40.7 %), with forest (29.2 %) and barren land (28.2 %) also prevalent (Canada Centre for Remote Sensing (CCRS) *et al.*, 2020).

The study basin selected as the focus of this dissertation (63.3°N, 129.8°W, 1264.8 – 1333.1 masl, 0.8 km^2) is located within the overlapping extent of the MRB and Taiga Cordillera ecozone (Figure 1.1). Specifically, the study basin is found within the Natla Plateau alpine-subalpine ecoregion, occupying a climatic transitional zone between mid-boreal and low subarctic systems (Ecosystem Classification Group, 2010). The study basin was selected during a preliminary field visit in 2017 with the intention of identifying a basin that was 1) of manageable areal extent for ground and drone surveys (~ 1 km^2); 2) accessible by foot from the established base camp; and 3) containing

a stream network, landforms, and vegetation common to the surrounding Tsichu River valley. Within the Tsichu River valley, a variety of Quaternary deposits are found including unsorted moraines, outwash sands, colluvium at hill slope bases, alluvium in flood plains, and fluvial deposits along active and relic riverbeds. Glacial retreat following the Wisconsin glaciation ~32-12 ka before present left till deposits up to 90m thick (Duk-Rodkin and Barendregt, 2011) and many stratified drift landforms following glacio-fluvial redistribution, including eskers, kame terraces, and outwash plains. The bedrock below these glacial deposits are shales, slates, and sandstones of late Precambrian/early Paleozoic origin (Ecosystem Classification Group, 2010). Additionally, there is a concentration of palsa and peat plateau features in the valley bottoms (Ecosystem Classification Group, 2010) where peat soils have accumulated to >1m depth and organic cryosols have formed (Geological Survey of Canada, 2014). The ground cover of the Tsichu River valley features *Betula glandulosa* shrubs above *Cladina spp.* and *Cetraria spp*. lichen mats on well drained soils, while *Salix spp.* and miscellaneous mosses dominate the near channel areas and *Carex aquatilis* sedge meadows are found near channel and/or in isolated depressions (Mamet *et al.*, 2017).

1.4 Thesis outline

1.4.1 Chapter Two

Mackenzie River basin alpine tundra land cover classification and associated hydrological properties

Attempts to characterise the hydrology of large and poorly understood regions is best served by initial detailed study of a representative basin. The use of land cover classification schemes can guide the selection of locations to observe hydrological characteristics and interactions among

the cover classes present. Chapter Two describes the land cover classification scheme for the study basin and the process of developing land cover specific and areally weighted basin wide estimates of physiography, surface characteristics, and subsurface characteristics controlling water storage and flow paths within and from the study basin. The findings of this Chapter identify the major storage and flow paths that are present with a conceptual model linking the hydrologically distinct land covers as they process precipitation inputs and generate basin discharge. In this model, the majority of the basin area contributes to the channel network, with high relief peat plateaus routing inputs to neighbouring fens and both fen and riparian swamp areas acting as primary contributors to the stream. In comparison, the glaciofluvial uplands are unique due to their separation from the channel network and role in routing inputs vertically to recharge aquifers at depth. The conceptual diagram presented captures the main hydrological function of each cover class and the linkages among them controlling basin storage and water loss following precipitation and/or groundwater inputs. As the climate warms, ice-rich permafrost below the peat plateaus will thaw, resulting in land cover transition as the plateaus are replaced with fens. In the long term, this may result in similar amounts of runoff production, but could temporarily result in reduced active contributing area as localized thermokarst depressions retain water in near-surface storage volumes confined by the remnant peat plateau features. This may result in increased evaporative loss from these ponding areas, or possibly additional groundwater recharge as taliks form below. These findings provide both the model structure and primary data sources necessary to quantify the water balance of alpine shrub tundra and predict the future hydrological function of these areas and the large northern rivers to which they contribute.

1.4.2 Chapter Three

Runoff-recharge partitioning in an alpine tundra catchment, Mackenzie Mountains, NT

Chapter two established the unique hydrological characteristics of each cover class, their respective proportions and positions, and a theoretical model for basin hydrology given the characteristics described and their arrangement within the larger basin. Chapter Three builds on these findings with a complete water balance assessment, introducing observations of the channel network and exploring temporal trends in prominent storage compartments and flow paths throughout the 2019 open water season (freshet, early summer, and late summer periods). This Chapter quantifies daily volumes for each water balance component utilizing the land cover classification established in Chapter Two and a series of additional complementary hydrometric measurement points and repeat surveys within the basin, with particular emphasis given to channel water loss via streamflow and channel bed infiltration. During the freshet, the glaciofluvial upland infiltration identified in Chapter Two was a large part of groundwater recharge, while the snowmelt received by the other cover classes retained shallow frost tables that limited storage and resulted in the majority of basin losses via rapid runoff and channel discharge. During the early summer, evapotranspiration was the primary means of basin water loss, but groundwater recharge also had an increasingly large role in basin water balance as the summer progressed. By the late summer, aquifer recharge via channel bed infiltration was the primary means of basin water loss. These late summer hydrological processes will become more prominent as the climate continues to warm, the open water season extends, and precipitation increases in these headwater systems. A coinciding decline in permafrost extent will result in a larger proportion of basin loss via groundwater recharge, although the less certain future evaporative regime may complicate this prediction as increasing water demands due to

shrubification and treeline expansion may reduce headwater contributions to lowland rivers. These findings will aid future water management decision makers and hydrological modellers focused on large river basins that overlap with the Taiga Cordillera Ecozone and in other regions where northern alpine shrub tundra is prevalent.

1.4.3 Chapter Four

Characterizing seasonal differences in hydrological flow paths and source water contributions to alpine tundra streamflow

Chapter Two established the key flow paths and storage compartments present within the basin. Chapter Three described the seasonality in flow paths and storage compartments controlling when certain water balance components are most important during the open water season. The conceptual importance of each cover class presented and the interpretation of long-term cumulative changes in water balance are both revealing, but focusing on the basin response to discrete large input events is important when characterizing and understanding basin hydrology. During large precipitation events, storage capacity can become filled, infiltrability can decline, and flow paths otherwise unused can become active and play an important role in controlling the resulting basin runoff response. In Chapter Four, volumetric estimates of precipitation, storage, and streamflow are paired with water isotope tracer data to quantify runoff volumes and their sources during the freshet, early summer, and late summer storm events. The basin received the greatest daily inputs as snowmelt during the freshet, which resulted in the greatest volume of streamflow composed of ~8 % event water. In comparison, the summer rain events produced much smaller streamflow responses composed of minor to negligible amounts of event water. The smaller headwater subbasin was less responsive to the freshet inputs, with peak flow delayed and composed of a smaller fraction of event water compared to the main basin outlet. The

summer rains had no effect on subbasin streamflow volume or isotope composition. The large proportion of pre-event waters found in streamflow identifies the importance of source waters displaced from near-surface storage frozen during the previous fall and/or the groundwater aquifer discharge sustained by an aquifer recharge zone external to and upslope of the study basin. Although the summer storm events described were not particularly large, this Chapter provides valuable data and process understanding of runoff generation from alpine shrub tundra terrain during the open water season, including streamflow volumes, water table depths, evaporative trends and groundwater exchange via both spring source discharge and aquifer recharge. Climate change will likely result in reduced snow water equivalent, but greater total annual precipitation and an extended open water season. In the context of this changing climate, the findings of this study suggest reduced streamflow will also occur from these headwater streams as more water is lost via evapotranspiration and aquifer recharge. These results provide important information and process understanding of the hydrological role of alpine tundra terrain in mixing source waters and generating both streamflow and groundwater recharge during large input events. These findings are a necessary precursor for research focused on predictions of future peak flows from alpine streams and the large northern rivers to which they contribute as the climate continues to change.

1.4.4 Chapter Five

Conclusions, future research recommendations, and self-reflections

The closing Chapter of this dissertation begins with a summary of the objectives, key findings, and important contributions of each previous Chapter given the current literature on alpine shrub tundra hydrology. Following this, a synthesis is provided to describe how each Chapter builds on the findings of the previous Chapter and intersects with other findings and research needs, as

described in other publications on the topic of northern alpine hydrology. Special attention is given to the broader implications of the findings of this dissertation in the context of a changing climate and the future importance of headwater recharge zones in large northern river systems. The synthesis is followed by a series of recommendations for future research to expand the study design and address the remaining and emerging knowledge gaps for this research. Finally, the dissertation concludes with a brief self reflection describing the importance of field work in northern natural sciences and the personal value of firsthand experience in the wild spaces we are attempting to understand. The field work involved in this project gave me an appreciation for scientific concepts that are difficult to fully conceptualize on the page alone, and hopefully this dissertation benefited from the insights gleaned while having a sip or taking a nap on the mossy shoreline of this beautiful headwater stream.

1.5 References

Asong EZ, Elshamy EM, Princz D, Wheater SH, Pomeroy J, Pietroniro A, Cannon A. 2020. High-resolution meteorological forcing data for hydrological modelling and climate change impact analysis in the Mackenzie River Basin. Earth System Science Data 12 (1): 629–645 DOI: 10.5194/essd-12-629-2020

Bailey W, Oke T, Rouse WR. 1997. The Surface Climates of Canada. McGill-Queen's University Press: Montreal.

Beniston M. 2003. Climatic change in mountain regions: a review of possible impacts. Climate Change 59: 5–31 DOI: 10.1007/978-94-015-1252-7_2

Cable JM, Ogle K, Bolton WR, Bentley LP, Romanovsky V, Iwata H, Harazono Y, Welker J. 2014. Permafrost thaw affects boreal deciduous plant transpiration through increased soil

water, deeper thaw, and warmer soils. Ecohydrology 7 (3): 982–997 DOI: 10.1002/eco.1423

Cable WL, Romanovsky VE, Jorgenson MT. 2016. Scaling-up permafrost thermal measurements in western Alaska using an ecotype approach. The Cryosphere 10: 2517–2532 DOI: 10.5194/tc-10-2517-2016

Canada Centre for Remote Sensing (CCRS), U.S. Geological Survey (UGS), National Institute of Statistics and Geography, National Commission for the Knowledge and Use of the Biodiversity, the National Forestry Commission of Mexico. 2020. 2010 Land Cover of North America at 30 meters. Commission for Environmental Cooperation: Montréal, Québec. Available at: http://www.cec.org/nalcms

Carey S, Quinton WL. 2004. Evaluating snowmelt runoff generation in a discontinuous permafrost catchment using stable isotope, hydrochemical and hydrometric data. Nordic Hydrology 35 (4–5): 309–324 DOI: 10.1002/hyp.5764

Carey S, Woo MK. 1999. Hydrology of two slopes in subarctic Yukon, Canada. Hydrological Processes 13: 2549–2562

Carey SK, Quinton WL. 2005. Evaluating runoff generation during summer using hydrometric, stable isotope and hydrochemical methods in a discontinuous permafrost alpine catchment. Hydrological Processes 19 (1): 95–114 DOI: 10.1002/hyp.5764

Carey SK, Boucher JL, Duarte CM. 2013. Inferring groundwater contributions and pathways to streamflow during snowmelt over multiple years in a discontinuous permafrost subarctic environment (Yukon, Canada). Hydrogeology Journal 21 (1): 67–77 DOI: 10.1007/s10040-012-0920-9

Connon RF, Quinton WL, Craig JR, Hayashi M. 2014. Changing hydrologic connectivity due to permafrost thaw in the lower Liard River valley, NWT, Canada. Hydrological Processes 28 (14): 4163–4178 DOI: 10.1002/hyp.10206

Craig JR, Brown G, Chlumsky R, Jenkinson W, Jost G, Lee K, Mai J, Serrer M, Snowdon AP, Sgro N, et al. 2020. Flexible watershed simulation with the Raven hydrological modelling framework. Environmental Modelling & Software 129 (April): 104728 DOI: 10.1016/j.envsoft.2020.104728

Danby RK, Hik DS. 2007. Variability, contingency and rapid change in recent subarctic alpine tree line dynamics. Journal of Ecology 95 (2): 352–363 DOI: 10.1111/j.1365-2745.2006.01200.x

de Jong C, Whelan F, Messerli B. 2005. Preface: The importance of a hydrological research framework for water balance studies in mountain basins. Hydrological Processes 19 (12): 2323–2328 DOI: 10.1002/hyp.5886

Dingman SL. 1981. Elevation: a major influence on the hydrology of New Hampshire and Vermont, USA. Hydrological Sciences Journal 26 (4): 399–413 DOI: 10.1080/02626668109490904

Duk-Rodkin A, Barendregt RW. 2011. Stratigraphical record of glacials/interglacials in northwest Canada. In Developments in Quaternary Science, Vol. 15, Ehlers J, Gibbard P, Hughes P (eds). Elsevier: Amsterdam; 661–698.

Ecosystem Classification Group. 2010. Ecological Regions of the Northwest Territories: Cordillera. Department of Environment and Natural Resources, Government of the Northwest Territories: Yellowknife.

Elmendorf SC, Henry GHR, Hollister RD, Björk RG, Boulanger-Lapointe N, Cooper EJ, Cornelissen JHC, Day TA, Dorrepaal E, Elumeeva TG, et al. 2012. Plot-scale evidence of tundra vegetation change and links to recent summer warming. Nature Climate Change 2 (6): 453–457 DOI: 10.1038/nclimate1465

Essery R, Pomeroy J. 2004. Vegetation and topographic control of wind-blown snow distributions in distributed and aggregated simulations for an arctic tundra basin. Journal of Hydrometeorology 5 (5): 735–744 DOI: 10.1175/1525-7541(2004)005<0735:VATCOW>2.0.CO;2

Geological Survey of Canada. 2014. Canadian Geoscience Map 195: Surficial Geology of Canada DOI: 10.4095/295462

Geris J, Tetzlaff D, Soulsby C. 2015. Resistance and resilience to droughts: hydropedological controls on catchment storage and runoff response. Hydrological Processes 29 (21): 4579–4593 DOI: 10.1002/hyp.10480

Granger RJ. 1998. Partitioning of energy during the snow-free season at the Wolf Creek Research Basin. In Wolf Creek Research Basin: Hydrology, Ecology, Environment, Pomeroy W, Granger R (eds.). National Water Research Institute, Saskatoon, SK; 3–44.

Hayashi M. 2013. The cold vadose zone: hydrological and ecological significance of frozen-soil processes. Vadose Zone Journal 12: 2136 DOI: 10.2136/vzj2013.03.0064

Hock R, Rasul G, Adler C, Cáceres B, Gruber S, Hirabayashi Y, Jackson M, Kääb A, Kang S, Kutuzov S, et al. 2019. Chapter 2: high mountain areas. In IPCC Special Report on the Ocean and Cryosphere in a Changing Climate: 131–202

Hoylman ZH, Jencso KG, Hu J, Holden ZA, Martin JT, Gardner WP. 2019. The climatic water balance and topography control spatial patterns of atmospheric demand, soil moisture, and shallow subsurface flow. Water Resources Research 55 (3): 2370–2389 DOI: 10.1029/2018WR023302

IPCC. 2013. Climate Change 2013 - The Physical Science Basis. DOI: 10.1038/446727a

Jacques JMS, Sauchyn DJ. 2009. Increasing winter baseflow and mean annual streamflow from possible permafrost thawing in the Northwest Territories, Canada. Geophysical Research Letters 36 (1): 1–6 DOI: 10.1029/2008GL035822

Knowles JF, Harpold AA, Cowie R, Zeliff M, Barnard HR, Burns SP, Blanken PD, Morse JF, Williams MW. 2015. The relative contributions of alpine and subalpine ecosystems to the water balance of a mountainous, headwater catchment. Hydrological Processes 29 (22): 4794–4808 DOI: 10.1002/hyp.10526

Kurylyk BL, Hayashi M. 2017. Inferring hydraulic properties of alpine aquifers from the propagation of diurnal snowmelt signals. Water Resources Research 53: 4271–4285 DOI: 10.1002/2016WR019651

Lamontagne-Hallé P, McKenzie JM, Kurylyk BL, Zipper SC. 2018. Changing groundwater discharge dynamics in permafrost regions. Environmental Research Letters 13 (8) DOI: 10.1088/1748-9326/aad404

Laudon H, Spence C, Buttle J, Carey SK, McDonnell JJ, McNamara JP, Soulsby C, Tetzlaff D. 2017. Save northern high-latitude catchments. Nature Geoscience 10 (5): 324–325 DOI: 10.1038/ngeo2947

Mamet SD, Chun KP, Kershaw GGL, Loranty MM, Kershaw GP. 2017. Recent increases in permafrost thaw rates and areal loss of palsas in the western Northwest Territories, Canada. Permafrost and Periglacial Processes 28 (4): 619–633 DOI: 10.1002/ppp.1951

Marsh CB, Pomeroy JW, Wheater HS. 2020. The Canadian Hydrological Model (CHM): A multi-scale, multi-extent, variable-complexity hydrological model - design and overview. Geoscientific Model Development Discussions 13 (2002): 225–247 DOI: 10.5194/gmd-2019-109

McGuire AD, Chapin FS, Walsh JE, Wirth C. 2006. Integrated regional changes in Arctic climate feedbacks: implications for the global climate system. Annual Review of Environment and Resources 31 (1): 61–91 DOI: 10.1146/annurev.energy.31.020105.100253

Meier MF, Dyurgerov MB, McCabe GJ. 2003. The health of glaciers: recent changes in glacier regime. Climatic Change 59 (1–2): 123–135 DOI: 10.1023/A:1024410528427

Mekonnen ZA, Riley WJ, Berner LT, Bouskill NJ, Torn MS, Iwahana G, Breen AL, Myers-Smith IH, Criado MG, Liu Y, et al. 2021. Arctic tundra shrubification: a review of mechanisms and impacts on ecosystem carbon balance. Environmental Research Letters 16 (5) DOI: 10.1088/1748-9326/abf28b

Ménard CB, Essery R, Pomeroy J. 2014. Modelled sensitivity of the snow regime to topography, shrub fraction and shrub height. Hydrology and Earth System Sciences 18 (6): 2375–2392 DOI: 10.5194/hess-18-2375-2014

Muir DL, Hayashi M, Mcclymont AF. 2011. Hydrological storage and transmission characteristics of an alpine talus. Hydrological Processes 25 (19): 2954–2966 DOI: 10.1002/hyp.8060

Myers-Smith IH, Elmendorf SC, Beck PS, Wilmking M, Hallinger M, Blok D, Tape KD, Rayback S, Macias-Fauria M, Forbes BC, et al. 2015. Climate sensitivity of shrub growth across the tundra biome. Nature Climate Change 5: 887–891 DOI: 10.1038/nclimate2697

Myers-Smith IH, Forbes BC, Wilmking M, Hallinger M, Lantz T, Blok D, Tape KD, Macias-Fauria M, Sass-Klaassen U, Lévesque E, et al. 2011. Shrub expansion in tundra ecosystems: dynamics, impacts and research priorities. Environmental Research Letters 6 (4): 045509 DOI: 10.1088/1748-9326/6/4/045509

Pepin N, Bradley RS, Diaz HF, Baraer M, Caceres EB, Forsythe N, Fowler H, Greenwood G, Hashmi MZ, Liu XD, et al. 2015. Elevation-dependent warming in mountain regions of the world. Nature Climate Change 5 (5): 424–430 DOI: 10.1038/nclimate2563

Pomeroy JW, Gray DM, Shook KR, Toth B, Essery RLH, Pietroniro A, Hedstrom N. 1998. An evaluation of snow accumulation and ablation processes for land surface modelling. Hydrological Processes 12 (15): 2339–2367 DOI: 10.1002/(SICI)1099-1085(199812)12:15<2339::AID-HYP800>3.0.CO;2-L

Qin Y, Abatzoglou JT, Siebert S, Huning LS, AghaKouchak A, Mankin JS, Hong C, Tong D, Davis SJ, Mueller ND. 2020. Agricultural risks from changing snowmelt. Nature Climate Change 10 (5): 459–465 DOI: 10.1038/s41558-020-0746-8

Quinton WL, Marsh P. 1999. A conceptual framework for runoff generation in a permafrost environment. Hydrological Processes 13 (July 1998): 2563–2581

Rasouli K, Pomeroy JW, Janowicz JR, Carey SK, Williams TJ. 2014. Hydrological sensitivity of a northern mountain basin to climate change. Hydrological Processes 28 (14): 4191–4208 DOI: 10.1002/hyp.10244

Roulet NT, Woo MK. 1986. Hydrology of a wetland in the continuous permafrost region. Journal of Hydrology 89 (1–2): 73–91 DOI: 10.1016/0022-1694(86)90144-7

Rouse WR. 2000. The energy and water balance of high-latitude wetlands: controls and extrapolation. Global Change Biology 6 (Supplement 1): 59–68 DOI: 10.1046/j.1365-2486.2000.06013.x

Smith C. 2008. The relationship between monthly precipitation and elevation in the Alberta foothills during the Foothills Orographic Precipitation Experiment. In Cold Region Atmospheric and Hydrologic Studies. The Mackenzie GEWEX Experience: Volume 1: Atmospheric Dynamics, Woo MK (ed.). Springer: New York, New York, US; 167–186.

Smith S, Duchesne C, Lewkowicz A. 2019. Tracking changes in permafrost thermal state in northern Canada. Cold Regions Engineering: 670–677

Stadnyk TA, Déry SJ. 2021. Canadian continental-scale hydrology under a changing climate: a review. Water (Switzerland) 13 (7): 1–14 DOI: 10.3390/w13070906

Stewart I. 2009. Changes in snowpack and snowmelt runoff for key mountain regions. Hydrological Processes 23: 78–94 DOI: 10.1002/hyp

Sturm M, Charles R, Tape K, Racine C, Tape K. 2001. Climate change: increasing shrub abundance in the Arctic. Nature 6 (6837): 141–150 Available at: http://dx.doi.org/10.1038/35079180

Swann AL, Fung IY, Levis S, Bonan GB, Doney SC. 2010. Changes in arctic vegetation amplify high-latitude warming through the greenhouse effect. Proceedings of the National Academy of Sciences of the United States of America 107 (4): 1295–1300 DOI: 10.1073/pnas.0913846107

Van Loon AF, Laaha G. 2015. Hydrological drought severity explained by climate and catchment characteristics. Journal of Hydrology 526: 3–14 DOI: 10.1016/j.jhydrol.2014.10.059

Van Tiel M, Teuling AJ, Wanders N, Vis MJP, Stahl K, Van Loon AF. 2018. The role of glacier changes and threshold definition in the characterisation of future streamflow droughts in glacierized catchments. Hydrology and Earth System Sciences 22 (1): 463–485 DOI: 10.5194/hess-22-463-2018

Viviroli D, Wehren B, Weingartner R, Scha B. 2010. General characteristics of alpine waters. In Alpine Waters, Bundi U (ed.). Springer: Berlin; 17-58. DOI: 10.1007/978-3-540-88275-6

Wallace CA, Baltzer JL. 2020. Tall shrubs mediate abiotic conditions and plant communities at the taiga–tundra ecotone. Ecosystems 23 (4): 828–841 DOI: 10.1007/s10021-019-00435-0

Walvoord MA, Kurylyk BL. 2016. Hydrologic impacts of thawing permafrost: a review. Vadose Zone Journal 15 (6) DOI: 10.2136/vzj2016.01.0010

Walvoord MA, Voss CI, Wellman TP. 2012. Influence of permafrost distribution on groundwater flow in the context of climate-driven permafrost thaw: example from Yukon Flats basin, Alaska, United States. Water Resources Research 48 (7): 1–17 DOI: 10.1029/2011WR011595

Wang Q, Fan X, Wang M. 2016. Evidence of high-elevation amplification versus Arctic amplification. Scientific Reports 6 (November 2015): 1–8 DOI: 10.1038/srep19219

Wilcox EJ, Keim D, de Jong T, Walker B, Sonnentag O, Sniderhan AE, Mann P, Marsh P. 2019. Tundra shrub expansion may amplify permafrost thaw by advancing snowmelt timing. Arctic Science: 1–16 DOI: 10.1139/as-2018-0028

Woo MK. 1986. Permafrost hydrology in North America. Atmosphere - Ocean 24 (3): 201–234 DOI: 10.1080/07055900.1986.9649248

Woo MK, Rouse W, Stewart R, Stone J. 2008. The Mackenzie GEWEX study: a contribution to cold region atmospheric and hydrologic sciences. In Cold Region Atmospheric and Hydrologic Studies. The Mackenzie GEWEX Experience: Volume 1: Atmospheric Dynamics, Woo MK (ed.). Springer: New York; 507.

Woo MK. 2012. Permafrost Hydrology. Springer: New York. DOI: 10.1007/978-3-642-23462-0

Woo MK, Thorne R. 2003. Streamflow in the Mackenzie basin, Canada. Arctic 56 (4): 328–340 DOI: 10.14430/arctic630

Zhang T, Barry R., Knowles K, Ling F, Armstrong RL. 2003. Distribution of seasonally and perennially frozen ground in the northern Hemisphere. In Permafrost, Phillips M, Springman S, Arenson L (eds). Swets & Zeitlinger: Lisse; 1289–1294.

1.6 Figure

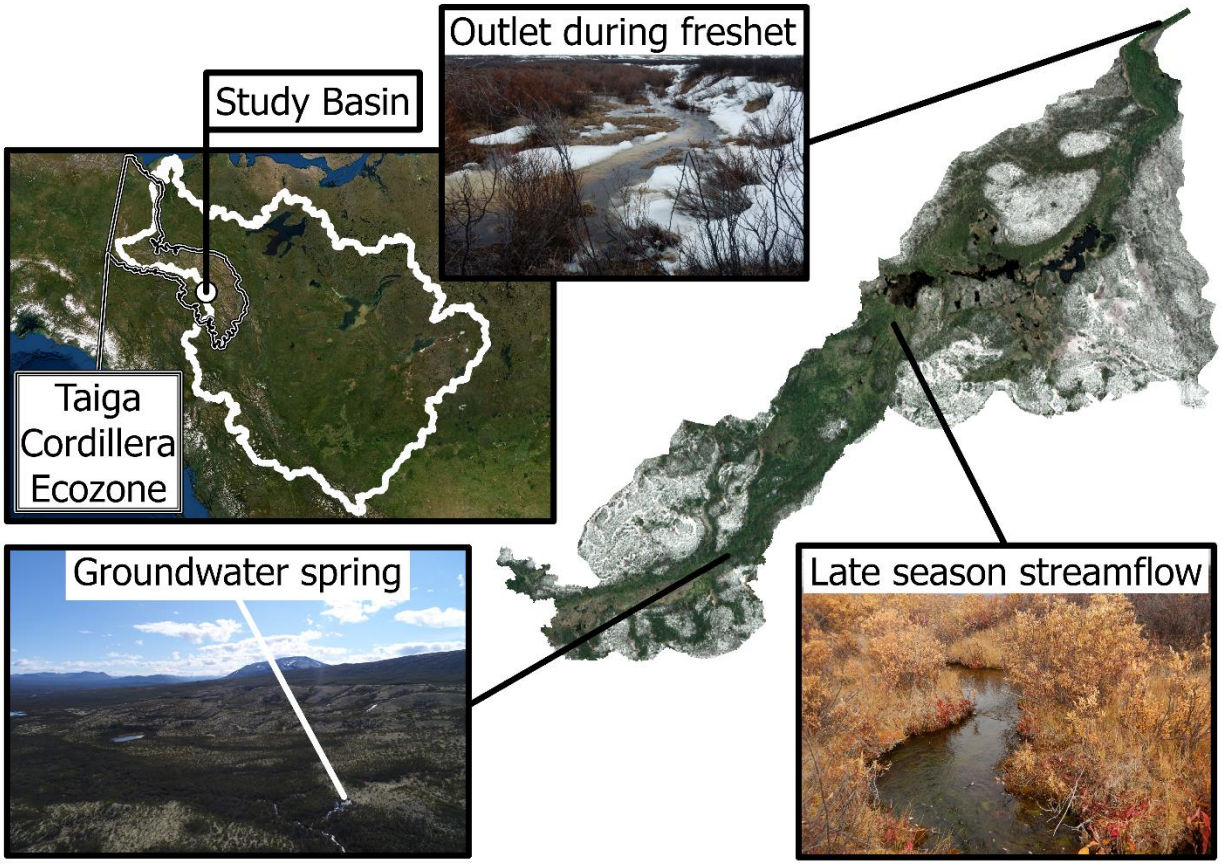

Figure 1-1: Location of the study basin relative to the Taiga Cordillera ecozone and the Mackenzie River basin. The study basin is shown in true color with inset images of the main channel network as observed during the 2019 open water season.

2. Mackenzie River basin alpine tundra land cover classification and associated hydrological properties

2.1 Abstract

The Mackenzie River Basin (MRB) drains 1.8 million km^2 and produces 7 % of total annual freshwater contributions to the Arctic Ocean. Approximately 60 % of MRB discharge is sourced from mountainous subbasins, yet hydrological study and understanding of the MRB has historically focused on lowland regions or relied on findings from alpine areas outside of the MRB. To address this knowledge gap, a field study was conducted to characterize the hydrology of a representative alpine tundra catchment within the Taiga Cordillera of the MRB. A range of hydrological properties were compared among the five dominant cover classes of peat plateau, fen, riparian swamp, glaciofluvial upland, and open water. A conceptual model is presented that accounts for flow paths among storage compartments and the hydrological processes controlling transfers within and from the study basin. Peat plateaus are isolated from sub-permafrost groundwater, routing precipitation inputs laterally to neighbouring terrain via a shallow, highly conductive suprapermafrost zone. Fens serve as primary contributors to the channel network, receiving throughflow from peat plateaus, as well as direct precipitation inputs. Riparian swamps also contributed to streamflow directly via surface and subsurface flow paths. Glaciofluvial uplands were the least effective at retaining moisture, routing inputs vertically to recharge groundwater and remaining disconnected from the channel network year-round. This study is an essential first step for future attempts to explicitly model and predict the hydrological function of alpine shrub tundra terrain in the Taiga Cordillera and the large regional river systems to which it contributes.

Keywords: hydrology, alpine, tundra, permafrost, land cover classification, Taiga Cordillera ecozone, Mackenzie River basin

2.2 Introduction

Northern latitudes have been warming at unprecedented rates and are expected to warm further and receive greater annual precipitation as climate change continues (McGuire *et al.*, 2006; IPCC, 2013; Environment and Climate Change Canada, 2021). Furthermore, higher elevation regions have reported greater rates of warming (Beniston, 2003), making alpine portions of large northern basins a priority area for understanding the hydrological implications of climate change. For example, 28 % of global permafrost is located in high mountain areas (Hock *et al.*, 2019) and due to its impeding effect on percolation into deeper groundwater reservoirs (Carey and Woo, 1999; Walvoord *et al.*, 2012), the loss of permafrost is anticipated to dampen annual peak flows and increase winter baseflow as a greater proportion of near-surface runoff is routed to aquifer recharge instead of surface flow (Walvoord *et al.*, 2012; Lamontagne-Hallé *et al.*, 2018). This is consistent with regional trends of increasing baseflow in recent decades observed in northern Canada (Jacques and Sauchyn, 2009) and elsewhere (Hock *et al.*, 2019).

In distributed hydrological models, hydrological properties and physical processes governing vertical water flux across the ground-atmosphere interface and horizontal water flux over or below the ground surface are made spatially explicit (Pomeroy *et al.*, 2007; Rasouli *et al.*, 2014; Krogh *et al.*, 2017; Craig *et al.*, 2020; Marsh *et al.*, 2020). In these hydrological models, ground surface characteristics are particularly important as they modulate energy and mass transfers across the soil matrix-atmosphere continuum (Kurylyk *et al.*, 2016; Hoylman *et al.*, 2019). The soil surface-atmosphere interface is also important in atmospheric circulation simulations, where

land cover designation constrains turbulent and radiative exchange at the lower boundary (Pomeroy *et al.*, 1998; Verseghy, 2000; Bélair *et al.*, 2003; Knist *et al.*, 2017). Furthermore, estimates of atmospheric inputs for a basin (Masson *et al.*, 2003; Kerkhoven and Yew Gan, 2008) and the hydrological response it generates (Rasouli *et al.*, 2014; Hoylman *et al.*, 2019) are less accurate when neglecting the effects of sub-grid heterogeneity (Armstrong and Martz, 2008; Kerkhoven and Yew Gan, 2008) and this is particularly important where spatial variability of hydrological parameters is greater, such as in alpine regions (Marsh *et al.*, 2020).

Field data on the physiographic, surface, and subsurface properties needed to parameterize and verify hydrological models are often lacking in cold climate systems (Pomeroy *et al.*, 2007; Walvoord and Kurylyk, 2016; Laudon *et al.*, 2017), particularly in alpine tundra areas (de Jong *et al.*, 2005). Terrain physiography is an important input in the discretization process, with aspect, slope, and elevation influencing basin mass and energy balances (Carey and Woo, 2001b; de Jong *et al.*, 2005; Rasouli *et al.*, 2014; Craig *et al.*, 2020). The representation of surface properties, including albedo, vegetation height, and density are also important (Ménard *et al.*, 2014) due to their influence on snowpack distribution, interception, and evapotranspiration rates (Armstrong and Martz, 2008; Craig *et al.*, 2020). Subsurface properties such as saturated hydraulic conductivity, thermal conductivity, and effective particle size are common parameters used for estimating mass and energy balances (Krogh *et al.*, 2017; Craig *et al.*, 2020; Marsh *et al.*, 2020), with water content particularly important in cold climate systems because of its influence on thaw rate, infiltration (Hoylman *et al.*, 2019; Craig *et al.*, 2020), and evaporation from the soil surface (Rasouli *et al.*, 2014; Craig *et al.*, 2020). The parameters necessary for refining water balance calculations are often assigned based on biophysical landscape units

(Pomeroy *et al.*, 2007), land cover classes, and/or soil classes (Kerkhoven and Yew Gan, 2008; Craig *et al.*, 2020).

The Mackenzie River Basin (MRB) covers 1.8 million km^2, encompasses 20 % of the Canadian land mass, and generates the greatest annual discharge of any river in Canada (Woo *et al.*, 2008b). Much of the Mackenzie Mountains are in the precipitation shadow of the Selwyn Mountains (Woo *et al.*, 2008b), yet mountainous sub-basins still contribute 60 % of the total MRB discharge from 40 % of the basin area (Woo and Thorne, 2003). For example, in the Athabasca River Basin, the upper mountainous region covers ~6 % of the drainage area, yet produces >23 % of the annual runoff (Peters *et al.*, 2013). Furthermore, a large portion of annual precipitation within the MRB falls as snow (up to 60 % annual) (Woo *et al.*, 2008b) and trends of earlier annual snowmelt are most pronounced in the mountainous subbasins (Derksen *et al.*, 2008) with implications downstream.

Field studies developing model structure and confirming land cover classifications within the MRB have been conducted in the tundra-taiga transition region where permafrost is continuous (Endrizzi *et al.*, 2011; Krogh *et al.*, 2017), and boreal systems where permafrost is discontinuous (Quinton *et al.*, 2003; Quinton and Baltzer, 2013), but not the western mountainous areas that compose the continental divide. In the absence of hydrological field studies in the alpine tundra portions of the MRB, researchers, water managers, and other stakeholders have relied on knowledge and predictive tools arising from studies beyond the extent of the MRB, such as Granger Basin, Yukon (60.5°N, 1312 masl) (Carey and Quinton, 2004; Quinton *et al.*, 2005; Debeer *et al.*, 2014; Rasouli *et al.*, 2014), Marmot Creek, Alberta (50.9^{o} N, 2300 masl) (Debeer *et al.*, 2014; Harder *et al.*, 2015), and other locations internationally (Genxu *et al.*, 2012; Landry *et al.*, 2014; Ménard *et al.*, 2019).

Field studies within the alpine tundra of the MRB are needed to provide direct measurements of the variables and parameters necessary for hydrological model calibration and execution. The objectives of this chapter are to 1) identify and characterise the major flow paths and storage compartments controlling the water balance of a Taiga Cordilleran alpine tundra catchment contributing to the Mackenzie River, and 2) present a conceptual model that describes the major hydrological processes that should be represented in numerical models of these headwater basins. A series of hydrological field observations and substrate samples were collected during 2018-2019 within a ~0.8 km^2 biophysically representative headwater basin to quantify spatial heterogeneity of local land cover 1) physiography, 2) surface hydrology, and 3) subsurface hydrology. This study is focused on the major land cover classes individually, their hydrological interactions, and the overall basin hydrological response to precipitation inputs.

2.3 Data and methods

2.3.1 Study site

The alpine tundra basin selected (63.3°N, 129.8°W, 1264.8 – 1333.1 masl, 0.8 km^2) occupies a low-lying portion of the Tsichu River valley within the Taiga Cordilleran ecozone and is a first order stream in the headwaters of the Mackenzie River basin (Figure 2.1a,b). The study basin was first visited during a 2017 preliminary field visit and selected based on 1) accessibility via the North Canol Heritage Trail and 2) its representativeness of shrub tundra terrain within the broader ecozone. The alpine tundra portion of the Taiga Cordillera ecozone lies between contiguous forests at lower elevation and rocky outcrops above; an area estimated to cover 38.8 % of the Taiga Cordilleran extent within the MRB (Canada Centre for Remote Sensing (CCRS) *et al.*, 2020). The nearest open-access climate station (Macmillan Pass; Climate ID: 2100693; 1379 masl), ~10 km west of the study basin, reports 1971-2000 mean annual air temperatures (MAAT) of -8.3 °C, with

January and July monthly means of -26.2 °C and 10.0 °C, respectively (Environment Canada, 2020).

Based on the 2017 field survey, five distinct cover classes were identified for comparison within the study basin: glaciofluvial upland, riparian swamp, fen, peat plateau and open water (Figure 2.1c). Glaciofluvial upland has sparse *Betula glandulosa* shrub cover above *Cladina spp.* and *Cetraria spp*. lichen mats on well-drained soils. Riparian swamp has *Salix sp.* shrub cover above a mix of *Sphagnum sp.* and brown moss ground cover atop minerotrophic soils with water table near-surface. Fen is the other wetland class present, distinct from the riparian swamp due to *Carex aquatilis* sedge meadows and >40 cm deep peat soils (National Wetlands Working Group, 1997). Peat plateau features also have soils with >40 cm peat, but also shallow ice-rich permafrost and ground cover more similar to the glaciofluvial uplands. Open water consisted of a series of a small ponds connected to the main channel network flowing towards the outlet.

2.3.2 Land cover classification

Land cover classes within the basin were assigned with a supervised maximum likelihood classification scheme created with ArcGIS Pro (Esri, Redlands, CA, USA). An object-oriented feature extraction was selected instead of a pixel-based approach to increase accuracy and reduce noise in the data (Chasmer *et al.*, 2020). This process utilized spectral characteristics captured with Worldview 2 satellite imagery, a multispectral 8-band remote sensing product with 0.46m resolution (DigitalGlobe Inc., Westminster, CO, USA). No cloud cover or shadowing was visible within the extent of the basin during the Worldview 2 image acquisition (June 20 2016). The spectral signatures for each cover class were sourced from manually delineated training areas (Appendix 1). Training area extents covered most locations of physical hydrology sampling, instrumentation, and observation documented in the following sections, but excluded 12

verification points visited on 10 September 2019 to confirm the classification accuracy (Figure 2.1d). Size constraints were placed on the classification using a segmented image of the raster with a minimum segment size of 20 pixels (9.2 m). Because the main channel network was often too narrow to be accurately classified with this segment size, a flow accumulation model with 0.5 m resolution was generated from the ArcticDEM product (Polar Geospatial Center, St. Paul, MN, USA) to assign the main channel length and a manually constructed polygon was overlain using available Worldview and drone orthomosaic imagery to corroborate the extent of the channel network.

2.3.3 Physiography

Remote sensing data were used to assign a series of physiographic characteristics to each land cover. First, the topographical boundary of the basin was delineated using a combination of ArcticDEM and drone orthomosaic DEM data. ArcticDEM covered the total basin area, but was of insufficient elevational accuracy to distinguish the divide in a low relief portion towards the headwaters (Figure 2.1b). Therefore, a DEM was created from 604 drone images taken 8 August 2019 processed in the structure from motion (SfM) photogrammetry software Pix4D Mapper Pro (Pix4D inc., Prilly, CH), generating an orthomosaic with sufficient pixel size (2.5 cm) and positional accuracy (8.8 cm xy, 18 cm z) to discern the basin boundary.

Cover classes were assigned elevation, slope, and aspect by combining the classified image with other remote sensing data sets. Elevation values were assigned to each segment generated in the land cover classification process using an ArcticDEM overlay, while elevation above and distance from the channel network were assigned relative to the channel network polygon created as part of the land cover classification. Slope and aspect values of each segment required better accuracy and resolution than ArcticDEM, and as such, 441 drone images were captured on 7 September

2018 to generate a georeferenced orthomosaic and high-resolution DEM created with Pix4D Mapper pro. Georeferencing was achieved with a Canadian geodetic survey benchmark (m222 bench) and 4 dGPS ground control points measured with a Leica Viva series GS10 differential GPS (Leica Geosystems AG, Heerbrugg, CH) on 8 September 2018. The density of ground control points was sufficient to result in georeferenced mosaics with RMSE of 0.01 m, less than the RMSE of 0.064 m generally considered acceptable for high-resolution DEMs (Roos *et al.*, 2018). The final DEM used to calculate slope and aspect of each 9.2 m resolution classified segment covered 38 % of the total basin area, with 1.4 cm xy accuracy and 21 cm z accuracy. Means and standard deviations of each physiographic variable were calculated for each land cover class using the ArcGIS Pro zonal statistics tool (Esri, Redlands, CA, USA).

2.3.4 Ground surface properties

2.3.4.1 SWE_{MAX}

Winter maximum snow water equivalent (SWE_{MAX}) represents a large portion of total annual precipitation accumulating over the winter months and has great hydrological importance in alpine nival systems. SWE_{MAX} was measured on 18 April 2018 and 17 April 2019 before snowpack ripening began and was calculated based on sample weights and depths collected with a 7 cm diameter snow tube sampler – a technique that commonly results in measurement errors of ±10 % (Pomeroy and Gray, 1995). Each cover class had a 60 m snow survey transect established in 2018 and was sampled with a snow tube sampler at 30 non-repeating randomly selected locations with a minimum spacing of 0.5 m.

2.3.4.2 Vegetation

Vegetation creates a roughness element on the ground surface, with implications for evapotranspiration, snowpack redistribution, and the mass-energy balance of the subsurface

storage volume below. In this study, the roughness length of the ground surface vegetation was estimated with the following equation:

Equation 2.1: $z_O = 0.5h^*s/S$

where z_O is the roughness length (cm), h^* is the average vegetation height (cm), s the silhouette area in the vertical plane (cm^2) and S the specific area (cm^2) in the horizontal plane (Lettau, 1969). s/S is also known as the frontal area index (λ), which can be estimated from canopy area index (Λ) based on the relationship $\Lambda = 2\lambda$ when roughness elements are arranged isotropically (Raupach, 1994). h^* and Λ measurements were collected at fifteen 4 m^2 biophysical quadrats spaced randomly along each land cover 60 m transect. Each quadrat was segmented into 16 0.25 m^2 subgrids for measurement of h^* from a randomly selected plant and Λ above the ground surface. This survey was done during maximum leaf out conditions (1 to 11 August 2019) to provide values representative of maximum surface roughness from the 320 random heights collected from each cover class (Brown and Hugenholtz, 2012).

2.3.4.3 Land cover albedo

Land cover albedo is an important variable in energy balance calculations that estimate snowmelt, soil thaw, and evaporation rates. At a central location within the peat plateau training area, a CNR4 four-component net radiometer (Kipp and Zonen, Delft, NL) measured incoming and outgoing longwave and shortwave radiation, allowing for estimation of landscape albedo at one-minute intervals and average values to be recorded every 30 minutes on a Campbell Scientific CR300 data logger (Logan, UT, US). Simultaneously, an albedometer station pairing a SP-110 upward facing and a P-610 downward facing shortwave pyranometer (Apogee Inc., Logan, UT, USA) measured landscape albedo within each training area (Figure 2.1d). The albedometer measured landscape albedo at one-minute intervals and recorded average values every 30 minutes on a Campbell

Scientific CR10x data logger (Logan, UT, US). The station was relocated to include periods within each cover class between 24 May and 30 August 2019, providing records of 14-30 days at each location. Biases in readings due to changing solar angle, atmospheric conditions, and sensor sensitivity were corrected by standardizing data to the CNR4 readings and limiting observations to a four hour window symmetrical to solar noon (Scarlett *et al.*, 2017).

2.3.5 Subsurface properties

Subsurface properties control the flow paths and storage compartments available for water inputs received from above ground. A series of subsurface instruments, imaging transects, test pits, and substrate samples were collected to characterize the subsurface and compare characteristics of each land cover class.

2.3.5.1 Soil stratigraphy

Permafrost presence/absence, organic soil thickness, and depths of glacio-fluvial deposits above bedrock were each estimated with subsurface imaging. During the late fall when thaw depths were at maximum, a combined approach utilizing Electrical Resistivity Tomography (ERT), Ground Penetrating Radar (GPR), verification boreholes, and soil probe measurements were implemented to map the subsurface of each land cover class (Figure 2.1d). ERT transects were completed between 2 to 6 September 2018 using an AGI Supersting R8 unit (Advanced Geosciences Inc., Austin, TX, USA). 56 electrodes were distributed with 1 m spacing and signals sequenced with an inverse Schlumberger array. Data processing and image inversion were completed with EarthImager 2D version 2.4.0 (Advanced Geosciences Inc., Austin, TX, USA). Each transect was topographically corrected before inversion with elevations collected using the Leica Viva series GS10 differential GPS. ERT subsurface images had 0.5 m resolution and a maximum penetration depth of 11.2 m (Appendix 2).

In the glaciofluvial upland, coarse, dry mineral substrates did not have sufficient contact resistance for effective ERT imaging (data not shown; RMS 55 %). As an alternative, GPR imaging was completed along a 92 m glaciofluvial upland transect in August 2019 using a RAMAC radar control unit attached to 500 MHz unshielded and/or 100 MHz rough terrain shielded antenna (Mala Geoscience, Mala, Sweden). Data processing, image filtering, and topographical correction were completed with ReflexW Version 7.2.3 (Sandmeier Software, Karlsruhe, Germany) to generate subsurface images with 0.1 and 1 m resolution for 500 and 100 MHz antennae, respectively.

Soils test pits were dug within each land cover class to establish mean strata thickness and soil characteristics between June 3 and September 9 2019. In total, 44 test pits were dug within the study basin, 26 within the training areas and 18 beyond to confirm the remote sensing classification (Figure 2.1d). Living vegetation, organic soil, and mineral soil depths were measured and identified according to the Canadian soil classification system (Canada Soil Classification Working Group, 1998). At 20 soil pits, samples of organic and/or mineral substrates were collected for laboratory analysis of hydraulic conductivity, dry bulk density, and effective particle size (Appendix 3). At one location within each terrestrial land cover, stilling wells were installed to record average water table depths below ground surface between 12 June and 9 September 2019. HOBO U20 and/or U20L pressure transducers recorded water table depths at 30-minute intervals with ± 1.5-3 cm accuracy after atmospheric correction (Onset Computer Corp, Bourne, MA, USA).

2.3.5.2 Temperature and volumetric moisture content

Thermal and moisture regimes of near-surface soils were monitored below each terrestrial cover class. 5TM sensors (Decagon Devices, Pullman, WA, USA) measured temperature and volumetric moisture content (VMC) at one location within the riparian swamp, fen, and peat plateau, and two locations within the glaciofluvial upland. 5TM sensors were installed in array at

10, 20, 30, 40, and 50 cm below ground surface and set to measure at one-minute interval with an EM50 data logger recording 30-minute averages between 10 September 2018 and 10 September 2019 (Decagon Devices, Pullman, WA, USA). Additionally, a peat plateau and peat plateau-fen transitional feature were instrumented with CS109 and CS655 arrays to collect temperature and VMC readings at one-minute intervals with a CR300 data logger recording 30-minute averages over the same timeframe (Logan, UT, USA). Sensors were installed in the peat plateau at 10, 20, 30, and 40 cm below ground surface and in the peat plateau-fen transitional feature at 10, 20, 30, 40, 60, and 80 cm below ground surface. CS109 sensors at 10, 30, and 80 cm depth measured temperature while CS655 sensors at 20, 40, and 60 cm depth measured temperature and VMC. Comparisons of daily mean VMC were limited to 19 April to 31 August 2019 at 10, 20, and 50 cm depths below ground surface as this interval was when liquid water was detectable and sensor malfunctions made comparison of VMC at other depths untenable.

At five of the soil temperature arrays, annual records allowed for estimates of zero annual amplitude temperatures and depths. Both zero annual amplitude temperatures and depths were estimated with exponential fitting functions through maximum and minimum temperature values, a technique commonly referred to as a trumpet curve (Romanovsky *et al.*, 2010). Given the relatively shallow depth of observations relative to the estimated zero annual amplitude depths, a linear fitting function was also applied to mean annual temperatures as an alternative estimate of zero annual amplitude temperature at each location.

2.3.5.3 Saturated hydraulic conductivity

Estimates of mineral and organic saturated hydraulic conductivity (K_{SAT}) were based on a combination of grain size distribution and permeameter testing in the laboratory (Appendix 3). Mineral samples were collected from the top 50 cm of the ground surface at 14 verification points

within the glaciofluvial upland, riparian swamp, and fen. Organic soil samples were collected from the top 10 cm of the ground surface at 13 locations within the riparian swamp, fen, and peat plateau (Figure 2.1d).

2.3.5.4 Thermal properties

Thermal properties of the soil matrix control heat transfer and retention, with major implications for the ability of soil to receive and retain moisture. A KD2 Pro Thermal properties analyzer (Decagon Devices, Pullman, WA, USA) was used to measure thermal conductivity (*K*), specific heat capacity (*C*), and thermal diffusivity (*D*) of near-surface soils (0 – 3 cm below ground surface) between May 30 and September 9 2019. To ensure similar antecedent conditions, values were collected from all land covers within 6-hour observation windows and >6 hours after the most recent precipitation event. Previous studies of similar coarse grained mineral soils reported issues with inconsistent thermal contact in coarse grained substrates (Ebel *et al.*, 2019). As such, outliers attributed to sensor malfunction related to convective heat flux and/or poor probe contact were identified and removed according to the 1.5*IQR rule, resulting in n values of 93, 100, and 98 for *K*, *C*, and *D*, respectively.

2.3.6 Statistical analysis

All field samples and observations collected were stratified by land cover class to allow for statistical comparison when possible. A Kruskal-Wallis rank sum test was conducted for each hydrological property with a sufficient sample size to determine if significant differences between group means were present. If significant differences were present, a Wilcoxon rank sum test was conducted for pairwise comparisons between group levels with corrections for multiple testing (Hollander and Wolfe, 1999). The confidence level for each test was set at 95 % and all statistical

assessments were conducted with the computer program R stats package 3.6.3 (R Core Team, 2020).

2.4 Results

2.4.1 Land cover classification

The land cover classes each comprised 20 % to 31 % of the basin area, while the open water portion was <1 %. These values were used to derive basin weighted averages for each surface (Tables 2.1 and 2.2) and subsurface (Table 2.3) hydrological property assessed. Of the twelve verification points surveyed beyond the training area extents, the classification scheme correctly assigned ten and misclassified two peat plateau locations as fen (Figure 2.1).

2.4.2 Physiography

The study basin contributing area was relatively limited (0.80 km^2), with elevations ranging from 1264.8 –1333.1 masl (Figure 2.1). The main channel had a gradient of 2.5 %, with a 2747 m channel length across a 68.3 m change in elevation. Riparian swamp areas had the greatest mean slope, followed by fen, peat plateau, and glaciofluvial upland (Table 2.1). These slope values should be interpreted with caution due to the inability of the high-resolution DEM to remove surface roughness elements that can create artificially large changes in elevation over short distances. All land covers were represented throughout the range of basin elevations, but glaciofluvial upland and peat plateau had the greatest mean distance from and elevation above the channel network while the riparian swamp and fen were closer to the channel (Table 2.1). All land covers had a similar distribution of aspect, with a tendency towards south facing with broad ranging variance (Table 2.1).

2.4.3 Ground surface properties

2.4.3.1 SWE_{MAX}

Among the cover classes, there were significant differences in SWE_{MAX} (Chi square = 119.94, p = 2.2e-6, df = 4). During the winter months, the fen retained the greatest amount of SWE (SWE_{MAX} 164 ± 68 mm), representing 51 % of total SWE within 31 % of the basin area. Open water retained the least (SWE_{MAX} 66 ± 32 mm) while SWE_{MAX} values of the other land covers were similar to each other and intermediate to the fen and open water values (Table 2.2).

2.4.3.2 Vegetation

Among the land covers, there were significant differences in average vegetation height (Chi square = 28.9, p = 2.4e-6, df = 3), canopy area index (Chi square = 20.5, p = 1.3e-4, df = 3), and roughness length (Chi square = 29.7, p = 1.6e-6, df = 3). Land covers with taller average vegetation heights and roughness lengths (glaciofluvial upland and riparian swamp) were found atop thinner organic soils without substantial peat deposits. Additionally, riparian swamps supported the greatest canopy area index (Table 2.2).

2.4.3.3 Land cover albedo

Statistically significant differences were found among land cover albedos (Chi square = 26.2, p = 8.5e-6, df = 3), but the close grouping of mean values suggests no meaningful difference exists in the shortwave radiative balance of these land covers (Table 2.2).

2.4.4 Subsurface properties

2.4.4.1 Soil stratigraphy

Soil types within the basin included hydric mesisols in the fens and terric mesic organic cryosols atop the peat plateaus with von Post humification scale values ranging from six to eight (Canada

Soil Classification Working Group, 1998). Based on verification boreholes, the organic strata thickness was 48 cm (n=1) in the peat plateau and 122 cm (n=1) in the fen (Figure 2.2). The riparian swamp organic strata thickness was 13 ± 7 cm (n=12), while the glaciofluvial uplands had little to no organic soil present with a thickness of 3 ± 1.5 cm (n=13) (Figure 2.2). The dry bulk density of organic soils within the study basin was 0.116 g cm^3 which is more dense than the 0.06 g cm^3 typical of near-surface organic soils found in lowland regions of the MRB (Woo *et al.*, 2008a).

The glaciofluvial upland mineral substrates were regosolic turbic cryosols possessing evidence of cryoturbation, while the riparian swamp soils were classified as gleyed humic regosols (Canada Soil Classification Working Group, 1998). Boreholes confirmed mineral deposits within the study basin >131 cm and >230 cm below ground surface (Figure 2.2). The average mineral sediment bulk density was 1.6 g cm^{-3}, the same as reported elsewhere in the MRB (Woo *et al.*, 2008a) and similar to that of silty (1.0 – 1.5 g cm^{-3}) and rocky (0.57 to 1.61 g cm^{-3}) soils in Alaska (Ebel *et al.*, 2019). Additionally, the effective particle size of glaciofluvial upland mineral sediments (641 µm) was larger than the riparian swamp (27 µm), consistent with the negligible clay mass fraction of glaciofluvial samples and 16–27 % clay content of the riparian swamp samples.

Mean water table depths from June to September 2019 were closest to the ground surface in the riparian swamp (16.4 ± 2 cm). The fen also maintained a water table near ground surface (32.6 ± 1 cm), while wells within the glaciofluvial upland and peat plateau remained dry year-round (Figure 2.2). Based on borehole excavations, the water table remained at a depth greater than 126 and 230 cm below ground surface in the glaciofluvial upland and peat plateau, respectively.

Based on ERT tomograms, shallow permafrost was present throughout the peat plateau transect (Figure 2.3c), limited in extent and deeper within the fen (Figure 2.3b), and isolated within the riparian swamp (Figure 2.3a,d). Permafrost presence was confirmed in the peat plateau (ice-rich

mesic peat at 48 cm depth) (Figure 2.3c) and in the riparian swamp (ice-rich glaciofluvial sediments at 52 cm depth) (Figure 2.3d) with borehole excavations during maximum thaw conditions. The contact resistance values of ERT surveys completed on riparian swamp, fen, and peat plateau features were sufficient to generate subsurface images with RMS from 1.84-8.46 % (Figure 2.3).

Frost probe depths are considered a more accurate measure of peat plateau permafrost table depth due to the limited resolution (0.5 m) of the ERT array (1 m electrode spacing). Frost probe measurements verified permafrost throughout the peat plateau (53 ± 10 cm below ground surface (n=56)) at a depth often shallower than estimates based on resistivity (Figure 2.3c). Frost probe measurement also confirmed permafrost at 96 cm below ground surface at one location along the fen transect (Figure 2.3b), but in general, probing was unreliable in glaciofluvial upland, riparian swamp, and fen transects where the depth of refusal was caused by stones and cobbles instead of ice content.

Based on the GPR images, no permafrost or bedrock interface was visible within the top 6.5 m of the glaciofluvial upland deposits (Figure 2.4). Signal attenuation of GPR antennae limited the depth of penetration below the glaciofluvial upland transect to ~6.5 m at 100 MHz and ~1.7 m at 500 MHz frequencies (Figure 2.4). ERT tomograms also confirmed no bedrock within 11.2 m of the ground surface below the other land covers.

2.4.4.2 Temperature profiles

The warmest temperature profile was located in the fen, with a zero annual amplitude depth of 9.5 m maintaining a temperature between 1.4 and 3.2 °C (Figure 2.5c). The glaciofluvial upland temperature profiles were also relatively warm, with zero annual amplitude depths between 6.5 and 10.8 m below ground surface maintaining temperatures between 0.4 to 1.3 °C (Figure 2.5a,

b). The peat plateau profile was the coldest, with a zero annual amplitude depth of 2.7 m maintaining a temperature between -0.7 and -2.1 °C that indicates a permafrost table depth of 50 cm below ground surface (Figure 2.5e). The fen–peat plateau transitional feature profile shared properties of both fen and peat plateau, with a zero annual amplitude depth of 0.8 m maintaining a temperature between -0.1 and 0.5 °C (Figure 2.5c). A data logger failure at the riparian swamp location resulted in loss of data during the period when annual minimum temperatures occur. As a result, estimates of mean annual ground temperature and the zero annual amplitude depth for riparian swamp were not obtainable.

2.4.4.3 Saturated hydraulic conductivity

The geometric mean K_{SAT} of organic soils collected within the top 10 cm of the soil profile were greatest within the riparian swamp (148 m day^{-1}), followed by the peat plateaus (169 m day^{-1}) and the fens (50 m day^{-1}). Geometric mean K_{SAT} for mineral sediments was lower, ranging from 0.0065 m day^{-1} in the riparian swamp to 8.1 m day^{-1}in the glaciofluvial uplands (Figure 2.6). This illustrates a stark contrast in horizontal subsurface flow rates within the riparian swamp based on whether the saturated zone is in the organic layer, which was 13 ± 7 cm thick, or the underlying mineral sediments.

2.4.4.4 Volumetric moisture content

Among the land covers, there were significant differences in daily mean VMC at 10 cm (Chi square = 218.1, p < 2.2e-16, df = 3), 20 cm (Chi square = 226.6, p < 2.2e-16, df = 3), and 50 cm (Chi square = 446.5, p < 2.2e-16, df = 3) depths below ground surface. The riparian swamp maintained the greatest VMC at 10 cm depth (0.30 ± 0.12), while the fen was wettest at 20 cm (0.38 ± 0.23) and 50 cm (0.63 ± 0.02). The peat plateau profile was similar to the glaciofluvial

upland at 10 cm and 50 cm depths, but reported the second highest mean VMC at 20 cm (0.27 ± 0.14). The glaciofluvial upland was relatively dry at all depths (Table 2.3).

2.4.4.5 Thermal properties

Among the land covers, there were significant differences in surface soil *K* (Chi square = 11.2, p = 0.01, df = 3), *C* (Chi square = 28.8, p = 2.4e-6, df = 3), and *D* (Chi square = 28.8, p = 2.4e-6, df = 3). When comparing means, *K* was greater in the fen (0.27 ± 0.05 W $m*K^{-1}$) than the peat plateau (0.21 ± 0.10 W $m*K^{-1}$); *C* was greater within the riparian swamp (1.78 ± 0.75 MJ m^3*K^{-1}) and the fen (2.04 ± 0.56 MJ m^3*K^{-1}) compared to the other land covers; and *D* was greatest within the glaciofluvial upland (0.22 ± 0.04 mm^2 s^{-1}) and least within the fen (0.15 ± 0.02 mm^2 s^{-1}) (Table 2.3).

2.5 Discussion

Many of the physiographic and hydrological properties assessed varied with land cover class. These differences result in distinctive roles for each land cover class in routing inputs and maintaining the water balance of the study basin that is biophysically representative of alpine tundra within the Mackenzie River Basin and/or the Taiga Cordillera ecozone. A conceptual model is presented describing water flow paths and storage compartments within and from the study basin (Figure 2.7), but not all variables assessed presented meaningful differences based on land cover class. Specifically, landscape albedo was not included in the structure of the conceptual model because it varied little with land cover (Table 2.2). As such, we advise that models of climate (Masson *et al.*, 2003) and/or basin hydrology (Craig *et al.*, 2020) for alpine tundra areas with limited open water under growing season conditions apply an albedo value of 0.17 when necessary.

2.5.1 Peat plateau

Peat plateaus are upland features with sparse shrub vegetation (Table 2.2) and thick organic soils (Figure 2.2) covering 23 % of the basin area. Permafrost in the region is likely limited to areas with well developed organic soils, or higher elevation ridgetops beyond the extent of the study basin (AMAX Environmental Services, 1976). The presence of permafrost below peat plateau was confirmed with temperature profiles (Figure 2.5e), ERT imagery, verification bore hole, and frost probe measurements (Figure 2.3c). Below peat plateaus, large amounts of groundwater flow are routed laterally through the near-surface suprapermafrost zone where highly conductive organic soils are found (Figure 2.7) consistent with other studies establishing horizontal flow rates greater than vertical (Beckwith *et al.*, 2003) due to the relationship between increasing depth below ground surface and increasing degree of decomposition, decreasing pore size, and decline in K_{SAT} (Quinton *et al.*, 2008). The ice-rich permafrost in peat plateaus also precludes vertical flow between suprapermafrost and subpermafrost layers due to hydraulic conductivities as low as 8.6 e-10 m day^{-1} (Egginton and Dyke, 1990). In this study, the K_{SAT} of near-surface (0-10 cm) peat plateau soils (Figure 2.6) above permafrost bodies was similar to peat deposits studied at Granger basin near Whitehorse, YT, Siksik Creek near Inuvik, NT, and Scotty Creek near Fort Simpson, NT (Quinton *et al.*, 2008). This is also consistent with a larger scale modelling study conducted for the Yukon Flats basin that estimated the suprapermafrost can contribute 25 % of groundwater flow from <1 % of sediment volume available for storage and routing (Walvoord *et al.*, 2012). Furthermore, the relatively low VMC retained in peat plateau soils above the permafrost table (Table 2.3) affects the thermal properties of the peat, as shown by the relatively low *K* and *C* for this land cover (Table 2.3). This creates an insulating layer of

dry peat that enables the preservation of underlying permafrost (Jorgenson *et al.*, 2010; Seppälä, 2011).

2.5.2 Fen

Fens are low elevation features with sparse vegetation (Table 2.2), thick organic soils, and elevated water tables (Figure 2.2) covering 31 % of the basin. Fens were near the channel and with steep slopes (Table 2.1), but the mean slope reported is likely overestimated due to 1) DEM inaccuracies cause by surface vegetation, 2) misassignment of peat plateau areas as fen due to spectral similarities, and 3) the 9.2 m minimum segment size resulting in assignment of steep edged transitional areas as fen when elements of peat plateau were also present. However, fens were observed in the field to often have steep relief at their margins, which is consistent with the greater SWE_{MAX} accumulation compared to the other cover classes (Table 2.2). In cold climates the duration of snow-free conditions during fall/winter will influence ground refreeze, such that shallower frost tables are found where snowpack forms later and/or is thinner (Hayashi, 2013). In other study areas with continuous permafrost extent, deeper snowpack has been shown experimentally to cause warming ground temperature profiles and the eventual formation and persistence of taliks (O'Neill and Burn, 2017). The relatively warm (1.4-3.2 °C) and deep (950 cm below ground surface) zero annual amplitude at the fen location (Figure 2.5d) suggests the absence of permafrost near the ground surface and a year-round hydrological connection with the channel network (Figure 2.7). This is consistent with the ERT imagery, which estimated permafrost was limited to ~35 % of the survey transect and at >1 m below the ground surface (Figure 2.3b).

2.5.3 Riparian swamp

The riparian swamp covers 20 % of the basin area and has the greatest mean slope and shortest mean distance to the channel network (Table 2.1). A sharp relief at the interface of riparian swamp with neighbouring land covers was observed in the field, but the mean slope values reported are likely overestimated due to the inability of the DEM to effectively negate the dense willow canopy. The shallow organic soils atop fine grained mineral sediments found within the riparian swamp is typical of active and relic glaciofluvial channels in the distal zone of glacial activity (10 to 100s of km beyond glacier), where sedimentation of silts and clays can occur (Bennet and Glasser, 2009). The compromised ground temperature record for this land cover class complicates interpretation of near-surface thermal regime in the riparian swamp, but the ERT profile paired with borehole excavations suggests the subsurface is permafrost free for most of its extent (Figure 2.3a, d). The relatively high VMC (Table 2.3) and water table near the ground surface (Figure 2.2) create unlikely conditions for permafrost to persist and the thick and tall willow canopy (Table 2.2) is also typical of permafrost-free areas with excess groundwater in northern systems (Muller, 1947).

In other northern study basins with thin organic soils, the primary flow direction can transition from horizontal to vertical as the thaw front progresses into the mineral sediments (Quinton *et al.*, 2005). The riparian swamp in this study basin has similarly thin organic soils (Figure 2.2), but the partitioning of flow vertically as the thaw front progresses is likely not as pronounced due to the low K_{SAT} of the underlying riparian swamp mineral sediments (Figure 2.6). The K_{SAT} values reported for riparian swamp mineral sediments were ≥2 orders of magnitude lower than other substrates in the basin (Figure 2.6) with small effective particle size and clay mass fractions ranging from 16-27 % (Table 2.3). Additionally, the mean water table depth within the riparian swamp from June to September 2019 (16.4 ± 2 cm below ground surface) is close to the near-

surface organics (top 13 cm of the soil profile), which is where the most conductive soil is found in the study basin (Figure 2.6). As such, horizontal flow would be rapid during times of year when the water table is elevated. Furthermore, infiltration in the riparian swamp is limited when near-surface pore spaces are blocked by seasonal frost and/or basal ice, which can result in overland flow atop this land cover (Figure 2.7b). Evidence of overland flow in the riparian swamp was found as aufeis formations in April and braided melt channels extending into the riparian swamp beyond the banks of the channel network in May 2018 and 2019.

2.5.4 Glaciofluvial upland

The glaciofluvial upland covers 25 % of the total basin area and has the greatest mean distance from and elevation above the channel network (Table 2.1). Gentle slopes (Table 2.1) and relatively dry mineral deposits (Table 2.3) below thin organic soils (Figure 2.2) suggest the glaciofluvial uplands are relatively stable, though evidence of differential frost heaving and cryoturbation is found in some areas as circular and elongated patterned ground (Embleton and King, 1975). While patterned ground commonly forms above permafrost, with the exception of unsorted polygons, it cannot be taken as strict evidence of the presence of permafrost (Embleton and King, 1975). Excavation within the study basin confirmed the absence of permafrost to a depth of 126 cm below ground surface and GPR imagery showed no reflection interface that could be interpreted as permafrost to a depth of 6.5 m (Figure 2.4). A report by Gravelle and Livingstone (2013) includes well logs for excavations within a glaciofluvial upland feature <1 km from the study basin boundary that also do not mention ice or water content up to 381 cm below ground surface. This is consistent with the annual temperature profiles below glaciofluvial land cover reported in this study, which had zero annual amplitude depths of 650 and 1080 cm below ground surface maintaining temperatures of 0.4 and 1.3 °C (Figure 2.5a, b). This is also

consistent with the low *C* and correspondingly high *D* of these dry, loose mineral deposits (Table 2.3).

Given the rapid K_{SAT} (Figure 2.6), large effective particle size, negligible clay content and low VMC of glaciofluvial sediments (Table 2.3), infiltration within this cover class can be classified as unlimited (Granger *et al.*, 1984), such that precipitation inputs received are routed vertically to aquifer recharge (Figure 7). The mean K_{SAT} for glaciofluvial upland deposits in the study basin was 8.1 m day^{-1}, with some samples reporting similar values to those of highly permeable near-surface organic soils (Figure 2.6). The Gravelle and Livingstone (2013) report provides similar estimates of K_{SAT} for the coarse-grained sand and cobble deposits they describe (8.64-86.4 m day^{-1}). This is consistent with K_{SAT} estimates from other alpine settings, including talus slopes with thin or absent organic soils within the Lake O'Hara watershed in the Canadian Rockies (Muir *et al.*, 2011; Langston *et al.*, 2013) and the upper range of K_{SAT} for rocky soils within interior Alaska (Ebel *et al.*, 2019). The absence of permafrost and/or bedrock within the top 6.5 m of the ground surface (Figure 2.4) means no interface is present that could impede vertical flow and route water towards the channel network. A study by Carey and Woo (2001) similarly found subalpine hillslopes contributing to groundwater recharge and circumventing runoff via streamflow.

2.5.5 Cover class hydrological interactions

Individual land cover classes have distinct attributes that regulate the amount of water retained in storage (as described above), but their relative positions and proximity to the channel network make certain linkages more prevalent and important in regulating flow among land cover classes and water loss from the basin as a whole. Despite the relatively low topographic gradient of peat plateaus, precipitation inputs received by this land cover class are routed horizontally via highly

conductive subsurface flow paths to neighbouring lower elevation fens (Figure 2.7). This is similar to lowland boreal systems where permafrost plateaus contribute runoff to neighbouring wetland terrain (Quinton *et al.*, 2009; Quinton and Baltzer, 2013). In comparison, the fen land cover has a thick suprapermafrost layer that once thawed can store runoff from neighbouring terrain, but the highly conductive near-surface soils and elevated water table also result in preferential horizontal flow via this land cover. Given the close proximity of both fen and riparian swamp land covers to the channel network (Table 2.1), these areas act as primary contributors to streamflow (Figure 2.7).

Open water areas within the basin are largely connected to the channel network (Figure 2.1) and act as a conduit for channel discharge and/or aquifer recharge via channel bed infiltration (Figure 2.7). During the open water season, stream water residence times are brief due to the short length (2747m) and steep gradient (2.5 %) of the channel, while in the winter months, the ice cover of open water areas retain the smallest SWE_{MAX} of all land cover classes (Table 2.2). The reduced SWE_{MAX} relates to the small roughness length and lack of topography to shelter the snow from wind driven redistribution and sublimation (Pomeroy *et al.*, 2006). Fen and riparian swamp areas have the closest proximity to the channel network (Table 2.1) and vegetation properties that allow for capture of blowing snow losses from open water areas (Table 2.2).

Finally, glaciofluvial uplands within the basin are isolated from the channel network and do not contribute to channel discharge (Figure 2.7). Instead, horizontal flow paths link precipitation received by glaciofluvial uplands to groundwater aquifers at depth. Such aquifers could be local, across 1-10s of kilometres, similar to the source water springs in the upper reaches of this study basin (Figure 2.1) and other alpine environments (Ma *et al.*, 2017); or regional, recharging lowland lake complexes via aquifer flow paths 100s of kilometres in length (Walvoord *et al.*,

2012). Aquifer discharge was observed in April 2019 before snowmelt began from springs in the basin headwaters (Figure 2.1c). This winter baseflow requires a large aquifer reservoir replenished by an area at higher elevation beyond the topographical extent of the study basin (Figure 2.1b) capable of sustaining flow when no rain was received during the winter months.

2.5.6 Climate change induced cover class transitions

Throughout the northern circumpolar region, peat plateaus and other ice-rich permafrost features are in a state of transition as permafrost thaws and landform subsidence occurs (Payette *et al.*, 2004; Quinton *et al.*, 2011; Borge *et al.*, 2016; Mamet *et al.*, 2017). This transition is primarily driven by climate and expected to accelerate (Grosse *et al.*, 2011; Hayashi, 2013). Climate model projections for the 300 arc second grid cell that includes the study basin predict a 2100 MAAT 0.6-5.8 °C warmer and total annual precipitation 24.2-139.8 mm greater (Environment and Climate Change Canada, 2021). The conceptual model presented in this chapter includes each land cover class as unique and discrete (Figure 2.7), but transitional elements are present that share characteristics of multiple classes. The peat plateau-fen transitional feature identified and monitored in this study (Figure 2.5c) was in a small thermokarst depression located in the peat plateau training area (Figure 2.1). This feature is likely hydrologically isolated from the channel network due to the higher elevation peat plateau surrounding it and the ice-rich permafrost within this land cover class. While this location maintains a small open talik with a shallow zero annual amplitude depth maintaining a temperature close to 0 °C (Figure 2.5c), other larger thermokarst features are recognizable in the classification as open water features isolated from the channel network and surrounded by fen and/or peat plateau complexes (Figure 2.1). Some of these larger transitional features likely maintain warmer soil profiles with depths of zero annual amplitude that allow for vertical flow via taliks connected to subpermafrost aquifers below (Figure 2.7).

In peat deposits, *K* and VMC have a strong positive association (Jorgenson *et al.*, 2010), which is important for positive feedback between increasing soil wetness and thermal erosion with depression formation and wetland expansion at the expense of degrading permafrost (Matthews *et al.*, 1997; Bosikov, 1998; Kurylyk *et al.*, 2016). The fen land cover class identified in this basin had greater mean VMC than the other classes, as well as elevated near-surface soil *C* and *K* values (Table 2.3) in part due to lower elevation than neighbouring peat plateaus (Table 2.1), suggesting the long-term process of permafrost land cover replacement observed throughout the North (Payette *et al.*, 2004; Quinton *et al.*, 2011; Borge *et al.*, 2016; Mamet *et al.*, 2017) is likely occurring within and at the margins of these fen features. This may result in an increase of open water extent and evaporative losses from localized thermokarst depressions (Figure 2.7), but such features will not likely maintain surface waters long term as through taliks deepen and open new flow paths connected to the aquifers below (Yoshikawa and Hinzman, 2003). Over a longer timeframe, the replacement of peat plateau with fen will increase the proportion of basin losses via aquifer recharge, a flow path important in maintaining lowland lake complexes and winter baseflow in large regional river systems (Walvoord *et al.*, 2012; Ma *et al.*, 2017; Lamontagne-Hallé *et al.*, 2018). As such, the conceptual model presented (Figure 2.7) should not be considered definitive and/or static in time as first order climate drivers make future energy-mass balance and hydrological function of such terrain uncertain until future studies describe these systems under those conditions.

2.6 Conclusions

This chapter characterizes the major flow paths and storage compartments of alpine tundra headwater systems within the Taiga Cordillera ecozone. The interannual variability of alpine climates can be extreme and the spatial heterogeneity of surface and subsurface characteristics of

local terrain makes attempts to model the local hydrology of these headwater systems challenging. Many of the hydrological properties reported in this study include observations from only one year, and replicates of equipment installations and/or sample collection were often limited. Further research is needed to better verify and refine each land cover class and their respective hydrological properties, extent within the Taiga Cordillera ecozone more broadly, and rate of change as climate change continues. With these limitations in mind, this study still provides direct observation of the physiographic, surface, and subsurface properties representative of alpine tundra terrain in the Taiga Cordillera, a system previously undocumented and otherwise requiring the transference of hydrological understanding established in other alpine areas and/or lowland regions. The key findings of this study concern the hydrologically distinct land cover classes described and their respective roles in water redistribution within and losses from alpine shrub tundra basins. The conceptual model presented accounts for principal flow paths, available storage, and linkages of each land cover class with neighbouring terrain.

Riparian swamps are primary contributors to streamflow due to their near channel proximity and the low hydraulic conductivity of mineral substrates impeding vertical groundwater recharge. Glaciofluvial uplands remain isolated from the channel network year-round and route inputs vertically through coarse rocky substrates to recharge aquifer reservoirs >6.5 m below ground surface. Peat plateaus route precipitation inputs laterally via a highly conductive suprapermafrost zone, while fens receive precipitation directly as well as from the neighbouring peat plateaus. Some small fen depressions store these inputs locally, but the majority of fens act as primary contributors to the channel network. As the climate continues to warm, ice-rich permafrost below the peat plateaus will continue to thaw and subside, converting peat plateau to fen and increasing the extent of isolated depressions storing water away from the channel network. As taliks deepen

below these local thermokarst features, the depression storage will be lost at the expense of increasing aquifer recharge. These findings support distributed hydrological models estimating terrestrial energy-mass balance and/or general circulation models needing to represent the boundary layer dynamics at the ground surface. Furthermore, this study supports larger scale remote sensing techniques capable of assigning hydrological properties to specific land cover classes, developing basin weighted means, and estimating the proportion of contributions to regional river systems via surface streams and/or aquifer recharge from current land cover assemblages and future assemblages as climate change continues.

2.7 References

AMAX Environmental Services 1976. Environmental report on the Macmillan Tungsten property located in the Northwest Territories and Yukon / Prepared for AMAX Northwest Mining Company

Armstrong R, Martz L. 2008. Effects of reduced land cover detail on hydrological model response. Hydrological Processes 22: 2395–2409 DOI: 10.1002/hyp.6830

Beckwith CW, Baird AJ, Heathwaite AL. 2003. Anisotropy and depth-related heterogeneity of hydraulic conductivity in a bog peat. I: laboratory measurements. Hydrological Processes 17: 89–101 DOI: 10.1002/hyp.1116

Bélair S, Crevier LP, Mailhot J, Bilodeau B, Delage Y. 2003. Operational implementation of the ISBA land surface scheme in the Canadian regional weather forecast model. part I: warm season results. Journal of Hydrometeorology 4 (2): 352–370 DOI: 10.1175/1525-7541(2003)4<352:OIOTIL>2.0.CO;2

Beniston M. 2003. Climatic change in mountain regions: A review of possible impacts. Climate Change 59: 5–31 DOI: 10.1007/978-94-015-1252-7_2

Bennet M, Glasser N. 2009. Glacial Geology: Ice Sheets and Land Forms. John Wiley & Sons, Ltd: Chichester, UK.

Borge AF, Westermann S, Solheim I, Etzelmüller B. 2016. Strong degradation of palsas and peat plateaus in northern Norway during the last 60 years. The Cryosphere Discussions 11(1): 1–16 DOI: 10.5194/tc-2016-12

Bosikov N. 1998. Wetness variability and dynamics of thermokarst processes in Central Yakutia. In Permafrost, Seventh International Conference. Collection Nordicana 55: 23–27.

Brown OW, Hugenholtz CH. 2012. Estimating aerodynamic roughness (zo) in mixed grassland prairie with airborne LiDAR. Canadian Journal of Remote Sensing 37 (4): 422–428 DOI: 10.5589/m11-051

Canada Centre for Remote Sensing (CCRS), U.S. Geological Survey (UGS), National Institute of Statistics and Geography, National Commission for the Knowledge and Use of the Biodiversity, the National Forestry Commission of Mexico. 2020. 2010 Land Cover of North America at 30 meters. Commission for Environmental Cooperation: Montréal, Québec. Available at: http://www.cec.org/nalcms

Canada Soil Classification Working Group. 1998. The Canadian System of Soil Classification (RH Haynes, ed.). National Research Council of Canada: Ottawa.

Carey S, Quinton WL. 2004. Evaluating snowmelt runoff generation in a discontinuous permafrost catchment using stable isotope, hydrochemical and hydrometric data. Nordic Hydrology 35 (4–5): 309–324 DOI: 10.1002/hyp.5764

Carey S, Woo MK. 1999. Hydrology of two slopes in subarctic Yukon, Canada. Hydrological Processes 13: 2549–2562

Carey S, Woo MK. 2001a. Slope runoff processes and flow generation in a subarctic, subalpine catchment. Journal of Hydrology 253 (1–4): 110–129 DOI: 10.1016/S0022-1694(01)00478-4

Carey SK, Woo MK. 2001b. Spatial variability of hillslope water balance, Wolf Creek Basin, subarctic Yukon. Hydrological Processes 15 (16): 3113–3132 DOI: 10.1002/hyp.319

Chasmer L, Mahoney C, Millard K, Nelson K, Peters D, Merchant M, Hopkinson C, Brisco B, Niemann O, Montgomery J, et al. 2020. Remote sensing of boreal wetlands 2: methods for evaluating boreal wetland ecosystem state and drivers of change. Remote Sensing 12 (8): 1–47 DOI: 10.3390/RS12081321

Craig JR, Brown G, Chlumsky R, Jenkinson W, Jost G, Lee K, Mai J, Serrer M, Snowdon AP, Sgro N, et al. 2020. Flexible watershed simulation with the Raven hydrological modelling framework. Environmental Modelling & Software 129 (April): 104728 DOI: 10.1016/j.envsoft.2020.104728

de Jong C, Whelan F, Messerli B. 2005. Preface: The importance of a hydrological research framework for water balance studies in mountain basins. Hydrological Processes 19 (12): 2323–2328 DOI: 10.1002/hyp.5886

Debeer CM, Wheater HS, Quinton WL, Carey SK, Stewart RE, Mackay MD, Marsh P. 2014. The Changing Cold Regions Network: observation, diagnosis and prediction of environmental change in the Saskatchewan and Mackenzie River Basins, Canada. Science China Earth Sciences 58 (1): 46–60 DOI: 10.1007/s11430-014-5001-6

Derksen C, Brown R, MacKay M. 2008. Mackenzie Basin snow cover: variability and trends from conventional data, satellite remote sensing, and Canadian regional climate model simulations. In Cold Region Atmospheric and Hydrologic Studies. The Mackenzie GEWEX Experience: Volume 1: Atmospheric Dynamics, Woo MK (ed.). Springer Berlin Heidelberg: Berlin, Heidelberg, Heidelberg; 213–239. DOI: 10.1007/978-3-540-73936-4_13

Ebel BA, Koch JC, Walvoord MA. 2019. Soil physical, hydraulic, and thermal properties in interior Alaska, USA: implications for hydrologic response to thawing permafrost conditions. Water Resources Research 55 (5): 4427–4447 DOI: 10.1029/2018WR023673

Egginton P, Dyke L. 1990. Apparent hydraulic conductivities associated with thawing, frost-susceptible soils. Permafrost and Periglacial Processes 1: 69–77

Embleton C, King C. 1975. Glacial and Periglacial Geomorphology. John Wiley & Sons: New York.

Endrizzi S, Quinton WL, Marsh P. 2011. Modelling the spatial pattern of ground thaw in a small basin in the arctic tundra. The Cryosphere Discussions 5 (1): 367–400 DOI: 10.5194/tcd-5-367-2011

Environment and Climate Change Canada. 2021. Climate data for a resilient Canada. Available at: https://climatedata.ca/ [Accessed 18 August 2021]

Environment Canada. 2020. Environment Canada historical data archive. Available at: https://climate.weather.gc.ca/historical_data/search_historic_data_e.html [Accessed 17 April 2020]

Genxu W, Guangsheng L, Chunjie L, Yan Y. 2012. The variability of soil thermal and hydrological dynamics with vegetation cover in a permafrost region. Agricultural and Forest Meteorology 162–163: 44–57 DOI: 10.1016/j.agrformet.2012.04.006

Granger RJ, Gray DM, Dyck GE. 1984. Snowmelt infiltration to frozen Prairie soils. Canadian Journal of Earth Sciences 21 (6): 669–677 DOI: 10.1139/e84-073

Gravelle C, Livingstone S. 2013. Case Study Program for Petroleum Hydrocarbon Stability and Ecological Integrity. Public Works and Government Services Canada Report 1692-1201:350125

Grosse G, Romanovsky V, Jorgenson T, Anthony KW, Brown J, Overduin PP. 2011. Vulnerability and feedbacks of permafrost to climate change. Eos 92 (9): 73–74 DOI: 10.1029/2011EO090001

Harder P, Pomeroy JW, Westbrook CJ. 2015. Hydrological resilience of a Canadian Rockies headwaters basin subject to changing climate, extreme weather, and forest management. Hydrological Processes 29 (18): 3905–3924 DOI: 10.1002/hyp.10596

Hayashi M. 2013. The cold vadose zone: hydrological and ecological significance of frozen-soil processes. Vadose Zone Journal 12: 2136 DOI: 10.2136/vzj2013.03.0064

Hock R, Rasul G, Adler C, Cáceres B, Gruber S, Hirabayashi Y, Jackson M, Kääb A, Kang S, Kutuzov S, et al. 2019. Chapter 2: high mountain areas. In IPCC Special Report on the Ocean and Cryosphere in a Changing Climate: 131–202

Hollander M, Wolfe D. 1999. Nonparametric Statistical Methods. John Wiley & Sons: New York.

Hoylman ZH, Jencso KG, Hu J, Holden ZA, Martin JT, Gardner WP. 2019. The climatic water balance and topography control spatial patterns of atmospheric demand, soil moisture, and shallow subsurface flow. Water Resources Research 55 (3): 2370–2389 DOI: 10.1029/2018WR023302

IPCC. 2013. Climate Change 2013 - The Physical Science Basis. DOI: 10.1038/446727a

Jacques JMS, Sauchyn DJ. 2009. Increasing winter baseflow and mean annual streamflow from possible permafrost thawing in the Northwest Territories, Canada. Geophysical Research Letters 36 (1): 1–6 DOI: 10.1029/2008GL035822

Jorgenson MT, Romanovsky V, Harden J, Shur Y, O'Donnell J, Schuur EAGG, Kanevskiy M, Marchenko S, Donnell JO, Schuur EAGG, et al. 2010. Resilience and vulnerability of permafrost to climate change. Canadian Journal of Forest Research 40 (7): 1219–1236 DOI: 10.1139/X10-060

Kerkhoven E, Yew Gan T. 2008. Development of a hydrologic scheme for use in land surface models and its application to climate change in the Athabasca River Basin. In Cold Region Atmospheric and Hydrologic Studies. The Mackenzie GEWEX Experience: Volume 2: Hydrologic Processes, Woo MK (ed.). Springer: New York, New York, US.

Knist S, Goergen K, Buonomo E, Christensen OB, Colette A, Cardoso RM, Fealy R, Fernández J, García-Díez M, Jacob D, et al. 2017. Land-atmosphere coupling in EURO-CORDEX evaluation experiments. Journal of Geophysical Research 122 (1): 79–103 DOI: 10.1002/2016JD025476

Krogh SA, Pomeroy JW, Marsh P. 2017. Diagnosis of the hydrology of a small Arctic basin at the tundra-taiga transition using a physically based hydrological model. Journal of Hydrology 550: 685–703 DOI: 10.1016/j.jhydrol.2017.05.042

Kurylyk BL, Hayashi M, Quinton WL, McKenzie JM, Voss CI. 2016. Influence of vertical and lateral heat transfer on permafrost thaw, peatland landscape transition, and groundwater flow. Water Resources Research 52 (2): 1286–1305 DOI: 10.1002/2015WR018057

Lamontagne-Hallé P, McKenzie JM, Kurylyk BL, Zipper SC. 2018. Changing groundwater discharge dynamics in permafrost regions. Environmental Research Letters 13 (8) DOI: 10.1088/1748-9326/aad404

Landry C, Buck K, Raleigh M, Clark M. 2014. Mountain system monitoring at Senator Beck basin, San Juan Mountains, Colorado: A new integrative data source to develop and evaluate models of snow and hydrologic processes. Water Resources Research 50: 1773–1788 DOI: 10.1002/2013WR013711.Received

Langston G, Hayashi M, Roy JW. 2013. Quantifying groundwater-surface water interactions in a proglacial moraine using heat and solute tracers. Water Resources Research 49: 5411–5426 DOI: 10.1002/wrcr.20372

Laudon H, Spence C, Buttle J, Carey SK, McDonnell JJ, McNamara JP, Soulsby C, Tetzlaff D. 2017. Save northern high-latitude catchments. Nature Geoscience 10 (5): 324–325 DOI: 10.1038/ngeo2947

Lettau H. 1969. Note on aerodynamic roughness-parameter estimation on the basin of roughness-element description. Journal of Applied Ecology 8: 828–832

Ma R, Sun Z, Hu Y, Chang Q, Wang S, Xing W, Ge M. 2017. Hydrological connectivity from glaciers to rivers in the Qinghai-Tibet plateau: roles of suprapermafrost and subpermafrost groundwater. Hydrology and Earth System Sciences 21 (9): 4803–4823 DOI: 10.5194/hess-21-4803-2017

Mamet SD, Chun KP, Kershaw GGL, Loranty MM, Kershaw GP. 2017. Recent increases in permafrost thaw rates and areal loss of palsas in the western Northwest Territories, Canada. Permafrost and Periglacial Processes 28 (4): 619–633 DOI: 10.1002/ppp.1951

Marsh CB, Pomeroy JW, Wheater HS. 2020. The Canadian Hydrological Model (CHM): A multi-scale, multi-extent, variable-complexity hydrological model - design and overview. Geoscientific Model Development Discussions 13 (2002): 225–247 DOI: 10.5194/gmd-2019-109

Masson V, Champeaux JL, Chauvin F, Meriguet C, Lacaze R. 2003. A global database of land surface parameters at 1-km resolution in meteorological and climate models. Journal of Climate 16 (9): 1261–1282 DOI: 10.1175/1520-0442-16.9.1261

Matthews JA, Dahl S, Berrisford MS, Nesje A. 1997. Cyclic development and thermokarstic degradation of palsas in the mid-alpine zone at Leirpullan , Dovrefjell , Southern Norway. Permafrost and Periglacial Processes 8: 107–122

McGuire AD, Chapin FS, Walsh JE, Wirth C. 2006. Integrated regional changes in Arctic climate feedbacks: implications for the global climate system. Annual Review of Environment and Resources 31 (1): 61–91 DOI: 10.1146/annurev.energy.31.020105.100253

Ménard CB, Essery R, Barr A, Bartlett P, Derry J, Dumont M, Fierz C, Kim H, Kontu A, Lejeune Y, et al. 2019. Meteorological and evaluation datasets for snow modelling at 10 reference sites: description of in situ and bias-corrected reanalysis data. Earth System Science Data 11 (2): 865–880 DOI: 10.5194/essd-11-865-2019

Ménard CB, Essery R, Pomeroy J. 2014. Modelled sensitivity of the snow regime to topography, shrub fraction and shrub height. Hydrology and Earth System Sciences 18 (6): 2375–2392 DOI: 10.5194/hess-18-2375-2014

Muir DL, Hayashi M, Mcclymont AF. 2011. Hydrological storage and transmission characteristics of an alpine talus. Hydrological Processes 25 (19): 2954–2966 DOI: 10.1002/hyp.8060

Muller SW. 1947. Permafrost or Permanently Frozen Ground and Related Engineering Problems. Military Intelligence Division Office, Chief of Engineers, U.S. Army.

National Wetlands Working Group. 1997. The Canadian Wetland Classification System, B Warner B and Rubec C (ed.). Wetlands Research Centre.

O'Neill HB, Burn CR. 2017. Talik formation at a snow fence in continuous permafrost, western Arctic Canada. Permafrost and Periglacial Processes 28 (3): 558–565 DOI: 10.1002/ppp.1905

Payette S, Delwaide A, Caccianiga M, Beauchemin M. 2004. Accelerated thawing of subarctic peatland permafrost over the last 50 years. Geophysical Research Letters 31: L18208

Peters DL, Atkinson D, Monk WA, Tenenbaum DE, Baird DJ. 2013. A multi-scale hydroclimatic analysis of runoff generation in the Athabasca River, Western Canada. Hydrological Processes 27 (13): 1915–1934 DOI: 10.1002/hyp.9699

Pomeroy JW, Gray DM. 1995. Snowcover: Accumulation, Relocation and Management. Minister of Supply and Services Canada, Saskatoon, Saskatchewan.

Pomeroy JW, Bewley DS, Essery RLH, Hedstrom NR, Link T, Granger RJ, Sicart JE, Ellis CR, Janowicz JR. 2006. Shrub tundra snowmelt. Hydrological Processes 20 (4): 923–941 DOI: 10.1002/hyp.6124

Pomeroy JW, Gray DM, Brown T, Hedstrom NR, Quinton WL, Granger RJ, Carey SK. 2007. The Cold Regions Hydrological Model: a platform for basing process representation and model structure on physical evidence. Hydrological Processes 21: 2650–2667 DOI: 10.1002/hyp

Pomeroy JW, Gray DM, Shook KR, Toth B, Essery RLH, Pietroniro A, Hedstrom N. 1998. An evaluation of snow accumulation and ablation processes for land surface modelling. Hydrological Processes 12 (15): 2339–2367 DOI: 10.1002/(SICI)1099-1085(199812)12:15<2339::AID-HYP800>3.0.CO;2-L

Quinton W, Shirazi T, Carey S, Pomeroy J. 2005. Soil water storage and active-layer development in a sub-alpine tundra hillslope, southern Yukon Territory, Canada. Permafrost and Periglacial Processes 16 (4): 369–382 DOI: 10.1002/ppp.543

Quinton WL, Baltzer JL. 2013. The active-layer hydrology of a peat plateau with thawing permafrost (Scotty Creek, Canada). Hydrogeology Journal 21 (1): 201–220 DOI: 10.1007/s10040-012-0935-2

Quinton WL, Hayashi M, Carey SK. 2008. Peat hydraulic conductivity in cold regions and its relation to pore size and geometry. Hydrological Processes 22: 2829–2837 DOI: 10.1002/hyp

Quinton WL, Hayashi M, Chasmer LE. 2009. Peatland hydrology of discontinuous permafrost in the Northwest Territories: overview and synthesis. Canadian Water Resources Journal 34 (4): 311–328 DOI: 10.4296/cwrj3404311

Quinton WL, Hayashi M, Chasmer LE. 2011. Permafrost-thaw-induced land-cover change in the Canadian subarctic: implications for water resources. Hydrological Processes 25 (1): 152–158 DOI: 10.1002/hyp.7894

Quinton WL, Hayashi M, Pietroniro A, Simpson F. 2003. Connectivity and storage functions of channel fens and flat bogs in northern basins. Hydrological Processes 17: 3665–3684 DOI: 10.1002/hyp.1369

R Core Team. 2020. R: A language and environment for statistical computing

Rasouli K, Pomeroy JW, Janowicz JR, Carey SK, Williams TJ. 2014. Hydrological sensitivity of a northern mountain basin to climate change. Hydrological Processes 28 (14): 4191–4208 DOI: 10.1002/hyp.10244

Raupach MR. 1994. Simplified expressions for vegetation roughness length and zero-plane displacement as functions of canopy height and area index. Boundary-Layer Meteorology 71 (1–2): 211–216 DOI: 10.1007/BF00709229

Romanovsky VE, Smith SL, Christiansen HH. 2010. Permafrost thermal state in the polar Northern Hemisphere during the international polar year 2007–2009: a synthesis. Permafrost and Periglacial Processes 21 (2): 106–116 DOI: 10.1002/ppp.689

Roos S De, Turner D, Lucieer A. 2018. Using digital surface models from UAS imagery of fire damaged Sphagnum peatlands for monitoring and hydrological restoration. Drones 2 (45): 16 DOI: 10.3390/drones2040045

Scarlett SJ, Petrone RM, Price JS. 2017. Controls on plot-scale evapotranspiration from a constructed fen in the Athabasca Oil Sands Region, Alberta. Ecological Engineering 100: 199–210 DOI: 10.1016/j.ecoleng.2016.12.020

Seppälä M. 2011. Synthesis of studies of palsa formation underlining the importance of local environmental and physical characteristics. Quaternary Research 75 (2): 366–370 DOI: 10.1016/j.yqres.2010.09.007

Verseghy DL. 2000. The Canadian Land Surface Scheme (CLASS): Its history and future. Atmosphere - Ocean 38 (1): 1–13 DOI: 10.1080/07055900.2000.9649637

Walvoord MA, Kurylyk BL. 2016. Hydrologic impacts of thawing permafrost — a review. Vadose Zone Journal 15 (6) DOI: 10.2136/vzj2016.01.0010

Walvoord MA, Voss CI, Wellman TP. 2012. Influence of permafrost distribution on groundwater flow in the context of climate-driven permafrost thaw: example from Yukon

Flats basin, Alaska, United States. Water Resources Research 48 (7): 1–17 DOI: 10.1029/2011WR011595

Woo MK, Mollinga M, Smith S. 2008a. Modeling maximum active layer thaw in boreal and tundra environments using limited data. In Cold Region Atmospheric and Hydrologic Studies. The Mackenzie GEWEX Experience: Volume 2: Hydrologic Processes, Woo MK (ed.). Springer: New York; 125–137.

Woo MK, Rouse W, Stewart R, Stone J. 2008b. The Mackenzie GEWEX study: a contribution to cold region atmospheric and hydrologic sciences. In Cold Region Atmospheric and Hydrologic Studies. The Mackenzie GEWEX Experience: Volume 1: Atmospheric Dynamics, Woo MK (ed.). Springer: New York; 507.

Woo MK, Thorne R. 2003. Streamflow in the Mackenzie basin, Canada. Arctic 56 (4): 328–340 DOI: 10.14430/arctic630

Yoshikawa K, Hinzman LD. 2003. Shrinking thermokarst ponds and groundwater dynamics in discontinuous permafrost near Council, Alaska. Permafrost and Periglacial Processes 14 (2): 151–160 DOI: 10.1002/ppp.451

2.8 Figures

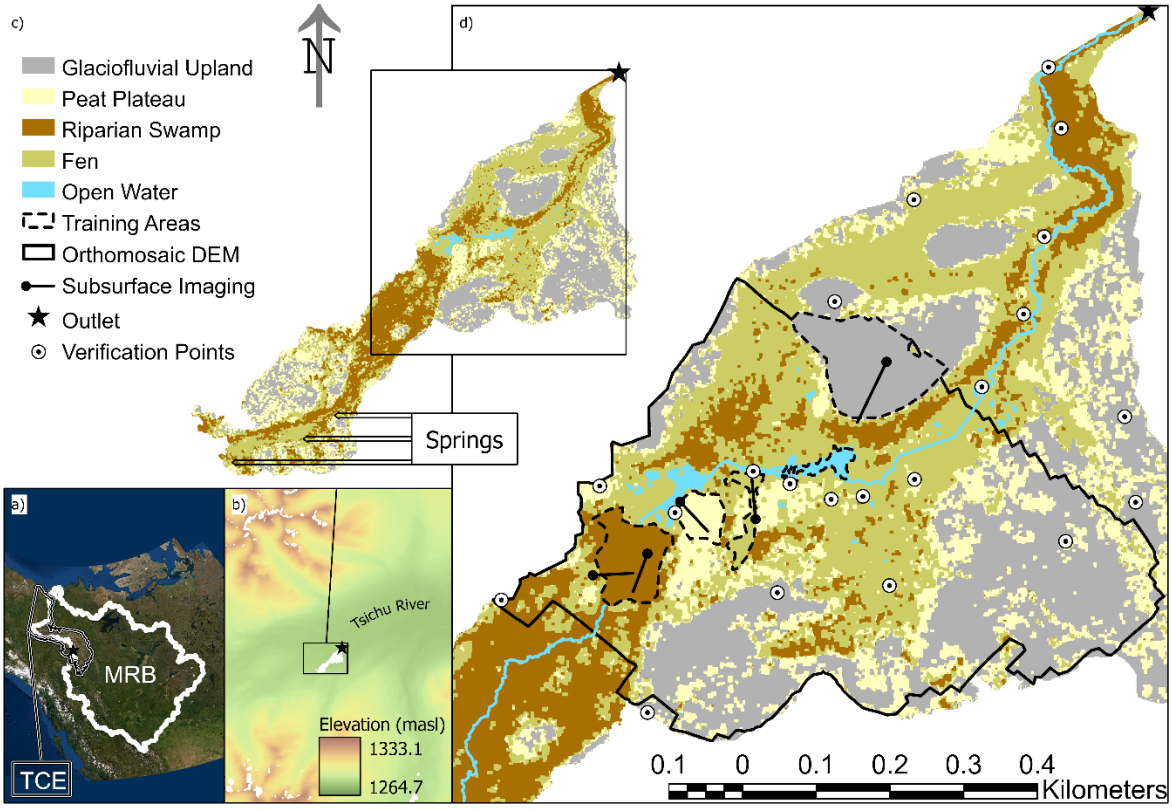

Figure 2-1: Location of study site relative to a) The Taiga Cordillera ecozone and the Mackenzie River basin, and b) The broader Tishu River valley to which the study basin contributes. c) Total study basin land cover classification with location of basin outlet and headwater springs. d) Study basin with extent of spectral signature training areas and verification points used to assign land cover, extent of high-resolution digital elevation model (DEM) used to characterize physiographic properties, and subsurface imaging lines with closed circles to designate zero-meter marker of ERT (Figure 2.3) and GPR (Figure 2.4) transects.

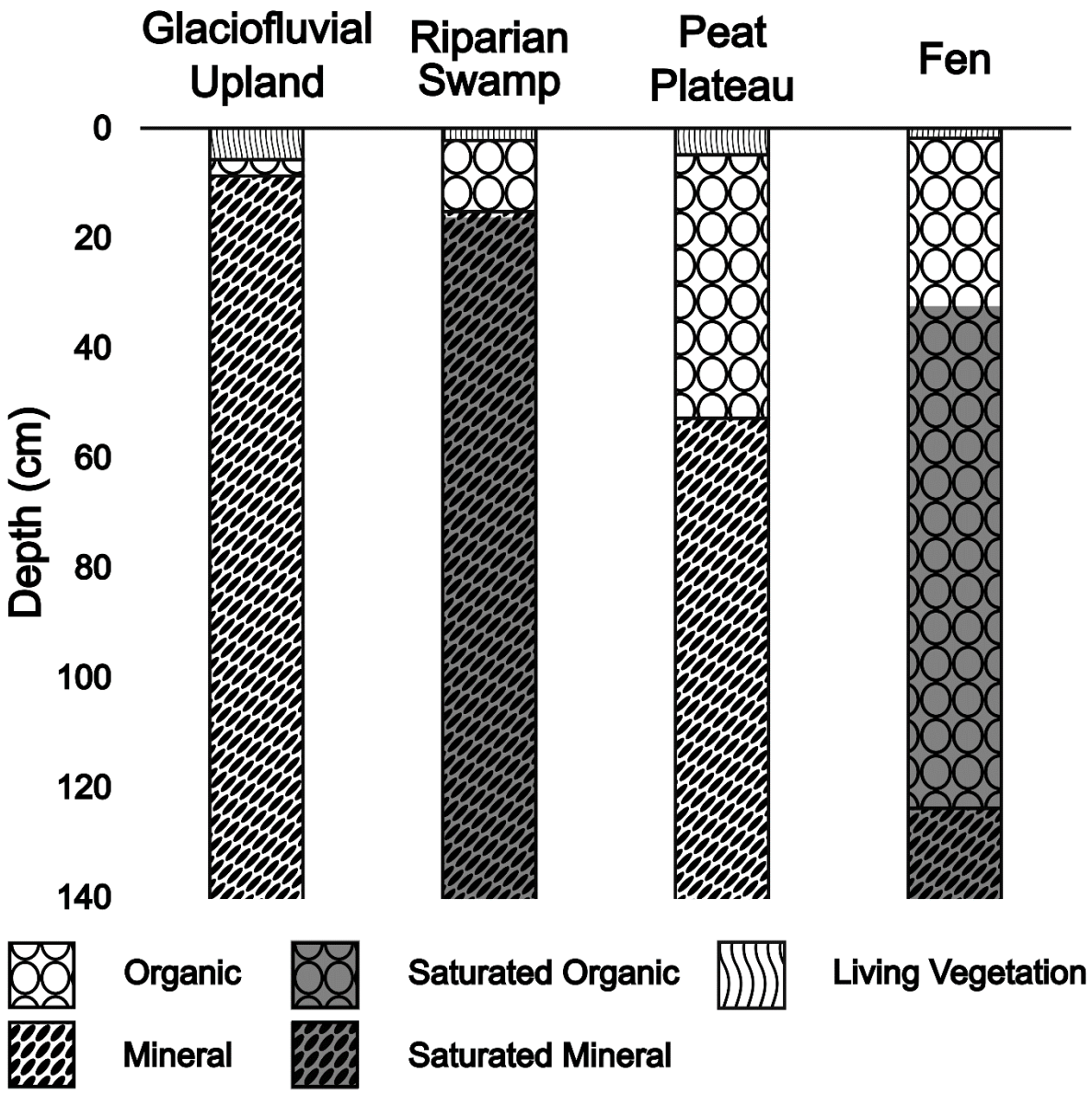

Figure 2-2: A generalized schematic of subsurface properties within each land cover class. Maximum depths of excavation were 144 cm (riparian swamp), 126 cm (glaciofluvial upland), 230 cm (peat plateau), and 210 cm (fen) below ground surface.

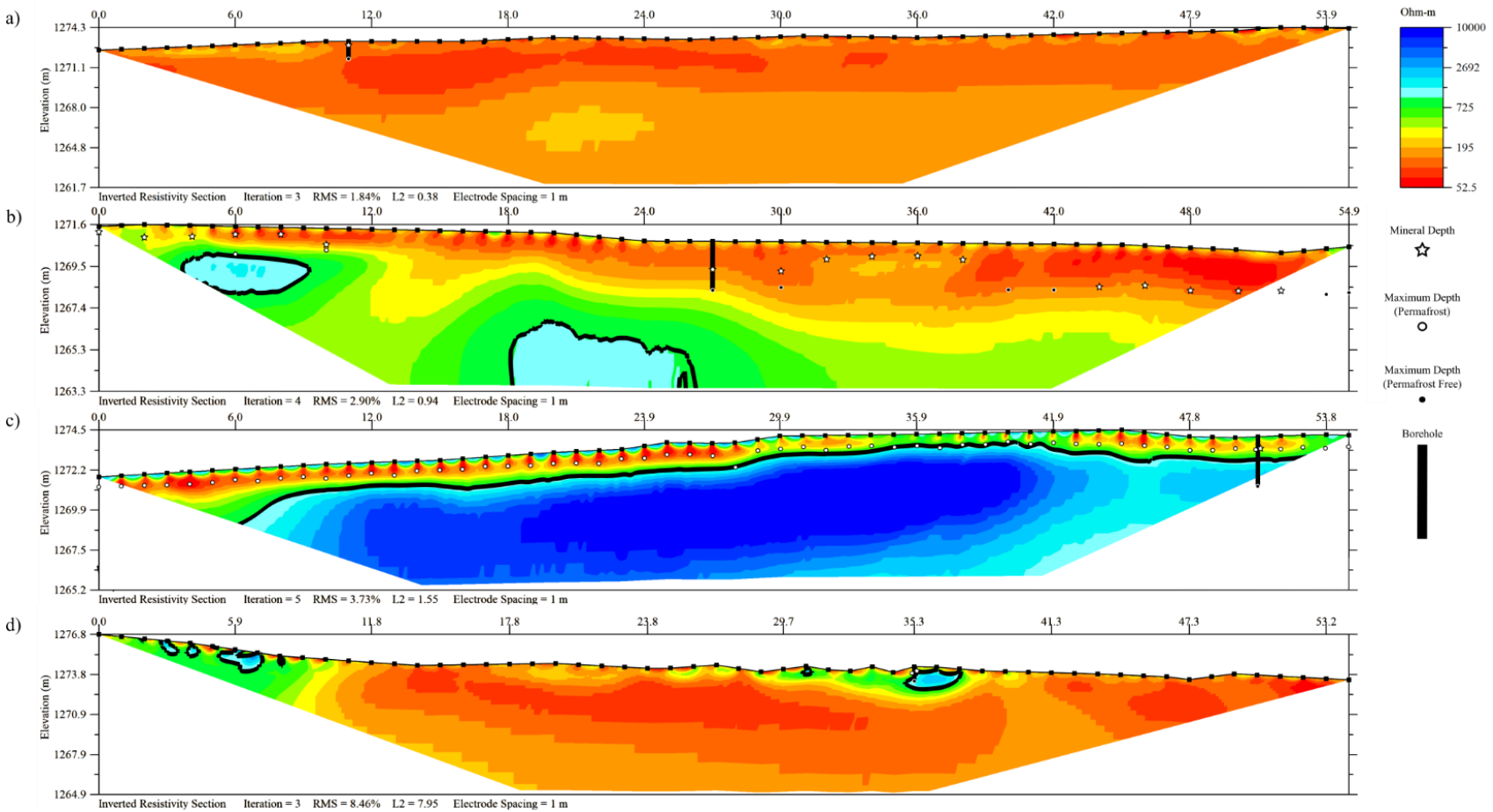

Figure 2-3: Electrical Resistivity Tomography (ERT) images of subsurface below a) riparian swamp, b) fen, c) peat plateau, and d) riparian swamp (10 – 54 m) close to a glaciofluvial upland feature (0 – 10 m). Estimates of permafrost presence presented in solid black, representing the 1000 Ohm value at the green-blue contour transition. Transects overlain with measurements of mineral, permafrost, and permafrost free depths of penetration, as confirmed with frost probe and/or borehole excavation. Refer to Figure 2.1 for transect locations within the study basin.

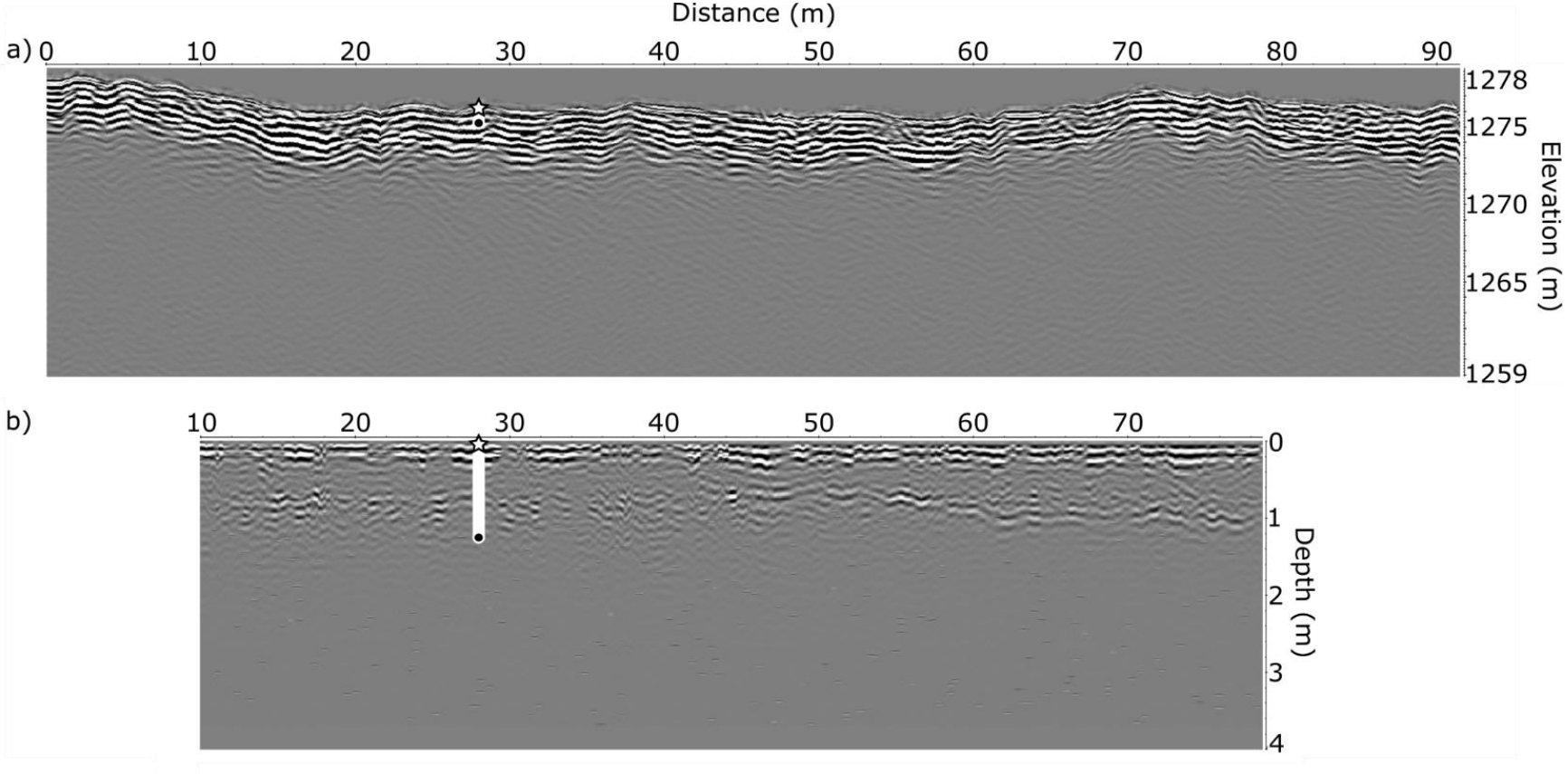

Figure 2-4: Ground Penetrating Radar (GPR) images of subsurface below a glaciofluvial upland feature. 100 MHz provides better depth of penetration (a) and 500 MHz antenna provides better spatial resolution (b). Location of borehole at 28 m marker excavated to 126 cm depth to confirm absence of near-surface permafrost. Depth to mineral substrate was 11 cm below vegetation surface (star). Refer to Figure 2.1 for transect location.

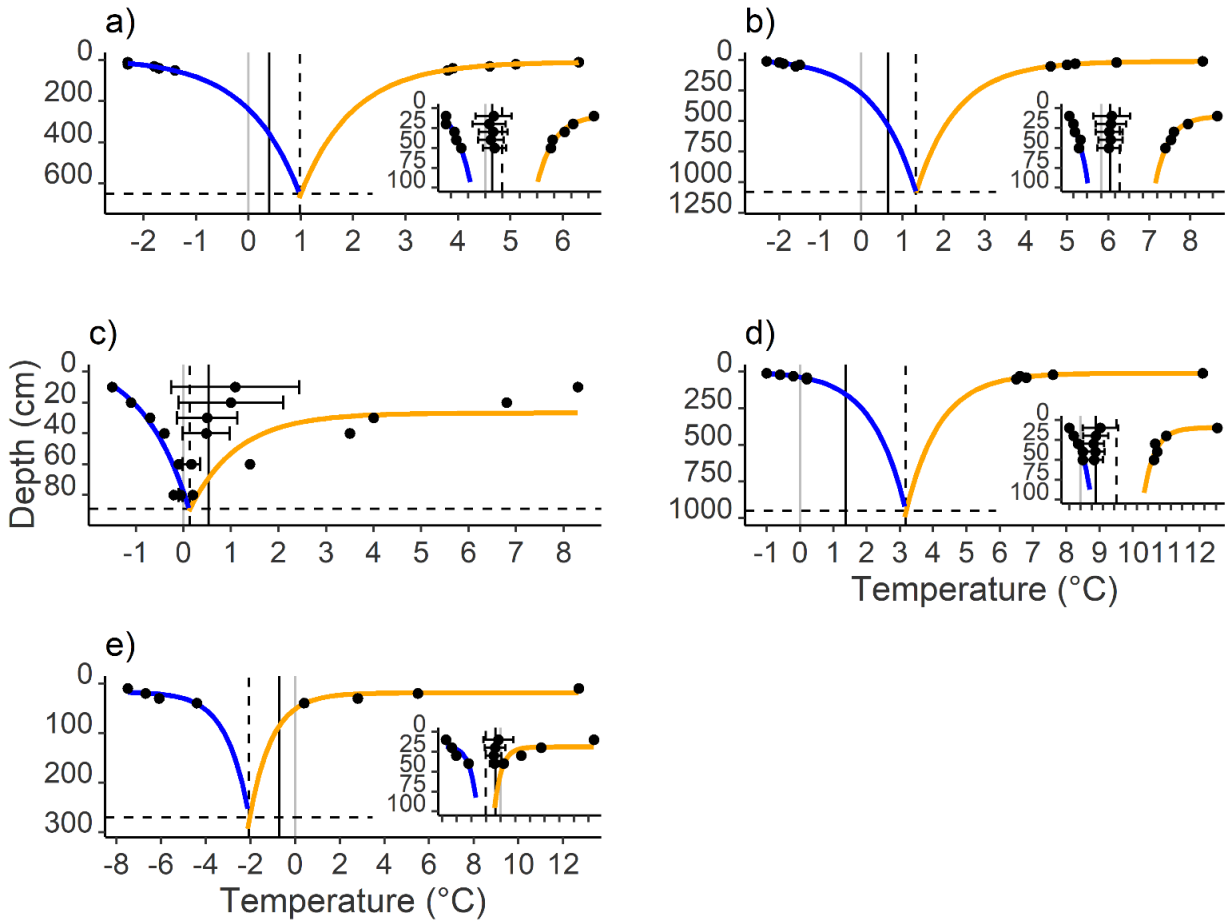

Figure 2-5: 1 September 2018 to 1 September 2019 soil temperature profiles at glaciofluvial upland (a, b), peat plateau-fen transition (c), fen (d), and peat plateau (e) locations. Trumpet curves present maximum and minimum temperature observations at depth below ground surface. Exponential lines of best fit for warmest (yellow) and coolest (blue) recorded temperatures converge at estimates of zero annual amplitude depth and temperature (dashed lines). Subset panes show mean annual temperatures with standard deviation whiskers used in linear models to estimate zero annual amplitude temperatures (solid black line).

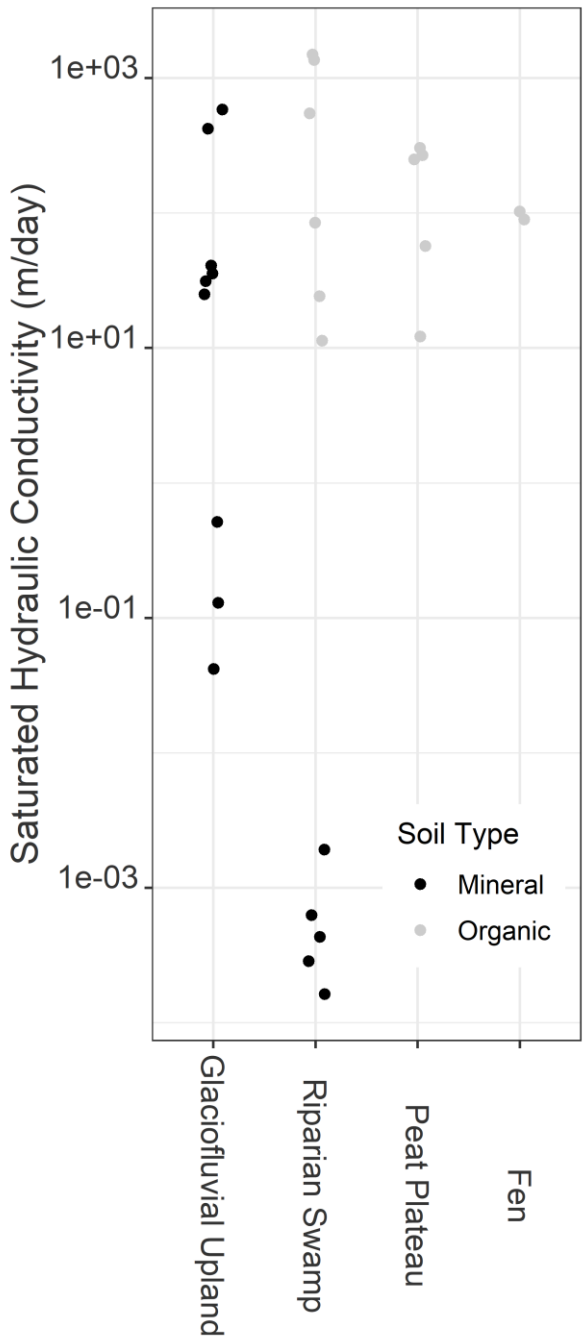

Figure 2-6: Saturated hydraulic conductivity (m day^{-1}) of near-surface mineral and organic substrates.

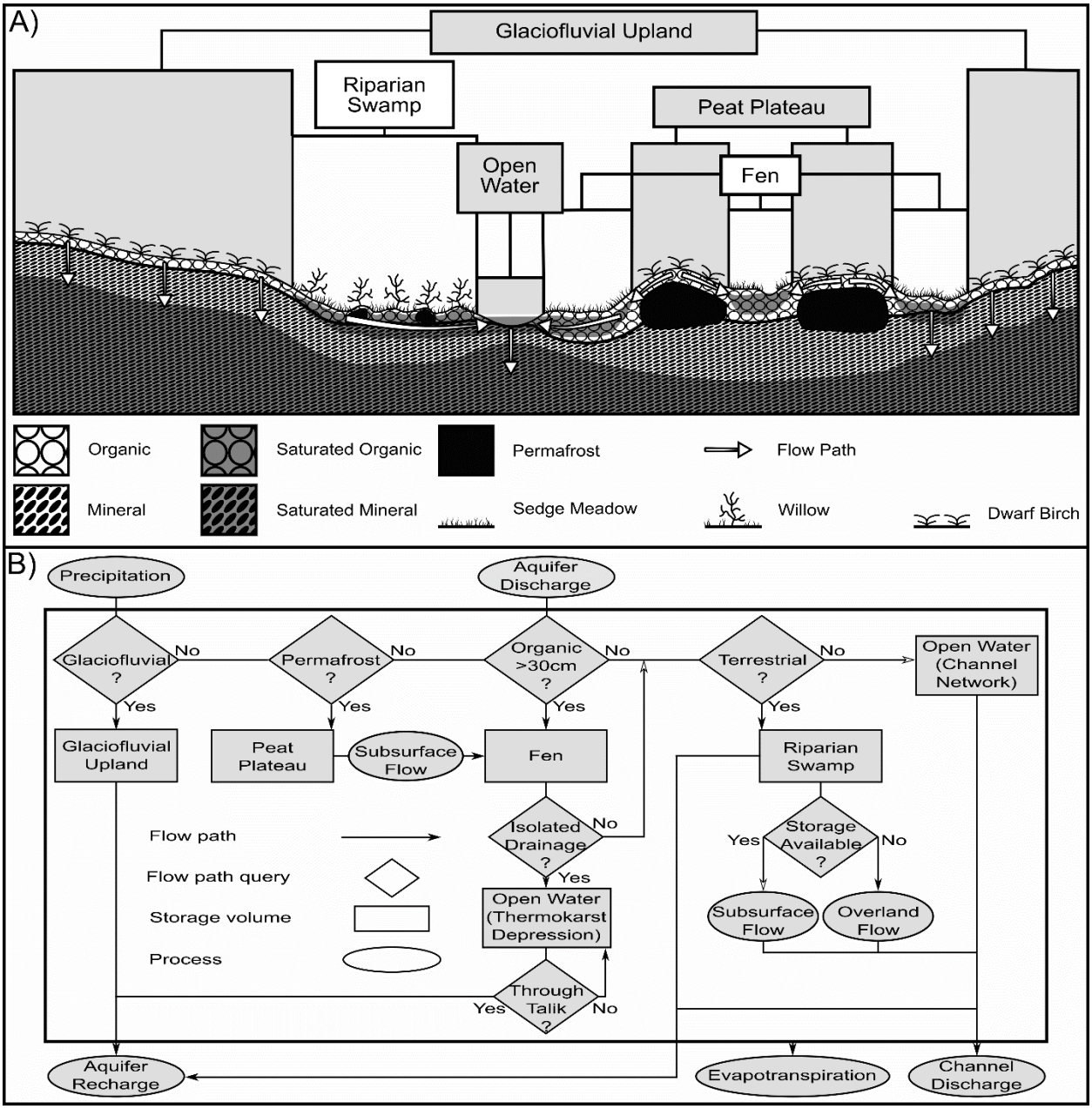

Figure 2-7: A conceptual model of water routing and storage functions for alpine tundra cover classes typical of the Taiga Cordillera ecozone. A) a generalized valley cross-section showing spatial relationships among land cover classes and flow paths available for routing of precipitation inputs received by the study basin. Vertical exaggeration is applied to help illustrate zones of saturation and flow paths between land cover classes. Channel flow is directed through the page. B) a schematic of water routing and storage volumes within the study basin. Queries assign cover classification to a receiving storage volume and active flow paths as water is redistributed within the basin before its eventual exit.

2.9 Tables

Table 2-1: Basin area of each land cover class and their respective physiographic properties (± one standard deviation from the mean). Minimum distance from channel and elevation above channel are not reported as each land cover class contacted the channel network.

			Basin Average	Glaciofluvial upland	Riparian swamp	Peat plateau	Fen
Basin area		**%**		**25**	**20**	**23**	**31**
Elevation	**MAX**	**masl**	**1333.1**	**1333.1**	**1327.6**	**1330.9**	**1329.7**
	MIN	**masl**	**1264.8**	**1268.4**	**1265.1**	**1266.1**	**1264.8**
	MEAN	**masl**	**1285.6 ± 14.8**	**1284.0 ± 13.2**	**1287.6 ± 14.8**	**1290.0 ± 16.5**	**1282.7 ± 15.2**
Aspect	**MEAN**	**Azimuth °**	**178.9 ± 109.8**	**188.5 ± 121.9**	**171.3 ± 104.7**	**188.4 ± 110.6**	**173.3 ± 105.4**
Slope	**MEAN**	**%**	**28.0 ± 45.8**	**16.8 ± 22.5**	**45.5 ± 110.6**	**22.7 ± 37.4**	**30.6 ± 73.5**
Distance from channel	**MAX**	**m**	**511.9**	**511.9**	**475.5**	**511.4**	**494**
	MEAN	**m**	**141.4 ± 93.6**	**197.4 ± 100.3**	**105.2 ± 93.7**	**160.2 ± 89.0**	**108.2 ± 93.7**
Elevation above channel	**MAX**	**m**	**25**	**25**	**22.2**	**25**	**22.5**
	MEAN	**m**	**3.5 ± 3.3**	**4.8 ± 3.5**	**2.9 ± 3.1**	**4.8 ± 3.9**	**2.0 ± 2.6**

Table 2-2 Basin area of each cover class and their respective surface properties (± one standard deviation from the mean). Superscripts denote significant differences between group means (alpha = 0.05).

		Basin Average	Glaciofluvial upland	Riparian swamp	Peat plateau	Fen	Open water
Basin area	**%**		**25**	**20**	**23**	**31**	**<1**
SWE_{MAX}	**mm**	**130 ± 41**	**125 ± 20^{C}**	**115 ± 47^{BC}**	**106 ± 23^{B}**	**164 ± 68^{D}**	**66 ± 32^{A}**
Vegetation height	**cm**	**34 ± 14**	**45 ± 12^{B}**	**53 ± 21^{B}**	**28 ± 13^{A}**	**21 ± 13^{A}**	
Canopy area index	**%**	**25 ± 13**	**20 ± 6^{A}**	**41 ± 12^{B}**	**18 ± 10^{A}**	**25 ± 23^{A}**	
Roughness length	**cm**	**9.0 ± 3.4**	**12.0 ± 2.9^{B}**	**13 ± 5.4^{B}**	**7.3 ± 3.2^{A}**	**5.4 ± 2.8^{A}**	
Albedo		**0.17 ± 0.01**	**0.16 ± 0.01^{A}**	**0.17 ± 0.00^{B}**	**0.18 ± 0.01^{C}**	**0.16 ± 0.01^{A}**	

Table 2-3: Basin area of each land cover class and their respective subsurface hydrological properties (± one standard deviation from the mean). Superscripts denote significant differences between group means (alpha = 0.05). Values with limited sample size are reported without standard deviations and/or significant differences.

			Basin Average	Glaciofluvial upland	Riparian swamp	Peat plateau	Fen
Basin area		**%**		**25**	**20**	**23**	**31**
Effective particle size		**µm**	**370**	**641**	**27**		
Dry bulk density	**Mineral**	**g/cm^3**	**1.606**	**1.740**	**1.438**		
	Organic	**g/cm^3**	**0.116**		**0.136**	**0.115**	**0.105**
Thermal properties at 0-3 cm depth below ground surface	***K***	**W/m*K**	**0.24 ± 0.07**	**0.23 ± 0.08^{AB}**	**0.26 ± 0.06^{AB}**	**0.21 ± 0.10^{A}**	**0.27 ± 0.05^{B}**
	C	**MJ/m^3*K**	**1.56 ± 0.56**	**1.15 ± 0.47^{A}**	**1.78 ± 0.75^{B}**	**1.21 ± 0.50^{A}**	**2.04 ± 0.56^{B}**
	D	**mm^2/s**	**0.18 ± 0.04**	**0.22 ± 0.04^{C}**	**0.18 ± 0.04^{B}**	**0.17 ± 0.05^{AB}**	**0.15 ± 0.02^{A}**
Volumetric moisture content at depth below ground surface	**10 cm**	**m^3/m^3**	**0.21 ± 0.09**	**0.19 ± 0.09^{B}**	**0.30 ± 0.12^{D}**	**0.10 ± 0.04^{A}**	**0.26 ± 0.12^{C}**
	20 cm	**m^3/m^3**	**0.26 ± 0.13**	**0.12 ± 0.04^{A}**	**0.24 ± 0.08^{B}**	**0.27 ± 0.14^{C}**	**0.38 ± 0.23^{D}**
	50 cm	**m^3/m^3**	**0.30 ± 0.05**	**0.14 ± 0.09^{A}**	**0.23 ± 0.10^{B}**	**0.11 ± 0.01^{A}**	**0.63 ± 0.02^{C}**

3. Runoff-recharge partitioning in an alpine tundra catchment, Mackenzie Mountains, NT

3.1 Abstract

Hydrological processes within the alpine tundra of the Taiga Cordillera ecozone in northwestern Canada are poorly understood, yet these areas receive more precipitation per unit area than lowlands and sustain late summer and winter flow in large river systems when contributions from other areas are reduced. The objective of this study is to quantify the spatial and temporal variability in streamflow and groundwater recharge within a discontinuous permafrost alpine tundra basin and explore the potential impacts of climate change on the timing and intensity of these hydrological processes. Hydrometric and remote sensing methods were used to complete a water balance assessment of the study basin, a headwater subbasin where groundwater springs were concentrated, and the five local cover classes of open water, glaciofluvial upland, riparian swamp, fen, and peat plateau. Comparisons of study basin inputs, outputs, runoff ratio, and runoff-recharge partitioning during the 2019 freshet, early summer, and late summer seasons are presented. During the freshet, 56 % of total precipitation was received as snowmelt over a 17-day period while frost tables and water tables were at or near ground surface. Consequently, the basin responded with highly efficient runoff, causing both headwater subbasin and basin hydrographs to peak and streamflow to be the primary means of water loss. Evapotranspiration from snow-free areas was relatively stable throughout the study duration and was the primary means of water loss in the early summer. As the summer progressed, cumulative storage and streamflow from the study basin declined, as no precipitation events sufficient to exceed storage occurred. Groundwater discharge within the headwater subbasin exceeded precipitation during

the summer months, while groundwater recharge occurred primarily via glaciofluvial upland infiltration during the freshet and channel bed infiltration during the summer. The average partitioning of basin outputs between runoff and groundwater recharge slightly favoured runoff (0.60), but highly seasonal differences occurred such that the freshet ratio favoured runoff (0.83) while the early and late summer favoured recharge (0.28 and 0.17, respectively). As climate change continues to progress, warmer air temperatures and greater precipitation are expected to result in declining permafrost extents and a greater proportion of inputs being routed to storage and/or groundwater recharge instead of the rapidly mobilized runoff important to sustaining summer streamflow. While regional winter baseflow may continue to increase, shrubification and treeline expansion may increase evaporative losses from alpine tundra areas, reducing headwater contributions to larger river systems via both rapid streamflow and delayed aquifer recharge.

Keywords: Taiga Cordillera, Mackenzie River, alpine tundra, runoff, groundwater recharge, water balance

3.2 Introduction

Water balance estimates of large northern basins often rely on understanding of hydrological processes in the lowland regions, where human population and infrastructure are concentrated, and hydrological data are more extensive in duration and coverage. Compared to lowland areas, alpine subbasins receive greater amounts of precipitation (Dingman, 1981; Granger, 1998; Viviroli *et al.*, 2010; Knowles *et al.*, 2015; Asong *et al.*, 2020), and generate disproportionately large amounts of streamflow (Woo and Thorne, 2003) due to their limited forest cover, storage capacity, and steeper gradients (Viviroli *et al.*, 2010). While alpine systems are typically efficient

runoff generators (Quinton *et al.*, 2004; Viviroli *et al.*, 2010), groundwater recharge can also be substantial, depending on the infiltrability of glacial deposits and subsurface bedrock (Wilson and Guan, 2004). The relatively high hydraulic conductivities of coarse mountain alluvium and colluvium (Kahn *et al.*, 2008) can result in a large proportion of precipitation being routed to groundwater recharge (Wilson and Guan, 2004; Hayashi, 2020). These deeper aquifer flow paths delay contributions to the river network and sustain baseflow during the winter months, when atmospheric inputs are accumulating as snowpack on the ground surface (Walvoord *et al.*, 2012; Crites *et al.*, 2020).

In the Mackenzie River basin, total precipitation and river discharge are expected to increase during 2020 - 2050, even though total SWE and headwater runoff from alpine areas are likely to decline over the same period (Stadnyk and Déry, 2021). The presence of permafrost plays an important role in these predictions because of its influence on the partitioning of atmospheric inputs between runoff and groundwater recharge. Where permafrost is present, rapid horizontal flow occurs via a shallow suprapermafrost layer, while the more delayed flow path of vertical flow recharging subpermafrost aquifers occurs through taliks (Walvoord *et al.*, 2012). As the climate warms, talik connections are expected to expand, increasing groundwater recharge within these basins (Walvoord *et al.*, 2012; Walvoord and Kurylyk, 2016). The increased diversion of surface water to groundwater can result in the expansion of lakes and/or aufeis in areas of groundwater discharge (Walvoord *et al.*, 2012; Walvoord and Kurylyk, 2016; Crites *et al.*, 2020). Increasing baseflow volumes during the late autumn and winter have been observed in many large northern basins, due in part to increasing fall precipitation, but also increasing hydrological connectivity and expanding contributing areas as permafrost thaw progresses (Jacques and Sauchyn, 2009; Rennermalm *et al.*, 2010; Connon *et al.*, 2014; Brown *et al.*, 2015;

Crites *et al.*, 2020). As Arctic warming intensifies during the next 50-100 years (McGuire *et al.*, 2006), these trends are anticipated to continue, although the uncertainty in these predictions are great given the lack of data-driven evidence to support model development (Stadnyk and Déry, 2021).

Alpine hydrology has been studied at multiple research basins along the North American continental divide (Carey and Quinton, 2004; Rasouli *et al.*, 2014; Harder *et al.*, 2015; Knowles *et al.*, 2015), with particular attention to the hydrological processes that govern the water balance of glaciers (Bailey *et al.*, 1997; Viviroli *et al.*, 2010; IPCC, 2013; Hock *et al.*, 2019) and recently deglaciated landscapes (Ronayne *et al.*, 2012; Hood and Hayashi, 2015). The majority of these study basins are characterized by a sharp transition between contiguous forest at lower elevations and the barren lands above, but a more extensive vegetated tundra ecotone is common in many northern alpine regions. For example, the Taiga Cordillera ecozone is largely mountainous and covers 260,000 km^2 of northern Canada between 60.7 °N and 68.5 °N. According to the North American Land Change Monitoring System classification (2020), much of the Taiga Cordillera is covered by grassland [graninoid tundra] and/or shrubland (40.7 %), with forested (29.2 %) and barren land (28.2 %) areas less prevalent.

To my knowledge, no hydrological study focused on streamflow and groundwater recharge partitioning has been conducted within the alpine tundra of the Taiga Cordillera. As the climate continues to change, altered precipitation regimes and permafrost extent will affect alpine tundra hydrology, altering important ecohydrological and human resource uses within the Mackenzie River and Yukon River basins to which the Taiga Cordillera contributes. In response to this knowledge gap, the objectives of this study are as follows:

1) Quantify the water balance of a northern alpine tundra basin within the Taiga Cordillera ecozone from the beginning of freshet to fall refreeze 2019.

2) Establish seasonal differences in primary basin inputs and outputs during freshet, early summer, and late summer periods.

3) Explore the potential impacts of a warming climate on precipitation, thermal regime, and flow path partitioning within the study basin and the larger regional watersheds to which the Taiga Cordillera alpine tundra contributes.

Results from this study contribute to our understanding of spatial and temporal variability in runoff efficiency and runoff-recharge partitioning within northern alpine tundra regions. These findings are a key first step to better representing the hydrology of northern alpine tundra basins in modelling efforts and predicting their future role in maintaining ecohydrological and human resource uses within the larger regional river systems to which they contribute.

3.3 Data and methods

3.3.1 Study site

3.3.1.1 Geomorphology and land cover

The study basin selected (63.3°N, 129.8°W, 1264.8 – 1333.1 masl, 0.8 km^2) is a first order stream contributing to the Tsichu River and is considered biophysically representative of Taiga Cordillera ecozone alpine tundra land cover with discontinuous permafrost. The basin is underlain with glaciofluvial sands and gravels deposited following the retreat of montane valley glaciers active during the Gayna River glaciation (22 000 years BP; Kershaw and Kershaw, 2016). Eskers, kame terraces, outwash plains, and other stratified drift landforms are common in the surrounding area (Kershaw and Kershaw, 1983; Ecosystem Classification Group, 2010) and

account for the presence of land cover with minimal organic soil development, namely the glaciofluvial upland and riparian swamp. Sand and gravel deposits below a glaciofluvial upland feature <1 km from the study basin boundary were excavated to >3.81 m depth without contacting bedrock (Gravelle and Livingstone, 2013), but the bedrock below is likely similar to that exposed on neighbouring ridges, and includes shale, slate, and sandstone of late Precambrian and early Paleozoic origin (Ecosystem Classification Group, 2010; Geological Survey of Canada, 2014). Organic cryosols with peat accumulation >1 m in depth were commonly found near the channel, resulting in the peat plateau and fen land covers identified (Figure 3.1). Historically, impeded drainage resulted in ice lensing processes to occur within fen systems, forming the ice-rich permafrost features with dry insulating peat that are recognized presently as palsas and peat plateaus (Ecosystem Classification Group, 2010; Mamet *et al.*, 2017). Additionally, a series of groundwater springs were found along a seepage front within the headwaters of the channel network. The contributing area containing these groundwater discharge points was gauged separately and designated as the headwater subbasin (Figure 3.1).

3.3.1.2 Climate

Historical climate records (1976-2005) modelled for the region estimate a mean annual air temperature (MAAT) of -8.4 °C (Prairie Climate Centre, 2019), while 2019 was warmer, with a MAAT of -7.5 °C 10 km up valley (63.2°N, 130.0°W, 1379 MASL) at the Environment Canada Macmillan Pass station (Environment Canada, 2020). Annual precipitation for the study area is likely 50 % falling as snow (Harris *et al.*, 2014), with an average of 503 mm received annually (Prairie Climate Centre, 2019), similar to the 448 mm reported for Macmillan Pass station in

2019 ~ 10 km up valley[1] (Figure 3.1). Personal observations of Kershaw and other long-term local land users suggest that the 113.2 mm of rain collected at the study basin from 20 April – 10 September 2019 (see 3.3.2.1) was less than a typical open water season for the area.

3.3.2 Water balance

A water balance was completed for the study basin, headwater subbasin, and each land cover using the following equation:

Equation 3.1: $(P + GW_{IN}) - (GW_{OUT} + ET + Q) + \Delta S = \varepsilon$

where P is precipitation, GW_{IN} is groundwater discharge, Q is streamflow, ET is evapotranspiration, GW_{OUT} is groundwater recharge, ΔS is change in storage, and ε is the water balance error. Each component was converted to equivalent depth (mm) for the respective area of interest, with basin and subbasin areas calculated as areally weighted contributions of each cover class. The runoff ratio $(Q/(P + GW_{IN})$ and runoff-recharge partitioning ratio $(Q/(Q + GW_{OUT})$ are also presented to describe flow path partitioning within the basin. Furthermore, comparison of seasonal differences in primary inputs, outputs, and flow path partitioning was assessed by segmenting the water balance of the study basin into three periods: the freshet (7 May – 2 June), early summer (3 June – 5 July), and late summer (6 July – 9 September).

3.3.2.1 Precipitation (P)

Daily precipitation inputs (P) were calculated as the sum of snowmelt (SWE_{MELT}) and rain (R). SWE_{MELT} was calculated with the following equation:

[1] The Macmillan Pass precipitation record should be interpreted with caution given the many missing and estimated flags appended to daily entries.

Equation 3.2: $SWE_{MELT} = \Delta A_n \times \Delta D_n \times \frac{\rho_s}{\rho_w}$

where ΔA is change in snow-covered area (%), ΔD is change in snowpack depth (m), ρ_s is the snowpack density (kg m^{-3}) and ρ_w is water density (997 kg m^{-3}) during the n daily time step. Daily values of ΔA for each cover class were interpolated from unmanned aerial vehicle (drone) surveys conducted every 3–4 days from 7 to 30 May 2019. Each survey collected 1500–2000 images to generate orthomosaics of a 0.51 km^2 target area (Figure 3.2) using the structure from motion (SfM) photogrammetry software Pix4D Mapper Pro (Pix4D inc., Prilly, CH). Orthomosaics had pixel sizes ranging from 1.8 to 2.0 cm and positional accuracies ranging from 9.7 to 55.1 cm after georeferencing with 10 dGPS ground control points collected 8 September 2018 using a Leica Viva series GS10 differential GPS (Leica Geosystems AG, Heerbrugg, CH). Snow-covered and snow-free areas were assigned with a supervised iso-cluster image classification using ArcGIS Pro Version 2.6.0 (Esri, Redlands, US) (Figure 3.2). Daily values of ΔD were interpolated from measurements collected every 1–3 days at snow depth frames of similar design to Heron & Woo (1978). Eleven randomly spaced frames were installed within each cover class along 60 m survey transects before snowmelt commenced (Figure 3.2). Measurements were collected at each frame from three subsampling points spaced 15 cm apart and 15 cm from each stake end. A snowpack ρ of 410 kg m^{-3} was selected to represent a densified version of snowpack measurements collected on 17 April 2019 before ripening and/or melt commenced that was within the range of values reported from other field studies (Anderson, 1976; Pomeroy and Gray, 1995; McCartney *et al.*, 2006) (Appendix 4.1). Sublimation from snow-covered areas was assigned at 0.25 mm day^{-1} based on Pomeroy *et al.'s* (2003) estimates at Granger Basin, Yukon (60.5°N, 1312 MASL), an alpine shrub tundra basin with similar SWE_{MAX} and vegetation characteristics.

Daily R was calculated as the amount received 34 cm above ground surface by a tipping bucket rain gauge mounted on a 1 m^2 platform where no impeding shrub cover was present (EML, North Shields, UK: 0.2 mm accuracy). Tipping bucket measurements were recorded on a Campbell Scientific CR300 data logger every 30 minutes (Logan, UT, US). The tipping bucket record was cross-referenced with manual rain gauge records collected at base camp ~350 m beyond the catchment boundary to confirm rain was evenly distributed across the study area (Appendix 4.1).

3.3.2.2 Evapotranspiration (ET)

ET observations were collected from nine soil lysimeters with weights measured using a hanging scale accurate to 5 g and three evaporation pans with depths measured accurate to 0.1 mm at four marked locations along the margin of each vessel. Lysimeters (27.7 cm inner diameter, 15 cm depth) were installed flush with the ground surface and contained locally collected soils with undisturbed vegetation cover. The lysimeters also had drain holes at the base to allow for gravity drainage and were rewetted as necessary to match the surrounding environment based on readings from a Campbell Scientific Hydrosense 2 probe (Logan, UT, USA). Evaporation pans (27.2 cm inner diameter, 35 cm depth) were partially submerged in the channel (Figure 3.1) and with each measurement collected, pan depths were adjusted to maintain the water level within 50 mm of the vessel lip (Appendix 4.2).

Daily evapotranspiration (ET) from snow-free surfaces was estimated using the Priestley-Taylor equation (1972):

Equation 3.3: $ET = \alpha E_{eq} = \alpha \left[\frac{S}{(S+\gamma)}\right]\left[\frac{Q^* - Q_G}{\lambda_W * \rho_W}\right]$

where α is the Priestley–Taylor coefficient, E_{eq} is the equilibrium evapotranspiration (mm day^{-1}), S is the slope of the saturation vapor pressure–temperature curve (kPa °C^{-1}), γ is the psychrometric constant (0.066 kPa °C^{-1} at 20°C), Q^* is the net radiation (J m^{-2} day $^{-1}$), Q_G is the ground heat flux (J m^{-2} day $^{-1}$), λ_W is the latent heat of vaporization (J kg $^{-1}$), and ρ_W is the density of water (997 kg m^{-3}). Cover class specific α coefficients were developed based on the ratio of calculated E_{eq} and observed ET collected with lysimeters and pans within each cover class.

To calculate E_{eq}, S was assigned using air temperature measurements collected with a shielded HC-S3 temperature probe with ± 0.2°C accuracy (Campbell Scientific, Logan, US) reading every minute and recorded 30-minute averages on a CR3000 data logger (Campbell Scientific, Logan, US) located at the basin meteorological station (Figure 3.1). Q^* was collected every minute with a CNR4 four-component net radiometer (Kipp and Zonen, Delft, NL) that also recorded 30-minute averages on the meteorological station CR3000. Q_G was estimated as 10 % of Q^*, based on a study conducted in an alpine shrub tundra basin at Niwot Ridge, Colorado (40.05°N, 105.58 °W, 3480 MASL) (Blanken *et al.*, 2009). λ_W was calculated using water temperature measurements collected and recorded every 30 minutes with ± 0.44°C accuracy at the centrally located HOBO U20 water level sensor (Figure 3.1).

3.3.2.3 Change in storage (ΔS)

Surface water storage in the channel network and in isolated depressions within the study basin was assumed to be negligible due to the limited extent of open water (Figure 3.1b). Shallow groundwater storage for each land cover class was estimated using the following equation:

Equation 3.4: $\Delta S = \Delta S_U + \Delta S_S = \Delta d_U \theta_U + \Delta d_s \theta_{sy}$

where ΔS_U and ΔS_S are changes in unsaturated and saturated groundwater storage (mm), respectively. Daily ΔS_U was calculated as the product of Δd_U, change in the unsaturated layer depth (mm), and θ_U, the unsaturated volumetric moisture content (VMC) (decimal fraction). Daily ΔS_S was calculated as the product of Δd_s, change in the change in water table depth (mm), and θ_{sy}, the specific yield (decimal fraction).

Fen and riparian swamp D and d values were estimated with water table depth records collected with pressure transducers installed in stilling wells of the same design described in section 3.3.2.4. Peat plateau and glaciofluvial pressure transducers indicated no saturated zone for the duration of observation ($\Delta d_s = 0$). D within the peat plateau was estimated with frost table depth measurements collected with a 1 cm graduated probe at 44 survey points visited five times between 23 May and 4 September 2019. D within the glaciofluvial upland was unknown due to the lack of water table, frost table, and/or bedrock constraining the unsaturated zone (Chapter 2) and was therefore set at 50 cm assuming percolation below 50 cm qualified as GW_{OUT}.

θ_U was measured at six locations with 5TM probes (Decagon Devices, Pullman, WA, USA) and/or CS655 probes (Campbell Scientific, Logan, UT, USA) installed at 10, 20, and 50 cm depths below the ground surface. Probes were programmed to collect measurements at one-minute intervals and to record 30-minute averages. Daily θ_U values for each cover class were estimated as the mean θ_U of all sensors above d. Daily θ_{sy} values for each cover class were estimated using the following equation:

Equation 3.5: $\theta_{sy} = \theta_s - \theta_{fc}$

where θ_s and θ_{fc} are volumetric moisture contents of saturated and field capacity conditions, respectively. θ_s values were estimated as the mean θ_s reported from gravimetric laboratory test

results (Appendix 4.3). θ_{fc} values were collected when the water table and/or frost table were below a given sensor and the basin was without precipitation >0.2 mm day^{-1} for >2 days.

3.3.2.4 Streamflow (Q)

In 2019, point observations of streamflow (Q, m^{3}s^{-1}) were collected at the basin and subbasin outlets (Figure 3.1). Q estimates were based on sodium dilution slug tests as described by Moore (2005) using an Orion electrical conductivity probe (Thermo Fisher Scientific Inc., Waltham, US) recalibrated weekly with 0.1413 µS cm^{-1} solution.

When possible, continuous records of Q were generated with rating curves. During the early freshet, a single centrally located HOBO U20 pressure transducer (Figure 3.1) measuring and recording water level at 30-minute intervals with ± 1.5-3 cm accuracy (Onset Computer Corp, Bourne, MA, US) provided change in stage values for rating curve calibration. Once the bedfast ice had melted, channel geometry stabilized, and local stilling wells thawed sufficient for pressure transducer installation, rating curves were recalibrated to pressure transducers installed at each outlet (Appendix 4.4).

3.3.2.5 Groundwater discharge (GW_{IN}) and recharge (GW_{OUT})

Groundwater exchange within the basin occurred as discharge from spring sources within the headwater subbasin contributing directly to the channel network (GW_{IN}) and recharge via channel bed infiltration and glaciofluvial upland infiltration (GW_{OUT}). The headwater subbasin springs were initially identified with visual assessment of 2016 Worldview 2 satellite imagery (DigitalGlobe Inc., Westminster, CO, USA) before being confirmed with ground-based reconnaissance at the beginning of the 2019 field season. The extent of gaining and losing channel length was confirmed with a series of 7 piezometers measuring the difference in head (Δh, cm) between the open water in channel and the groundwater below the channel bed

(Rosenberry and LaBaugh, 2008). Δh values were collected during maximum thaw, low flow conditions on 3 September 2019 (Figure 3.3). Freshet, early summer, and late summer seasonal mean values of spring discharge (GW_{IN}) occurring within the headwater subbasin and channel bed infiltration (GW_{OUT}) occurring between the headwater subbasin and basin outlets were then estimated based on comparison of streamflow records during periods with precipitation ≤0.2 mm day^{-1} for ≥3 days (Donato, 1998; Rosenberry and LaBaugh, 2008) (Appendix 4.5). This required the assumptions that 1) channel bed infiltration along the 100 m segment between the uppermost piezometer and the subbasin outlet (Figure 3.3) is negligible, and 2) differences in outlet record streamflow are due to channel bed infiltration and not evaporation occurring along the channel length.

Glaciofluvial upland features in the basin are known to be hydrologically isolated from the channel network and composed of coarse substrates that result in unlimited infiltration when P is received (Chapter 2). As such, daily GW_{OUT} via glaciofluvial upland infiltration was estimated as the residual of the simplified water balance for this cover class ($P - ET - \Delta S = GW_{OUT}$).

3.3.3 Statistical analysis and water balance error (Ɛ)

Statistical tests were conducted to establish if significant differences between group means existed for a given water balance component. When sample size was sufficient for cover class comparisons, a Kruskal-Wallis rank sum test was applied to determine if there were significant differences between group means. If significant differences were found, a Wilcoxon rank sum test was conducted for pairwise comparisons between group levels with corrections for multiple testing (Hollander and Wolfe, 1999). When sample size was sufficient for catchment area comparisons, a Wilcoxon signed-ranks test was conducted to determine if there were significant differences between basin areas. The confidence level for each test was set at 95 % and all

statistical assessments were conducted with the computer program R stats package 3.6.3 (R Core Team, 2020).

The water balance required a series of assumptions and there are inherent uncertainties when quantifying each component. Sample collection and sensor installation were stratified across cover classes to maintain temporal and spatial accuracy, but limits in sensor sensitivities, laboratory techniques, and sufficient replicates for each measurement were not always optimal. To identify when uncertainties in specific component estimates (Appendix 4) were potentially problematic, daily water balance error (Ɛ) was calculated as the remainder term of the water balance calculation (Trask *et al.*, 2017) and a cumulative Ɛ time series was developed.

3.4 Results

The results of each water balance component are presented in the following subsections. Patterns of both spatial (Table 3.1) and temporal (Table 3.2; Figure 3.4) change are presented, before runoff ratio and runoff-recharge ratio are discussed in the flow path partitioning subsection. Finally, temporal trends in the water balance error are reported.

3.4.1 Precipitation (P)

There were significant differences in total SWE_{MELT} among cover classes (Chi square = 69.52, p = 2.9e – 14, df = 4), but not between basin areas. Although daily SWE_{MELT} was similar for the headwater subbasin and basin areas (Figure 3.5a), snowpack depleted earlier in areas where ripe snowpack was shallowest, namely open water, peat plateau, and glaciofluvial uplands (Figure 3.5b). A total of 143.2 mm of snowmelt (SWE_{MELT}) occurred in the study basin between 7 and 23 May 2019, with an average of 8.4 mm day^{-1} and a maximum daily melt of 38.3 mm (Figure

3.4a; Table 3.2). In addition, sublimation losses were considered minor (2.3 mm) and had little influence on daily and seasonal SWE_{MELT} rates.

A total of 113.2 mm of rain (R) was received between 17 May and 8 September 2019, accounting for 44 % of total precipitation and 25 % of total water inputs (Table 3.1). R was evenly distributed across the study area, as manual rain gauge values collected at the meteorological station and base camp ~300 m beyond the study area border were not statistically different (Appendix 4.1). Additionally, the Environment Canada Macmillan Pass station received similar R (107.5 mm) during the same observation period (Environment Canada, 2020).

3.4.2 Evapotranspiration (ET)

After adjusting for precipitation and removing erroneous entries (i.e., potentially significant condensation and/or measurement error), 508 evapotranspiration (ET) observations were collected from the lysimeters and evaporation pans between 5 June and 10 September 2019. Based on these observations, the mean Priestley–Taylor α within the basin ranged from 0.85 in the glaciofluvial uplands to 1.98 in open water, with a basin weighted mean of 1.0. There were significant differences in ET among cover classes (Chi square = 167.8, p < 2.2e-16, df = 11), but not between headwater subbasin and basin areas. Transpiration from open water (3.0 ± 1.4 mm) was twice that of ET from the peat plateau (1.7 ± 0.8 mm), fen (1.5 ± 0.7 mm), glaciofluvial upland (1.4 ± 0.7 mm) and riparian swamp (1.4 ± 0.7 mm), but had little influence on basin weighted losses due to its limited extent (Table 3.1). Daily ET losses calculated with equation 3.3 peaked in the early summer at 2.2 mm day^{-1}, while freshet and late summer rates were ~ 0.5 mm day^{-1} less. In total, 220 mm of ET occurred, accounting for 35 % of total basin outputs (Figure 3.4a).

3.4.3 Change in storage (ΔS)

All cover classes reported daily gains in vadose zone volumetric moisture content (VMC) across all seasons in response to precipitation inputs, with the fen reporting the largest unsaturated soil volume change due to the greater storage available as the freshet thaw progressed and the water table dropped (Figure 3.6a). At the fen and riparian swamp, VMC losses from the phreatic zone occurred during the freshet and early summer, but these daily losses were largely offset by gains in the vadose zone above (Figure 3.6b,c). In the glaciofluvial upland, unrestricted infiltration and a lack of a water table near-surface resulted in minimal ΔS. On a basin scale, daily gains in storage occurred during the freshet and first half of the early summer (Figure 3.4a) when vadose zone VMC was limited by shallow frost and water tables (Figure 3.6a), but this accumulation was mostly lost during the second half of the early summer and late summer periods.

3.4.4 Streamflow (Q)

Streamflow (Q) accounted for 256.5 mm (37 %) of total basin outputs, with the freshet period generating the greatest seasonal average at 7.9 mm day^{-1}. In comparison, summer Q was relatively minor, resulting in 42.7 mm of basin losses over a much longer timeframe (Figure 3.4a; Table 3.2).

3.4.5 Groundwater discharge (GW_{IN}) and recharge (GW_{OUT})

Groundwater discharge (GW_{IN}) contributions were active for the entire observation period, sustaining Q from the upper subbasin during both summer dry and winter cold conditions. Prior to the freshet, Q from the upper subbasin occurred at an average rate of 0.004 m^3 s^{-1}, representing a baseflow contribution to the study basin of 0.4 mm day^{-1}. After the freshet, the GW_{IN}

contribution was much larger, with seasonal averages of 1.9–2.0 mm day^{-1} for the early and late summer periods, respectively, resulting in 202.5 mm (44 %) of total basin inputs (Table 3.2).

Along the 2292 m channel length between the headwater subbasin and basin outlets, 164 mm of total groundwater recharge (GW_{OUT}) occurred via channel bed infiltration (Table 3.2). This is consistent with the negative difference in head across the channel bed along this length of the channel network (Figure 3.3). Of note, the two lowest elevation piezometers did not reach the water table within 50 cm of the channel bed. With the addition of GW_{OUT} via glaciofluvial upland infiltration, a relatively stable rate of aquifer recharge occurred across the seasons, ranging from 1.7 to 2.2 mm day^{-1} and resulting in 208.9 mm (31 %) of total basin outputs (Figure 3.4a).

3.4.6 Flow path partitioning

During the freshet (7 May–2 June 2019) the primary means of water loss was Q, as reflected in the maximum observed seasonal runoff ratio (1.29) and runoff-recharge ratio (0.83). During the early summer (3 June–5 July 2019), ET became the primary means of water loss, Q declined, and GW_{OUT} via channel bed infiltration became more prominent, resulting in a sharp decline in the early summer runoff ratio (0.20) and the runoff-recharge ratio (0.28). By the late summer (6 July–9 September 2019), channel bed infiltration was the primary means of basin water loss, as reflected in the further decline of both runoff ratio (0.12) and runoff-recharge ratio (0.17) (Table 3.2).

3.4.7 Water balance error (Ɛ)

During the first half of the freshet, the cumulative error (Ɛ) was positive, peaking at 71.4 mm on 5 May before a steady day over day decline in Ɛ reaching -111.4 mm cumulatively by the end of

the freshet (2 June 2019). As the freshet transitioned to summer, the negative trend in Ɛ continued, resulting in a final cumulative Ɛ of -207.4 mm on 9 September 2019 (Figure 3.4b).

3.5 Discussion

3.5.1 Water balance assumptions and sources of error

The cumulative error (Ɛ) of the water balance was used to help identify periods when the quantification of specific water balance components and/or associated hydrological processes were less reliable. The early freshet was characterized by a steadily accumulating positive Ɛ (Figure 3.4b), likely due to underestimation of ΔS. During snowmelt, local depressions and temporary snow dams are known to retain surface water (Woo and Heron, 1987; Metcalfe and Buttle, 2001), and while such features were observed visually during the freshet, the methods applied for estimation of ΔS did not capture this. The influence of this error declined as the freshet progressed, snow dams failed, and local depressions thawed, such that the cumulative Ɛ began to decline on 5 May as other sources of error became more influential. The decline in cumulative Ɛ during this period is likely due to underestimation of GW_{IN}, as pre-freshet rates were applied for the freshet period because continuous daily precipitation inputs did not allow for estimation of GW_{IN} as described in 3.3.2.5. Pre-freshet GW_{IN} was likely less than would occur during the freshet, particularly during the 5 May – 2 June period as SWE_{MELT} delayed by shallow aquifer flow paths entered the channel from sources beyond the topographical extent of the basin via the headwater subbasin springs.

The continued decline in cumulative Ɛ during the summer months (Figure 3.4b) was likely due to overestimation of ET and/or GW_{OUT} via channel bed infiltration. Soil lysimeters and evaporation pan measurements used in calculation of daily ET may have introduced error if soil and water

volumes were not representative of their surroundings. Pan temperatures were consistent with the surrounding waters (Appendix 4.2), but lysimeters regularly needed rewetting during dry periods, suggesting ET from the measured soil volumes was greater than the undisturbed surroundings. Regular soil replacement and/or a modified lysimeter design may have resulted in more accurate ET measurement (Baker and Norman, 2002) and reduced Ɛ, particularly during the early summer when ET was the primary means of basin water loss (Table 3.2). In addition, the limited number of periods that met the criteria for GW_{OUT} estimates (Appendix 4.5) may have missed some of the temporal variation in this component, particularly during the late summer when GW_{OUT} was the primary means of basin water loss (Table 3.2).

Given the limitations of study design and instrumental accuracy, a water balance error was expected. The maximum and minimum cumulative Ɛ reported above are substantial. However, the data support understanding the influence of hydrological processes occurring in the basin and establishing seasonal differences in primary basin inputs, outputs, and potential impacts on local alpine shrub tundra and regional river water balances as the climate continues to change.

3.5.2 Freshet water balance

Prior to the freshet, GW_{IN} from headwater springs sustained streamflow at the headwater subbasin, but this water did not reach the basin outlet. While some GW_{IN} contributions received over winter were retained in storage as aufeis, these features were limited in extent (Figure 3.2), suggesting the majority of over-winter GW_{IN} rapidly returned to recharge via channel bed infiltration (GW_{OUT}) along a short length of the channel network below the headwater subbasin outlet, as directed by the negative Δh across the channel bed (Figure 3.3).

During the freshet, 83 % of total open water season Q occurred, resulting in the highest observed seasonal runoff ratio (Table 3.2). This is consistent with a typical nival regime, whereby a large proportion of total annual inputs is received during snowmelt and the basin responds with rapid peak flow. Some nival regimes in the Mackenzie Mountains have reported a second peak in the autumn months from late season rain events (Woo and Thorne, 2003), although this did not occur during this study likely due to limited rainfall during the summer months.

During the freshet, the study basin received 56 % of its total precipitation (P) as snowmelt (SWE_{MELT}) over a 17-day period, consistent with the typical precipitation regime of circumpolar cold climate systems (Woo, 2012). The average daily SWE_{MELT} within the study basin was similar to the 3.8–8.2 mm day^{-1} of an alpine shrub tundra basin in the neighbouring Boreal Cordilleran ecozone (Granger Basin, Yukon, 60.5°N, 1312 MASL) (McCartney *et al.*, 2006). While variable SWE_{MELT} rates have been associated with shrub fraction and shrub exposure above snowpack in other tundra settings (Pomeroy *et al.*, 2006; Wilcox *et al.*, 2019), no such spatial pattern was observed in this study basin as SWE_{MELT} rates were consistent across cover classes (Figure 3.5). The riparian swamp and fen took longer for the snowpack to completely melt having accumulated greater SWE_{MAX} over winter (Table 3.1), as greater shrub density and/or topographical depression allowed these areas to capture blowing snow redistributed from the other cover classes (Pomeroy and Gray, 1995; Pomeroy *et al.*, 2006).

Snowmelt infiltration can occur in both frozen and unfrozen substrates (Gray *et al.*, 2001; Zhang *et al.*, 2010), but ice-rich substrates are often impermeable to flow (Hayashi, 2013). As such, the shallow frost table within the peat plateau limited infiltration during the freshet (Figure 3.6a), similar to observations of other permafrost peat deposits (Slaughter and Kane, 1979; Zhang *et al.*, 2010). At the same time, GW_{OUT} via glaciofluvial upland infiltration was unlimited (Table

3.2), which is confirmed by the minor daily changes in VMC within this cover class (Figure 3.6b). During the freshet, upland infiltration was ~3x greater than channel bed infiltration (Table 3.2) as much of the channel network retained an impermeable layer of bedfast ice with low hydraulic conductivity (K), similar to Woo *et al.'s* (1994) observations of ice content inhibiting channel bed infiltration.

3.5.3 Summer water balance

Water storage within the study basin peaked on 3 June 2019 at 23.6 mm on the first day of the early summer period (Figure 3.4a). In comparison, groundwater storage of a partially glaciated barren land cirque valley in BC named the Opabin watershed (51.35°N, 116.33°W, 2000-3500 MASL) was estimated to peak at the end of June, as deep proglacial moraine deposits retained ~60 mm of the ~700 mm snowmelt received (Hood and Hayashi, 2015). The timing of maximum storage is similar, but the discrepancy in volume relates to 1) inability of the glaciofluvial upland to retain soil water, and 2) peat plateau ice-rich permafrost restricting the soil volume available for storage within this study basin (Figure 3.6). In general, the study basin was unsuccessful in retaining soil water following precipitation inputs, particularly during the freshet when the mean daily gains in the vadose zone were largely compensated for by losses from the phreatic zone as the water table declined (Table 3.2).

During the summer months, GW_{IN} was the largest daily input, with an early summer rate ~3.8x greater than during the freshet (Table 3.2). This increase is likely due to delayed discharge from aquifers receiving SWE_{MELT} inputs from a much larger recharge zone at higher elevation (Figure 3.1a). Flow path extensions such as this have been documented in other alpine basins, with daily to monthly delays in aquifer discharge following freshet inputs (Andermann *et al.*, 2012;

Langston *et al.*, 2013). As the summer progressed, the average rate of P continued to decline, while GW_{IN} remained stable and slightly increased in the late summer (Table 3.2).

During the early summer, ET accounted for the largest volume of basin water losses (Figure 3.4a; Table 3.2). The basin weighted mean Priestley–Taylor α of 1.0 is similar to that reported for the partially glaciated Opabin basin in BC (Hood and Hayashi, 2015), and other shrub tundra basins in Trail Valley, NT and Churchill, MB (Eaton *et al.*, 2001). This mean α also confirms the water limited condition of the basin throughout the summer months, as ET was unable to achieve the α of 1.26 typical of terrain with unlimited water supply (Priestley and Taylor, 1972). Open water had an average α of 1.98, but this cover class had little influence on basin-wide ET due to its limited areal extent (Table 3.1).

The series of 2 to 5 mm rain events during the summer months may have been too small to change the water limited condition of the basin, as confirmed by the evaporative losses of similar magnitude and minor gains in ΔS following P events during the summer months (Figure 3.4). This resulted in reduced runoff ratios during the summer periods, but the decline in runoff ratio from early to late summer can also be explained in part by the deepening frost tables (3.6a). As the frost table deepens, water previously routed laterally via near-surface organic soils with high K instead follows extended flow paths through less conductive organic and/or mineral substrates at depth (Quinton and Marsh, 1999; Quinton et al., 2005). Also, as the summer progressed, thawing bedfast ice and channel bank frost allowed for infiltration to occur along the entire extent of the channel network between the headwater subbasin and basin outlets (Figure 3.3). The sharp decline in Q and runoff ratio at the end of the freshet and beginning of the early summer (Figure 3.4a) reflects the end of SWE_{MELT} inputs, the extension of the typical flow paths en route to the channel network, and a change in runoff-recharge partitioning as GW_{OUT} via

channel bed infiltration became the dominant mode of water loss from the study basin by the late summer (Table 3.2).

3.5.4 Climate change implications

To explore climate change implications for water balance and seasonally important hydrological processes within the study basin, mean temperature and total precipitation projections from climatedata.ca were analyzed for the 300 arc second grid cell that included the study basin (Environment and Climate Change Canada, 2021). Fifty percent likelihood scenarios using 2.6, 4.5, and 8.5 representative concentration pathways were modelled for 2020-2100 and simple linear regressions applied to develop annual and/or monthly trends[2]. Based on this analysis, the study basin is expected to warm and receive greater precipitation depths in the future, with 2.6 and 8.5 representative concentration pathways predicting 2100 MAATs warming between 0.6 and 5.8 °C, while total annual precipitation is predicted to increase between 24.2 and 139.8 mm (Environment and Climate Change Canada, 2021). Mean monthly temperatures are also expected to increase, with the 2.6 RCP scenario predicting an increase of 0.3, 0.3, and 0.6°C, while the 8.5 RCP scenario predicts much larger increases of 4.5, 5.3, and 5.6 °C, for the freshet (May), early summer (June), and late summer (July - August) months, respectively. Total precipitation changes for each seasonal period are less dramatic, with 2.6 RCP scenarios predicting a stable regime with 2.3, -0.3, and 4.6 mm, while the 8.5 RCP scenario predicts 5.6, 8.8, and 25.8 mm for the freshet, early summer, and late summer, respectively (Environment and Climate Change Canada, 2021). The greater magnitude change in total precipitation during the late summer in part reflects the longer duration of this seasonal window, but may also relate to a shift from nival

[2] For more information on model development, observational data set, and model initialization of the climatedata.ca resource, I suggest the reader refer to the website < https://climatedata.ca/about/>

to pluvial runoff regimes, as has been observed in other northern basins (Spence *et al.*, 2011; Beel *et al.*, 2021). Within this study basin the nival regime will likely be maintained, but the shift in precipitation phase and timing will likely result in a greater proportion of annual basin outputs via GW_{OUT}, as the early and late summer periods extend. Modelling of an alpine basin in the neighbouring Boreal Cordillera ecozone reported a general sensitivity of snowpack condition and freshet runoff to temperature and precipitation trends, such that a 5˚C warming and ±20 % change in precipitation resulted in a 46-60 day extension of the snow-free period (Rasouli *et al.*, 2014). Streamflow from larger basins with alpine areas, such as the Athabasca River basin, are also sensitive to changes in winter temperature and snowfall characteristics (Kerkhoven and Yew Gan, 2008).

A warming climate will influence the temporal availability of channel bed infiltration flow paths, as well as the distribution of landforms known to limit infiltration within the surrounding contributing area. Ice-rich organic soils were found below the peat plateau features and accounted for 23 % of the study basin area (Figure 3.1). Locally, these permafrost features have been thawing and reducing in areal extent (Mamet *et al.*, 2017), consistent with trends of permafrost thaw and land cover change reported throughout the circumpolar region (Grosse *et al.*, 2011; Quinton *et al.*, 2011; Hayashi, 2013; Baltzer *et al.*, 2014). In high elevation permafrost areas, climate-driven permafrost thaw has implications for storage availability, streamflow, and the distribution of taliks (Rogger *et al.*, 2017), impacting the timing and magnitude of groundwater recharge in alpine regions and the distant discharge to the large regional river systems to which they contribute (Walvoord *et al.*, 2012; Ma *et al.*, 2017).

Climate warming is also likely to increase ET from northern regions as energy availability and woody stemmed biomass increase, with the Wolf Creek study basin in the Boreal Cordillera

Ecozone estimated to have a 30 % increase in ET if a 5°C increase in mean annual temperature occurs in the coming decades (Rasouli *et al.*, 2014). At Wolf Creek, ET has been reported to exceed P, with cumulative losses between 220 – 372 mm over an observation period similar to that of this study (Carey and Woo, 2001a). Compared to this study basin, the enhanced ET at Wolf Creek highlights the importance of transpiring canopy and root systems accessing groundwater (Chen *et al.*, 2021). At Havikpak Creek (68.2° N, 133° W), 150 MASL), a tundra-taiga arctic basin with 50 % forested extent, evaporation was the greatest means of annual water loss (47 % total), with ET from forested areas (164 mm) only exceeded by wetlands (218 mm) (Krogh *et al.*, 2017).

3.6 Conclusions

The goal of this study was to characterize seasonal differences in the water balance of a northern alpine tundra basin from the beginning of freshet to autumn refreeze and consider the long-term implications of these findings in the context of climate change. During the freshet, a large volume of SWE_{MELT} was received and routed quickly to Q. Elevated frost tables within peat plateaus and high-water tables within the fen and riparian swamp resulted in a large contributing area that included all of the basin except the glaciofluvial uplands, where unlimited infiltration quickly transferred P to GW_{OUT}. As the freshet ended and summer began, runoff-recharge partitioning switched to favour GW_{OUT} and the runoff ratio declined. This relates to increasing efficiency in channel bed infiltration as bedfast ice melted and frozen soils thawed. During the summer months P was limited, but GW_{IN} from spring sources sustained channel flow, although the majority of channel water left the basin as GW_{OUT} instead of Q. Throughout the observation period, GW_{IN} was concentrated within the headwater subbasin, where springs discharged water

sourced from areas beyond the topographical extent of the basin. During the early summer, the primary mode of basin water loss was ET, which then declined during the late summer and became supplanted by GW_{OUT} as the primary means of water loss. In general, the study basin had limited storage capacity compared to other alpine basins typified by sparse vegetation and proglacial deposits because ice-rich permafrost features routed inputs horizontally toward the channel network and glaciofluvial uplands routed inputs vertically to aquifer recharge. Also, compared to subalpine basins and larger basin areas with established forest extent, ET losses from alpine shrub tundra were less influential due to the lack of canopy vegetation and water limited conditions during the dry late summer period.

Alpine tundra is prominent within the Taiga Cordillera ecozone and other northern regions, partitioning large volumes of precipitation between rapid streamflow and the more extended flow path of aquifer recharge. As such, the alpine tundra plays a key hydrological role in northern systems by sustaining baseflow during summer drought and winter cold conditions. Climate-driven changes in precipitation regime, evaporative potential, and land cover in alpine shrub tundra regions will have major implications for the future water balance of northern basins. Specifically, warmer temperatures and greater precipitation coupled with shrubification and treeline expansion are likely to increase ET from the ground surface, while a decline in permafrost extent will likely increase GW_{OUT}. These findings should be considered in future water management decisions and efforts to model the water balance of basins that include the Taiga Cordillera ecozone, or more broadly, alpine shrub tundra.

3.7 References

Andermann C, Longuevergne L, Bonnet S, Crave A, Davy P, Gloaguen R. 2012. Impact of transient groundwater storage on the discharge of Himalayan rivers. Nature Geoscience 5 (2): 127–132 DOI: 10.1038/ngeo1356

Anderson E. 1976. A point energy and mass balance model of a snow cover: NOAA technical report NWS; 19 Available at: https://repository.library.noaa.gov/view/noaa/6392

Asong EZ, Elshamy EM, Princz D, Wheater SH, Pomeroy J, Pietroniro A, Cannon A. 2020. High-resolution meteorological forcing data for hydrological modelling and climate change impact analysis in the Mackenzie River Basin. Earth System Science Data 12 (1): 629–645 DOI: 10.5194/essd-12-629-2020

Bailey W, Oke T, Rouse WR. 1997. The Surface Climates of Canada. McGill-Queen's University Press: Montreal.

Baker J, Norman J. 2002. Evaporation from natural surfaces. In Methods of Soil Analysis Part 4 - Physical Methods, Dane J, Topp G (eds). Soil Science Society of America: Madison, Wisconsin; 1047–1071.

Baltzer JL, Veness T, Chasmer LE, Sniderhan AE, Quinton WL. 2014. Forests on thawing permafrost: fragmentation, edge effects, and net forest loss. Global Change Biology 20 (3): 824–834 DOI: 10.1111/gcb.12349

Beel C, Heslop J, Orwin J, Pope M, Schevers A, Hung J, Lafrenière M, Lamoureux S. 2021. Emerging dominance of summer rainfall driving High Arctic terrestrial-aquatic connectivity. Nature Communications 12: 1448 DOI: 10.1038/s41467-021-21759-3

Blanken PD, Williams MW, Burns SP, Monson RK, Knowles J, Chowanski K, Ackerman T. 2009. A comparison of water and carbon dioxide exchange at a windy alpine tundra and subalpine forest site near Niwot Ridge, Colorado. Biogeochemistry 95 (1): 61–76 DOI: 10.1007/s10533-009-9325-9

Brown D, Jorgenson. MT, Douglas T, Ruess R. 2015. Interactions of fire and climate exacerbate permafrost degradation in Alaskan lowland forests. Journal of Geophysical Research, Biogeosciences 120(8): 1619–1637 DOI: 10.1002/2015JG003033.Received

Canada Centre for Remote Sensing (CCRS), U.S. Geological Survey (UGS), National Institute of Statistics and Geography, National Commission for the Knowledge and Use of the Biodiversity, the National Forestry Commission of Mexico. 2020. 2010 Land Cover of North America at 30 meters. Commission for Environmental Cooperation: Montréal, Québec. Available at: http://www.cec.org/nalcms

Carey S, Quinton WL. 2004. Evaluating snowmelt runoff generation in a discontinuous permafrost catchment using stable isotope, hydrochemical and hydrometric data. Nordic Hydrology 35 (4–5): 309–324 DOI: 10.1002/hyp.5764

Carey S, Woo MK. 2001. Slope runoff processes and flow generation in a subarctic, subalpine catchment. Journal of Hydrology 253 (1–4): 110–129 DOI: 10.1016/S0022-1694(01)00478-4

Chen H, Jeanne Huang J, McBean E, Singh VP. 2021. Evaluation of alternative two-source remote sensing models in partitioning of land evapotranspiration. Journal of Hydrology 597: 126029 DOI: 10.1016/j.jhydrol.2021.126029

Connon RF, Quinton WL, Craig JR, Hayashi M. 2014. Changing hydrologic connectivity due to permafrost thaw in the lower Liard River valley, NWT, Canada. Hydrological Processes 28 (14): 4163–4178 DOI: 10.1002/hyp.10206

Crites H, Kokelj S V., Lacelle D. 2020. Icings and groundwater conditions in permafrost catchments of northwestern Canada. Scientific Reports 10 (1): 1–11 DOI: 10.1038/s41598-020-60322-w

Dingman SL. 1981. Elevation: a major influence on the hydrology of New Hampshire and Vermont, USA. Hydrological Sciences Journal 26 (4): 399–413 DOI: 10.1080/02626668109490904

Donato MM. 1998. Surface-water/ground-water relations in the Lemhi River Basin, east-central Idaho Available at: http://pubs.er.usgs.gov/publication/wri984185

Eaton AK, Rouse WR, Lafleur PM, Marsh P, Blanken PD. 2001. Surface energy balance of the western and central Canadian subarctic: variations in the energy balance among five major terrain types. Journal of Climate 14 (17): 3692–3703 DOI: 10.1175/1520-0442(2001)014<3692:SEBOTW>2.0.CO;2

Ebel BA, Koch JC, Walvoord MA. 2019. Soil physical, hydraulic, and thermal properties in interior Alaska, USA: implications for hydrologic response to thawing permafrost conditions. Water Resources Research 55 (5): 4427–4447 DOI: 10.1029/2018WR023673

Ecosystem Classification Group. 2010. Ecological Regions of the Northwest Territories: Cordillera. Department of Environment and Natural Resources, Government of the Northwest Territories: Yellowknife.

Environment and Climate Change Canada. 2021. Climate data for a resilient Canada. Available at: https://climatedata.ca/ [Accessed 18 August 2021]

Environment Canada. 2020. Environment Canada historical data archive. Available at: https://climate.weather.gc.ca/historical_data/search_historic_data_e.html [Accessed 17 April 2020]

Geological Survey of Canada. 2014. Canadian Geoscience Map 195: Surficial Geology of Canada DOI: 10.4095/295462

Granger RJ. 1998. Partitioning of energy during the snow-free season at the Wolf Creek Research Basin. In Wolf Creek Research Basin: Hydrology, Ecology, Environment, Pomeroy W, Granger R (eds.). National Water Research Institute, Saskatoon, SK; 3–44.

Gravelle C, Livingstone S. 2013. Case Study Program for Petroleum Hydrocarbon Stability and Ecological Integrity. Public Works and Government Services Canada Report 1692-1201:350125

Gray DM, Toth B, Zhao L, Pomeroy JW, Granger RJ. 2001. Estimating areal snowmelt infiltration into frozen soils. Hydrological Processes 15: 3095–3111 DOI: 10.1002/hyp.320

Grosse G, Romanovsky V, Jorgenson T, Anthony KW, Brown J, Overduin PP. 2011. Vulnerability and feedbacks of permafrost to climate change. Eos 92 (9): 73–74 DOI: 10.1029/2011EO090001

Harder P, Pomeroy JW, Westbrook CJ. 2015. Hydrological resilience of a Canadian Rockies headwaters basin subject to changing climate, extreme weather, and forest management. Hydrological Processes 29 (18): 3905–3924 DOI: 10.1002/hyp.10596

Harris I, Jones PD, Osborn TJ, Lister DH. 2014. Updated high-resolution grids of monthly climatic observations - the CRU TS3.10 dataset. International Journal of Climatology 34 (3): 623–642 DOI: 10.1002/joc.3711

Hatch CE, Fisher AT, Ruehl CR, Stemler G. 2010. Spatial and temporal variations in streambed hydraulic conductivity quantified with time-series thermal methods. Journal of Hydrology 389 (3–4): 276–288 DOI: 10.1016/j.jhydrol.2010.05.046

Hayashi M. 2013. The cold vadose zone: hydrological and ecological significance of frozen-soil processes. Vadose Zone Journal 12: 2136 DOI: 10.2136/vzj2013.03.0064

Hayashi M. 2020. Alpine hydrogeology: the critical role of groundwater in sourcing the headwaters of the world. Groundwater 58 (4): 498–510 DOI: 10.1111/gwat.12965

Heron R, Woo MK. 1978. Snowmelt computation for a high arctic site. In Proceedings of the 35th Annual Eastern Snow Conference. Hanover, New Hampshire; 162–172.

Hock R, Rasul G, Adler C, Cáceres B, Gruber S, Hirabayashi Y, Jackson M, Kääb A, Kang S, Kutuzov S, et al. 2019. Chapter 2: high mountain areas. In IPCC Special Report on the Ocean and Cryosphere in a Changing Climate: 131–202

Hollander M, Wolfe D. 1999. Nonparametric Statistical Methods. John Wiley & Sons: New York.

Hood JL, Hayashi M. 2015. Characterization of snowmelt flux and groundwater storage in an alpine headwater basin. Journal of Hydrology 521: 482–497 DOI: 10.1016/j.jhydrol.2014.12.041

IPCC. 2013. Climate Change 2013 - The Physical Science Basis. DOI: 10.1038/446727a

Jacques JMS, Sauchyn DJ. 2009. Increasing winter baseflow and mean annual streamflow from possible permafrost thawing in the Northwest Territories, Canada. Geophysical Research Letters 36 (1): 1–6 DOI: 10.1029/2008GL035822

Kahn KG, Ge S, Caine JS, Manning A. 2008. Characterization of the shallow groundwater system in an alpine watershed: Handcart Gulch, Colorado, USA. Hydrogeology Journal 16 (1): 103–121 DOI: 10.1007/s10040-007-0225-6

Kerkhoven E, Yew Gan T. 2008. Development of a hydrologic scheme for use in land surface models and its application to climate change in the Athabasca River Basin. In Cold Region Atmospheric and Hydrologic Studies. The Mackenzie GEWEX Experience: Volume 2: Hydrologic Processes, Woo MK (ed.). Springer: New York, New York, US.

Kershaw G, Kershaw L. 1983. Geomorphology and vegetation of the MacTung study area, Yukon/NWT. Sherwood Park, AB.

Kershaw G, Kershaw L. 2016. A Guide To The Canol Heritage Trail and Doı T'oh Territorial Park Reserves. Norman Wells Historical Society: Norman Wells, NT.

Knowles JF, Harpold AA, Cowie R, Zeliff M, Barnard HR, Burns SP, Blanken PD, Morse JF, Williams MW. 2015. The relative contributions of alpine and subalpine ecosystems to the water balance of a mountainous, headwater catchment. Hydrological Processes 29 (22): 4794–4808 DOI: 10.1002/hyp.10526

Krogh SA, Pomeroy JW, Marsh P. 2017. Diagnosis of the hydrology of a small Arctic basin at the tundra-taiga transition using a physically based hydrological model. Journal of Hydrology 550: 685–703 DOI: 10.1016/j.jhydrol.2017.05.042

Langston G, Hayashi M, Roy JW. 2013. Quantifying groundwater-surface water interactions in a proglacial moraine using heat and solute tracers. Water Resources Research 49: 5411–5426 DOI: 10.1002/wrcr.20372

Ma R, Sun Z, Hu Y, Chang Q, Wang S, Xing W, Ge M. 2017. Hydrological connectivity from glaciers to rivers in the Qinghai-Tibet plateau: roles of suprapermafrost and subpermafrost groundwater. Hydrology and Earth System Sciences 21 (9): 4803–4823 DOI: 10.5194/hess-21-4803-2017

Mamet SD, Chun KP, Kershaw GGL, Loranty MM, Kershaw GP. 2017. Recent increases in permafrost thaw rates and areal loss of palsas in the western Northwest Territories, Canada. Permafrost and Periglacial Processes 28 (4): 619–633 DOI: 10.1002/ppp.1951

McCartney SE, Carey SK, Pomeroy JW. 2006. Intra-basin variability of snowmelt water balance calculations in a subarctic catchment. Hydrological Processes 20 (4): 1001–1016 DOI: 10.1002/hyp.6125

McGuire AD, Chapin FS, Walsh JE, Wirth C. 2006. Integrated regional changes in Arctic climate feedbacks: implications for the global climate system. Annual Review of Environment and Resources 31 (1): 61–91 DOI: 10.1146/annurev.energy.31.020105.100253

Metcalfe RA, Buttle JM. 2001. Soil partitioning and surface store controls on spring runoff from a boreal forest peatland basin in north-central Manitoba, Canada. Hydrological Processes 15 (12): 2305–2324 DOI: 10.1002/hyp.262

Moore RDD. 2005. Slug injection using salt in solution. Streamline, Watershed management bulletin 8 (2): 1–6 DOI: 10.1592/phco.23.9.1S.32890

Pomeroy JW, Gray DM. 1995. Snowcover Accumulation, Relocation and Management. Minister of Supply and Services Canada, Saskatoon, Saskatchewan.

Pomeroy JW, Bewley DS, Essery RLH, Hedstrom NR, Link T, Granger RJ, Sicart JE, Ellis CR, Janowicz JR. 2006. Shrub tundra snowmelt. Hydrological Processes 20 (4): 923–941 DOI: 10.1002/hyp.6124

Pomeroy JW, Toth B, Granger RJ, Hedstrom NR, Essery RLH. 2003. Variation in surface energetics during snowmelt in a subarctic mountain catchment. Journal of Hydrometeorology 4 (4): 702–719 DOI: 10.1175/1525-7541(2003)004<0702:VISEDS>2.0.CO;2

Prairie Climate Centre. 2019. Sekwi Mountain statistically downscaled climate scenarios. Climate Atlas of Canada, Version 2 Available at: https://climateatlas.ca/data/grid/1118/plus30_2030_85/line [Accessed 20 June 2020]

Priestley C, Taylor R. 1972. On the assessment of surface heat flux and evaporation using large-scale parameters. Monthly Weather Review 100 (2): 81–92 DOI: 10.1175/1520-0493(1972)100<0081:OTAOSH>2.3.CO;2

Quinton WL, Carey SK, Goeller NT. 2004. Snowmelt runoff from northern alpine tundra hillslopes: major processes and methods of simulation. Hydrology and Earth System Sciences 8 (5): 877–890 DOI: 10.5194/hess-8-877-2004

Quinton WL, Hayashi M, Chasmer LE. 2011. Permafrost-thaw-induced land-cover change in the Canadian subarctic: implications for water resources. Hydrological Processes 25 (1): 152–158 DOI: 10.1002/hyp.7894

R Core Team. 2020. R: A language and environment for statistical computing

Rasouli K, Pomeroy JW, Janowicz JR, Carey SK, Williams TJ. 2014. Hydrological sensitivity of a northern mountain basin to climate change. Hydrological Processes 28 (14): 4191–4208 DOI: 10.1002/hyp.10244

Rennermalm A, Wood E, Troy T. 2010. Observed changes in pan-arctic cold-season minimum monthly river discharge. Climate Dynamics 35: 923–939 DOI: http://dx.doi.org.libproxy.wlu.ca/10.1007/s00382-009-0730-5

Rogger M, Chirico G, Hausmann H, Krainer K, Bruckl E, Stadler P, Bloschl G. 2017. Impact of mountain permafrost on flow path and runoff response in a high alpine catchment. Water Resources Research 53: 1288–1308 DOI: 10.1002/2016WR019341.Received

Ronayne MJ, Houghton TB, Stednick JD. 2012. Field characterization of hydraulic conductivity in a heterogeneous alpine glacial till. Journal of Hydrology 458–459: 103–109 DOI: 10.1016/j.jhydrol.2012.06.036

Rosenberry DO, LaBaugh JW. 2008. Field techniques for estimating water fluxes between surface water and ground water: techniques and methods 4–D2. U.S. Geological Survey.

Slaughter C, Kane D. 1979. Hydrological role of shallow organic soils in cold climates. In Canadian Hydrology Symposium 380–389.

Spence C, Kokelj SV, Ehsanzadeh E. 2011. Precipitation trends contribute to streamflow regime shifts in northern Canada. In Proceedings of Symposium H02 held during IUGG2011. IAHS Press: Melbourne; 3–8.

Stadnyk TA, Déry SJ. 2021. Canadian continental-scale hydrology under a changing climate: a review. Water (Switzerland) 13 (7): 1–14 DOI: 10.3390/w13070906

Trask JC, Fogg GE, Puente CE. 2017. Resolving hydrologic water balances through a novel error analysis approach, with application to the Tahoe basin. Journal of Hydrology 546: 326–340 DOI: 10.1016/j.jhydrol.2016.12.029

Unnikrishnan M, Virender P, Sarda K. 2016. Streambed hydraulic conductivity - a state of art. International Journal of Modern Trends in Engineering and Research 3 (6): 209–217

Viviroli D, Wehren B, Weingartner R, Scha B. 2010. General characteristics of alpine waters. In Alpine Waters, Bundi U (ed.). Springer: Berlin; 17-58. DOI: 10.1007/978-3-540-88275-6

Walvoord MA, Kurylyk BL. 2016. Hydrologic impacts of thawing permafrost — a review. Vadose Zone Journal 15 (6) DOI: 10.2136/vzj2016.01.0010

Walvoord MA, Voss CI, Wellman TP. 2012. Influence of permafrost distribution on groundwater flow in the context of climate-driven permafrost thaw: example from Yukon Flats basin, Alaska, United States. Water Resources Research 48 (7): 1–17 DOI: 10.1029/2011WR011595

Wilcox EJ, Keim D, de Jong T, Walker B, Sonnentag O, Sniderhan AE, Mann P, Marsh P. 2019. Tundra shrub expansion may amplify permafrost thaw by advancing snowmelt timing. Arctic Science: 1–16 DOI: 10.1139/as-2018-0028

Wilson JL, Guan H. 2004. Mountain-block hydrology and mountain-front recharge. In Groundwater Recharge in a Desert Environment: The Southwestern United States. Washington; 113–137. DOI: 10.1029/009WSA08

Woo MK, Yang Z, Xia Z, Yang D. 1994. Streamflow processes in an alpine permafrost catchment, Tianshan, China. Permafrost and Periglacial Processes 5: 71–85. DOI:10.1002/ppp.3430050202

Woo MK. 2012. Permafrost Hydrology. Springer: New York. DOI: 10.1007/978-3-642-23462-0

Woo MK, Heron R. 1987. Breakup of small rivers in the subarctic (Canada). Canadian Journal of Earth Sciences 24 (4): 784–795 DOI: 10.1139/e87-076

Woo MK, Thorne R. 2003. Streamflow in the Mackenzie basin, Canada. Arctic 56 (4): 328–340 DOI: 10.14430/arctic630

Zhang Y, Carey SK, Quinton WL, Janowicz JR, Pomeroy JW, Flerchinger GN. 2010. Comparison of algorithms and parameterisations for infiltration into organic-covered permafrost soils. Hydrology and Earth System Sciences 14 (5): 729–750 DOI: 10.5194/hess-14-729-2010

3.8 Figures

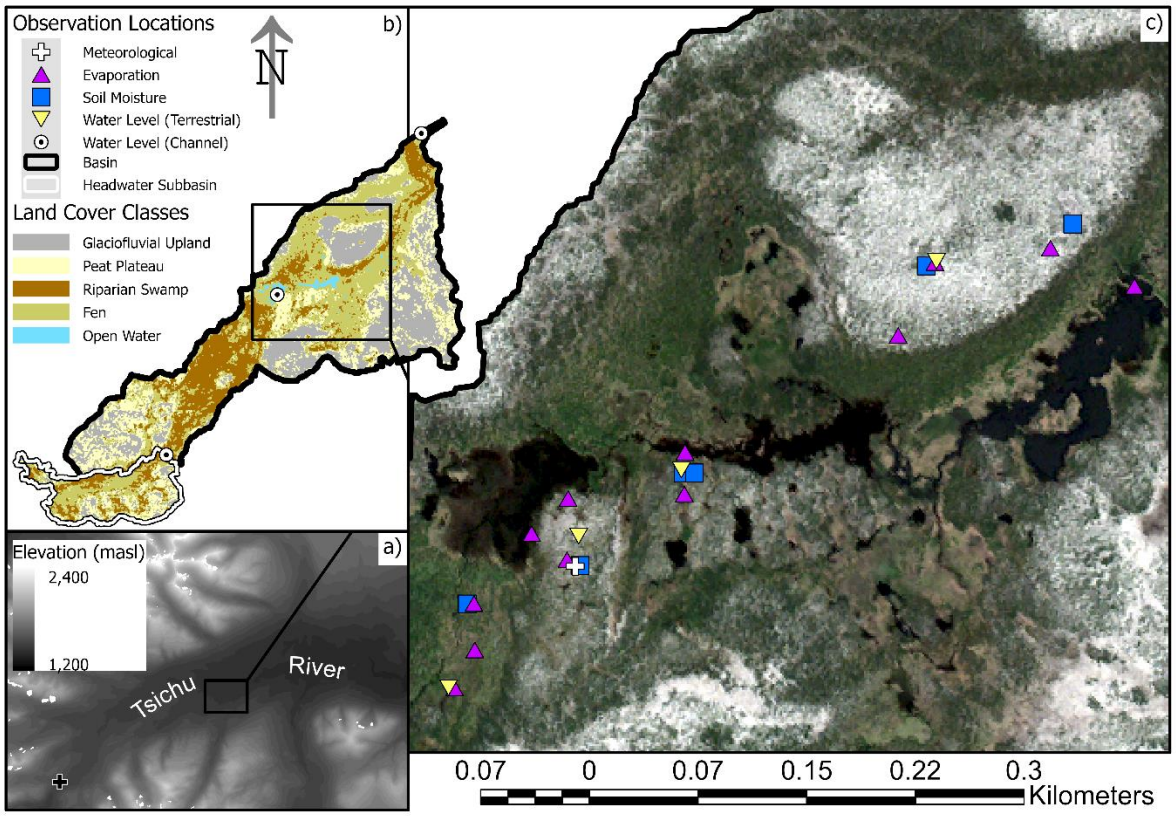

Figure 3-1: Map of a) study basin relative to the surrounding Tsichu River valley; b) study basin and headwater subbasin outlets and catchment areas; c) close up of study basin with all locations where hydrological observations were collected, except for observations related to snowmelt (Figure 3.2) and vertical differences in head across the channel bed (Figure 3.3). Of note, permafrost is found within the basin below the peat plateau features identified in b).

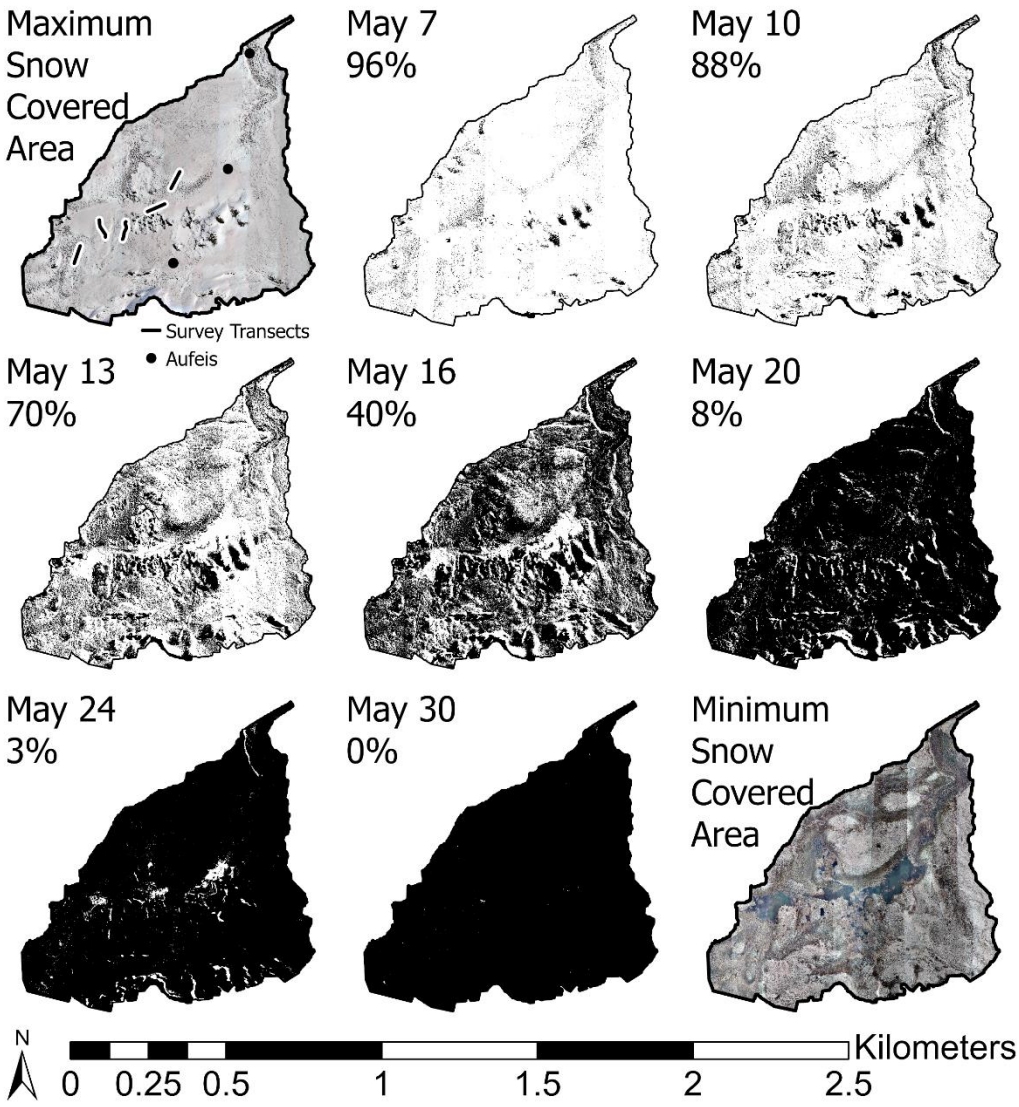

Figure 3-2: Change in snow-covered area from repeat drone surveys during the freshet period. Snow-covered area reported for each date is based on presence (white) and absence (black) assigned with iso cluster supervised image classification. Repeat snow survey transects and aufeis locations are shown in the maximum snow-covered area image.

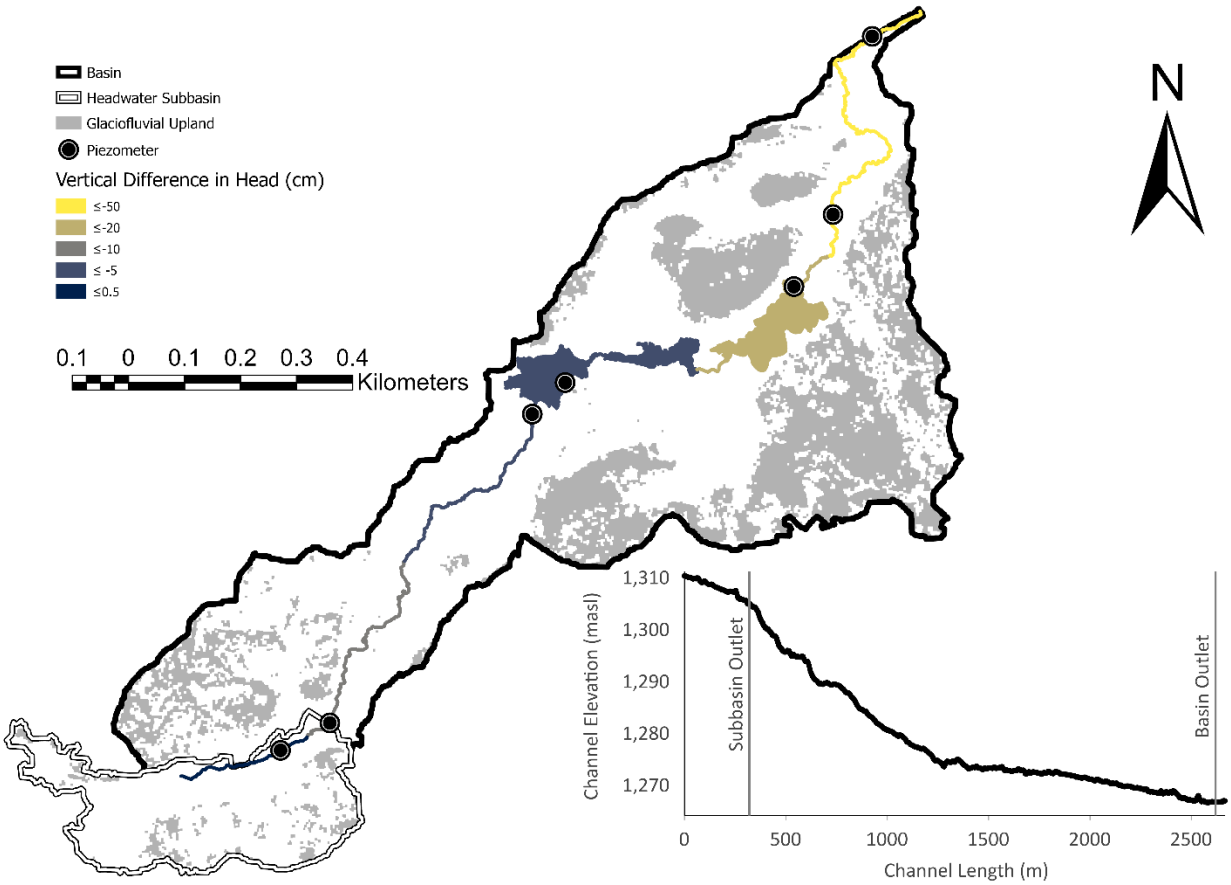

Figure 3-3: Map of study basin groundwater exchange. Groundwater discharge (GW_{IN}) received from spring sources concentrated within the headwater subbasin. Groundwater recharge (GW_{OUT}) occurred via glaciofluvial upland infiltration and channel bed infiltration between the headwater subbasin and basin outlets. Vertical difference in head (Δh) along the channel length shown in plan view with each channel length value extrapolated from centroid piezometer readings. Channel network area based on maximum extent observed 30 May, 2019. Change in elevation shown in long profile view.

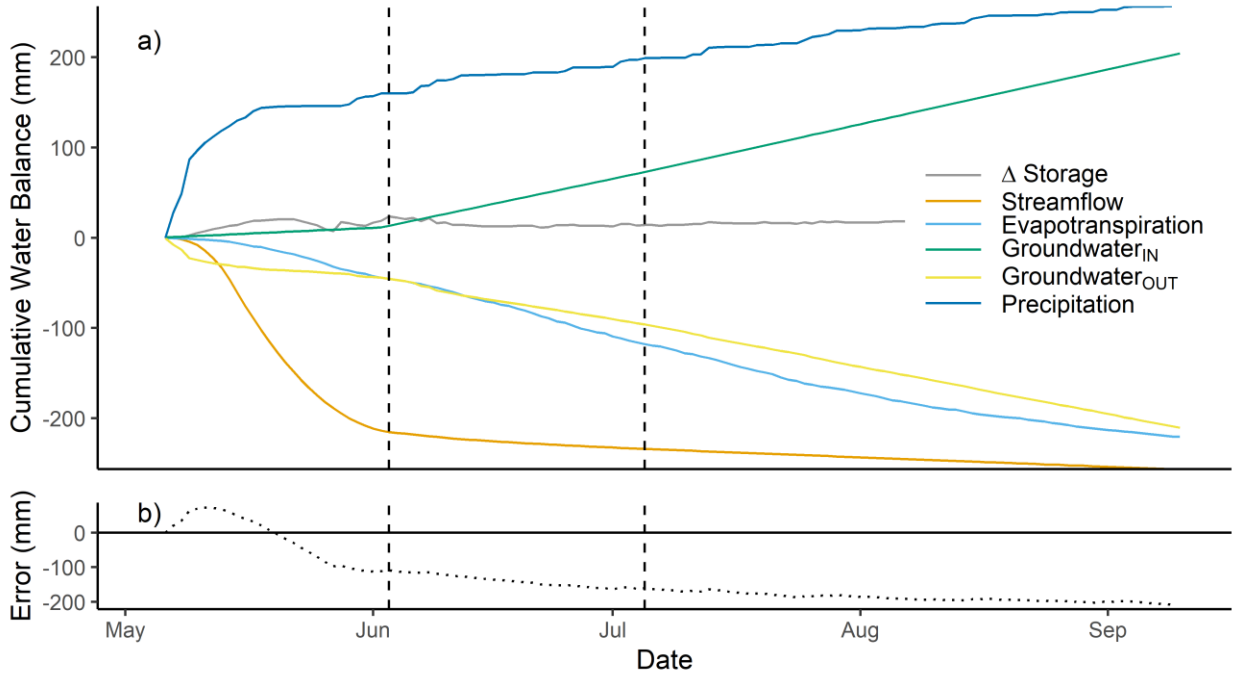

Figure 3-4: a) Cumulative water balance and b) cumulative error term from beginning of freshet to autumn refreeze. Vertical dotted lines denote seasonal transitions between freshet, early summer, and late summer periods.

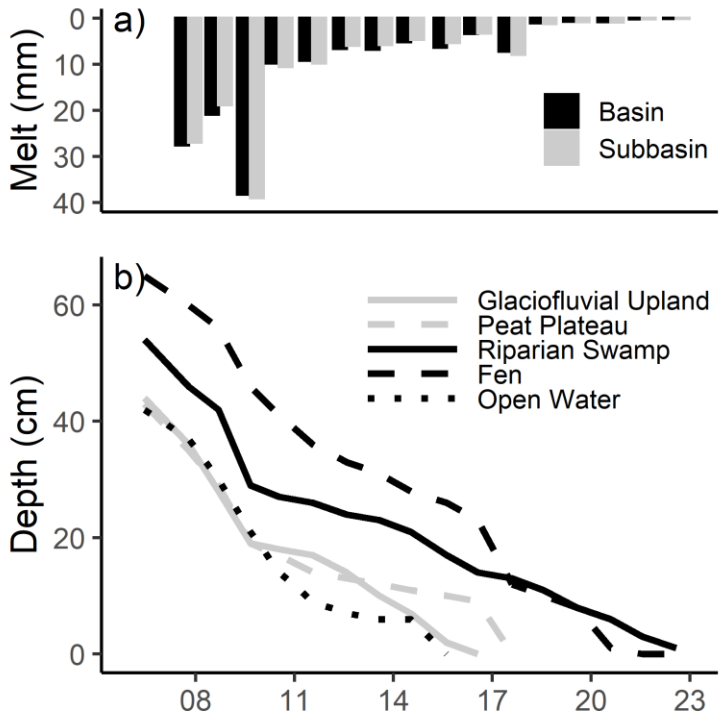

Figure 3-5: a) Daily basin and headwater subbasin melt (SWE_{MELT}). b) Cover class specific change in snowpack depth (ΔD) from time of snowpack ripeness (7 May) to >95 % basin area snow free (23 May).

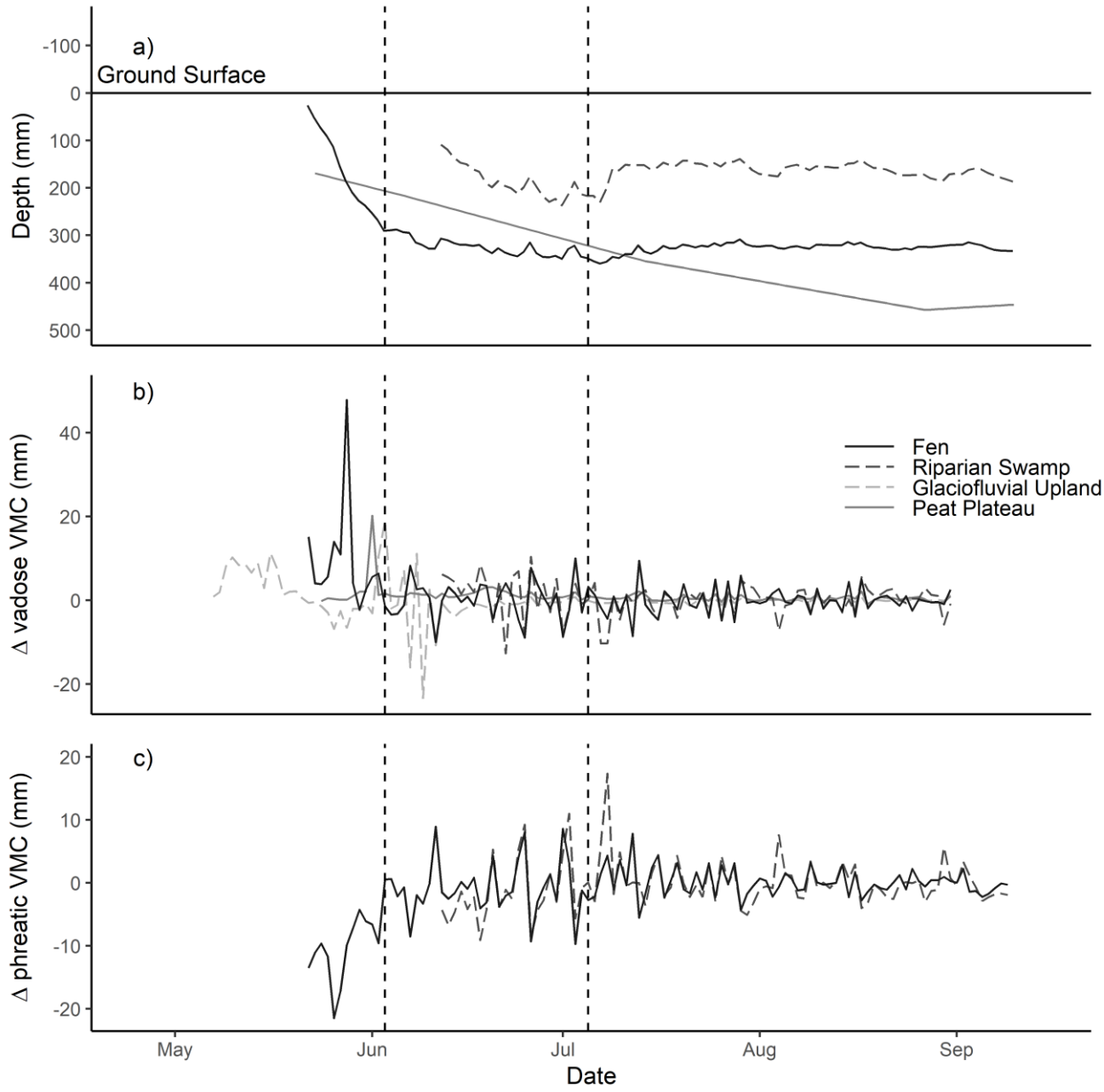

Figure 3-6: a) Daily water table (fen and riparian swamp) and frost table (peat plateau) depths below ground surface. b) Daily change in storage within the vadose zone above water table and/or frost table. c) Daily change in storage due to water table fluctuations. Vertical dotted lines denote seasonal transitions between freshet, early summer, and late summer periods.

3.9 Tables

Table 3-1: Comparison of water balance components from 7 May to 9 September 2019 for each contributing area and land cover class assessed. Cover class areas reported as percent cover of total basin area. All water balance components reported as mm depths.

	Basin	Headwater Subbasin	Glaciofluvial Upland	Riparian swamp	Peat Plateau	Fen	Open Water
Area	**0.8 km^2**	**0.1 km^2**	**25 %**	**20 %**	**23 %**	**31 %**	**<1 %**
P SWE_{MELT}	143.2	148.4	131.4	153.4	113	196	92.5
P **R**	113.2	113.2	113.2	113.2	113.2	113.2	113.2
GW_{IN}	202.5	1619.9	na	na	na	na	na
ΔS **Vadose**	68.8	77.6	18.8	28.2	98.0	115.9	na
ΔS **Phreatic**	-49.7	-49.8	na	-22.8	na	-145.7	na
ET	-220	-223	-189.8	-212.3	-265.4	-209.1	-422.2
GW_{OUT}	-208.9	-19.8	-179.8	na	na	na	na
Q	-256.5	-2194.1	na	na	na	na	na

Table 3-2: Seasonal differences in basin water balance and flow path partitioning ratios during freshet (7 May–2 June), early summer (3 June–5 July), and late summer (6 July–9 September).

			Total	Freshet	Early Summer	Late Summer
			mm	mm day^{-1}	mm day^{-1}	mm day^{-1}
Inputs	**P**	**SWE_{MELT}**	143.2	5.1		
		R	113.2	0.6	1.2	0.9
	GW_{IN}		202.5	0.4	1.9	2.0
Outputs	**GW_{OUT}**	**Upland Infiltration**	-44.9	-1.2	-0.2	-0.1
		Channel Infiltration	-164.0	-0.4	-1.4	-1.6
	Q		-256.5	-7.9	-0.6	-0.3
	ET		-220.0	-1.6	-2.2	-1.5
ΔS	**Vadose**		68.8	2.1	0.3	0.0
	Phreatic		-49.7	-1.4	-0.4	0.1
runoff ratio			0.56	1.29	0.20	0.12
runoff - recharge ratio			0.55	0.83	0.28	0.17

4. Characterizing seasonal differences in hydrological flow paths and source water contributions to alpine tundra streamflow

4.1 Abstract

Major changes in precipitation regime and runoff generation have been observed throughout the subarctic due to climate change and its consequences for factors influencing hydrological processes, such as permafrost thaw. Alpine headwaters are important to the water balance of continental river systems as they collect larger volumes of precipitation per unit area than neighbouring lowlands, recharge regional aquifers, and generate a greater proportion of river discharge than their limited extent would suggest. Despite the importance of alpine headwaters, field observations and assessments of source water contributions to streamflow in subarctic alpine settings are sparse, and thus it remains uncertain how changes to seasonally specific hydrological processes control runoff generation to the larger river systems to which they contribute. This study quantified the variability in source water contributions and flow paths during the 2019 open water season within a Mackenzie Mountain alpine tundra basin based on measurements of stable isotope compositions, specific conductivity (SPC), and water volumes during runoff generating events. During the freshet, large daily snowmelt volumes resulted in the greatest streamflow that was composed mainly of pre-event water (~92 %). As the summer progressed, evapotranspiration increased, and groundwater flow paths extended, resulting in reduced event water fractions, hydrograph amplitude, and an extended duration of streamflow response. A headwater subbasin within the larger study basin was both hydrologically and isotopically unresponsive to summer rains and had a delayed hydrograph response with reduced event water fraction during the freshet, indicating this portion of the catchment was regulated by

discharge from groundwater springs capable of sustaining streamflow before snowmelt commenced and during the dry summer months. As climate change continues, greater precipitation depths and a longer open water season will likely result in reduced runoff and stream discharge from alpine basins as greater evapotranspiration and channel bed infiltration occur. This is consistent with observations of increasing regional river winter baseflow and the modelled explanation of increasing alpine headwater aquifer recharge following extended flow paths en route to these lowland rivers. This study provides a valuable data set and observations of seasonally distinct runoff generation processes important to northern hydrology modelling as the climate and alpine tundra terrain continue to change.

Keywords: Taiga Cordillera, alpine tundra, runoff, stable isotopes, source waters, groundwater recharge, groundwater discharge

4.2 Introduction

Climate change is most pronounced at northern latitudes where warmer air temperatures and greater annual precipitation are projected to occur (McGuire *et al.*, 2006; IPCC, 2013), but alterations in the timing and magnitude of streamflow that results from these meteorological changes is less certain (Stadnyk and Déry, 2021). Throughout the North, soil temperatures have been warming (Hinzman *et al.*, 2005; Kokelj *et al.*, 2017), resulting in land cover change where ice-rich permafrost thaws (Hinzman *et al.*, 2005; Quinton *et al.*, 2011). In alpine regions, this is expected to increase the average flow path and residence time of precipitation received as a greater proportion of water is routed to recharge aquifers at depth instead of being impeded by permafrost and contributing directly to streamflow (Bense *et al.*, 2009; Walvoord *et al.*, 2012; Walvoord and Kurylyk, 2016).

A disproportionally large amount of discharge from the Mackenzie River is sourced from alpine basins (Woo and Thorne, 2003). The Yukon and Mackenzie river basins both have substantial alpine extent and are among the 12 largest pan-arctic rivers expected to experience the most significant increase in discharge by 2070 due to climate change (Stadnyk *et al.*, 2021). This is due in part to increased precipitation with elevation on local (Granger, 1998; Knowles *et al.*, 2015) and regional scales (Dingman, 1981; Gruber and Hoelzle, 2001; Viviroli *et al.*, 2010; Asong *et al.*, 2020), but also surface and subsurface basin attributes of alpine terrain including steeper gradients, limited forest cover, and reduced soil water storage capacity (Quinton *et al.*, 2004; Viviroli *et al.*, 2010; Staudinger *et al.*, 2017).

In northern alpine regions, snow accumulation over the winter months commonly results in a freshet period when the majority of annual inputs are received within a 2 to 4-week period as accumulated snowpack melts and streamflow responds with annual maximum discharge volumes (Woo, 1986; Quinton *et al.*, 2004; Pomeroy *et al.*, 2007). During this period, the runoff response is sensitive to the large snowmelt volume, but also storage availability, as the elevated frost table limits storage and results in efficient runoff production via short horizontal flow paths (Gray *et al.*, 2001; Woo *et al.*, 2008b; Lamoureux and Lafrenière, 2017; Marsh *et al.*, 2020). As the summer progresses, the ground thaws and storage volume increases, shifting the dominant flow path from horizontal to vertical and reducing runoff efficiency following precipitation events (Kuchment *et al.*, 2000; Quinton *et al.*, 2005). Yet alpine contributions to streamflow can sustain baseflow during summer drought and winter cold conditions (Walvoord *et al.*, 2012; Ma *et al.*, 2017; Crites *et al.*, 2020), supporting key ecosystem services and human resource uses during these sensitive periods. However, our understanding of the seasonality in source waters and

active flow paths regulating headwater contributions to specific northern river systems under current and future climatic regimes requires further research attention.

Detailed hydrological field studies are difficult to initiate and maintain long-term in northern settings due to harsh environmental conditions and their remote location (Laudon *et al.*, 2017). The lack of field observations is most pronounced in alpine areas (Asong *et al.*, 2020; Hayashi, 2020), where substantial research effort is required because of the spatial heterogeneity in geomorphology, land cover and hydrological processes (Matsuoka, 2006; Walvoord and Kurylyk, 2016). On-the-ground research efforts are needed to provide observations and fundamental knowledge of hydrological pathways and source water contributions to alpine streamflow discharge. Isotope-mass balance calculations and hydrograph separation have proven effective for characterizing the hydrological function of headwater basins during runoff generating precipitation events, providing details on local storage, primary flow paths, and source waters contributions (Gibson *et al.*, 1993; Carey and Quinton, 2004, 2005; St Amour *et al.*, 2005; Piovano *et al.*, 2019). This approach is particularly well suited to smaller, ungauged catchments (Buttle, 1998) and for capturing effects of short duration high intensity rain events (Sklash and Farvolden, 1979).

The objective of this research is to quantify the spatial and temporal variability in runoff event streamflow and its source water contributions in a ~0.8 km^2 Taiga Cordillera alpine tundra basin during the 2019 open water season. Hydrometric measurements of precipitation, streamflow, and water table depth paired with stable isotope measurements of precipitation and streamflow produce a robust account of storage availability, active flow paths, and source water contributions to streamflow during freshet, early summer, and late summer conditions. These findings provide knowledge to constrain hydrological models aimed at predicting how a

warming climate and changing precipitation regime will impact future northern alpine tundra runoff generation and the larger river systems to which they contribute.

4.2.1 Study area

4.2.1.1 Geomorphology and land cover

The study basin selected (63.3°N, 129.8°W, 1264.8 – 1333.1 masl, 0.8 km^2) is a first order stream contributing to the Tsichu River and is considered representative of alpine shrub tundra areas within the Taiga Cordilleran, an ecozone which occupies 260,000 km^2 of northern Canada and covers large portions of both the Mackenzie River and Yukon River basins (Figure 4.1). The land cover is composed of five distinct cover classes: glaciofluvial upland, peat plateau, fen, riparian swamp, and open water, described in detail in Chapter 2. Sands and gravels deposited as eskers, kame terraces, outwash plains, and other stratified drift landforms created the glaciofluvial upland features present (Kershaw and Kershaw, 1983; Ecosystem Classification Group, 2010), while peatland development has resulted in peat plateaus where ice-rich permafrost is present and fens where permafrost is absent (Ecosystem Classification Group, 2010; Mamet *et al.*, 2017). The stream channel is small (~120 cm wide, ~15 cm deep) with a mean gradient of 2.5 % and a series of ponding segments midway along its 2747 m length. The riparian swamp is found near the channel and has minerotrophic soils with a water table that remains near the ground surface throughout the open water season. Open water areas are limited in extent and concentrated along the channel network. The study basin also includes a headwater subbasin where groundwater springs are concentrated (1304.7 – 1333.1 masl, 0.1 km^2; Figure 4.1c). This headwater subbasin was monitored and sampled with the same frequency as the main basin outlet to compare streamflow volume and source water contributions and resolve spatial differences in hydrological processes active within the study basin.

4.2.1.2 Meteorological conditions

Multiple sources of meteorological data were considered to provide context for the 2019 observation period. These data sources included modelled 0.5° grid cells overlapping the study basin (Harris *et al.*, 2014; Prairie Climate Centre, 2019; Environment and Climate Change Canada, 2021), ground-based observations within the basin (Mamet *et al.*, 2017) and an Environment Canada (2020) meteorological station maintained ~10 km up valley (Macmillan Pass station, 63.2°N, 130.0°W, 1379 masl; Figure 4.1b). In 2019, the modelled climate for the region reported a mean annual air temperature (MAAT) of -6.3 °C, warmer than the 1950-2019 MAAT of -7.6±0.6 °C (± 1 standard deviation) (Environment and Climate Change Canada, 2021). The Macmillan Pass station reported a 2019 MAAT of -7.5 °C, similarly warmer than its long-term (1971-2000) MAAT of -8.3 °C (Environment Canada, 2020). Independent observations of local precipitation are less reliable than the temperature records[3], but modelled 2019 total precipitation (480 mm) was similar to the long-term modelled mean for the region (472 ± 18 mm) (Environment and Climate Change Canada, 2021), 50 % of which is likely received as snow (Harris *et al.*, 2014). However, based on personal observations during previous summers and verbal communications with other long-term local land users, the 113.2 mm of rain received by the study basin (see 4.3.1.1) and 107.5 mm recorded at the Environment Canada Macmillan Pass station ~10km up valley (Environment Canada, 2020) between 20 April – 10 September are considered to have resulted in a relatively dry 2019 open water season.

[3] The Macmillan Pass precipitation record reports 448 mm in 2019, but this should be interpreted with caution given the many missing data flags appended to daily entries.

4.3 Data and methods

Seasonal changes in basin characteristics and source water contributions to streamflow during the 2019 open water season were assessed by comparing basin streamflow volumes, water table depths, and stable isotope compositions during the freshet, early summer, and late summer periods. Within each period, a distinct runoff event was identified following precipitation of sufficient amount and duration to cause an increase in basin and/or headwater subbasin streamflow. These events were identified in the field and sampled more intensively, with each event beginning as initial precipitation was received and ending when observed baseflow conditions returned to pre-event normal flow rates. Based on these criteria, the freshet runoff event was much longer in duration (7 May – 2 June) than the early summer (12:30 9 June – 19:30 10 June) and late summer (5:00 29 July – 10:30 30 July) events. As such, freshet precipitation and streamflow were reported at daily intervals while the summer events were recorded and assessed at 30-minute intervals.

4.3.1. Hydrometric measurements

4.3.1.1 Precipitation

Both snowmelt and rain contributions to the basin were estimated for the entire study duration (20 April - 10 September 2019). During the freshet, daily snow water equivalent inputs (SWE_{MELT}) were calculated using the following equation:

Equation 4.1: $$SWE_{MELT} = \Delta A_n \times \Delta D_n \times \frac{\rho_s}{\rho_w}$$

where ΔA is change in snow-covered area (%), ΔD is change in snowpack depth (m), ρ_s is the snowpack density (kg m^{-3}) and ρ_w is water density (997 kg m^{-3}) during the n daily time step. ΔA was interpolated from repeat drone surveys conducted seven times from 7 - 30 May 2019. ΔD

was interpolated from repeat snow depth measurements collected every 1-3 days at 11 locations along five survey transects ~60 m in length (Figure 4.1). ρ_s was held constant at 410 kg m^{-3}, representing a densified version of the depth integrated ρ_s measurements collected prior to snowpack ripening on 17 April 2019 at 30 points along each survey transect. SWE_{MELT} was calculated for each cover class present and both headwater subbasin and basin areas based on areal weights of their respective cover class compositions (Chapter 3; Appendix 4.1). Rain was measured for the entire study duration with an ARG 100 tipping bucket rain gauge (0.2 mm sensitivity) (EML, North Shields, UK) recording on a Campbell Scientific CR300 data logger every 30 minutes (Logan, UT, US).

4.3.1.2 Streamflow

Streamflow discharge from the headwater subbasin and basin outlets was estimated with rating curves relating point observations of streamflow (m^3 s^{-1}) to continuous records of water depth (mm). Point observations were based on sodium dilution tests as described by Moore (2005) using an Orion electrical conductivity probe (Thermo Fisher Scientific Inc., Waltham, US). Water depth was recorded at 30-minute intervals with HOBO U20 pressure transducers (1.5 - 3.0 cm accuracy) (Onset Computer Corp, Bourne, MA, US). During the early freshet, outlets had bedfast ice and unstable channel geometry. As such, a single centrally located pressure transducer recorded change in water depth for rating curve calibration. When channel geometry had stabilized, rating curves were created for both headwater subbasin and basin outlets using water depth records from locally installed pressure transducers (Figure 4.1) (Chapter 3; Appendix 4.4).

4.3.1.3 Water table depth

Pressure transducers were installed below ground in stilling wells at areas representative of each land cover to track changes in water table depth (Figure 4.1). Fen and riparian swamp records began when stilling wells thawed sufficiently for pressure transducer installation (21 May and 11 June, respectively), while peat plateau and glaciofluvial stilling wells remained dry for the duration of observation. Well lengths ranged from 36.4 – 106.9 cm below ground surface.

4.3.2 Stable isotope sampling and analysis

In addition to hydrometric measurements of water volumes, water isotope compositions of precipitation source waters and streamflow were also sampled throughout the 2019 observation period. Snowpack samples were collected in bulk at four locations within the basin using a 7 cm diameter snow tube sampler (Figure 4.1c). Snowpack samples were transported to base camp and allowed to completely melt before transfer to 20 ml scintillation vials with displacement caps <6 hours after collection. Rain samples were collected ~1 m above the ground surface with large stainless-steel vessels ~40 cm in diameter deployed during rain events and transferred to vials for storage <1 hour after capture. When possible, multiple rain samples were collected per event to assess the variability in isotope composition and contribution to runoff. Mean monthly isotope compositions of precipitation were also derived using Bowen's Online Isotopes in Precipitation Calculator (Bowen, 2019). Samples from groundwater springs and permafrost ice were also collected (Figure 4.1c) to compare their isotope composition with measured and modelled precipitation isotope composition.

To characterize seasonal differences in source water contributions to the stream and the influence of evaporation, streamflow samples were collected frequently from both basin and headwater subbasin outlets throughout the 2019 open water season (Figure 4.1c). A subset of the

streamflow samples collected was analyzed to capture isotope compositions before, during, and following the freshet and summer rainfall events. With each streamflow sample, specific conductivity (SPC) was also measured in situ with an Orion electrical conductivity probe (Thermo Fisher Scientific Inc., Waltham, US). SPC can be used as a flow path tracer because water contact time in mineral substrates results in greater SPC than in precipitation and/or shallow organic soil waters (Pilgrim *et al.*, 1979; Carey and Quinton, 2005). To estimate the influence of evaporation on streamflow, isotope results were examined in relation to the Global Meteoric Water Line (GMWL; Craig, 1961) and a Local Evaporation Line (LEL) was estimated with linear regression of all streamflow isotope sample values. Also, deuterium excess (d-excess), a measure of offset from the GMWL, was used to detect evaporative enrichment of streamflow (Landwehr and Coplen, 2004; Turner *et al.*, 2014) and calculated using the Dansgaard (1964) equation:

Equation 4.2: $\text{d-excess} = \delta^2\text{H} - (8 \times \delta^{18}\text{O})$

where oxygen and hydrogen isotope compositions are reported as δ-values, such that $\delta^{18}\text{O}$ and $\delta^2\text{H}$ are deviations per mil (‰) of $^{18}\text{O}/^{16}\text{O}$ and $^{2}\text{H}/^{1}\text{H}$ ratios relative to Vienna Standard Mean Ocean Water (VSMOW). All water samples were collected with 20 ml scintillation vials pre-rinsed with sample ≥3 times and processed at the Environmental Isotope Laboratory at the University of Waterloo, ON. Laboratory analysis used an AT-LWIA-45-EP model Los Gatos Research Liquid Water Isotope Analyser (LWIA) capable of ± 0.2‰ for $\delta^{18}\text{O}$ and ± 0.8‰ for $\delta^2\text{H}$ measurement precisions.

Oxygen isotope data were used to identify source water contributions to streamflow during each of the three runoff events (freshet, early summer, late summer), following Sklash and Farvolden's (1979) steady-state mass-balance equation:

Equation 4.3: $C_T Q_T = C_P Q_P + C_E Q_E$

arranged to calculate both pre-event and event contributions as follows:

Equation 4.4: $Q_P = \left[\frac{C_T - C_E}{C_P - C_E}\right] Q_T$

Equation 4.5: $Q_E = Q_T - Q_P$

where C is δ^{18}O (‰), Q is streamflow (m^3), and the subscripts T, P, and E denote total, pre-event, and event waters, respectively. During the summer runoff events, monthly modelled rain isotope compositions were used for C_E because measured isotope compositions were highly variable (see 4.4.1). During the freshet, the mean isotope composition of the four depth integrated snowpack samples was used for C_E. During the freshet, the Gaussian standard error method for two-component separation was used to calculate Q_E uncertainty for each time step with C_T sample collection, as described by Genereux (1998). C_T and C_P uncertainties were based on the LWIA analytical errors (±0.2 ‰) while the C_E uncertainty selected (+3 ‰) was relatively high to account for potential errors resulting from fractionation during snowmelt (Taylor *et al.*, 2002) (Appendix 5).

4.4 Results

4.4.1. Isotope composition of alpine source waters and streamflow

Snow and rain source waters sampled in the alpine basin possessed distinct isotope compositions (Figure 4.2a). As expected, precipitation received by the basin plotted along the GMWL and had distinct $\delta^{18}O$ and $\delta^{2}H$ values for the isotopically-depleted depth-integrated snow samples ($\delta^{18}O$: -25.0 ± 0.3 ‰ [mean ± 1 standard deviation]; $\delta^{2}H$: -191.7 ± 2.5 ‰) compared to the isotopically-enriched rain samples ($\delta^{18}O$: -19.9 ± 2.4 ‰; $\delta^{2}H$: -156.1 ± 18.9 ‰). In comparison to the Bowen (2019) modelled precipitation, depth-integrated snow samples were within the range of isotope compositions estimated for the colder months (October – April), while rain samples collected from discrete events were more variable than modelled estimates for the open water season (May – September). Groundwater samples ($\delta^{18}O$: -23.1 ± 0.2 ‰; $\delta^{2}H$: -178.1 ± 0.5 ‰) were tightly grouped and similar to the estimated weighted mean annual precipitation (LEL-GMWL intersection) with isotope compositions more similar to snow than rain, while permafrost values ($\delta^{18}O$: -21.2 ± 0.6 ‰; $\delta^{2}H$: -167.3 ± 2.4 ‰) displayed slight evaporative enrichment along the LEL (Figure 4.2a).

Streamflow isotope compositions measured at the headwater subbasin and basin outlet were scattered along the LEL indicating varying degrees of evaporative enrichment throughout the open water season (Figure 4.2b). Generally, samples above the LEL are influenced more by rainfall while values below the LEL are influenced more by snowmelt, given that these source waters would naturally draw the isotope composition of the streamflow in those directions in $\delta^{18}O$-$\delta^{2}H$ space. The observed evaporative enrichment was seasonal, with less pronounced enrichment before and during the freshet in April – May and more pronounced enrichment from June to August (Figure 4.2c,d). Furthermore, the seasonal pattern of streamflow evaporative

enrichment was less pronounced at the headwater subbasin than the basin outlet, especially for the summer months.

4.4.2 Seasonal differences in alpine runoff generation

4.4.2.1 Basin response to spring freshet

Further examination of the precipitation, discharge, SPC and isotope (d-excess) data versus time reveals probable source waters and flow paths en route to streamflow during the freshet and summer rain events (Figure 4.3, 4.4). The majority of the precipitation inputs and highest basin streamflow discharge occurred during the freshet as 143 mm of SWE_{MELT} was liberated from 7 - 23 May, with a peak daily contribution of 38.3 mm received on 9 May (Figure 4.3a). Both outlets reported an initial increase in streamflow on 8 May, but peak daily mean flow rates occurred on 15 May at the basin (0.14 $m^3 s^{-1}$), 10 days before the headwater subbasin peak (0.07 $m^3 s^{-1}$) (Figure 4.3b).

Streamflow isotope values during the freshet were not exclusively similar to snowmelt (Figure 4.2), but rather represent a mix of sources including pre-event waters likely received from groundwater springs and rain the previous fall. During the freshet, SPC values of <100 μS cm^{-1} were recorded from 13-24 May at the basin and 20-31 May at the headwater subbasin (Figure 4.3c), well below the 263 to 297 μS cm^{-1} observed in April prior to the freshet when aquifer discharge alone sustained headwater subbasin streamflow. Based on stable isotope data and calculations using equation 4.5, freshet event waters contributed 8.4 % of total freshet basin streamflow, with the daily maximum event water contribution of 35.3 % occurring on 14 May as a daily average flow rate of 0.12 $m^3 s^{-1}$ occurred (Figure 4.4a). In comparison, headwater subbasin freshet event water contributions were less, accounting for 6.3 % of total freshet streamflow and a daily maximum of 20.6 % on 11 May as a daily average flow rate of 0.02 $m^3 s^{-}$

[1] occurred (Figure 4.4a). Streamflow d-excess ranged from 5.0 – 9.9 ‰ during this period, indicating minimal loss by evaporation compared to the summer months (Figure 4.3d).

Stilling wells in the surrounding land cover were either dry or frozen during the freshet. The only exception to this was the fen, below which the water table was at or near the ground surface for the majority of SWE_{MELT}, followed by a rapid decline from 21 May to 2 June parallel to the falling limbs of both hydrographs (Figure 4.4a).

4.4.2.2 Basin response to summer rainfall events

After the freshet concluded, precipitation inputs became exclusively rain. A total of 113.2 mm of rain was received by the basin during the summer months, with frequent daily events <4 mm and a daily maximum of 7.4 mm on 13 July (Figure 4.3a). While the larger contributing area of the basin generated greater streamflow than the headwater subbasin during the freshet, this reversed with the start of summer, such that the basin generated a mean summer streamflow of 0.004 ± 0.002 $m^3 s^{-1}$ (± standard deviation) compared to the greater discharge of 0.017 ± 0.002 $m^3 s^{-1}$ for the headwater subbasin (Figure 4.3b). This is not likely due to changes in contributing area storage availability, as water table depths were relatively shallow throughout the summer months (326 ± 13 mm below fen and 169 ± 25 mm below riparian swamp; Figure 4.4c). Instead, it is likely that as the channel bed thawed, groundwater imports and precipitation received by the headwater subbasin were subsequently lost via channel bed infiltration en route to the main basin outlet (Chapter 3). In addition, evaporative losses from the basin contributing area likely played a role during the late summer, as evidenced by the lower d-excess values at the basin outlet compared to the freshet and headwater subbasin values (Figure 4.3d).

Two runoff events were identified to allow for comparison of early and late summer source water contributions and streamflow responses following rain events of similar size and duration.

The early summer runoff event occurred during snow-free conditions, beginning with 5.8 mm of rain from 12:30 to 22:00 on 9 June and ending with the return to baseflow conditions on 10 June at 19:30 (Figure 4.4b). During this event, streamflow from the headwater subbasin was unresponsive, while the basin outlet had a 71 % increase in flow volume above the baseflow rate of 0.007 $m^3 s^{-1}$ with a peak flow rate of 0.012 $m^3 s^{-1}$. Based on calculations using equations 4.5 and the Bowen (2019) modelled rainfall isotope composition, rainfall accounted for 6.8 % of basin streamflow during the peak of this event and 2.4 % during the receding limb of the hydrograph response. Furthermore, SPC remained low and similar to freshet values at both the headwater subbasin and basin outlets during the early summer, suggesting groundwater flow paths through mineral sediments remained limited (Figure 4.3c). While the glaciofluvial upland, peat plateau, and riparian swamp stilling wells remained dry and/or frozen, storage in the neighbouring fen was short-lived during the early summer event as the water table rose with little delay after rainfall was received and returned to previous levels rapidly after the rain event (Figure 4.4b).

The late summer runoff event occurred in late July during peak summer conditions with full foliage and much deeper thaw depths (Chapter 3). The event began with 3.8 mm of rain from 5:00 – 11:00 on 29 July and ended with the return to baseflow conditions on 30 July at 10:30 (Figure 4.4c). Headwater subbasin streamflow volumes were unresponsive to the late summer rain, while the baseflow rate of 0.004 $m^3 s^{-1}$ at the basin outlet rose by 25 % to 0.005 $m^3 s^{-1}$ at the peak of the runoff response. Rainfall contributions were negligible at both the headwater subbasin and basin outlets during the late summer event (Figure 4.4c). SPC records were also unresponsive, although the SPC values of 390 and 338 $\mu S\ cm^{-1}$ at the headwater subbasin and basin outlets, respectively, indicate mineral substrate flow paths became active during this phase

of the open water season. During the late summer event, the water table below the fen and riparian swamp remained shallow and ineffective in retaining rainfall, similar to the early summer event (Figure 4.4b,c).

4.5 Discussion

4.5.1 Assumptions and uncertainties in streamflow source water separation

In order to estimate source water contributions to streamflow using isotope measurements, a series of assumptions must be met that can be summarized as follows: 1) event and pre-event waters have distinct isotope compositions; 2) event water isotope compositions are constant through time and/or sampling is sufficient to characterize how they vary with time; 3) pre-event water isotope compositions are constant through time and/or sampling is sufficient to characterize how they vary with time; 4) pre-event vadose zone water contributions are negligible or isotopically equivalent to pre-event waters; 5) additional source waters are negligible, such that surface storage remains isolated from streamflow (Sklash and Farvolden, 1979; Klaus and McDonnell, 2013). Concerning the freshet, a limited number of pre-event and event samples were collected, but the low variability in isotope composition of snow and streamflow during the freshet (Figure 4.2a,c) supports assumptions 1-3. The sampling regime was not designed to test assumption 4, but assumption 5 is also likely satisfied as open water isolated from the channel network is limited within the basin (Figure 4.1). Furthermore, when event water contributions were greater than 10 % of total streamflow, uncertainties were relatively small (4-10 %) (Appendix 5) and similar to uncertainties reported in other hydrograph separation studies during freshet events (Metcalfe and Buttle, 2001; Carey and Quinton, 2004; Laudon *et al.*, 2004).

Satisfying assumptions required to estimate source water contributions to streamflow were more challenging during the early and late summer runoff events. Synoptic scale variations in local climate and isotopic enrichment of rainfall before reaching the ground surface often result in highly variable isotope compositions of rain within a given season and/or precipitation event (St Amour *et al.*, 2005; Tian *et al.*, 2018), but sampling was limited to one or two samples per rain event for this study. Furthermore, the difference between measured isotope compositions of rain and pre-event streamflow samples collected was less than the analytical error (± 0.2 ‰) for the early summer event, contravening assumption 1. When comparing measured and modelled rain isotopic values, samples were also highly variable and distinct from the modelled estimates (Figure 4.2). Consequently, source water separation of streamflow during summer storm events used modelled rain isotope compositions supplied by Bowen (2019), which satisfied assumption 1. Also, the short duration and intensity of runoff made the frequency of streamflow sampling challenging. As such, only discrete source water separations are presented for the summer rain events (Figure 4.4b,c). Given these data limitations and uncertainties in source water separation, quantitative evaluation of rainfall contributions to runoff during summer events should be interpreted with caution. Nonetheless, these estimates are useful when comparing headwater subbasin and basin values and are bolstered by SPC, streamflow volume, and water table depth records to characterize differences in source waters and hydrological processes regulating runoff generation during the open water season.

4.5.2 Basin response to spring freshet

The streamflow of the study basin can be classified as a nival regime, typical for northern alpine environments where the freshet period is the most prominent annual hydrological event (Ahmed *et al.*, 2020). During this period, discharge volumes were greater at the basin outlet than the

headwater subbasin outlet (Figure 4.4a) due to the larger contributing area available to generate runoff (Figure 4.1). Source water separation for the freshet determined that the vast majority (~92 %) of basin streamflow was sourced from pre-event waters, similar to other studies conducted in northern alpine basins with discontinuous permafrost. The majority of the pre-event waters identified in these other studies were sourced from near-surface storage including shallow soil water in alpine basins (Carey and Quinton, 2004; Boucher and Carey, 2010; Carey *et al.*, 2013) and lake-wetland complexes in lowland basins (Hayashi *et al.*, 2004). In this study basin, shallow soil water liberated from the contributing area was also more prominent than water stored over winter in deeper mineral substrates, as the low SPC values reported confirm (Figure 4.3c).

The daily proportion of event water contributions to streamflow are known to vary depending on snowmelt rate, storage availability, and antecedent moisture content (Metcalfe and Buttle, 2001). As the freshet begins, snowmelt percolates and refreezes near-surface, delaying event water contributions to the channel network until the snowpack is depleted and the soils begin to thaw (Kuchment *et al.*, 2000). Carey *et al.* (2013) proposed a similar process, where transfer of water to the stream is limited during the early stages of snowmelt until unsaturated storage capacity of near-surface substrates become satisfied and sufficient sensible heat has been introduced with the infiltrating meltwater to bring ground temperatures to 0 °C. At this time, event and pre-event water mixing occurs and runoff generation begins (Piovano *et al.*, 2019) with additional snowmelt infiltration displacing water stored in the soil matrix over winter (Carey and Quinton, 2004; Carey *et al.*, 2013). This same process of source water mixing in near-surface soils and resultant delay in peak flow is consistent with the relatively small event water fraction reported

for the freshet and the alignment of peak flow with maximum event water fraction at the basin outlet (Figure 4.4a).

When comparing headwater subbasin and basin freshet streamflow, differences in freshet flow paths and source waters become apparent. The delay in headwater subbasin SPC decline (Figure 4.3c) and peak flow (Figure 4.4a) reveal that near-surface processes generating runoff in the study basin, as described above, are less influential in the headwater subbasin. Instead, headwater subbasin streamflow is evidently controlled by aquifer discharge via a more extended and delayed flow path beginning with snowmelt infiltration within a larger recharge zone at higher elevation beyond the topographical extent of the study basin (Figure 4.1b). In general, first and second order alpine basins are thought to sustain baseflow of larger regional river systems with aquifer recharge and hydraulic turnover times typically on the order of weeks to months (Hayashi, 2020). Langston *et al.*'s (2013) study of a small alpine basin (10^3 m^2 area) estimated throughflow of proglacial moraines to cause diurnal patterns of recharge and discharge sustained by meltwater inputs. On larger scales, Himalayan rivers with basin areas ranging from 1,100 – 57,700 km^2 had streamflow response times delayed by 37±13 - 120±35 days, depending on the basin size and aquifer hydraulic diffusivity (Andermann *et al.*, 2012). Relative to these examples, this study basin is intermediate in both scale and the ~10-day delay in freshet streamflow response (Figure 4.4a) and supports the importance of shallow aquifer flow paths regulating alpine streamflow.

4.5.3 Basin response to summer rain events

Following the freshet, streamflow stabilized such that the headwater subbasin consistently generated a greater volume of baseflow than the basin outlet (Figure 4.3b). The atypical pattern of decreasing streamflow with increasing contributing area during the summer months can be

explained by groundwater recharge via channel bed infiltration along the channel length between outlets and evaporative losses from the surrounding contributing area (Chapter 3). During the summer rains, headwater subbasin streamflow was unresponsive and composed entirely of pre-event waters (Figure 4.4b,c), reflecting the continued dominance of aquifer discharge within the headwater subbasin. In comparison, basin outlet streamflow increased in response to summer rain events, with the early summer hydrograph peaking higher while the late summer recession limb was more extended (Figure 4.4b,c). The early summer peak was accompanied by a measurable but minor amount of rainfall event source water, while no detectible contribution occurred during the late summer event. These differences are in part due to the 2.0 mm greater precipitation depth during the early summer event, but also reflect seasonal differences in basin characteristics that control runoff production and event water contributions.

In northern cold climates, maximum annual soil moisture content typically occurs during the early summer due to the presence of recently received freshet inputs and limited storage capacity above shallow frost tables (Quinton *et al.*, 2005; Hoylman *et al.*, 2019). In this study, the water table decline below the fen during the freshet reflects the deepening thaw front while the riparian swamp stilling well remained frozen (Figure 4.4a). By early summer, the water table had stabilized below the fen, providing storage capacity for rain and resulting in reduced streamflow response and rainfall event water contributions at the basin outlet (Figure 4.4b). By the late summer period, near-surface ice content in the riparian swamp had also thawed, further increasing basin storage capacity and rainfall event water retention, such that streamflow volumes and event water contributions were further reduced (Figure 4.4c). This is also supported by the increase in late summer streamflow SPC (Figure 4.3c), consistent with findings from other studies of catchment runoff generation which found a deepening frost table opens mineral

substrate pores previously occupied with ice, increasing basin storage capacity and extending the flow path for rainfall inputs en route to the channel network (Quinton and Marsh, 1999; Piovano *et al.*, 2019). A similar pattern of declining runoff production and recession limb extension as the open water season progressed was observed at Wolf Creek, an alpine basin where upslope areas contributing to the slope base during the early summer became disconnected in the late summer as substrates thawed and near-surface moisture content declined (Carey and Woo, 2001a).

4.5.4 Climate change implications for alpine runoff generation

As the climate continues to change, precipitation is expected to increase across the North (IPCC, 2013) and to a greater degree in high elevation areas (Hock *et al.*, 2019; Asong *et al.*, 2020). The increase in mean annual temperatures and total precipitation is also expected to lead to a greater proportion of rain (Asong *et al.*, 2020) and a shorter snow-covered season (Derksen et al., 2008). Other studies have reported a shift from nival to nival/pluvial regimes in parts of northern Canada as more frequent large rain events exceed basin storage capacity and cause summer streamflow peaks of similar amplitude to the freshet (Spence *et al.*, 2011; Beel *et al.*, 2021). The 2019 open water season likely received below average rainfall, and as such, these findings likely did not fully capture runoff generation processes active during large magnitude rainfall events that exceed local storage capacity. Further study of the basin over multiple years would be required to better characterize the potential influence of increased rainfall and/or large magnitude rain events, a topic of particular importance given the predicted increase in precipitation of 24.2 - 139.8 mm annually and 6.6 - 40.2 mm for the open water season by 2100 (Environment and Climate Change Canada, 2021).

Wetter conditions are the primary driver for observed shifts from nival to pluvial stream regimes (Spence *et al.*, 2011; Beel *et al.*, 2021), but other basin specific factors should be considered for

their role in buffering runoff generation as increasing temperatures affect permafrost extent (Payette *et al.*, 2004; Quinton *et al.*, 2011; Borge *et al.*, 2016; Mamet *et al.*, 2017), vegetation density (Swann *et al.*, 2010; Myers-Smith *et al.*, 2011; Mekonnen *et al.*, 2021), and other hydrological characteristics controlling local storage capacity of shrub tundra regions. As the climate continues to warm, an extended snow-free season and/or forest encroachment at the alpine shrub tundra ecotone may result in greater cumulative evapotranspiration (Nicholls and Carey, 2021), enhancing the pronounced evaporation signal in the stream observed in the late summer (Figure 4.3d). The timing of this shift will be long-term and complex, as plant physiognomy and seed dispersal processes delay the ecosystem response to changing climatic conditions (Holtmeier and Broll, 2005).

While increased evapotranspiration from alpine shrub tundra may cause a decline in runoff unless offset by increased rainfall, groundwater losses are also susceptible to climate change and important to basin water balance on local and regional scales. High elevation alpine zones with absent and/or sparse vegetation are known to recharge groundwater (Wilson and Guan, 2004; Hayashi, 2020) with greater efficiency than was previously thought (Clow *et al.*, 2003). The groundwater samples collected during the 2019 open water season had isotope compositions similar to the weighted mean annual precipitation of the system, suggesting highly efficient recharge of the aquifer sustaining the headwater subbasin springs (St Amour *et al.*, 2005). An earlier start to the open water season will result in an earlier decline in frost table depths, effectively extending the duration that channel bed infiltration is active and reducing the proportion of basin water loss via channel discharge (Chapter 3). Evidence of this shift to deeper flow paths has been observed on regional scales (Jacques and Sauchyn, 2009; Rennermalm *et al.*, 2010; Connon *et al.*, 2014; Brown *et al.*, 2015; Crites *et al.*, 2020) with aquifer discharge and winter baseflow volumes

for large river systems anticipated to increase further as the climate continues to warm (Walvoord *et al.*, 2012; Stadnyk and Déry, 2021). Of note, among the 12 largest pan-Arctic rivers, the Yukon and Mackenzie rivers are likely to have the most significant rate of increase in discharge, accompanied with a shift toward greater fall and winter baseflow (Stadnyk *et al.*, 2021).

4.6 Conclusion

Sparse regional observation networks across the subarctic make it difficult to characterize the role of alpine tundra in maintaining the annual discharge of large northern rivers. This study provides important field observations of the seasonal differences in source water contributions and flow paths generating runoff from an alpine tundra basin following spring freshet and summer rain events in 2019. During the freshet, daily melt volumes were large and storage capacity was limited by frozen soils, but isotope-mass balance calculations estimate the freshet streamflow was only composed of 8.4 % snowmelt event water. As the freshet concluded, the frost table descended, storage capacity within the near channel contributing area increased, and water infiltrated the previously frozen channel bed substrates. As a result, the magnitude of basin streamflow and event-water contributions following rain events declined as the summer progressed. Furthermore, evidence of evaporative losses en route to the main outlet became more prominent in the late summer. As the climate continues to change, warming temperatures and greater precipitation will affect the timing and magnitude of subarctic alpine tundra streamflow. An earlier freshet and delayed fall refreeze will extend the open water season, resulting in a larger proportion of annual water losses via aquifer recharge and evaporation. Alpine tundra is also vulnerable to climate-driven land-cover change, which is liable to affect permafrost extent, vegetation densities, and seasonally distinct characteristics controlling near-surface storage capacity and the partitioning of basin losses between streamflow and aquifer recharge. Field

observations and results from a suite of hydrometric and isotopic measurements provide vital information for future hydrological modelling efforts seeking to better represent the role of alpine tundra terrain in maintaining the water balance of large northern river systems as the climate and cryosphere landforms continue to change.

4.7 References

Ahmed R, Prowse T, Dibike Y, Bonsal B, O'Neil H. 2020. Recent trends in freshwater influx to the Arctic Ocean from four major Arctic-draining rivers. Water 12 (4): 1–13 DOI: 10.3390/W12041189

Andermann C, Longuevergne L, Bonnet S, Crave A, Davy P, Gloaguen R. 2012. Impact of transient groundwater storage on the discharge of Himalayan rivers. Nature Geoscience 5 (2): 127–132 DOI: 10.1038/ngeo1356

Asong EZ, Elshamy EM, Princz D, Wheater SH, Pomeroy J, Pietroniro A, Cannon A. 2020. High-resolution meteorological forcing data for hydrological modelling and climate change impact analysis in the Mackenzie River Basin. Earth System Science Data 12 (1): 629–645 DOI: 10.5194/essd-12-629-2020

Beel C, Heslop J, Orwin J, Pope M, Schevers A, Hung J, Lafrenière M, Lamoureux S. 2021. Emerging dominance of summer rainfall driving High Arctic terrestrial-aquatic connectivity. Nature Communications 12: 1448 DOI: 10.1038/s41467-021-21759-3

Bense VF, Ferguson G, Kooi H. 2009. Evolution of shallow groundwater flow systems in areas of degrading permafrost. Geophysical Research Letters 36 (22): 1–7 DOI: 10.1029/2009GL039225

Borge AF, Westermann S, Solheim I, Etzelmüller B. 2016. Strong degradation of palsas and peat plateaus in northern Norway during the last 60 years. The Cryosphere Discussions (February): 1–31 DOI: 10.5194/tc-2016-12

Boucher JL, Carey SK. 2010. Exploring runoff processes using chemical, isotopic and hydrometric data in a discontinuous permafrost catchment. Hydrology Research 41 (6): 508–519 DOI: 10.2166/nh.2010.146

Bowen GJ. 2019. The Online Isotopes in Precipitation Calculator, version 3.1 Available at: http://www.waterisotopes.org. [Accessed 19 April 2021]

Brown D, Jorgenson. MT, Douglas T, Ruess R. 2015. Interactions of fire and climate exacerbate permafrost degradation in Alaskan lowland forests. Journal of Geophysical Research, Biogeosciences 120(8): 1619–1637 DOI: 10.1002/2015JG003033.Received

Buttle J. 1998. Fundamentals of small catchment hydrology. In Isotope Tracers in Catchment Hydrology, Kendall C, McDonnell J (eds). Elsevier: Amsterdam; 1–43.

Carey S, Woo MK. 2001. Slope runoff processes and flow generation in a subarctic, subalpine catchment. Journal of Hydrology 253 (1–4): 110–129 DOI: 10.1016/S0022-1694(01)00478-4

Carey S, Quinton WL. 2004. Evaluating snowmelt runoff generation in a discontinuous permafrost catchment using stable isotope, hydrochemical and hydrometric data. Nordic Hydrology 35 (4–5): 309–324 DOI: 10.1002/hyp.5764

Carey SK, Quinton WL. 2005. Evaluating runoff generation during summer using hydrometric, stable isotope and hydrochemical methods in a discontinuous permafrost alpine catchment. Hydrological Processes 19 (1): 95–114 DOI: 10.1002/hyp.5764

Carey SK, Boucher JL, Duarte CM. 2013. Inferring groundwater contributions and pathways to streamflow during snowmelt over multiple years in a discontinuous permafrost subarctic environment (Yukon, Canada). Hydrogeology Journal 21 (1): 67–77 DOI: 10.1007/s10040-012-0920-9

Clow DW, Schrott L, Webb R, Campbell DH, Torizzo A, Dornblaser M. 2003. Ground water occurrence and contributions to streamflow in an alpine catchment, Colorado front range. Ground Water 41 (7): 937–950 DOI: 10.1111/j.1745-6584.2003.tb02436.x

Connon RF, Quinton WL, Craig JR, Hayashi M. 2014. Changing hydrologic connectivity due to permafrost thaw in the lower Liard River valley, NWT, Canada. Hydrological Processes 28 (14): 4163–4178 DOI: 10.1002/hyp.10206

Craig H. 1961. Isotopic variations in meteoric waters. Science 133 (3465): 1702–1703

Crites H, Kokelj S V., Lacelle D. 2020. Icings and groundwater conditions in permafrost catchments of northwestern Canada. Scientific Reports 10 (1): 1–11 DOI: 10.1038/s41598-020-60322-w

Dansgaard W. 1964. Stable isotopes in precipitation. Tellus 16: 436–46

Derksen C, Brown R, MacKay M. 2008. Mackenzie Basin snow cover: variability and trends from conventional data, satellite remote sensing, and Canadian regional climate model simulations. In Cold Region Atmospheric and Hydrologic Studies. The Mackenzie

GEWEX Experience: Volume 1: Atmospheric Dynamics, Woo MK (ed.). Springer Berlin Heidelberg: Berlin, Heidelberg, Heidelberg; 213–239. DOI: 10.1007/978-3-540-73936-4_13

Dingman SL. 1981. Elevation: a major influence on the hydrology of New Hampshire and Vermont, USA. Hydrological Sciences Journal 26 (4): 399–413 DOI: 10.1080/02626668109490904

Ecosystem Classification Group. 2010. Ecological Regions of the Northwest Territories: Cordillera. Department of Environment and Natural Resources, Government of the Northwest Territories: Yellowknife.

Environment and Climate Change Canada. 2021. Climate data for a resilient Canada. Available at: https://climatedata.ca/ [Accessed 18 August 2021]

Environment Canada. 2020. Environment Canada historical data archive. Available at: https://climate.weather.gc.ca/historical_data/search_historic_data_e.html [Accessed 17 April 2020]

Genereux D. 1998. Quantifying uncertainty in tracer-based hydrograph separations. Water Resources Research 34 (4): 915–919 DOI: 10.1029/98WR00010

Gibson JJ, Edwards TWD, Prowse TD. 1993. Runoff generation in a high boreal wetland in northern Canada. Nordic Hydrology 24 (October): 213–224

Granger RJ. 1998. Partitioning of energy during the snow-free season at the Wolf Creek Research Basin. In Wolf Creek Research Basin: Hydrology, Ecology, Environment, Pomeroy W, Granger R (eds.). National Water Research Institute, Saskatoon, SK; 3–44.

Gray DM, Toth B, Zhao L, Pomeroy JW, Granger RJ. 2001. Estimating areal snowmelt infiltration into frozen soils. Hydrological Processes 15: 3095–3111 DOI: 10.1002/hyp.320

Gruber S, Hoelzle M. 2001. Statistical modelling of mountain permafrost distribution: local calibration and incorporation of remotely sensed data. Permafrost and Periglacial Processes 12: 69–77 DOI: 10.1002/ppp

Harris I, Jones PD, Osborn TJ, Lister DH. 2014. Updated high-resolution grids of monthly climatic observations - the CRU TS3.10 dataset. International Journal of Climatology 34 (3): 623–642 DOI: 10.1002/joc.3711

Hayashi M. 2020. Alpine hydrogeology: the critical role of groundwater in sourcing the headwaters of the world. Groundwater 58 (4): 498–510 DOI: 10.1111/gwat.12965

Hayashi M, Quinton WL, Pietroniro A, Gibson JJ. 2004. Hydrologic functions of wetlands in a discontinuous permafrost basin indicated by isotopic and chemical signatures. Journal of Hydrology 296 (1–4): 81–97 DOI: 10.1016/j.jhydrol.2004.03.020

Hinzman LD, Bettez ND, Bolton WR, Chapin FS, Dyurgerov MB, Fastie CL, Griffith B, Hollister RD, Hope A, Huntington HP, et al. 2005. Evidence and implications of recent climate change in northern Alaska and other Arctic regions. Climatic Change 72 (3): 251–298 DOI: 10.1007/s10584-005-5352-2

Hock R, Rasul G, Adler C, Cáceres B, Gruber S, Hirabayashi Y, Jackson M, Kääb A, Kang S, Kutuzov S, et al. 2019. Chapter 2: high mountain areas. In IPCC Special Report on the Ocean and Cryosphere in a Changing Climate: 131–202

Holtmeier FK, Broll G. 2005. Sensitivity and response of northern hemisphere altitudinal and polar treelines to environmental change at landscape and local scales. Global Ecology and Biogeography 14 (5): 395–410 DOI: 10.1111/j.1466-822X.2005.00168.x

Hoylman ZH, Jencso KG, Hu J, Holden ZA, Martin JT, Gardner WP. 2019. The climatic water balance and topography control spatial patterns of atmospheric demand, soil moisture, and shallow subsurface flow. Water Resources Research 55 (3): 2370–2389 DOI: 10.1029/2018WR023302

IPCC. 2013. Climate Change 2013 - The Physical Science Basis. DOI: 10.1038/446727a

Jacques JMS, Sauchyn DJ. 2009. Increasing winter baseflow and mean annual streamflow from possible permafrost thawing in the Northwest Territories, Canada. Geophysical Research Letters 36 (1): 1–6 DOI: 10.1029/2008GL035822

Kershaw G, Kershaw L. 1983. Geomorphology and vegetation of the MacTung study area, Yukon/NWT. Sherwood Park, AB.

Klaus J, McDonnell JJ. 2013. Hydrograph separation using stable isotopes: review and evaluation. Journal of Hydrology 505: 47–64 DOI: 10.1016/j.jhydrol.2013.09.006

Knowles JF, Harpold AA, Cowie R, Zeliff M, Barnard HR, Burns SP, Blanken PD, Morse JF, Williams MW. 2015. The relative contributions of alpine and subalpine ecosystems to the water balance of a mountainous, headwater catchment. Hydrological Processes 29 (22): 4794–4808 DOI: 10.1002/hyp.10526

Kokelj SV, Palmer MJ, Lantz TC, Burn CR. 2017. Ground temperatures and permafrost warming from forest to tundra, Tuktoyaktuk coastlands and Anderson Plain, NWT, Canada. Permafrost and Periglacial Processes 28 (3): DOI: 10.1002/ppp.1934

Kuchment LS, Gelfan AN, Demidov VN. 2000. A distributed model of runoff generation in the permafrost regions. Journal of Hydrology 240 (1–2): 1–22 DOI: 10.1016/S0022-1694(00)00318-8

Lamoureux SF, Lafrenière MJ. 2017. More than just snowmelt: integrated watershed science for changing climate and permafrost at the Cape Bounty Arctic Watershed Observatory. Wiley Interdisciplinary Reviews: Water 5 (February): e1255 DOI: 10.1002/wat2.1255

Landwehr JM, Coplen TB. 2004. Line-conditioned excess: a new method for characterizing stable hydrogen and oxygen isotope ratios in hydrologic systems. In Isotopes in Environmental Studies. Monaco; 713.

Langston G, Hayashi M, Roy JW. 2013. Quantifying groundwater-surface water interactions in a proglacial moraine using heat and solute tracers. Water Resources Research 49: 5411–5426 DOI: 10.1002/wrcr.20372

Laudon H, Seibert J, Köhler S, Bishop K. 2004. Hydrological flow paths during snowmelt: congruence between hydrometric measurements and oxygen 18 in meltwater, soil water, and runoff. Water Resources Research 40 (3) DOI: 10.1029/2003WR002455

Laudon H, Spence C, Buttle J, Carey SK, McDonnell JJ, McNamara JP, Soulsby C, Tetzlaff D. 2017. Save northern high-latitude catchments. Nature Geoscience 10 (5): 324–325 DOI: 10.1038/ngeo2947

Ma R, Sun Z, Hu Y, Chang Q, Wang S, Xing W, Ge M. 2017. Hydrological connectivity from glaciers to rivers in the Qinghai-Tibet plateau: roles of suprapermafrost and subpermafrost groundwater. Hydrology and Earth System Sciences 21 (9): 4803–4823 DOI: 10.5194/hess-21-4803-2017

Mamet SD, Chun KP, Kershaw GGL, Loranty MM, Kershaw GP. 2017. Recent increases in permafrost thaw rates and areal loss of palsas in the western Northwest Territories, Canada. Permafrost and Periglacial Processes 28 (4): 619–633 DOI: 10.1002/ppp.1951

Marsh CB, Pomeroy JW, Wheater HS. 2020. The Canadian Hydrological Model (CHM): A multi-scale, multi-extent, variable-complexity hydrological model - design and overview. Geoscientific Model Development Discussions 13 (2002): 225–247 DOI: 10.5194/gmd-2019-109

Matsuoka N. 2006. Monitoring periglacial processes: towards construction of a global network. Geomorphology 80 (1–2): 20–31 DOI: 10.1016/j.geomorph.2005.09.005

McGuire AD, Chapin FS, Walsh JE, Wirth C. 2006. Integrated regional changes in Arctic climate feedbacks: implications for the global climate system. Annual Review of Environment and Resources 31 (1): 61–91 DOI: 10.1146/annurev.energy.31.020105.100253

Mekonnen ZA, Riley WJ, Berner LT, Bouskill NJ, Torn MS, Iwahana G, Breen AL, Myers-Smith IH, Criado MG, Liu Y, et al. 2021. Arctic tundra shrubification: a review of mechanisms and impacts on ecosystem carbon balance. Environmental Research Letters 16 (5) DOI: 10.1088/1748-9326/abf28b

Metcalfe RA, Buttle JM. 2001. Soil partitioning and surface store controls on spring runoff from a boreal forest peatland basin in north-central Manitoba, Canada. Hydrological Processes 15 (12): 2305–2324 DOI: 10.1002/hyp.262

Moore RDD. 2005. Slug injection using salt in solution. Streamline: Watershed Management Bulletin 8 (2): 1–6 DOI: 10.1592/phco.23.9.1S.32890

Myers-Smith IH, Forbes BC, Wilmking M, Hallinger M, Lantz T, Blok D, Tape KD, Macias-Fauria M, Sass-Klaassen U, Lévesque E, et al. 2011. Shrub expansion in tundra ecosystems: dynamics, impacts and research priorities. Environmental Research Letters 6 (4): 045509 DOI: 10.1088/1748-9326/6/4/045509

Nicholls EM, Carey SK. 2021. Evapotranspiration and energy partitioning across a forest-shrub vegetation gradient in a subarctic, alpine catchment. Journal of Hydrology 602 (March): 126790 DOI: 10.1016/j.jhydrol.2021.126790

Payette S, Delwaide A, Caccianiga M, Beauchemin M. 2004. Accelerated thawing of subarctic peatland permafrost over the last 50 years. Geophysical Research Letters 31: L18208

Pilgrim D, Huff D, Steele T. 1979. Use of specific conductance contact time relations for separating flow components in storm runoff. Water Resources Research 15: 329–339

Piovano TI, Tetzlaff D, Carey SK, Shatilla NJ, Smith A, Soulsby C. 2019. Spatially distributed tracer-aided runoff modelling and dynamics of storage and water ages in a permafrost-influenced catchment. Hydrology and Earth System Sciences 23 (6): 2507–2523 DOI: 10.5194/hess-23-2507-2019

Pomeroy JW, Gray DM, Brown T, Hedstrom NR, Quinton WL, Granger RJ, Carey SK. 2007. The Cold Regions Hydrological Model: a platform for basing process representation and model structure on physical evidence. Hydrological Processes 21: 2650–2667 DOI: 10.1002/hyp

Prairie Climate Centre. 2019. Sekwi Mountain statistically downscaled climate scenarios. Climate Atlas of Canada, Version 2 Available at: https://climateatlas.ca/data/grid/1118/plus30_2030_85/line [Accessed 20 June 2020]

Quinton W, Shirazi T, Carey S, Pomeroy J. 2005. Soil water storage and active-layer development in a sub-alpine tundra hillslope, southern Yukon Territory, Canada. Permafrost and Periglacial Processes 16 (4): 369–382 DOI: 10.1002/ppp.543

Quinton WL, Marsh P. 1999. A conceptual framework for runoff generation in a permafrost environment. Hydrological Processes 13 (July 1998): 2563–2581

Quinton WL, Carey SK, Goeller NT. 2004. Snowmelt runoff from northern alpine tundra hillslopes: major processes and methods of simulation. Hydrology and Earth System Sciences 8 (5): 877–890 DOI: 10.5194/hess-8-877-2004

Quinton WL, Hayashi M, Chasmer LE. 2011. Permafrost-thaw-induced land-cover change in the Canadian subarctic: implications for water resources. Hydrological Processes 25 (1): 152–158 DOI: 10.1002/hyp.7894

Rennermalm A, Wood E, Troy T. 2010. Observed changes in pan-arctic cold-season minimum monthly river discharge. Climate Dynamics 35: 923–939 DOI: http://dx.doi.org.libproxy.wlu.ca/10.1007/s00382-009-0730-5

Sklash MG, Farvolden RN. 1979. The role of groundwater in storm runoff. Journal of Hydrology 43: 45–65 DOI: 10.1016/S0167-5648(09)70009-7

Spence C, Kokelj SV, Ehsanzadeh E. 2011. Precipitation trends contribute to streamflow regime shifts in northern Canada. In Proceedings of Symposium H02 Held during IUGG2011IAHS Press: Melbourne; 3–8.

St Amour NA, Gibson JJ, Edwards TWDD, Prowse TD, Pietroniro A. 2005. Isotopic time-series partitioning of streamflow components in wetland-dominated catchments, lower Liard river basin, Northwest Territories, Canada. Hydrological Processes 19 (17): 3357–3381 DOI: 10.1002/hyp.5975

Stadnyk TA, Déry SJ. 2021. Canadian continental-scale hydrology under a changing climate: a review. Water 13 (7): 1–14 DOI: 10.3390/w13070906

Stadnyk TA, Tefs A, Broesky M, Déry SJ, Myers PG, Ridenour NA, Koenig K, Vonderbank L, Gustafsson D. 2021. Changing freshwater contributions to the Arctic: a 90-year trend analysis (1981- 2070). Elementa - Science of the Anthropocene 9 (1): 1–26 DOI: 10.1525/elementa.2020.00098

Staudinger M, Stoelzle M, Seeger S, Seibert J, Weiler M, Stahl K. 2017. Catchment water storage variation with elevation. Hydrological Processes 31 (11): 2000–2015 DOI: 10.1002/hyp.11158

Swann AL, Fung IY, Levis S, Bonan GB, Doney SC. 2010. Changes in arctic vegetation amplify high-latitude warming through the greenhouse effect. Proceedings of the National Academy of Sciences of the United States of America 107 (4): 1295–1300 DOI: 10.1073/pnas.0913846107

Taylor S, Feng X, Williams M, Mcnamara J. 2002. How isotopic fractionation of snowmelt affects hydrograph separation. Hydrological Processes 16: 3683–3690 DOI: 10.1002/hyp.1232

Tian C, Wang L, Kaseke KF, Bird BW. 2018. Stable isotope compositions (δ^2H, $\delta^{18}O$ and $\delta^{17}O$) of rainfall and snowfall in the central United States. Scientific Reports 8 (1): 1–15 DOI: 10.1038/s41598-018-25102-7

Turner KW, Edwards TWD, Wolfe BB. 2014. Characterising runoff generation processes in a lake-rich thermokarst landscape (Old Crow Flats, Yukon, Canada) using $\delta^{18}O$, δ^2H and d-excess measurements. Permafrost and Periglacial Processes 25 (1): 53–59 DOI: 10.1002/ppp.1802

Viviroli D, Wehren B, Weingartner R, Scha B. 2010. General characteristics of alpine waters. In Alpine Waters, Bundi U (ed.). Springer: Berlin; 17-58. DOI: 10.1007/978-3-540-88275-6

Walvoord MA, Kurylyk BL. 2016. Hydrologic impacts of thawing permafrost — a review. Vadose Zone Journal 15 (6) DOI: 10.2136/vzj2016.01.0010

Walvoord MA, Voss CI, Wellman TP. 2012. Influence of permafrost distribution on groundwater flow in the context of climate-driven permafrost thaw: example from Yukon Flats basin, Alaska, United States. Water Resources Research 48 (7): 1–17 DOI: 10.1029/2011WR011595

Wilson JL, Guan H. 2004. Mountain-block hydrology and mountain-front recharge. In Groundwater Recharge in a Desert Environment: The Southwestern United States, Phillips F, Hogan J, and Scanlon B, (eds.). Washington; 113–137. DOI: 10.1029/009WSA08

Woo MK. 1986. Permafrost hydrology in North America. Atmosphere - Ocean 24 (3): 201–234 DOI: 10.1080/07055900.1986.9649248

Woo MK, Rouse W, Stewart R, Stone J. 2008. The Mackenzie GEWEX study: a contribution to cold region atmospheric and hydrologic sciences. In Cold Region Atmospheric and Hydrologic Studies. The Mackenzie GEWEX Experience: Volume 1: Atmospheric Dynamics, Woo MK (ed.). Springer: New York; 507.

4.8 Figures

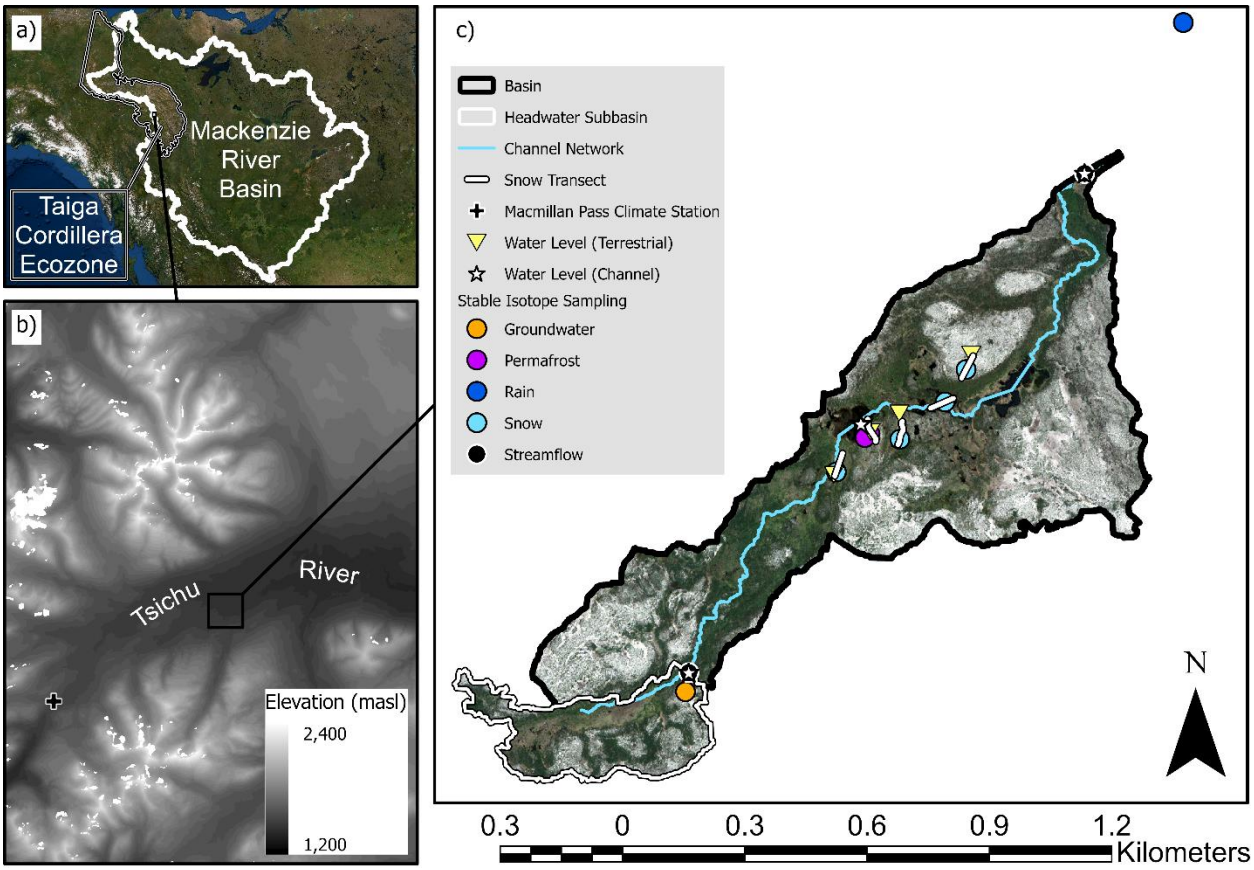

Figure 4-1: Map of a) study basin relative to the Taiga Cordillera ecozone and the Mackenzie River basin; b) study basin relative to the Tsichu River valley and Macmillan Pass climate station; c) headwater subbasin and study basin outlets, catchment extents, field measurement and water sampling locations.

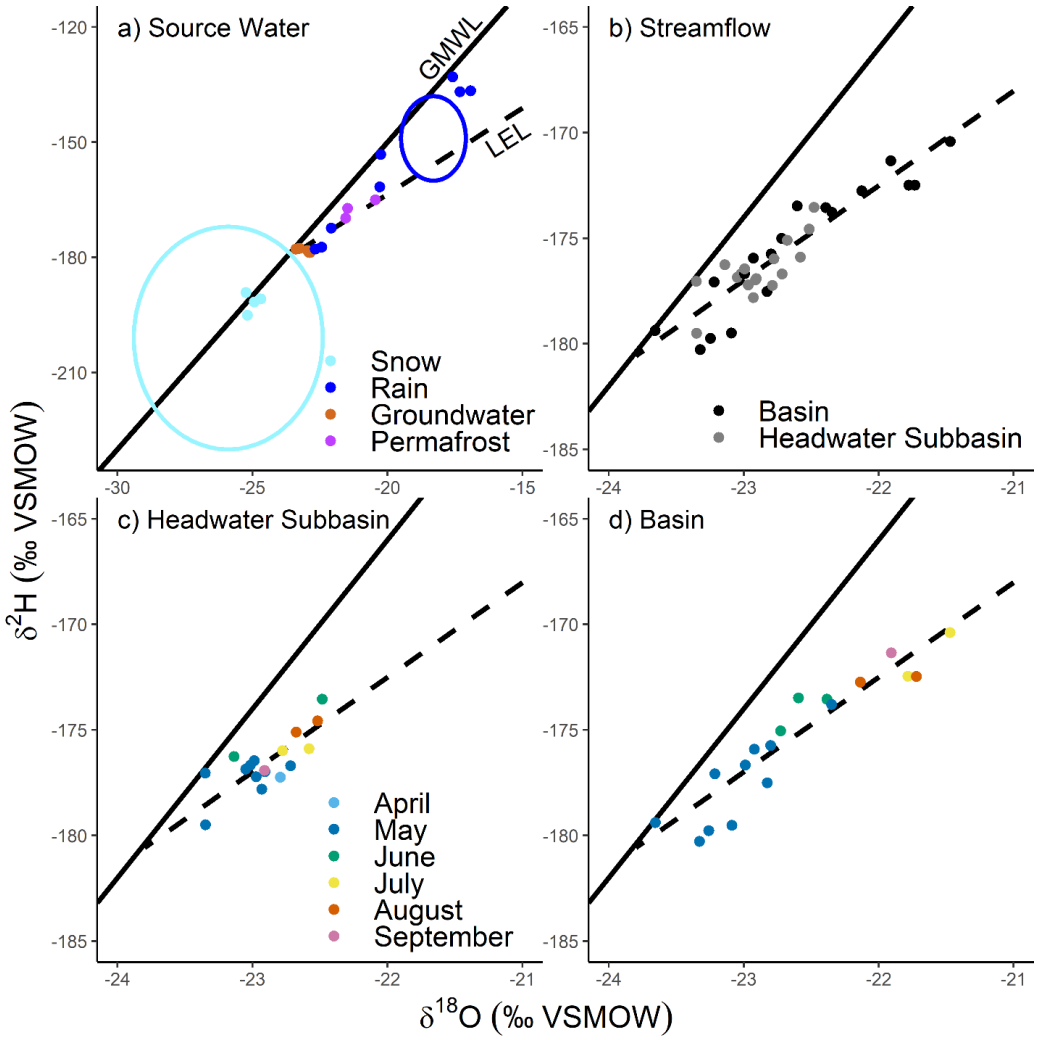

Figure 4-2: Isotope composition of a) source water and b) streamflow collected from the c) headwater subbasin and d) basin outlets. Source water sample values (points) and modelled values (circles) for rain and snow are reported, with the range of modelled compositions shown reflecting the minimum and maximum estimates of Bowen (2019) for months of rain (May – September) and snow (October – April). The Global Meteoric Water Line (GMWL: $\delta^2H = 8\ \delta^{18}O + 10$; Craig, 1961) and Local Evaporation Line (LEL: $\delta^2H = 4.5\ \delta^{18}O - 73.9$) are shown, the latter derived from linear regression through the streamflow isotope compositions. Bottom panes reflect the range of isotope compositions of streamflow at the c) headwater subbasin and d) study basin outlets grouped by month of collection.

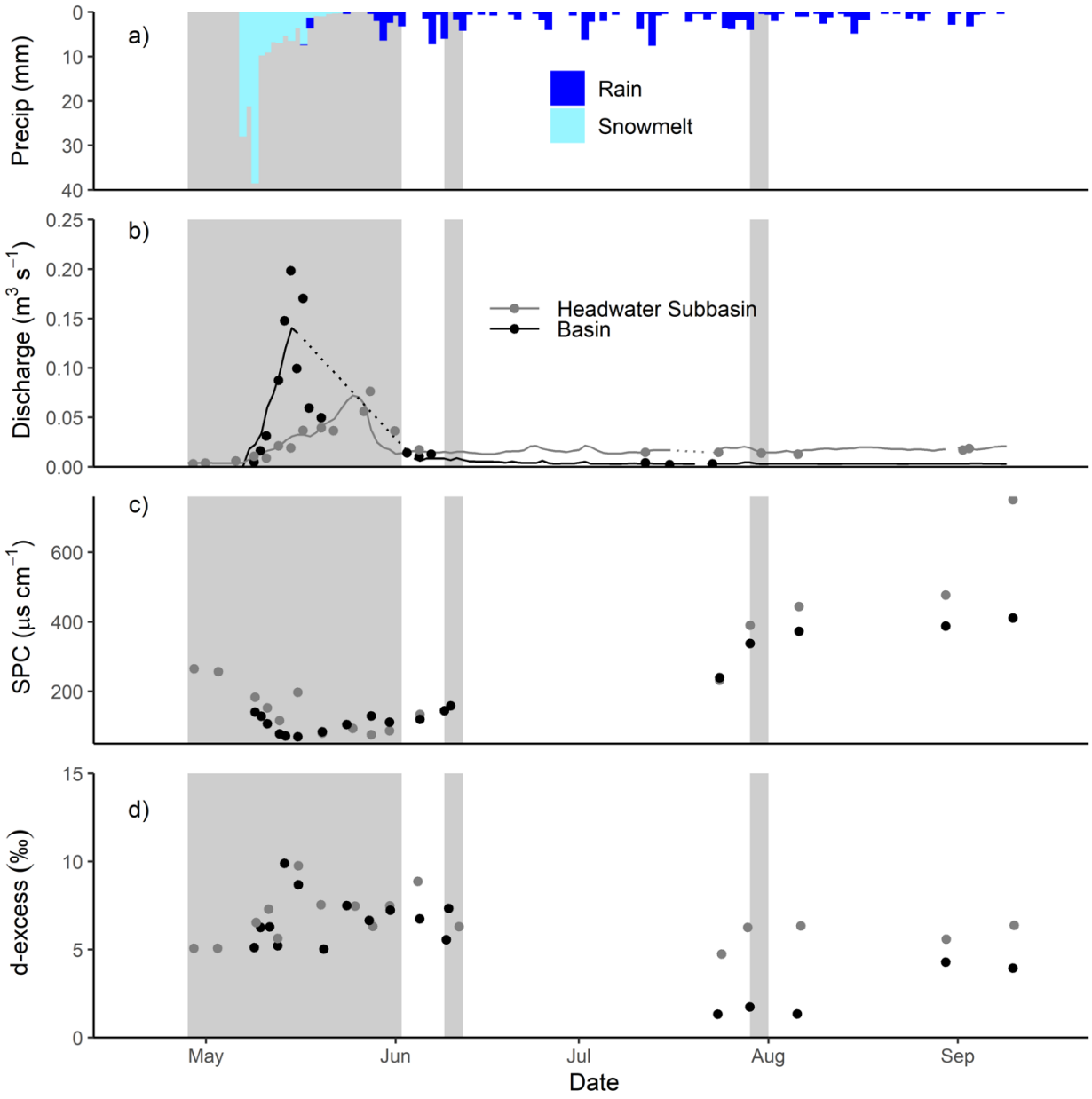

Figure 4-3: Time series of a) daily precipitation hyetograph; b) daily mean streamflow hydrographs; c) streamflow specific conductivity; and d) streamflow d-excess values. Hydrograph segments with solid lines when discrete observations (points) allowed for stage-discharge relationship to be used and dotted lines when linear interpolation was required (Appendix 4.4). Greyed segments denote duration of seasonal runoff events of interest.

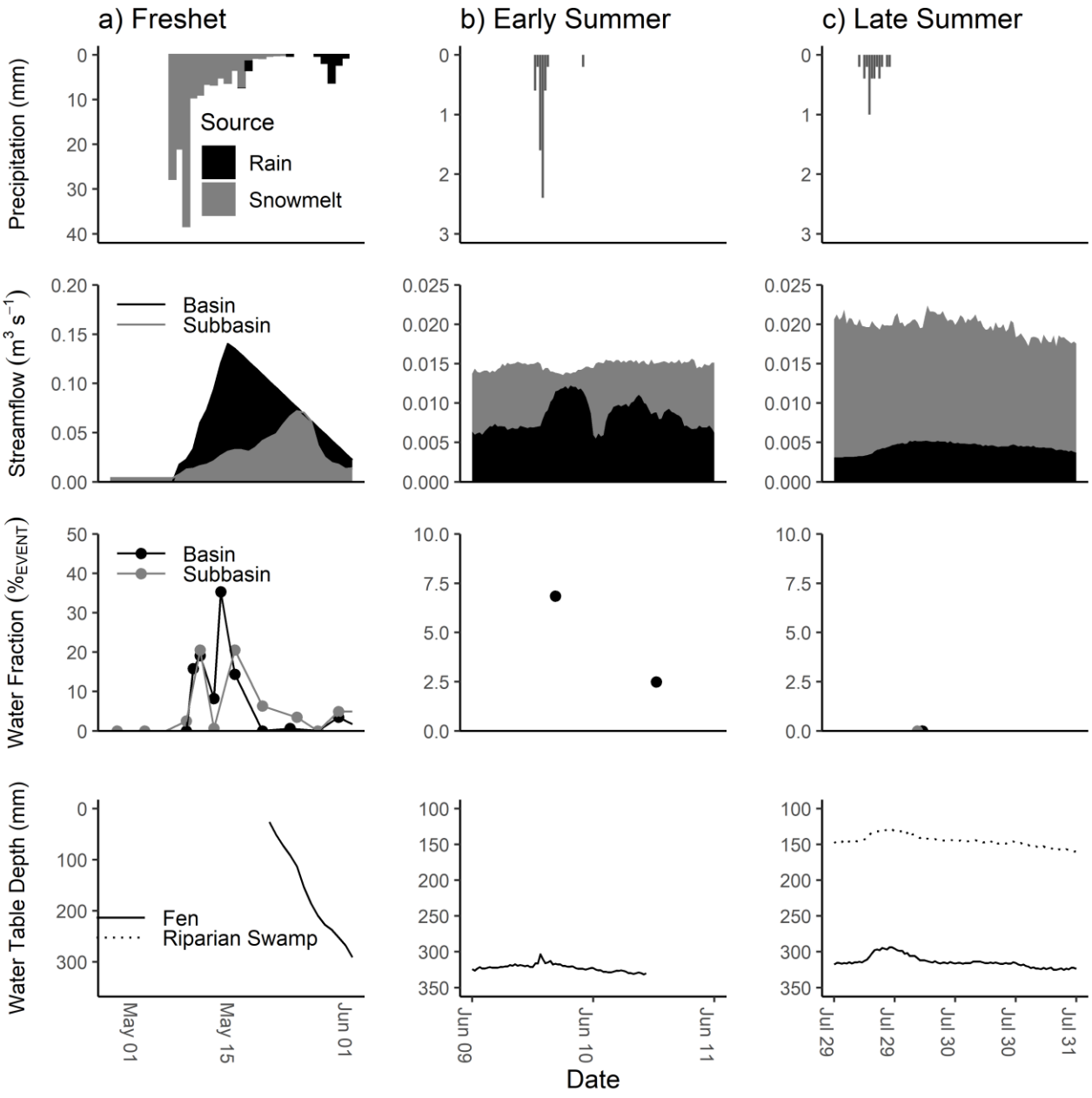

Figure 4-4: Seasonal runoff events of interest when precipitation resulted in a runoff response from the study basin during a) freshet, b) early summer, and c) late summer conditions. The fraction of streamflow composed of event water is based on streamflow samples (points) and calculations using equation 4.5. Water table depths are presented for cover classes capable of maintaining water tables during unfrozen conditions. Temporal resolution is daily for the freshet and 30-minutes for the summer runoff events.

5. Conclusions, future research recommendations, and self-reflections

5.1 Thesis summary

Mountains are known as the "water towers of the world" because they receive disproportionately large amounts of precipitation and produce correspondingly large amounts of runoff, contributing alpine sourced waters to lowland regions during sensitive periods of the annual cycle when other sources are reduced (Viviroli *et al.*, 2010). Northern alpine systems are particularly susceptible to climate change due to amplification of observed and predicted warming with both latitude and elevation (Beniston, 2003; Pepin *et al.*, 2015; Wang *et al.*, 2016). Furthermore, hydrological characteristics of alpine areas exhibit a high degree of spatial heterogeneity, with sharp transitions in relief, exposure, vegetation and substrate characteristics (Viviroli *et al.*, 2010; Marsh *et al.*, 2020) making attempts to quantify the impacts of climate change for alpine basin water balance challenging. Currently there is a lack of understanding concerning the hydrological processes operating in deglaciated northern alpine systems and how they vary spatially and temporally (Matsuoka, 2006; Walvoord and Kurylyk, 2016) as the number of research sites focused on hydrology are sparse (Laudon *et al.*, 2017), and generally found in lowland areas (de Jong *et al.*, 2005). To my knowledge, prior to this research no study basin with a focus on hydrological processes had been established within the alpine tundra of the Taiga Cordillera; a northern Canadian ecozone characterized by subarctic climates and mountainous terrain. It is imperative that we develop our understanding of northern alpine hydrology to anticipate future changes to this water resource, particularly in the tundra regions below exposed ridges and above contiguous forests where field-based observations are lacking.

5.1.1 Objectives

The goal of this dissertation was to characterize the hydrology of an alpine shrub tundra study basin (~0.8 km^2) in the Mackenzie Mountains, Sahtu territory, NT by fulfilling three primary research objectives:

1. Establish the alpine shrub tundra cover classes that are present within the study basin, the hydrological characteristics unique to each, and the hydrological function they have in isolation and collectively.
2. Use the land cover classification to guide a water balance assessment of the study basin and describe seasonal differences in primary inputs, outputs, and hydrological processes active during the 2019 open water season.
3. Assess and compare runoff generating hydrological processes during 2019 freshet snowmelt and summer rain events, including changes in contributing area storage, streamflow volumes, and source water contributions using water isotope tracers.

The fulfillment of each objective was presented in detail in Chapters two, three, and four, respectively, with the key findings of each briefly restated here.

5.1.2 Major findings

5.1.2.1 Chapter Two - Mackenzie River basin alpine tundra land cover classification and associated hydrological properties

In Chapter Two, the study basin was segmented into an assemblage of five cover classes, each with a unique set of surface, subsurface, and topographical characteristics that controls storage capacity and flow paths within and from the basin. Glaciofluvial uplands composed of coarse-grained sands and gravels with sparse vegetation and thin to absent organic soils remained disconnected from the channel network. Instead, this cover class served to route precipitation to

recharge groundwater reservoirs at greater depth. The near-surface soils were relatively dry, with temperature profiles and subsurface images showing no evidence of permafrost. Peat plateaus had similar elevation and relief to the glaciofluvial uplands, but thick organic soils and impermeable ice-rich permafrost resulted in shallow soil storage volumes and inhibited exchange with aquifers below. Precipitation inputs received at the surface of peat plateaus were routed efficiently via lateral subsurface flow paths to neighbouring fens. The cover classes in closer proximity to the channel network (riparian swamp and fen) received both precipitation directly and groundwater inputs from neighbouring higher elevation terrain. Both the riparian swamp and fen acted as primary contributors to channel discharge via subsurface flow and evidence of overland flow was found within the riparian swamp. Some fen areas existed in isolation from the channel network, but what proportion of these features act as storage compartments and/or exchange water with subpermafrost aquifers via taliks remains unclear. Lastly, open water areas were limited in extent, and due to the steep gradient of the channel network, any precipitation and/or runoff received would have a short residence time before passing the outlet or recharging groundwater through the channel bed.

5.1.2.2 Chapter Three - Runoff-recharge partitioning in an alpine tundra catchment, Mackenzie Mountains, NT

Chapter Three expanded on the description of alpine shrub tundra cover class characteristics and interactions controlling storage and routing within and from the basin provided in Chapter Two by quantifying the basin water balance and introducing a temporal component to the analysis. The basin water balance was compared among freshet, early summer, and late summer periods for the 2019 open water season to establish when specific storage compartments and/or transport conduits were most important. During the freshet, snowmelt largely bypassed potential storage as

isolated surface depressions were few and ice-rich frost tables and/or overflow ice limited infiltration in the surrounding terrain. As such, snowmelt inputs resulted in rapid streamflow and high runoff efficiency during the freshet. As the summer progressed, runoff efficiency declined, as well as the runoff-recharge ratio due to increasing subsurface storage, flow path extension, and aquifer recharge via channel bed infiltration. Evapotranspiration (ET) also became more prominent from snow-free areas, with greatest mean daily ET losses occurring during the early summer. These findings provide information on the maintenance of regional river systems by alpine headwaters. Surface water runoff occurred mostly during the freshet while aquifer recharge became more important as the open water season progressed.

5.1.2.3 Chapter Four - Characterizing seasonal differences in hydrological flow paths and source water contributions to alpine tundra streamflow

Seasonal changes in water balance and runoff efficiency reported in Chapter Three were based on daily changes and seasonal mean contributions of each water balance component, but the hydrological response of a basin to discrete large volume inputs is also important. The conceptual model of storage and flow paths established in Chapter Two should also effectively represent the response of the basin on shorter time scales when large snowmelt and rainstorm events occur. As such, Chapter four utilized water isotope tracers to report changes in storage, streamflow, and source water contributions following runoff generation events occurring during freshet, early summer, and late summer conditions. During the freshet, streamflow from the basin outlet was composed mostly of pre-event waters (~92 %) and the largest streamflow volumes were observed. As the summer progressed, the streamflow response to rain events became more extended, with lower maximum flows and declining event water contributions. Assessment of water table fluctuations in the surrounding terrain and streamflow specific

conductivities suggested this change in runoff response was in part due to extended groundwater flow paths as the thaw depth below ground surface increased. At the headwater subbasin outlet, groundwater spring contributions dominated streamflow. As such, freshet peak flow from the headwater subbasin was delayed and composed of less melt water than the main basin outlet, and summer storm events did not influence either the volume or event water fraction of streamflow.

5.1.3 Synthesis and conclusions

This thesis presented results demonstrating 1) alpine shrub tundra land covers and their associated hydrological characteristics; 2) the spatial and temporal variability in hydrological processes, water storage compartments, and flow paths controlling basin water balance throughout the open water season; and 3) the seasonality of runoff generating processes and source water contributions during freshet snowmelt and summer rain events. These results developed an understanding of how this hydrological system functioned during the 2019 open water season, but it is imperative that the study also inform and refine our ability to predict the future hydrological function of this basin and similar alpine systems given the current and ongoing reality of climate change. As such, the results of each Chapter were considered in the context of ongoing climate change and its potential implications for future hydrological processes and water balance of alpine shrub tundra basins and the larger regional river systems to which they contribute. In this context, the major findings of the study have enhanced our collective understanding of alpine tundra northern hydrology, as elaborated on below.

5.1.3.1 Hydrological model structure and parameterization

Physically based hydrological models designed to handle cold climate conditions are a focal point of basin scale hydrological research (Pomeroy *et al.*, 2007; Craig *et al.*, 2020; Marsh *et al.*, 2020). The variety of hydrological processes that can be represented in hydrological models has

grown and computational power increased to allowed for more efficient model execution with finer spatial resolutions, but the lack of observational data available to calibrate and verify these models has remained a challenge for reducing model uncertainties (Pomeroy *et al.*, 2007; Stadnyk and Déry, 2021). Advancements in remote sensing data have helped fill this gap by generating digital elevation models (Polar Geospatial Center, St. Paul, MN, USA), estimates of snow water equivalent (Rees *et al.*, 2014; Hood and Hayashi, 2015), vegetation (Masson *et al.*, 2003) and soil moisture (Chasmer *et al.*, 2020), but field verification is still required to assess the accuracy of these data products. Furthermore, confirming the subsurface characteristics of a basin area with remote sensing data is even more challenging (Gruber and Hoelzle, 2001; Chasmer *et al.*, 2020).

A key contribution of this dissertation was the conceptual model structure developed and the complementing parameter values collected, both of which are necessary for an accurate distributed hydrological model representing alpine shrub tundra terrain. For example, vegetation height was collected in this study, a parameter found to be the most influential on modelled basin streamflow by Krogh et al. (2017). Fall soil moisture content was also measured, a parameter required for an earlier iteration of the Cold Regions Hydrological Model to function (Pomeroy *et al.*, 2007). Finally, the hydraulic conductivity and soil horizon thicknesses reported are necessary for modelled subsurface routing processes, such as those applied in RAVEN (Craig *et al.*, 2020). Alpine systems can have a highly varied spatial response to precipitation and net radiation given the heterogeneity of slope, relief, substrate and vegetation (Granger, 1998; Carey and Woo, 2005; Marsh *et al.*, 2020), and as such, distributed models of alpine headwaters and/or the larger river basins they contribute to will benefit from both the model structure and land cover specific values presented in this dissertation.

5.1.3.2 Permafrost thaw and contributing area dynamics

The conceptual model presented in Chapter Two, water balance presented in Chapter Three, and runoff event analysis presented in Chapter Four each account for water storage and flow paths available within the study basin, but the arrangement and proportion of cover classes and their hydrological connections as presented are not static through time. Larger scale regional transitions in land cover associated with permafrost thaw have been observed in this study area (Mamet *et al.*, 2017) and throughout the northern circumpolar region (Payette *et al.*, 2004; Quinton *et al.*, 2011; Borge *et al.*, 2016), with the greatest hydrological changes expected to result where continuous and discontinuous permafrost extents intersect (Walvoord *et al.*, 2012).

In the context of climate change driven permafrost thaw, the shallow suprapermafrost soil volume of the peat plateaus (25 % basin area), which route inputs towards neighbouring fens (31 % basin area) in this study basin, is unstable and likely to degrade. The Taiga Cordillera ecozone in northern Canada is currently estimated to contain 2.5 % wetland, but this coverage is expected to increase with the changing climate and permafrost thaw (Mahdianpari *et al.*, 2020). As permafrost thaw progresses, increasing active layer depth and the formation of taliks will slow subsurface drainage, delay the annual hydrograph peak, and generate higher flow in the later summer and fall seasons (Walvoord *et al.*, 2012; Woo, 2012; Lamontagne-Hallé *et al.*, 2018). These hydrological changes accompanying the replacement of peat plateaus with fen are likely irreversible over hundreds of years as they represent ecosystem protected, relict permafrost that was established under colder climatic conditions (Muller, 1947; Luoto and Seppälä, 2003; Bonnaventure and Lamoureux, 2013). As such, these areas can be considered sentinels of change for alpine basin storage and runoff processes, similar to the alterations in water balance and runoff generation processes from

lowland wetland complexes where organic-rich elevated areas are thawing and subsiding (Connon *et al.*, 2014; Kurylyk *et al.*, 2016).

5.1.3.3 Local and regional aquifer recharge

Declining permafrost extent, as described in the previous section, has implications for groundwater exchange through the vertical flow paths previously impeded by the permafrost (Walvoord and Kurylyk, 2016; Rogger *et al.*, 2017). This will impact the timing and magnitude of groundwater recharge in alpine regions and discharge to large regional river systems as more groundwater exchange can occur year-round via thicker open taliks routing flow laterally in the suprapermafrost zone and wider taliks routing flow vertically to and from aquifers in the subpermafrost zone (Woo *et al.*, 2008b; Walvoord *et al.*, 2012; Ma *et al.*, 2017; Hayashi, 2020). Increases in late fall and winter baseflow have been observed for multiple large northern rivers, and are connected to the expanding contributing areas and more active groundwater flow paths that have resulted from permafrost thaw (Jacques and Sauchyn, 2009; Rennermalm *et al.*, 2010; Connon *et al.*, 2014; Brown *et al.*, 2015; Crites *et al.*, 2020).

Groundwater exchange was identified as a prominent component of the water balance for this study basin, with headwater springs sustaining streamflow during winter conditions and aquifer recharge accounting for ~1/3 of total basin outputs during the open water season. The prominence of groundwater springs sourced from a larger upland recharge zone sustaining headwater subbasin streamflow was unexpected and identifies the importance of this ecotone in processing both precipitation inputs received directly and routing throughflow from exposed ridge tops, glacial masses, and extensive glaciofluvial deposits at higher elevation. The glaciofluvial upland features covered 25 % of the total basin area and played an important role in aquifer recharge as well, particularly during the freshet when large magnitude daily inputs were

being received. The infiltration via the glaciofluvial upland features has likely been stable for a long time, as these features were established during the last glaciation ~32-12 ka before present (Duk-Rodkin and Barendregt, 2011), are permafrost free, and are not at risk of failure due to freeze/thaw cycles because of their inability to retain moisture content.

In this study, the channel bed played an important role in partitioning basin outputs between surface flow as outlet discharge and subsurface flow as channel bed infiltration. In cold climates, more than half of annual precipitation inputs can be liberated within 2-4 weeks during the freshet as the winter accumulated snowpack melts (Woo, 1986), which is consistent with the freshet basin response observed during this study. Within the Mackenzie Basin, the timing of these freshet events has been advancing at a rate of ~3 days per decade (Woo and Thorne, 2003), and as the climate continues to warm, an increasing proportion of precipitation will be received as rain during ice-free channel conditions (Environment and Climate Change Canada, 2021). This will likely result in an increasing proportion of basin losses via groundwater recharge and reduced runoff efficiency for the basin, as the late summer flow paths and hydrological processes described in Chapter Three and Four become more prevalent.

There are regional water balance implications for the shift in precipitation regime favoring rain and flow path partitioning favoring groundwater recharge. The trend in increasing winter baseflow will likely continue as a greater proportion of headwater alpine losses occurs via groundwater recharge (Rogger *et al.*, 2017), increasing the aquifer discharge received by the lowland areas (Walvoord *et al.*, 2012). This may also result in the expansion of lowland lakes and/or aufeis features (Walvoord *et al.*, 2012; Walvoord and Kurylyk, 2016; Crites *et al.*, 2020).

5.2 Future research recommendations

5.2.1 Characterizing interannual variability in basin hydrology

The primary limitation of this study and its findings is that for the majority of data presented, the observation period was limited to the 2019 open water season, and it is difficult to evaluate the representativeness of this temporal perspective on the characterization of the hydrological processes described. For example, some studies have reported that variable SWE_{MAX} between years did not influence the freshet runoff ratio of a subarctic alpine basin (Carey *et al.*, 2013), while other studies in cold climates have drawn attention to the importance of fall antecedent moisture content during freeze up in regulating runoff ratios during the subsequent spring (Metcalfe and Buttle, 2001; Suzuki *et al.*, 2006). Additionally, in 2019, unfortunately few large volume rain events occurred. As a result, a basin response including overland flow, large channel discharge, and other characteristics of major flooding did not occur during the summer months. Observations collected during additional open water seasons would likely capture large magnitude summer rain events, providing an opportunity to sample source waters during these events and interpret changes in storage compartments and streamflow at the outlets already instrumented.

To build upon the findings of this work, additional data collected during future open water seasons are necessary to better constrain the interannual variability in basin inputs, timing of seasonally specific hydrological processes, and overall basin water balance. If additional open water seasons were assessed as an extension of this dissertation, it would also provide opportunity to explore some aspects of the basin hydrology that the methods applied in 2019 were unable to discern. For example, a more complete assessment of source water contributions focused on separating shallow soil water and aquifer discharge from the pre-event waters (Liu *et*

al., 2004; Ala-aho *et al.*, 2018) would greatly enhance the description of when and where in the basin these flow paths were most important to runoff generation. As such, a more long-term study with expanded water sampling design under varying meteorological and hydrological conditions would enhance the foundation for assessment of future changes in basin hydrology as climate change proceeds.

5.2.2 Numerical model development and climate change scenario projections

This project provides valuable ground-truthed data from a shrub tundra mountainous environment – something lacking in many model calibration and verification projects that rely on lowland and coastal datasets. Current hydrological models of alpine basins in larger regional river systems often apply lumped representations of the thermal and physical characteristics controlling their storage capacity and runoff production following precipitation inputs (Walvoord *et al.*, 2012; Ma *et al.*, 2017). Other studies of alpine hydrology are often characterized by study basins within a narrow ecotone between treeline and barren outcrops, atypical of the expansive shrub tundra transition that occupies this ecotone in the Taiga Cordillera and other northern regions.

A natural extension of the findings of this study is to apply the conceptual model and parameter sets developed to allow for more detailed assessment of the basin water balance and quantify future potential hydrological conditions for the study basin given a range of potential climate change scenarios. This type of research has been done in tundra-taiga transitional areas (Endrizzi et al., 2011; Krogh et al., 2017), boreal systems (Quinton et al., 2003; Quinton and Baltzer, 2013), and alpine basins beyond the Taiga Cordillera extent (Landry *et al.*, 2014; Rasouli *et al.*, 2014; Harder *et al.*, 2015; Ménard *et al.*, 2019). While adjusting temperature and precipitation inputs for the basin and gauging its predicted response on the order of 10-100 years would be

revealing, the potential for second-order impacts of climate change (vegetation composition and permafrost distribution) extends the range of uncertainty for these estimates, and may confound predictions based on mass-energy balance alone (Rasouli *et al.*, 2014). As such, future research should populate hydrological models informed by the structure of the conceptual diagram (Figure 2.7) and parameter sets provided, but then adjust the basin coverage of each land cover and/or introduce land covers from lower elevations that may be encroaching in this ecotone. This exercise could be dynamic, based on the thermal balance of the peat plateau features shrinking in extent as vertical and lateral heat transfers thaw the permafrost at depth (Kurylyk *et al.*, 2016), or manual, assigning changing land cover compositions based on the modeller's judgement and assessing the basin-response. Irrespective of this choice, such an effort would provide a stronger basis for estimating the implications of climate change and its influence on land cover composition in alpine shrub tundra systems, as discussed throughout this dissertation.

5.2.3 Land cover classification and water balance estimation of larger basins

One of the key limitations in northern hydrology is the lack of direct observation across the extensive and sparsely populated geography of the North. This dissertation describes and quantifies the hydrology of an alpine shrub tundra basin based on direct observations and measurements, but a natural next step in this line of investigation is to apply these findings to a broader study extent in which similar basin areas are prevalent. The use of high-resolution DEMs and multispectral remote sensing data has tremendous potential to characterize northern basin hydrology and atmospheric exchanges over larger spatial scales than the typical ground-based observational network allows (Dornes *et al.*, 2008; Kerkhoven and Yew Gan, 2008).

As shown in this study, alpine shrub tundra cover classes have specific hydrological characteristics and roles in basin water storage and routing within and from these headwater

systems, and these distinct cover classes can be identified based on their spectral characteristics. A land-cover based transference scheme would require complementing barren land and forested basin hydrology studies be included to represent the portions of these large basins not reflected in this dissertations findings, but collectively, such an effort would allow for a more detailed assessment of hydrological processes occurring and more accurate estimates of terrestrial water balance and/or atmospheric exchange (Masson *et al.*, 2003; Kerkhoven and Yew Gan, 2008; Asong *et al.*, 2020). This approach is preferable to transference schemes at risk of misrepresenting flux and storage processes that take the hydrological observations of lowland systems and apply them to alpine basins after compensating for differences in elevation, slope and relief (Dingman, 1981; Staudinger *et al.*, 2017).

The findings of this dissertation provide the data and model structure necessary for a land cover-based representation of alpine tundra headwater contributions to larger river basins overlapping with the Taiga Cordillera ecozone, including the Yukon and Mackenzie rivers, but these large continental rivers have highly complex land cover and regionally distinct climates. Of note, it would be important in this study to limit the distance between the representative basins where observations are collected and the larger basin area of interest where these findings are applied (Merz and Blöschl, 2004). As such, a more intermediary scale basin would be advisable; for example, the upper portion of the Keele River. Environment Canada has gauged the Keele River just above its confluence with the Twitya River since 1993, which represents a 11,200 km^2 contributing area that includes the study basin described in this dissertation.

5.3 Self-reflections

It is important that researchers are given the opportunity to approach their subject with the same raw sense of wonder that first drew them into their area of study. It is easy to drift from one's personal appreciation for the natural world and focus on the intellectual challenge of cultivating narrowly defined, potent scientific objectives, and the execution of the appropriate methods to achieve them. The data I presented in this dissertation do not include everything I collected during the three consecutive field seasons I spent in the area. There were experimental failures, excess materials, and observations collected as I explored, developed, and finally executed the planned 2019 observation and sample collection regime. Between July 2017 and September 2019, I spent 254 days in the field, and much of that time was spent developing an appreciation for the study basin and the study area independent of the project objectives and quantifications as captured in this dissertation. Some of the knowledge collected does not count among the many gigabytes of drone imagery and .csv files in my data folders, though it undoubtedly helped inform my study design, research objectives, and interpretation of the data. I visited neighbouring streams just to find out if the water tasted different. I dug soil pits just to rub the deeper stones clean and see if they had been gouged with glacial striations. For me, there was meaning in more than the instruments and samples and measurements so important to collect. There was something to be gleaned simply in watching the water and everything around it in flux, right from the first cymbal clashing *whoomph* of snowpack collapse announcing the impending freshet through to the closing curtain of the first snowfall in the autumn. These experiences are not captured in the pages above, but are among the most indelible when it comes to what I will remember many years from now looking back on this endeavour.

I remember the Caribou, heads held high as they wove through the bare willows and birch single file in the early spring (Figure 5.1). Some walks between camp and the study basin we would meet them in small groups, pregnant Matriarchs leading their daughters and an accompaniment of last year's young who survived the winter. They would circle us, curious and trusting, before a snort and upward jolting spring from one would announce the need to move on. Other times, early in the morning where our snowshoe trail crested the final ridge before the stream network, we would find them collected on the wind-swept ice, using the frozen thoroughfare as sure footing en route to their calving grounds.

I remember four owls rising in unison through the fog. I remember a vole surfing down the stream mid-channel. I remember extreme frost heave and freeze-thaw forcing large fissures open that cut through the remaining snowpack and ground below along the edge of a riparian hummock. I remember glassy droplets of water held aloft by the dwarfed limbs of succulents, even on the hottest days, as the rocky current tossed its spray into the shallow mossy shores (Figure 5.2). I remember these moments and so many more, though I remember them best and see the purpose of this dissertation with the greatest clarity as I stand on the shore of the stream after dunking my head and filling my belly and stare across the valley towards the ever-watchful Mt. Fred Andrew (Figure 5.3).

5.4 References

Ala-aho P, Soulsby C, Pokrovsky OS, Kirpotin SN, Karlsson J, Serikova S, Vorobyev SN, Manasypov RM, Loiko S, Tetzlaff D. 2018. Using stable isotopes to assess surface water source dynamics and hydrological connectivity in a high-latitude wetland and permafrost influenced landscape. Journal of Hydrology 556: 279–293 DOI: 10.1016/j.jhydrol.2017.11.024

Asong EZ, Elshamy EM, Princz D, Wheater SH, Pomeroy J, Pietroniro A, Cannon A. 2020. High-resolution meteorological forcing data for hydrological modelling and climate change impact analysis in the Mackenzie River Basin. Earth System Science Data 12 (1): 629–645 DOI: 10.5194/essd-12-629-2020

Beniston M. 2003. Climatic change in mountain regions: A review of possible impacts. Climate Change 59: 5–31 DOI: 10.1007/978-94-015-1252-7_2

Bonnaventure P, Lamoureux SF. 2013. The active layer: a conceptual review of monitoring, modelling techniques and changes in a warming climate. Progress in Physical Geography 37 (3): 352–376 DOI: 10.1177/0309133313478314

Borge AF, Westermann S, Solheim I, Etzelmüller B. 2016. Strong degradation of palsas and peat plateaus in northern Norway during the last 60 years. The Cryosphere Discussions (February): 1–31 DOI: 10.5194/tc-2016-12

Brown D, Jorgenson. MT, Douglas T, Ruess R. 2015. Interactions of fire and climate exacerbate permafrost degradation in Alaskan lowland forests. Journal of Geophysical Research, Biogeosciences 120(8): 1619–1637 DOI: 10.1002/2015JG003033

Carey SK, Woo MK. 2005. Freezing of subarctic hillslopes, Wolf Creek basin, Yukon, Canada. Arctic, Antarctic, and Alpine Research 37 (1): 1–10

Carey SK, Boucher JL, Duarte CM. 2013. Inferring groundwater contributions and pathways to streamflow during snowmelt over multiple years in a discontinuous permafrost subarctic environment (Yukon, Canada). Hydrogeology Journal 21 (1): 67–77 DOI: 10.1007/s10040-012-0920-9

Chasmer L, Mahoney C, Millard K, Nelson K, Peters D, Merchant M, Hopkinson C, Brisco B, Niemann O, Montgomery J, et al. 2020. Remote sensing of boreal wetlands 2: methods for evaluating boreal wetland ecosystem state and drivers of change. Remote Sensing 12 (8): 1–47 DOI: 10.3390/RS12081321

Connon RF, Quinton WL, Craig JR, Hayashi M. 2014. Changing hydrologic connectivity due to permafrost thaw in the lower Liard River valley, NWT, Canada. Hydrological Processes 28 (14): 4163–4178 DOI: 10.1002/hyp.10206

Craig JR, Brown G, Chlumsky R, Jenkinson W, Jost G, Lee K, Mai J, Serrer M, Snowdon AP, Sgro N, et al. 2020. Flexible watershed simulation with the Raven hydrological modelling framework. Environmental Modelling & Software 129 (April): 104728 DOI: 10.1016/j.envsoft.2020.104728

Crites H, Kokelj S V., Lacelle D. 2020. Icings and groundwater conditions in permafrost catchments of northwestern Canada. Scientific Reports 10 (1): 1–11 DOI: 10.1038/s41598-020-60322-w

de Jong C, Whelan F, Messerli B. 2005. Preface: The importance of a hydrological research framework for water balance studies in mountain basins. Hydrological Processes 19 (12): 2323–2328 DOI: 10.1002/hyp.5886

Dingman SL. 1981. Elevation: a major influence on the hydrology of New Hampshire and Vermont, USA. Hydrological Sciences Journal 26 (4): 399–413 DOI: 10.1080/02626668109490904

Dornes PF, Tolson BA, Davison B, Pietroniro A, Pomeroy JW, Marsh P. 2008. Regionalisation of land surface hydrological model parameters in subarctic and arctic environments. Physics and Chemistry of the Earth 33 (17–18): 1081–1089 DOI: 10.1016/j.pce.2008.07.007

Duk-Rodkin A, Barendregt RW. 2011. Stratigraphical record of glacials/interglacials in northwest Canada. In Developments in Quaternary Science, Vol. 15, Ehlers J, Gibbard P, Hughes P (eds).Amsterdam; 661–698.

Granger RJ. 1998. Partitioning of energy during the snow-free season at the Wolf Creek Research Basin. In Wolf Creek Research Basin: Hydrology, Ecology, Environment, Pomeroy W, Granger R (eds.). National Water Research Institute, Saskatoon, SK; 3–44.

Gruber S, Hoelzle M. 2001. Statistical modelling of mountain permafrost distribution: local calibration and incorporation of remotely sensed data. Permafrost and Periglacial Processes 12: 69–77 DOI: 10.1002/ppp

Harder P, Pomeroy JW, Westbrook CJ. 2015. Hydrological resilience of a Canadian Rockies headwaters basin subject to changing climate, extreme weather, and forest management. Hydrological Processes 29 (18): 3905–3924 DOI: 10.1002/hyp.10596

Hayashi M. 2020. Alpine hydrogeology: the critical role of groundwater in sourcing the headwaters of the world. Groundwater 58 (4): 498–510 DOI: 10.1111/gwat.12965

Hood JL, Hayashi M. 2015. Characterization of snowmelt flux and groundwater storage in an alpine headwater basin. Journal of Hydrology 521: 482–497 DOI: 10.1016/j.jhydrol.2014.12.041

Jacques JMS, Sauchyn DJ. 2009. Increasing winter baseflow and mean annual streamflow from possible permafrost thawing in the Northwest Territories, Canada. Geophysical Research Letters 36 (1): 1–6 DOI: 10.1029/2008GL035822

Kerkhoven E, Yew Gan T. 2008. Development of a hydrologic scheme for use in land surface models and its application to climate change in the Athabasca River Basin. In Cold Region Atmospheric and Hydrologic Studies. The Mackenzie GEWEX Experience: Volume 2: Hydrologic Processes, Woo MK (ed.). Springer: New York, New York, US.

Krogh SA, Pomeroy JW, Marsh P. 2017. Diagnosis of the hydrology of a small Arctic basin at the tundra-taiga transition using a physically based hydrological model. Journal of Hydrology 550: 685–703 DOI: 10.1016/j.jhydrol.2017.05.042

Kurylyk BL, Hayashi M, Quinton WL, McKenzie JM, Voss CI. 2016. Influence of vertical and lateral heat transfer on permafrost thaw, peatland landscape transition, and groundwater flow. Water Resources Research 52 (2): 1286–1305 DOI: 10.1002/2015WR018057

Lamontagne-Hallé P, McKenzie JM, Kurylyk BL, Zipper SC. 2018. Changing groundwater discharge dynamics in permafrost regions. Environmental Research Letters 13 (8) DOI: 10.1088/1748-9326/aad404

Landry C, Buck K, Raleigh M, Clark M. 2014. Mountain system monitoring at Senator Beck basin, San Juan Mountains, Colorado: A new integrative data source to develop and evaluate models of snow and hydrologic processes. Water Resources Research 50: 1773–1788 DOI: 10.1002/2013WR013711.Received

Laudon H, Spence C, Buttle J, Carey SK, McDonnell JJ, McNamara JP, Soulsby C, Tetzlaff D. 2017. Save northern high-latitude catchments. Nature Geoscience 10 (5): 324–325 DOI: 10.1038/ngeo2947

Liu F, Williams MW, Caine N. 2004. Source waters and flow paths in an alpine catchment, Colorado Front Range, United States. Water Resources Research 40 (9): 1–16 DOI: 10.1029/2004WR003076

Luoto M, Seppälä M. 2003. Thermokarst ponds as indicators of the former distribution of palsas in Finnish Lapland. Permafrost and Periglacial Processes 14 (1): 19–27 DOI: 10.1002/ppp.441

Ma R, Sun Z, Hu Y, Chang Q, Wang S, Xing W, Ge M. 2017. Hydrological connectivity from glaciers to rivers in the Qinghai-Tibet plateau: roles of suprapermafrost and subpermafrost groundwater. Hydrology and Earth System Sciences 21 (9): 4803–4823 DOI: 10.5194/hess-21-4803-2017

Mahdianpari M, Salehi B, Mohammadimanesh F, Brisco B, Homayouni S, Gill E, DeLancey ER, Bourgeau-Chavez L. 2020. Big data for a big country: the first generation of Canadian wetland inventory map at a spatial resolution of 10-m using Sentinel-1 and Sentinel-2 data on the Google Earth Engine cloud computing platform. Canadian Journal of Remote Sensing 46 (1): 15–33 DOI: 10.1080/07038992.2019.1711366

Mamet SD, Chun KP, Kershaw GGL, Loranty MM, Kershaw GP. 2017. Recent increases in permafrost thaw rates and areal loss of palsas in the western Northwest Territories, Canada. Permafrost and Periglacial Processes 28 (4): 619–633 DOI: 10.1002/ppp.1951

Marsh CB, Pomeroy JW, Wheater HS. 2020. The Canadian Hydrological Model (CHM): A multi-scale, multi-extent, variable-complexity hydrological model - design and overview. Geoscientific Model Development Discussions 13 (2002): 225–247 DOI: 10.5194/gmd-2019-109

Masson V, Champeaux JL, Chauvin F, Meriguet C, Lacaze R. 2003. A global database of land surface parameters at 1-km resolution in meteorological and climate models. Journal of Climate 16 (9): 1261–1282 DOI: 10.1175/1520-0442-16.9.1261

Matsuoka N. 2006. Monitoring periglacial processes: towards construction of a global network. Geomorphology 80 (1–2): 20–31 DOI: 10.1016/j.geomorph.2005.09.005

Ménard CB, Essery R, Barr A, Bartlett P, Derry J, Dumont M, Fierz C, Kim H, Kontu A, Lejeune Y, et al. 2019. Meteorological and evaluation datasets for snow modelling at 10 reference sites: description of in situ and bias-corrected reanalysis data. Earth System Science Data 11 (2): 865–880 DOI: 10.5194/essd-11-865-2019

Merz R, Blöschl G. 2004. Regionalisation of catchment model parameters. Journal of Hydrology 287 (1–4): 95–123 DOI: 10.1016/j.jhydrol.2003.09.028

Metcalfe RA, Buttle JM. 2001. Soil partitioning and surface store controls on spring runoff from a boreal forest peatland basin in north-central Manitoba, Canada. Hydrological Processes 15 (12): 2305–2324 DOI: 10.1002/hyp.262

Muller SW. 1947. Permafrost or Permanently Frozen Ground and Related Engineering Problems. Military Intelligence Division Office, Chief of Engineers, U.S. Army.

Payette S, Delwaide A, Caccianiga M, Beauchemin M. 2004. Accelerated thawing of subarctic peatland permafrost over the last 50 years. Geophysical Research Letters 31: L18208

Pepin N, Bradley RS, Diaz HF, Baraer M, Caceres EB, Forsythe N, Fowler H, Greenwood G, Hashmi MZ, Liu XD, et al. 2015. Elevation-dependent warming in mountain regions of the world. Nature Climate Change 5 (5): 424–430 DOI: 10.1038/nclimate2563

Pomeroy JW, Gray DM, Brown T, Hedstrom NR, Quinton WL, Granger RJ, Carey SK. 2007. The Cold Regions Hydrological Model: a platform for basing process representation and model structure on physical evidence. Hydrological Processes 21: 2650–2667 DOI: 10.1002/hyp

Quinton WL, Hayashi M, Chasmer LE. 2011. Permafrost-thaw-induced land-cover change in the Canadian subarctic: implications for water resources. Hydrological Processes 25 (1): 152–158 DOI: 10.1002/hyp.7894

Rasouli K, Pomeroy JW, Janowicz JR, Carey SK, Williams TJ. 2014. Hydrological sensitivity of a northern mountain basin to climate change. Hydrological Processes 28 (14): 4191–4208 DOI: 10.1002/hyp.10244

Rees A, English M, Derksen C, Toose P, Silis A. 2014. Observations of late winter Canadian tundra snow cover properties. Hydrological Processes 28 (12): 3962–3977 DOI: 10.1002/hyp.9931

Rennermalm A, Wood E, Troy T. 2010. Observed changes in pan-arctic cold-season minimum monthly river discharge. Climate Dynamics 35: 923–939 DOI: http://dx.doi.org.libproxy.wlu.ca/10.1007/s00382-009-0730-5

Rogger M, Chirico G, Hausmann H, Krainer K, Bruckl E, Stadler P, Bloschl G. 2017. Impact of mountain permafrost on flow path and runoff response in a high alpine catchment. Water Resources Research 53: 1288–1308 DOI: 10.1002/2016WR019341.Received

Stadnyk TA, Déry SJ. 2021. Canadian continental-scale hydrology under a changing climate: a review. Water 13 (7): 1–14 DOI: 10.3390/w13070906

Staudinger M, Stoelzle M, Seeger S, Seibert J, Weiler M, Stahl K. 2017. Catchment water storage variation with elevation. Hydrological Processes 31 (11): 2000–2015 DOI: 10.1002/hyp.11158

Suzuki K, Kubota J, Ohata T, Vuglinsky V. 2006. Influence of snow ablation and frozen ground on spring runoff generation in the Mogot Experimental Watershed, southern mountainous taiga of eastern Siberia. Nordic Hydrology 37 (1): 21–29 DOI: 10.1557/jmr.2006.0001

Viviroli D, Wehren B, Weingartner R, Scha B. 2010. General characteristics of alpine waters. In Alpine Waters, Bundi U (ed.). Springer: Berlin; 17-58. DOI: 10.1007/978-3-540-88275-6

Walvoord MA, Kurylyk BL. 2016. Hydrologic impacts of thawing permafrost — a review. Vadose Zone Journal 15 (6) DOI: 10.2136/vzj2016.01.0010

Walvoord MA, Voss CI, Wellman TP. 2012. Influence of permafrost distribution on groundwater flow in the context of climate-driven permafrost thaw: example from Yukon

Flats basin, Alaska, United States. Water Resources Research 48 (7): 1–17 DOI: 10.1029/2011WR011595

Wang Q, Fan X, Wang M. 2016. Evidence of high-elevation amplification versus Arctic amplification. Scientific Reports 6 (November 2015): 1–8 DOI: 10.1038/srep19219

Woo MK. 1986. Permafrost hydrology in North America. Atmosphere - Ocean 24 (3): 201–234 DOI: 10.1080/07055900.1986.9649248

Woo MK, Rouse W, Stewart R, Stone J. 2008. The Mackenzie GEWEX study: a contribution to cold region atmospheric and hydrologic sciences. In Cold Region Atmospheric and Hydrologic Studies. The Mackenzie GEWEX Experience: Volume 1: Atmospheric Dynamics, Woo MK (ed.). Springer: New York; 507.

Woo MK. 2012. Permafrost Hydrology. Springer: New York. DOI: 10.1007/978-3-642-23462-0

Woo MK, Thorne R. 2003. Streamflow in the Mackenzie basin, Canada. Arctic 56 (4): 328–340 DOI: 10.14430/arctic630

5.5 Figures

Figure 5-1: A herd of *Rangifer tarandus* (Caribou) crossing a glaciofluvial feature within the study basin.

Figure 5-2: A *Sedum roseum* with fresh water droplets cradled among the petals.

Figure 5-3: Mount Fred Andrew – the cirque headwaters of the neighbouring basin.

6. Appendices

Appendix 1: Worldview 2 spectral signatures

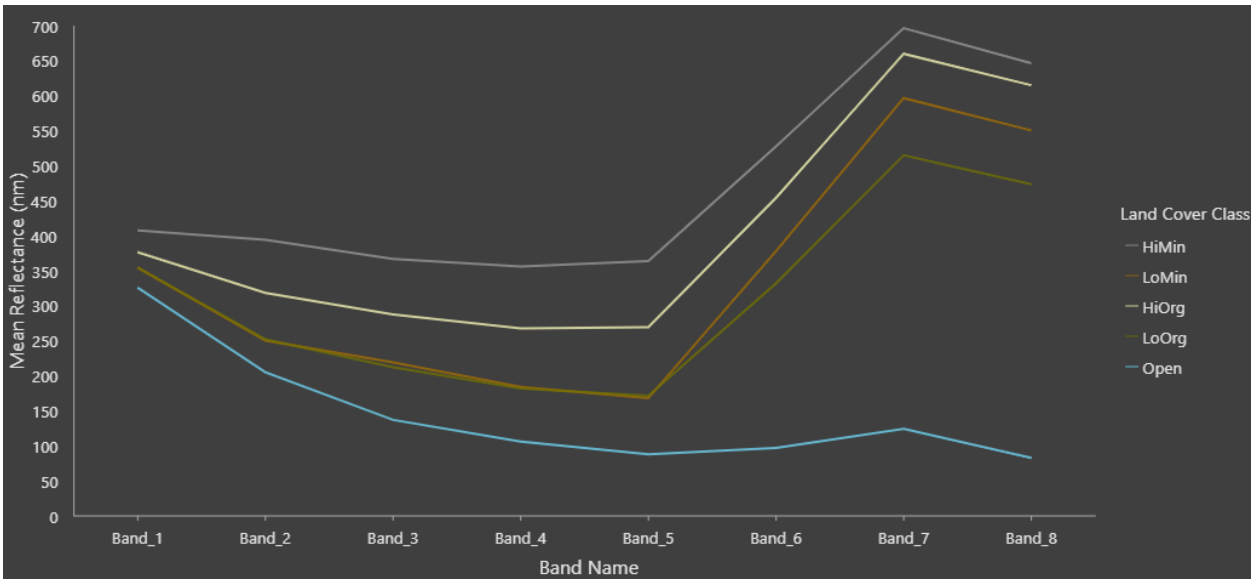

Figure 6-1: Spectral reflectance signatures used in land cover classification scheme. Values derived from Worldview 2 8-band pixels within assigned training areas for each cover class (Figure 2.1;3.1)

Appendix 2: Electrical resistivity tomography (ERT) inversion reports

EarthImager 2D (Advanced Geosciences Inc., Austin, TX, USA) was used to process measured, apparent, and inverted resistivity images for each electrical resistivity tomography (ERT) transect completed. To reduce RMS, ≤ 5 iterations of data misfit removal were performed, removing <5 % of data points with each iteration and maintaining >300 data grid points. Below are all inverted resistivity panes created during the inversion process, including frost probe and borehole locations. A relative model sensitivity pane is also included for each, with green to blue contour colour transition set at the 0.1 threshold (see below).

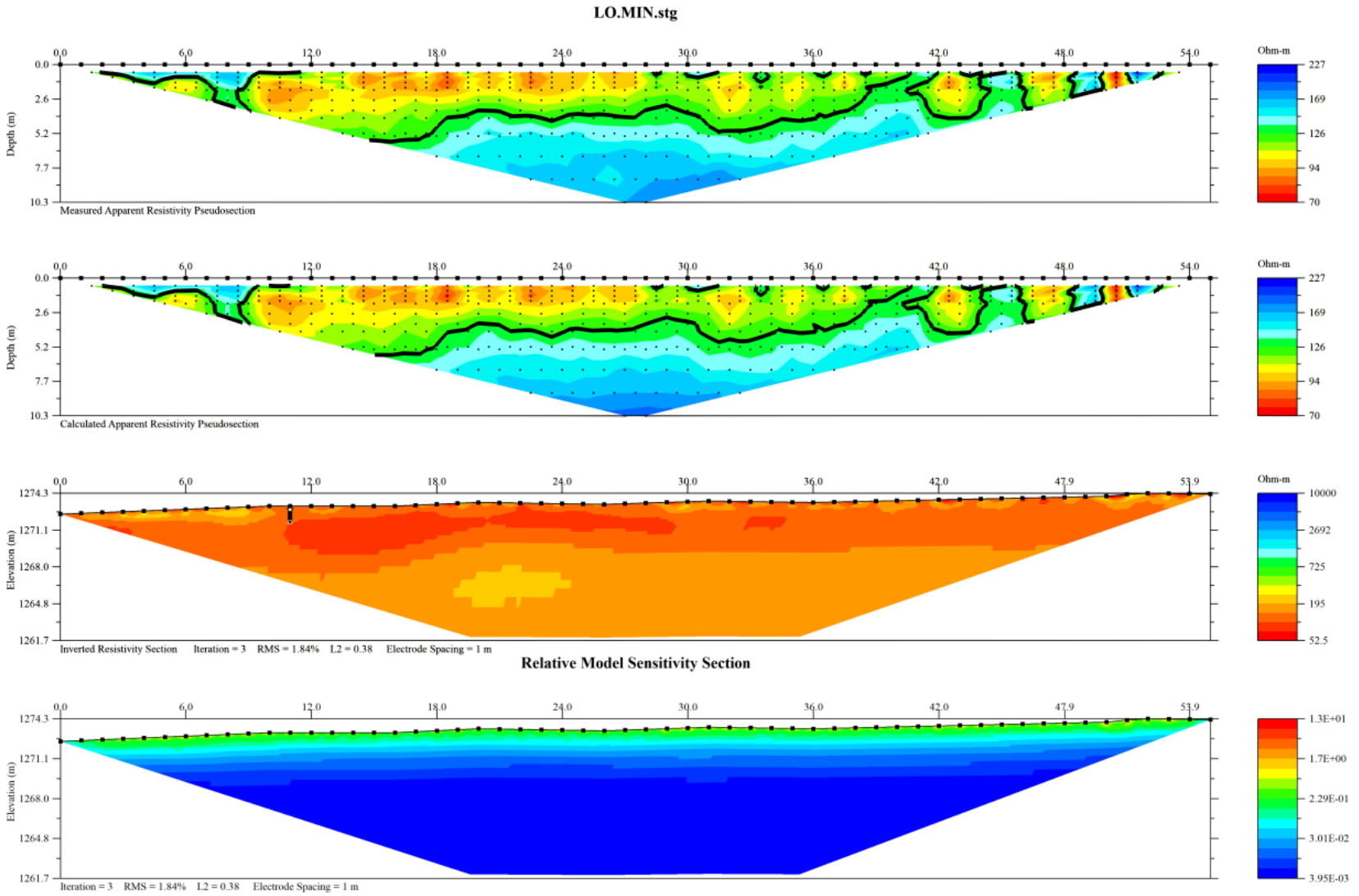

Figure 6-2: Riparian swamp ERT resistivity report

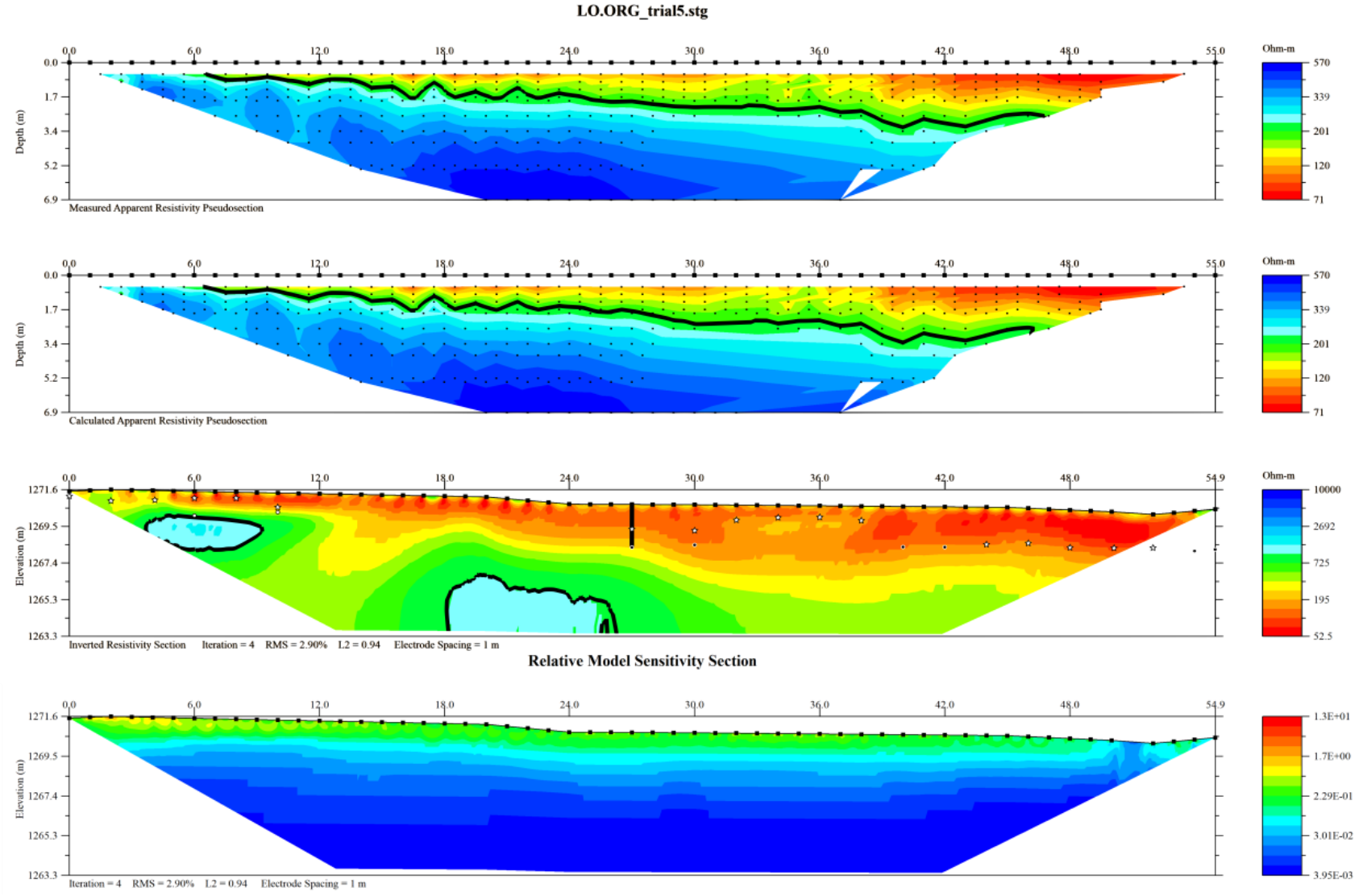

Figure 6-3: Fen ERT resistivity report

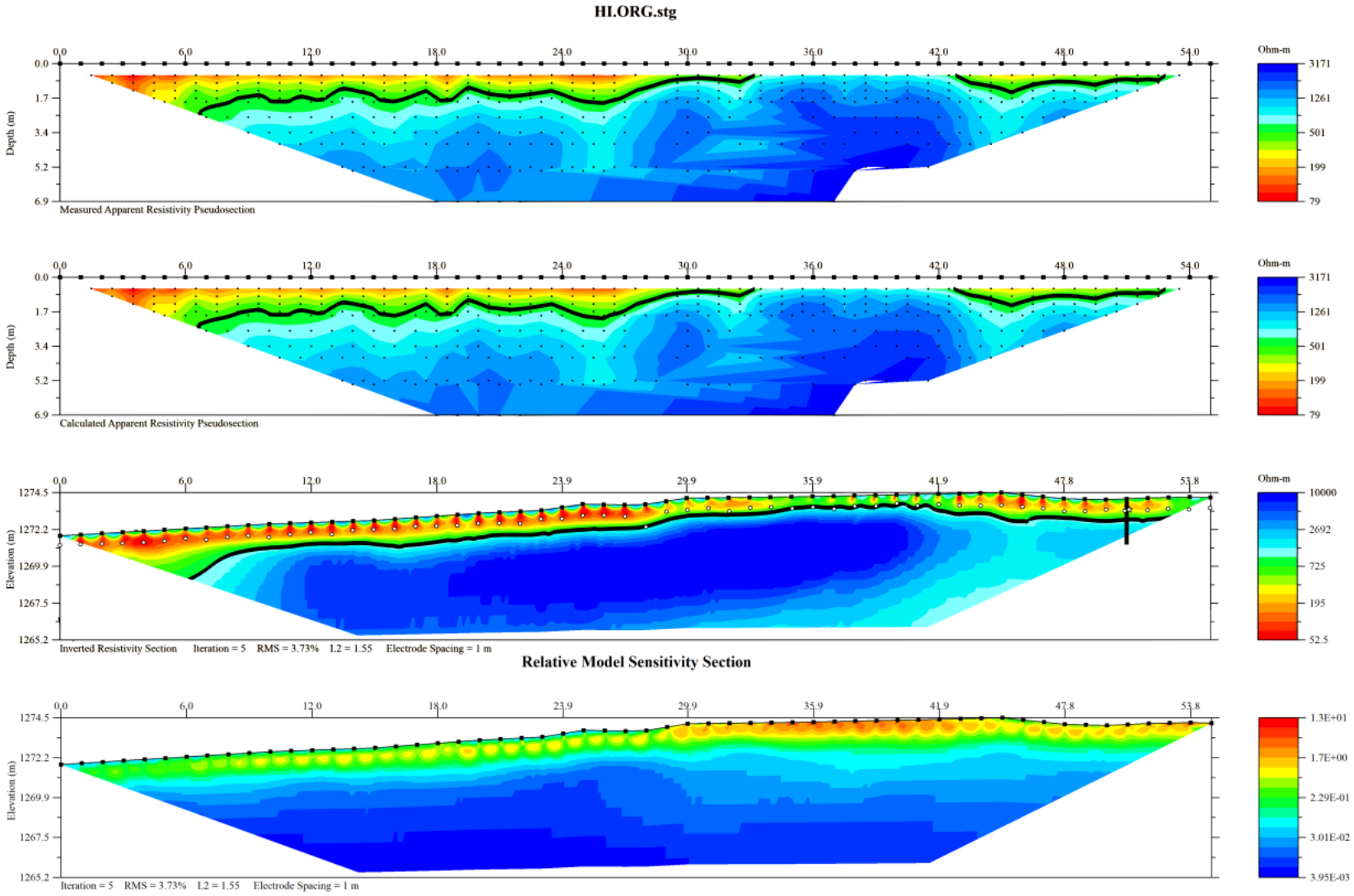

Figure 6-4: Peat plateau ERT resistivity report

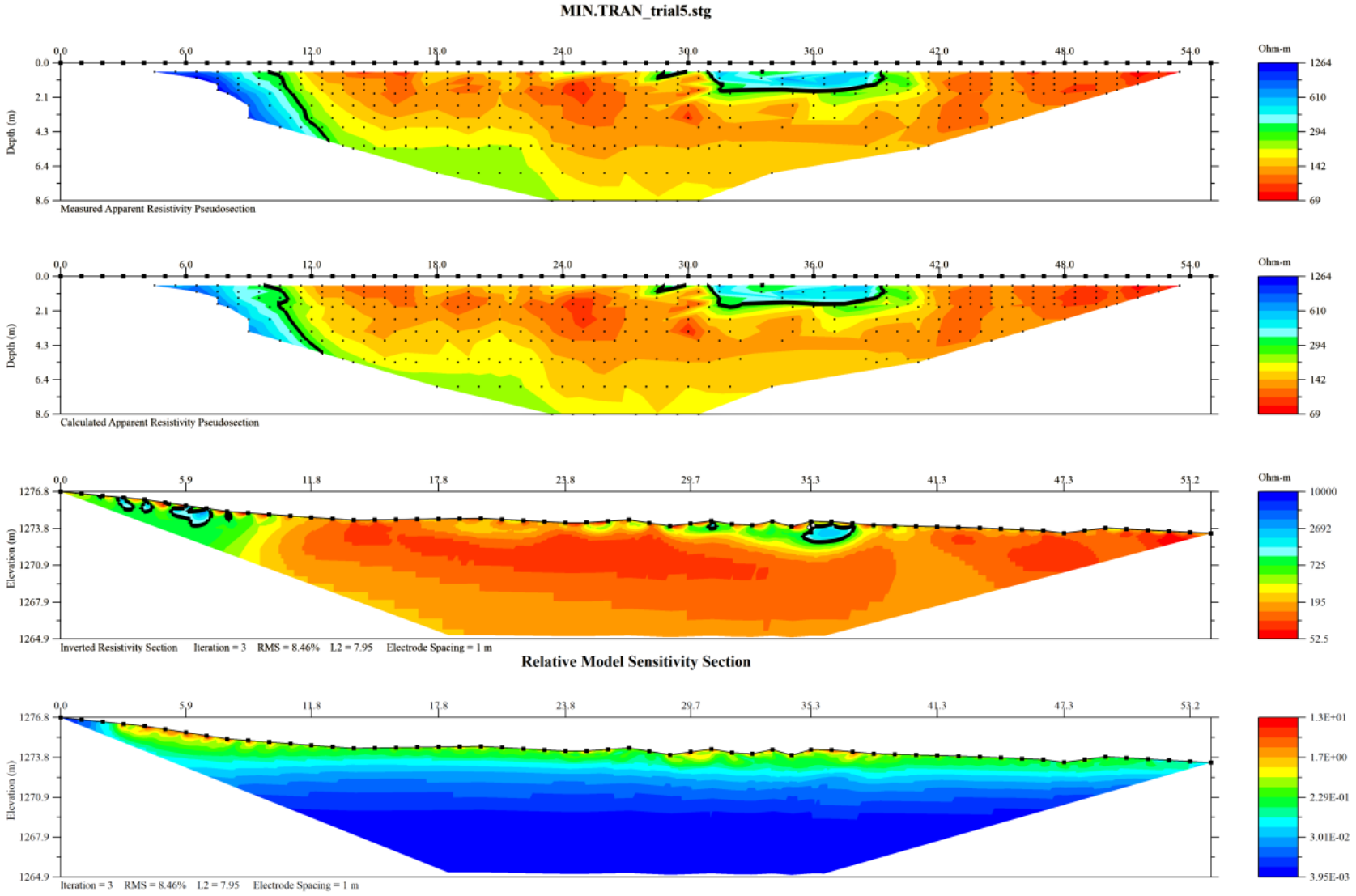

Figure 6-5: Riparian swamp (10 – 54 m) close to a glaciofluvial upland feature (0 – 10 m) ERT resistivity report

Appendix 3: Saturated hydraulic conductivity test results

Saturated hydraulic conductivities (K_{SAT}) reported are the result of five different methods of K_{SAT} estimation: well displacement, grain size distribution, falling head flexible wall permeameter, constant head solid wall permeameter, and constant head split cell permeameter. Final values reported represent the geometric mean of all tests applied to samples from a given cover class of a given soil type (Table 6.2). Details on specific test procedures and test results are as follows.

Bulk K_{SAT} was estimated based on displacement tests used a large slug volume of water and observations of water table response logged at 1s with ±1-2 cm accuracy using U20 and/or U20L HOBO water level recorders (Onset Computer Corp, Bourne, MA, USA). The water table response time series was limited to the portion of the record not reflecting the double straight line draw down effect (Bouwer, 1989). Data on water table response and well dimensions were managed with the computer program AQTESOLV version 4.5 (HydroSOLVE Inc., Reston, VA, USA).

Mineral soils excavated for laboratory analysis commonly had grain sizes up to 75mm in diameter, requiring 20 kg of sample to be processed to assure representativeness of each sample (Gee and Or, 2002). Given that mineral samples could not be extracted and transported intact, these samples where pre-sifted in the field when possible and only subsamples with <12mm diameter were returned to the lab for testing. Manual separation was completed on >500 g subsamples from each location with 4 - 63 µm sieving trays following >24hr oven drying at 105 °C. When silt/clay bonding to larger grains occurred and D10 values were anticipated to be < 40 µm, grain size distributions required the hydrometer technique following sample dispersion with Calgon solution to assess smaller fraction percentages. Specifically, samples with a greater fraction of sand and larger grains (Glaciofluvial upland 1-8) were analyzed with mechanical

sieve separation methods as the D10 values were greater than 40 µm. Samples with a greater clay-silt fraction (Glaciofluvial upland 9, Riparian 1-5) required a 10 % Calgon solution to disperse fine particles and hydrometer analysis to estimate D10 values <40 µm. A range of K_{SAT} estimates is possible with particle size distribution data and empirical fitting functions related to mass proportions (Russell, G., 2005; ASTM, 2007). The Barr equation (Barr, 2001) was applied for estimates of K_{SAT} based on D10 diameters. This was considered reasonable given the only assumption required for this equation is laminar flow conditions and the K_{SAT} estimates generated were similar to the geometric mean of the other ~14 equations considered for each sample analysis (data not shown).

Additionally, K_{SAT} of 7 mineral samples were assessed in laboratory with soil permeameters. For samples with D10 <40 µm, a constant head test was conducted according to AASHTO T 215-14 Method A (AASHTO, 2014) using a permeameter with an 11.3 cm inner diameter and 12.5 cm manometer spacing. When the D10 of a sample was composed of particles >40 µm in diameter, K_{SAT} was estimated with a falling head test using a permeameter with 5.09 cm inner diameter and sample heights between 5.46 – 5.81 cm (ASTM International, 2016).

For organic substrates, K_{SAT} was estimated using a constant head permeameter test (Nagare *et al.*, 2013). Organic soil monoliths were extracted on site with minimal disruption of the soil structure and transported to the laboratory in cellophane wrapped packages in coolers. In the lab, monoliths were frozen before segmentation into 5 cm^3 squares from within the top 10 cm of the soil surface.

Table 6-1: Bulk saturated hydraulic conductivity (Bulk K_{SAT}) test results from slug tests conducted on in situ stilling wells located within the training area of each land cover (Figure 2.1). K_{SAT} values based on the empirical Bouwer & Rice equation (Bouwer, 1989). Testing depth relates the bottom of each test volume below the ground surface.

Land Cover	Testing Depth (cm)	K_{SAT} (m/day)
Glaciofluvial Upland	119.2	0.006
Peat Plateau	114.9	0.311
Peat Plateau	117	0.045
Riparian Swamp	98	0.025
Riparian Swamp	72.1	0.070
Fen	104.5	0.250
Fen	84.7	0.016

Table 6-2: Strata specific saturated hydraulic conductivity test results (Mineral K_{SAT} and Organic K_{SAT}). 'GSA' denotes estimates for mineral samples based on grain size analysis and the empirical Barr equation (Barr, 2001). 'Falling H' denotes falling head flexible wall permeameter estimates for mineral samples with D10 <40 µm (ASTM International, 2016). 'Constant H' denotes constant head solid wall permeameter estimates for mineral samples with D10 >40 µm (AASHTO, 2014). 'Split C' denotes constant head split-container estimates for organic samples (Nagare et al., 2013). Depth relates the top and bottom of each test volume below the ground surface. One standard deviation from the mean (SD) reported for tests with ≥24 runs.

Sample #	Test Type	Cover Class	Soil Type	K_{SAT} m/day	Test Runs	Depth cm	
1	GSA	Glaciofluvial Upland	Mineral	0.130	3	5	50
1	Constant H	Glaciofluvial Upland	Mineral	4.204	1	6.5	27
2	GSA	Glaciofluvial Upland	Mineral	0.518	3	5	50
2	Constant H	Glaciofluvial Upland	Mineral	2.915	1	12	26
3	GSA	Glaciofluvial Upland	Mineral	25.2	1	15	29
4	GSA	Glaciofluvial Upland	Mineral	31.0	1	15	30
5	GSA	Glaciofluvial Upland	Mineral	425.3	1	7	27
6	GSA	Glaciofluvial Upland	Mineral	40.6	1	7	32
7	GSA	Glaciofluvial Upland	Mineral	35.2	1	20	38
8	GSA	Glaciofluvial Upland	Mineral	594.4	1	16	32
9	GSA	Glaciofluvial Upland	Mineral	0.042	1	0	24
10	Split C	Peat Plateau	Organic	268.8±24.3	36	2	7
10	Split C	Peat Plateau	Organic	302.4±44.4	37	2	7
10	Split C	Peat Plateau	Organic	248.3±52.2	45	2	7
11	Split C	Peat Plateau	Organic	12.4±1.7	36	3	8
12	Split C	Peat Plateau	Organic	546.6±63.8	36	3	8
13	GSA	Riparian Swamp	Mineral	1.6E-04	1	15	33
13	Falling H	Riparian Swamp	Mineral	0.119	1	15	33
13	Split C	Riparian Swamp	Organic	57.9±7.1	36	3	8
14	GSA	Riparian Swamp	Mineral	0.002	1	28	54
14	Falling H	Riparian Swamp	Mineral	0.069	1	28	54
14	Split C	Riparian Swamp	Organic	85.9±6.1	36	2	7

15	GSA	Riparian Swamp	Mineral	0.001	1	21	35
15	Falling H	Riparian Swamp	Mineral	0.108	1	21	35
15	Split C	Riparian Swamp	Organic	1358.4±63.7	36	2	7
16	GSA	Riparian Swamp	Mineral	4.3E-04	1	22	54
16	Falling H	Riparian Swamp	Mineral	0.081	1	22	54
16	Split C	Riparian Swamp	Organic	1512.6±145.8	24	2	7
17	GSA	Riparian Swamp	Mineral	2.9E-04	1	25	45
17	Falling H	Riparian Swamp	Mineral	0.044	1	25	45
17	Split C	Riparian Swamp	Organic	11.3±1.3	36	3.5	8.5
18	Split C	Riparian Swamp	Organic	90.7±14.3	36	2	7
19	Split C	Fen	Organic	24.3±29.4	36	2	7
20	Split C	Fen	Organic	102.3±5.2	36	2	7

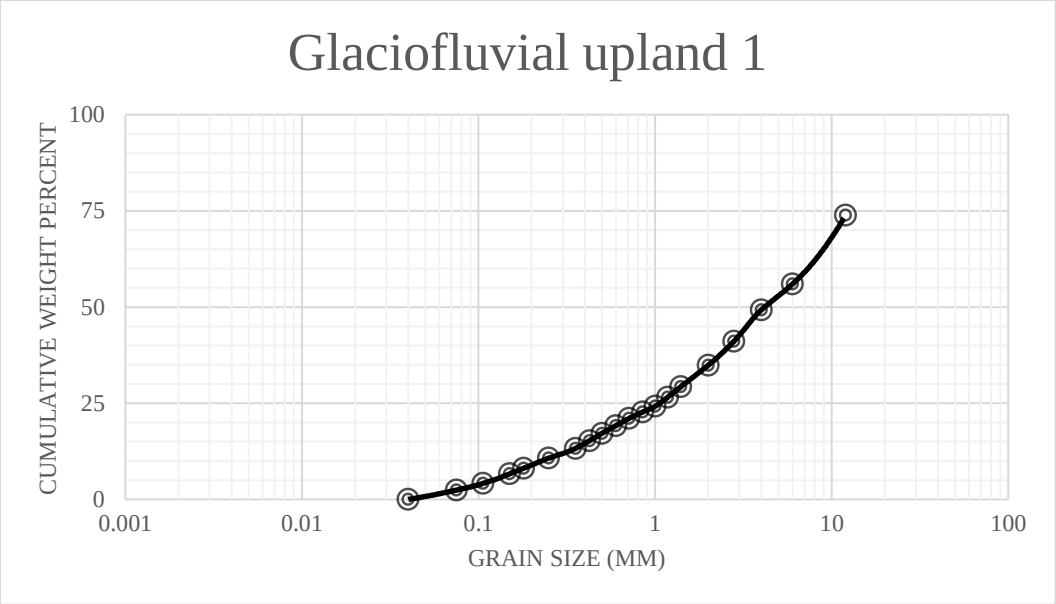

Figure 6-6: Glaciofluvial upland sample 1 GSA results

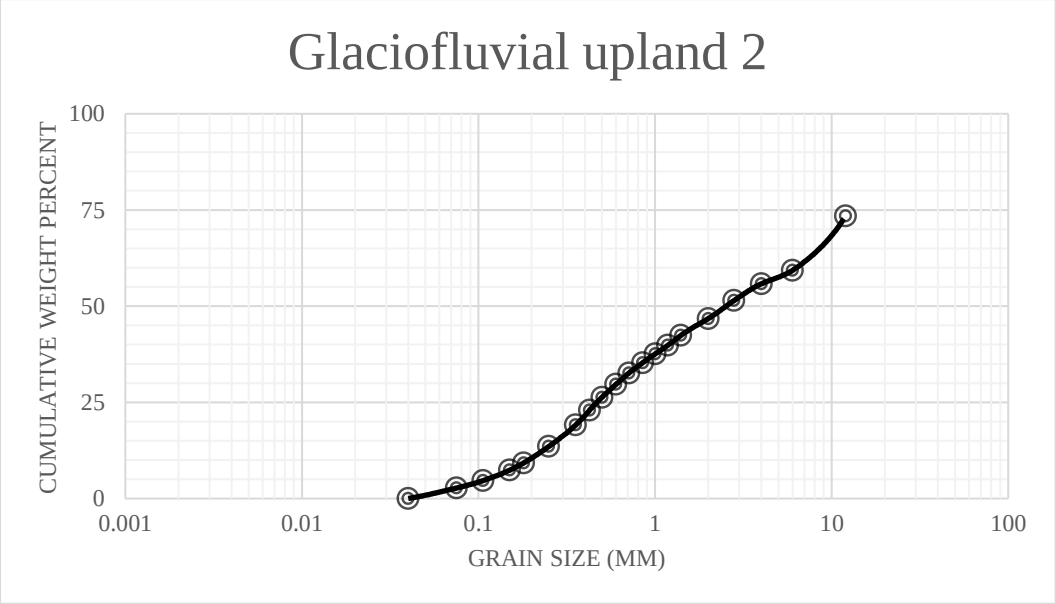

Figure 6-7: Glaciofluvial upland sample 2GSA results

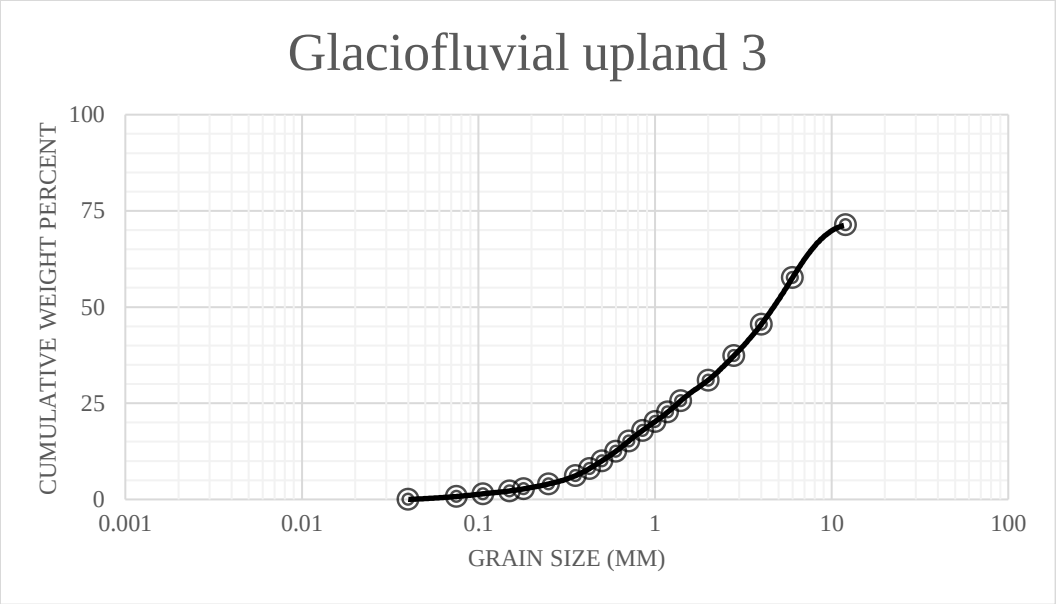

Figure 6-8: Glaciofluvial upland sample 3 GSA results

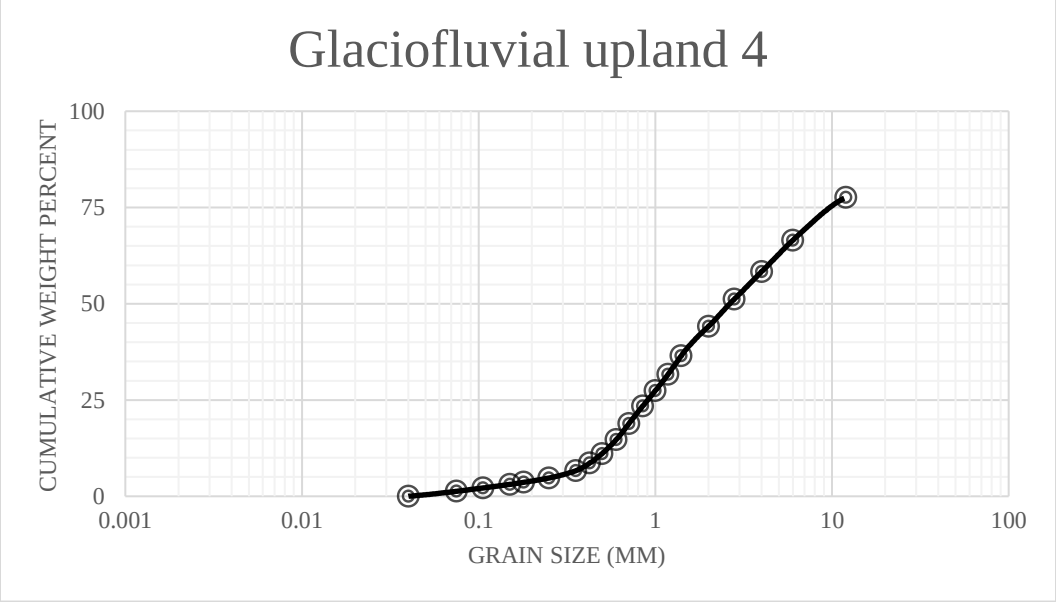

Figure 6-9: Glaciofluvial upland sample 4 GSA results

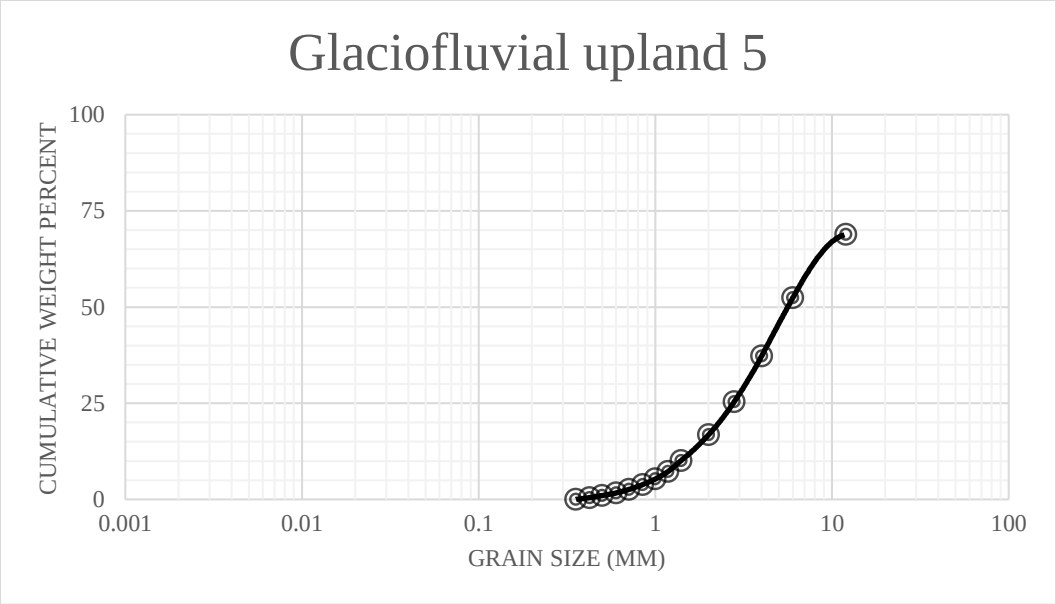

Figure 6-10: Glaciofluvial upland sample 5 GSA results

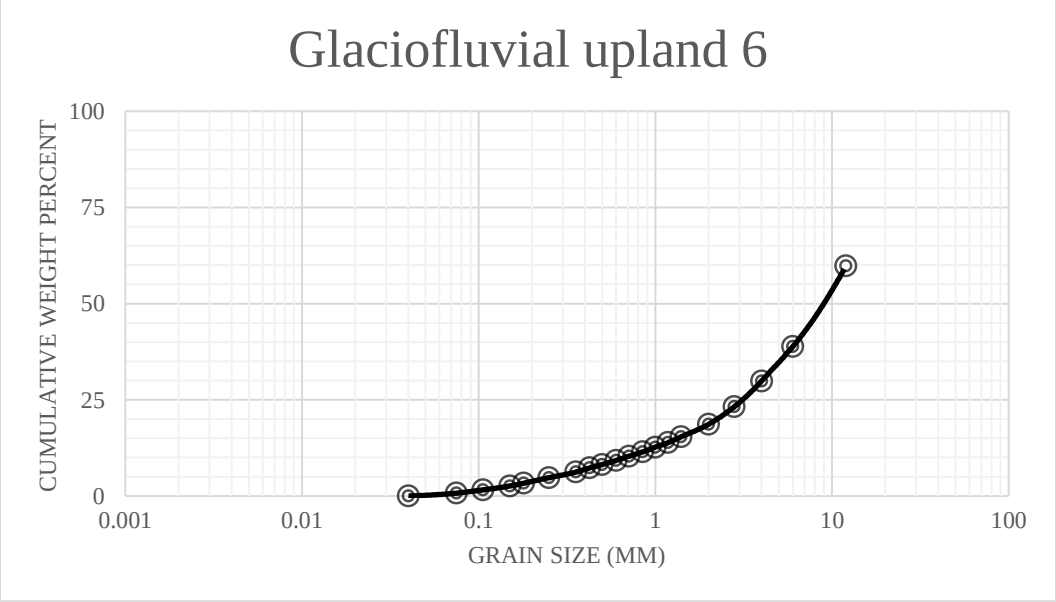

Figure 6-11: Glaciofluvial upland sample 6 GSA results

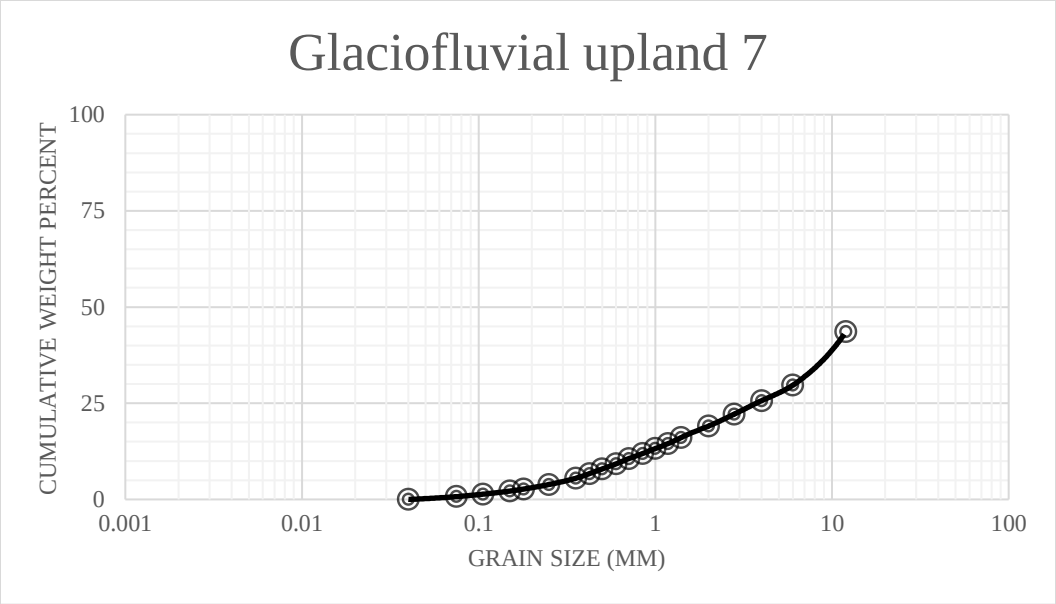

Figure 6-12: Glaciofluvial upland sample 7 GSA results

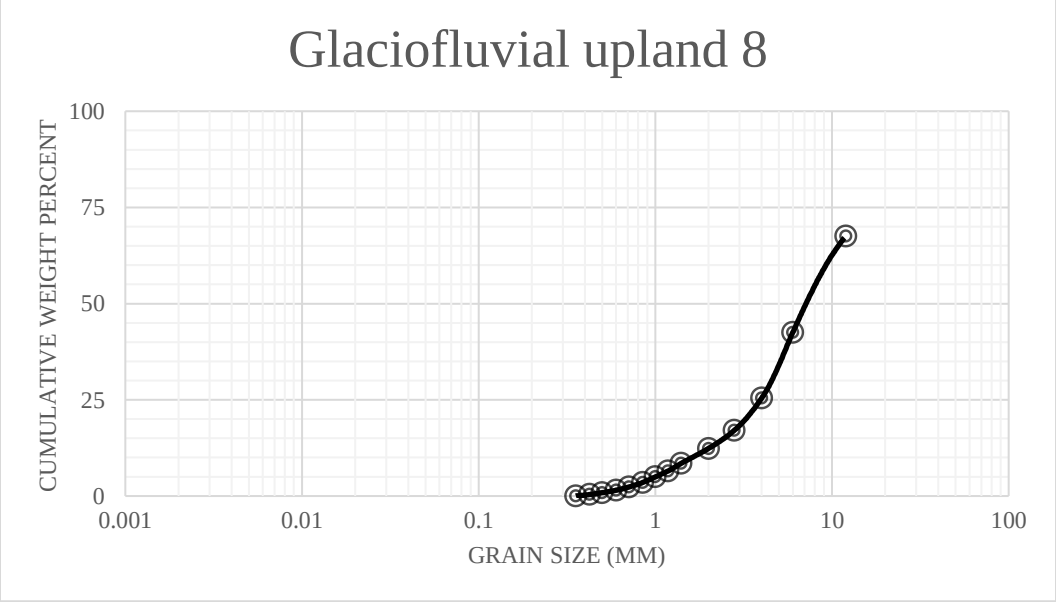

Figure 6-13: Glaciofluvial upland sample 8 GSA results

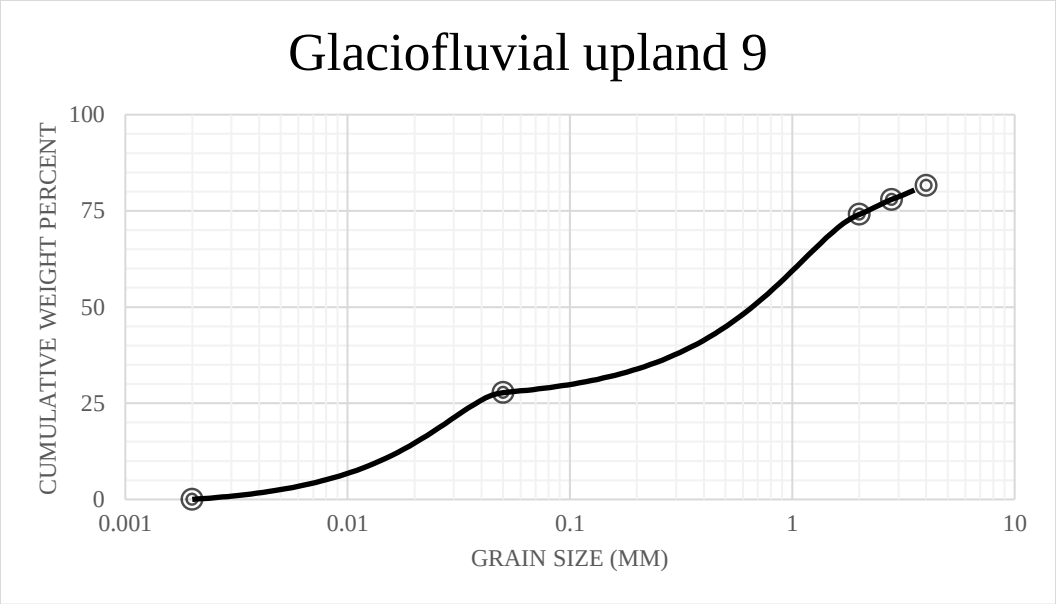

Figure 6-14: Glaciofluvial upland sample 9 GSA results

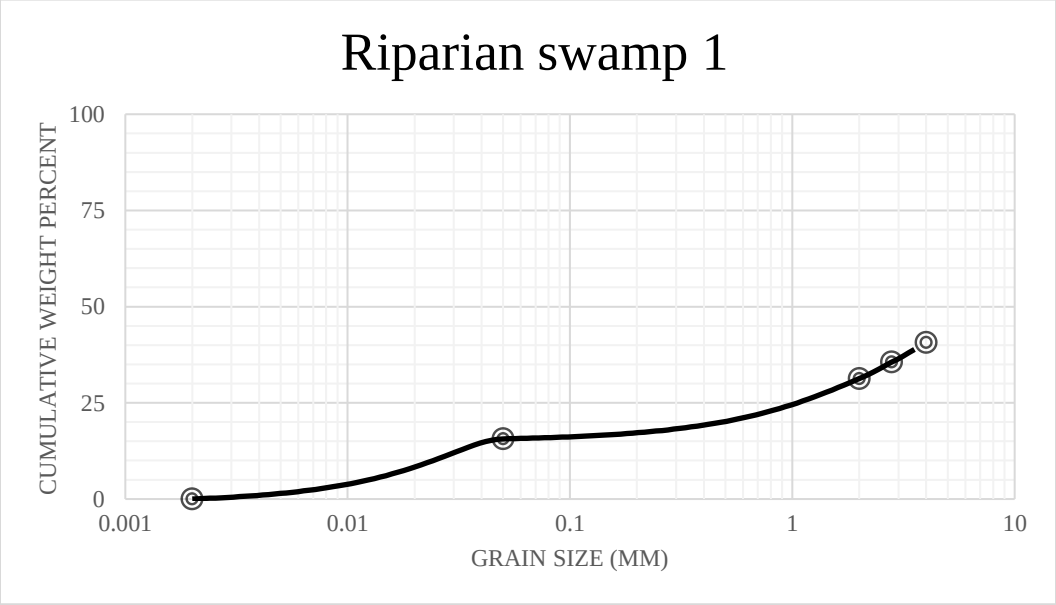

Figure 6-15: Riparian swamp sample 1 GSA results

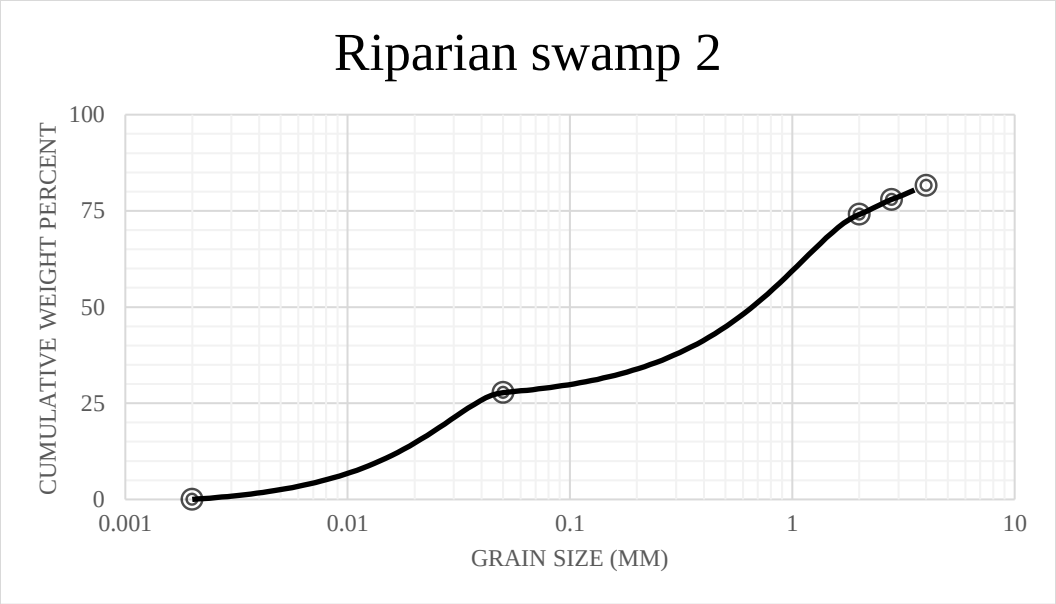

Figure 6-16: Riparian swamp sample 2 GSA results

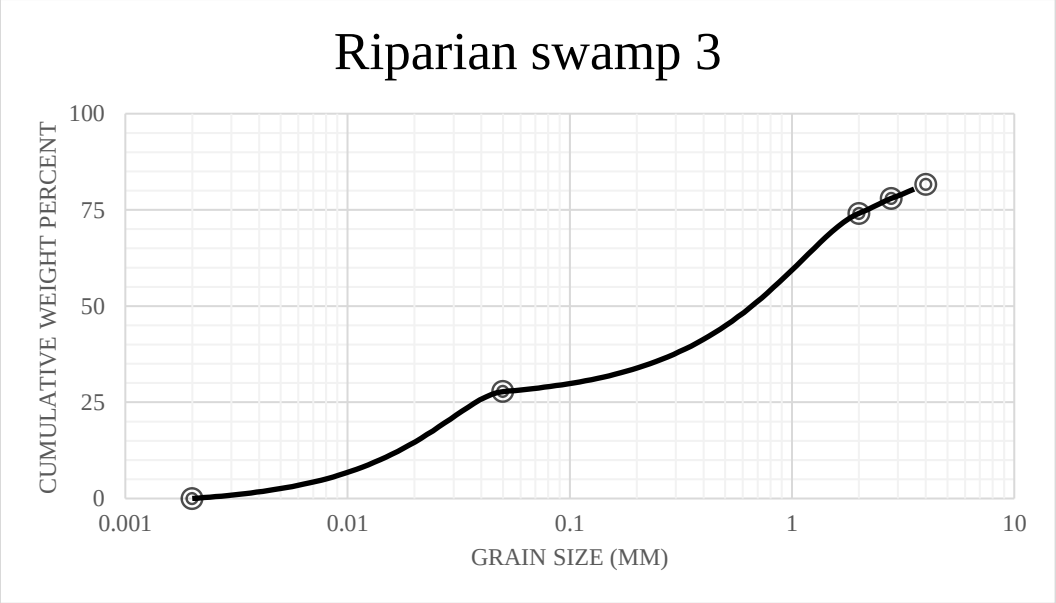

Figure 6-17: Riparian swamp sample 3 GSA results

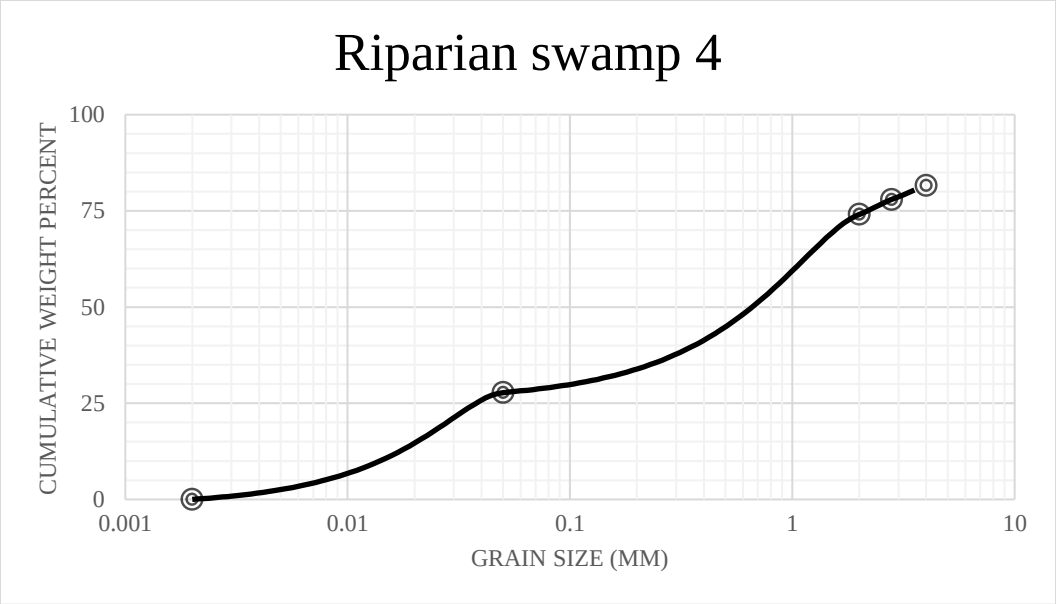

Figure 6-18: Riparian swamp sample 4 GSA results

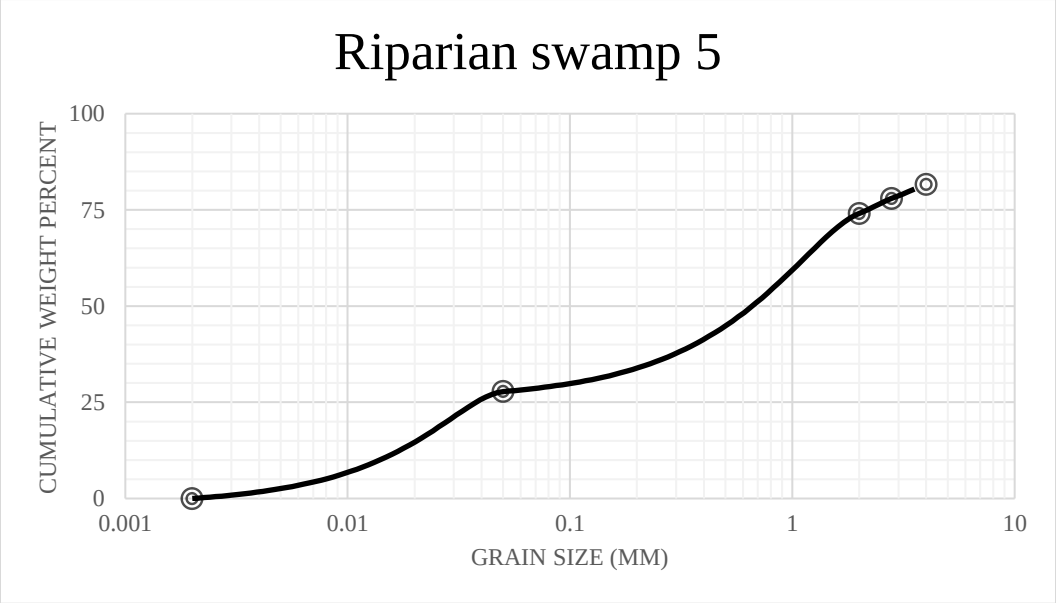

Figure 6-19: Riparian swamp sample 5 GSA results

Appendix 4: Water balance uncertainties

Table 6-3: Reported accuracies (Acc) for each sensor and/or measurement technique applied in calculation of the basin water balance

Component	Measurement	Unit	Acc	Sensor	Company	Comments
Precipitation	rain	mm	0.2	tipping bucket rain gauge	EML, North Shields, UK	
	snow depth	cm	1	snow depth frame		
	snow covered area	m^2	0.01 - 0.3	Phantom 4 Drone	DJI Technology Co, Shenzhen, CHN	FC6310 rgb camera (5472 x 3648 resolution)
	snow density	kg m^{-3}	7 - 38	7 cm diameter SWE coring tube	SnowHydro, Fairbanks, US	
GW_{IN}, GW_{OUT}, Streamflow	channel water depth	cm	0.5-1	U20 HOBO pressure transducer	Onset Computer Corp, Bourne, MA, US	
	channel water discharge	m^3 s^{-1}	5 %	Orion EC probe	Thermo Fisher Scientific Inc., Waltham, US	accuracy based on technique (Moore et al. 2005) as manual only reports measurement range (10 µS/cm to 200 mS/cm)
	channel network maximum wetted area	m^2	0.02	Phantom 4 Drone	DJI Technology Co, Shenzhen, CHN	FC6310 rgb camera (5472 x 3648 resolution)
	vertical hydraulic gradient	cm	1			Gradient is dimensionless, but the height and length measurements required were both accurate to 1 cm
Evapotranspiration	evaporation pan	mm	1			
	soil lysimeter	mm	0.1			accuracy based on 5 g threshold to weight scale adjusted to lysimeter area
	net radiation	J m^{-2} day^{-1}	10 %	CNR4 net radiometer	Kipp and Zonen, Delft, NL	

	water temperature	°C	0.44	U20 HOBO	Onset Computer Corp, Bourne, MA, US	
	air temperature	°C	0.2	HC-S3	Campbell Scientific, Logan, US	
Change in Storage	water table depth	cm	0.5-1	U20 HOBO	Onset Computer Corp, Bourne, MA, US	
	volumetric moisture content	%	3	5TM	Decagon Devices, Pullman, WA, USA	Used for estimate of θ_{fc} and VMC continuous record
	volumetric moisture content	%	3	CS655	Campbell Scientific, Logan, UT, USA	
	frost table depth	cm	1			
	Saturated VMC (θ_s)					

4.1 Precipitation (***P***)

4.1.1 Rain

Due to the limited size and narrow elevational range of the study basin, it is reasonable to assume rain was evenly distributed across the basin area. Therefore, confidence in estimates of rain inputs are limited by the 0.2 mm accuracy and tendency of tipping bucket rain collection to underestimate total rain received due to missing trace events (Adam and Lettenmaier, 2003).

Manual rain gauge measurements collected every ~6 days confirm no significant difference in rain received ~3 m from the meteorological station (129.84°W 63.29°N, 1273.7 masl) (4.0 ± 3.4) and ~350 m north-west of the study basin boundary at base camp (129.82°W 63.30°N, 1268.0 masl) (3.7 ± 304) ($t = 0.31$, $p = 0.756$, $df = 28$).

Table 6-4: Manual rain gauge comparison record

Timestamp	Interval (Days)	Rain (mm)		Comments
		Base Camp	Basin	
2019-05-09 10:00	0.0	0	0	
2019-05-20 13:30	11.1	2	1	
2019-05-29 13:30	9.0	1.5	1	
2019-06-04 14:00	6.0	7	8	
2019-06-10 14:00	6.0	10	11.5	
2019-06-12 14:00	2.0	4.5	3	last entry before summer break.
2019-07-07 12:00	0.0	0	0	first entry after summer break
2019-07-12 10:30	4.9	1	3	
2019-07-17 12:30	5.1	6	6	
2019-07-22 11:30	5.0	1	1	
2019-07-25 17:00	3.2	4	4	
2019-08-02 17:00	8.0	8.5	9.5	
2019-08-07 10:30	4.7	0.5	1	
2019-08-11 11:00	4.0	1.5	2	
2019-08-12 13:30	1.1	1	1	
2019-08-16 9:00	3.8	3	3	
2019-08-31 14:00	15.2	4	6	

4.1.2 Snow water equivalent and snowmelt

Measurements of change in snow covered area (ΔA) were collected with drone surveys (Table 6-5). Measurements of change in snowpack depth (ΔD) were collected at 11 snow depth frames randomly spaced along each snow transect. Frames consisted of wooden and/or PVC stakes anchored in the substrate with sufficient length to suspend 1.25 cm doweling crossarms ~10 cm above the SWE_{MAX} snowpack surface (Figure 6-20;6-21). Prior to and during the freshet, repeat measurements of snowpack depth were collected at three subsampling points spaced 15 cm apart and 15 cm from each stake (3.3.2.1). Frames were installed facing south and perpendicular to the prevailing winds to minimize the influence of shadowing and wind redistribution at the repeat observation points. Snow depth frames could not be installed in the Open cover class due to our inability to anchor wooden stakes in the solid ice below the snowpack. Instead, changes in snow depth above open water were measured relative to the reference datum of the snowpack base. The disturbance caused by penetrating the snowpack was mitigated by moving repeat sampling points ~5-10 cm west whenever evidence of preferential melt and/or wind scour around penetration points became obvious.

The ρ_s assigned in SWE_{MELT} was static, though it is known to vary on a daily and seasonal basis as melt progresses. This approach was considered reasonable as the ρ_s assigned (410 kg m^{-3}) was within the range of values reported by other studies documenting snowmelt (Anderson, 1976; Pomeroy and Gray, 1995; McCartney *et al.*, 2006) and resulted in total snowmelt volumes (3.4.1) similar to the SWE_{MAX} measurements collected before melt commenced (2.4.3.1).

Table 6-5: Snow covered area (ΔA) metadata for each orthomosaic of the 0.51 km^2 target area assessed from 7 - 30 May, 2019

Date	Pixel size (m)	Average ground sampling distance (m)	Positional accuracy (m)	Photo count
07-May	0.02	0.02	0.27	1910
10-May	0.02	0.02	0.11	1927
13-May	0.02	0.02	0.09	1977
16-May	0.02	0.02	0.12	1631
20-May	0.02	0.02	0.12	1716
24-May	0.02	0.02	0.12	1785
30-May	0.02	0.02	0.14	1829

Figure 6-20: Photograph of snow depth frames along the fen survey transect during SWE_{MAX} conditions. Stakes are perpendicular and doweling crossarms are parallel to the snowpack surface.

Figure 6-21: Photograph of snow depth frames along the glaciofluvial survey transect during SWE_{MELT} conditions. Stakes are perpendicular and doweling crossarms are parallel to the snowpack surface.

4.2 Evapotranspiration (***ET***)

The lysimeter created a barrier between the soils within and without. As such, there is a tendency for accelerated drying of the soil within as 1) the vessel can cause preferential warming at the soil volume edges, and 2) moisture content from deeper and/or neighbouring soils cannot redistribute across the barrier. When this became an issue, re-wetting was done to bring the VMC of the lysimeter volume back within the range of the surrounding environment. This VMC comparison was done after each weighing using Hydrosense 2 measurements collected once within the lysimeter and three times within the surrounding terrain.

Evaporation pan depths were maintained within 5 cm of the vessel lip and volumetric soil moisture contents (VMC) of lysimeters were maintained within 10 % of values observed in the surrounding soils using a Campbell Scientific Hydrosense 2 probe (Logan, UT, USA) inserted to 10cm depth (data not shown). Additionally, water temperatures inside and outside the pans were checked with each measurement to assure preferential warming did not occur (Figure 6-22).

Figure 6-22: Comparison of evaporation pan water temperatures inside and outside of submerged pans. Linear regressions for Beaver Pond (y = 0.98*x + 0.16 R2 = 0.98, DF=56), Duck Bridge (y = 0.99*x + 0.2 R2 = 0.99, DF= 61), and Lower Pond (y = 0.89*x + 1.32 R2 = 0.97, DF= 62) report minimal deviation of pan temperatures from channel temperatures.

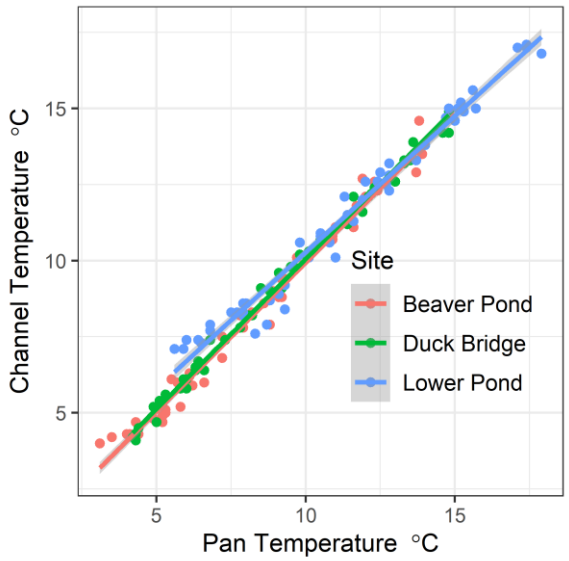

Table 6-6: Priestley–Taylor α values derived from ET calculations (Eq. 3.3). Superscripts denote significant differences between group means (alpha = 0.05).

Basin	Subbasin	Glaciofluvial Upland	Riparian swamp	Peat Plateau	Fen	Open Water
1.04 ± 0.55	0.99 ± 0.57	0.85 ± 0.43^{A}	0.94 ± 0.55^{A}	1.18 ± 0.74^{B}	0.94 ± 0.49^{A}	1.98 ± 1.31^{C}

4.3 Change in Storage ($\Delta \boldsymbol{S}$)

Intact peat blocks were extracted from the top 25 cm of the soil profile in 2018 and returned to the lab for estimation of saturated VMC as part of constant head split cell permeameter testing (Nagare *et al.*, 2013). Mineral samples were extracted from the top 50 cm of the soil profile in 2019 and returned to the lab for estimate of saturated VMC as part of falling head flexible wall permeameter (riparian swamp) and constant head solid wall permeameter (glaciofluvial upland) testing conducted by GHD laboratories (Waterloo, Canada). An additional 15 smaller peat blocks (125 cm^3) were also extracted in 2019, but saturated volumes could not be maintained during testing procedures (data not shown).

Daily θ_{sy} depended on gravimetric laboratory tests of θ_s , field observations of θ_{fc} and continuous records of VMC in the field. Furthermore, the VMC readings were collected from two different sensors (Decagon 5TM and Campbell Scientific CS655), each with calibrations that should result in ± 3 % accuracy.

Table 6-7: Laboratory assessment of peat block and mineral sample saturated volumetric moisture content.

Sample	Cover Class	Soil Type	Volume cm^3	Saturated mass g	Dry bulk density g/cm^3	Saturated VMC
1	**Riparian swamp**	**Mineral**	111	176.7	1.05	0.59
2	**Riparian swamp**	**Mineral**	111	196.8	1.28	0.42
3	**Riparian swamp**	**Mineral**	118	240.6	1.60	0.26
4	**Riparian swamp**	**Mineral**	118	239.3	1.63	0.25
5	**Riparian swamp**	**Mineral**	117	237	1.67	0.24
6	**Glaciofluvial Upland**	**Mineral**	1151	2105.1	1.77	0.35
7	**Glaciofluvial Upland**	**Mineral**	1263	2203.1	1.72	0.38
8	**Peat Plateau**	**Organic**	2294	2241.2	0.07	0.91
9	**Peat Plateau**	**Organic**	7250	6912.4	0.17	0.78
10	**Peat Plateau**	**Organic**	7940	7329.3	0.20	0.73
11	**Peat Plateau**	**Organic**	6890	7047.2	0.21	0.81

4.4 Streamflow ($\boldsymbol{Q}$)

Point observations of discharge were based on salt dilution tests using electrical conductivity (EC) values temperature corrected and calibrated to the unique salt slug and channel water EC observed prior to each test. Slug volumes were sufficient for total dissolution of salt and peak EC values during testing were 5 to 10 times greater than background levels. As such, assumptions required for sodium dilution slug tests as described by Moore (2005) were satisfied, allowing for ± 5 % accuracy for discrete observations of streamflow.

Continuous records of change in stage were collected with U20 pressure transducers measuring and recording water level at 30-minute intervals with ± 1.5-3 cm accuracy (Onset Computer Corp, Bourne, MA, US). Each water level recorder was installed in a stilling well with depth and location selected such that the sensor was submerged, hydrological connection to the channel was maintained, and wave action was minimal. Water levels were converted from pressure (kPa) to cm depth (cm) with a synchronous U20 record of atmospheric pressure installed in a dry stilling well ~20 cm below ground surface and ~ 8 m from the meteorological station. Ideally, a greater number of individual discharge measurements ($n \geq 30$) would have been collected to calibrate the stage discharge rating curves.

4.4.1 Rating curves when local discharge and central stage observations available.

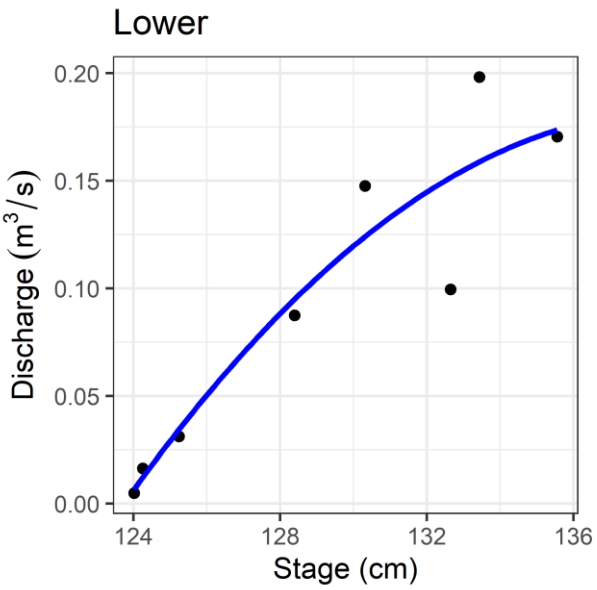

Figure 6-23: Stage-discharge rating curve for the basin outlet record between 9 and 17 May, 2019. The fitting function selected was a second order polynomial with adjusted R-square 0.82 and p-value <0.01.

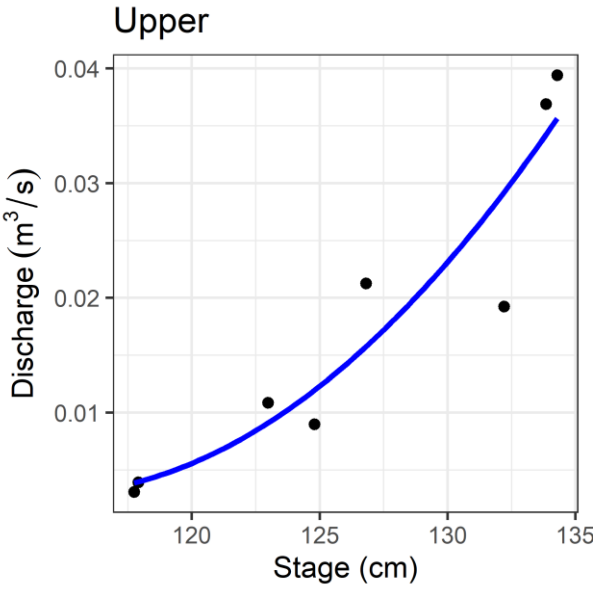

Figure 6-24: Stage-discharge rating curve for the headwater subbasin outlet between 4 April and 27 May, 2019. The fitting function selected was a second order polynomial with adjusted R-square 0.83 and p-value <0.03.

4.4.2 Rating curves when both local discharge and local stage observations available.

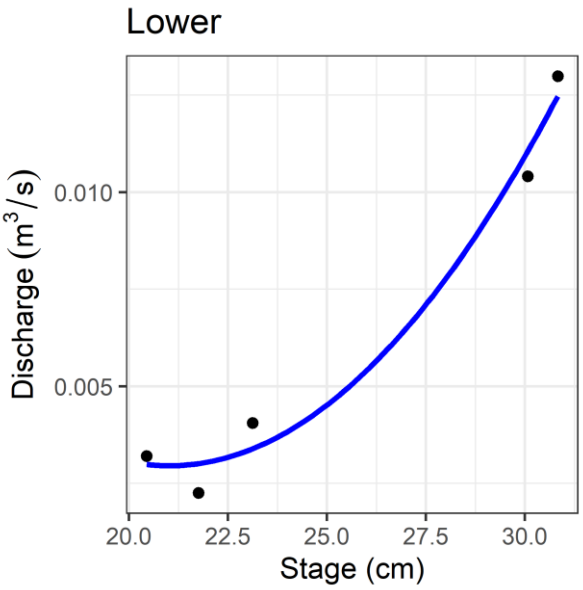

Figure 6-25: Stage-discharge rating curve for the basin outlet record between 05 June and 10 September, 2019. The fitting function selected was a second order polynomial with adjusted R-square 0.96 and p-value <0.02.

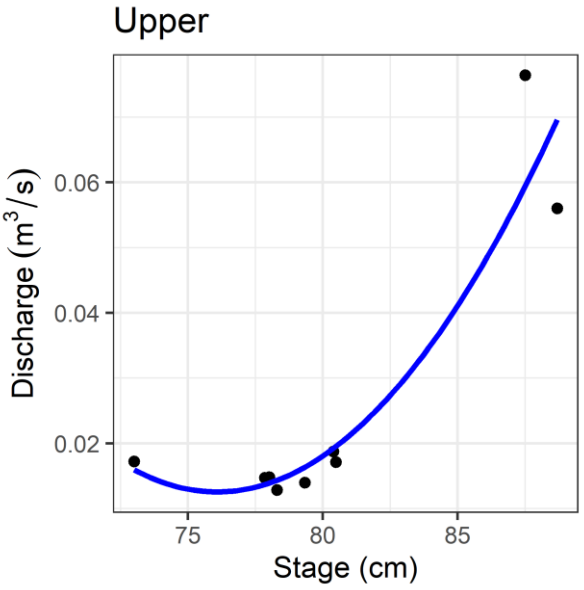

Figure 6-26: Stage-discharge rating curve for the headwater subbasin outlet record between 27 May and 10 September, 2019. The fitting function selected was a second order polynomial with adjusted R-square 0.84 and p-value <0.01.

4.5 Groundwater Discharge (GW_{IN}) and Recharge (GW_{OUT})

Estimates of spring contributions (GW_{IN}) within the headwater subbasin and channel bed infiltration (GW_{OUT}) between the headwater subbasin and basin outlets were based on comparison of daily outlet records that met the conditions described in 3.3.2.5. This resulted in seasonal means based on 9, 3, and 8 days from the freshet, early summer, and late summer periods, respectively. Of note, the freshet observations reported were collected before the melt began.

Table 6-8: Comparison of headwater subbasin and basin outlet discharge records used in estimation of Groundwater Discharge (GW_{IN}) and Recharge (GW_{OUT}).

Date	Season	Discharge ($m^3 s^{-1}$)		Groundwater Exchange	
		Headwater Subbasin	Basin	GWIN	GWOUT
2019-04-28	Freshet	0.00388	NA	0.00388	NA
2019-04-29	Freshet	0.00389	NA	0.00389	NA
2019-04-30	Freshet	0.00392	NA	0.00392	NA
2019-05-01	Freshet	0.00385	NA	0.00385	NA
2019-05-02	Freshet	0.00381	NA	0.00381	NA
2019-05-03	Freshet	0.00377	NA	0.00377	NA
2019-05-04	Freshet	0.00375	NA	0.00375	NA
2019-05-05	Freshet	0.00372	NA	0.00372	NA
2019-05-06	Freshet	0.00382	NA	0.00382	NA
2019-06-05	Early Summer	0.01519	0.00612	0.01519	-0.009067
2019-06-24	Early Summer	0.0214	0.00401	0.0214	-0.017396
2019-06-29	Early Summer	0.01508	0.00346	0.01508	-0.011617
2019-07-10	Late Summer	0.01501	0.00365	0.01501	-0.01136
2019-08-05	Late Summer	0.015	0.00339	0.015	-0.01161
2019-08-20	Late Summer	0.01879	0.00308	0.01879	-0.015709
2019-08-21	Late Summer	0.01824	0.00315	0.01824	-0.015088
2019-08-22	Late Summer	0.01798	0.00302	0.01798	-0.014963
2019-08-23	Late Summer	0.01775	0.00298	0.01775	-0.014774
2019-08-29	Late Summer	0.01737	0.00301	0.01737	-0.014363
2019-08-30	Late Summer	0.018	0.00324	0.018	-0.01476
2019-09-07	Late Summer	0.02028	0.00307	0.02028	-0.017212
2019-09-08	Late Summer	0.02079	0.003	0.02079	-0.017796
2019-09-09	Late Summer	0.02071	0.00298	0.02071	-0.017732

Appendix 5: Additional Stable Isotope Information

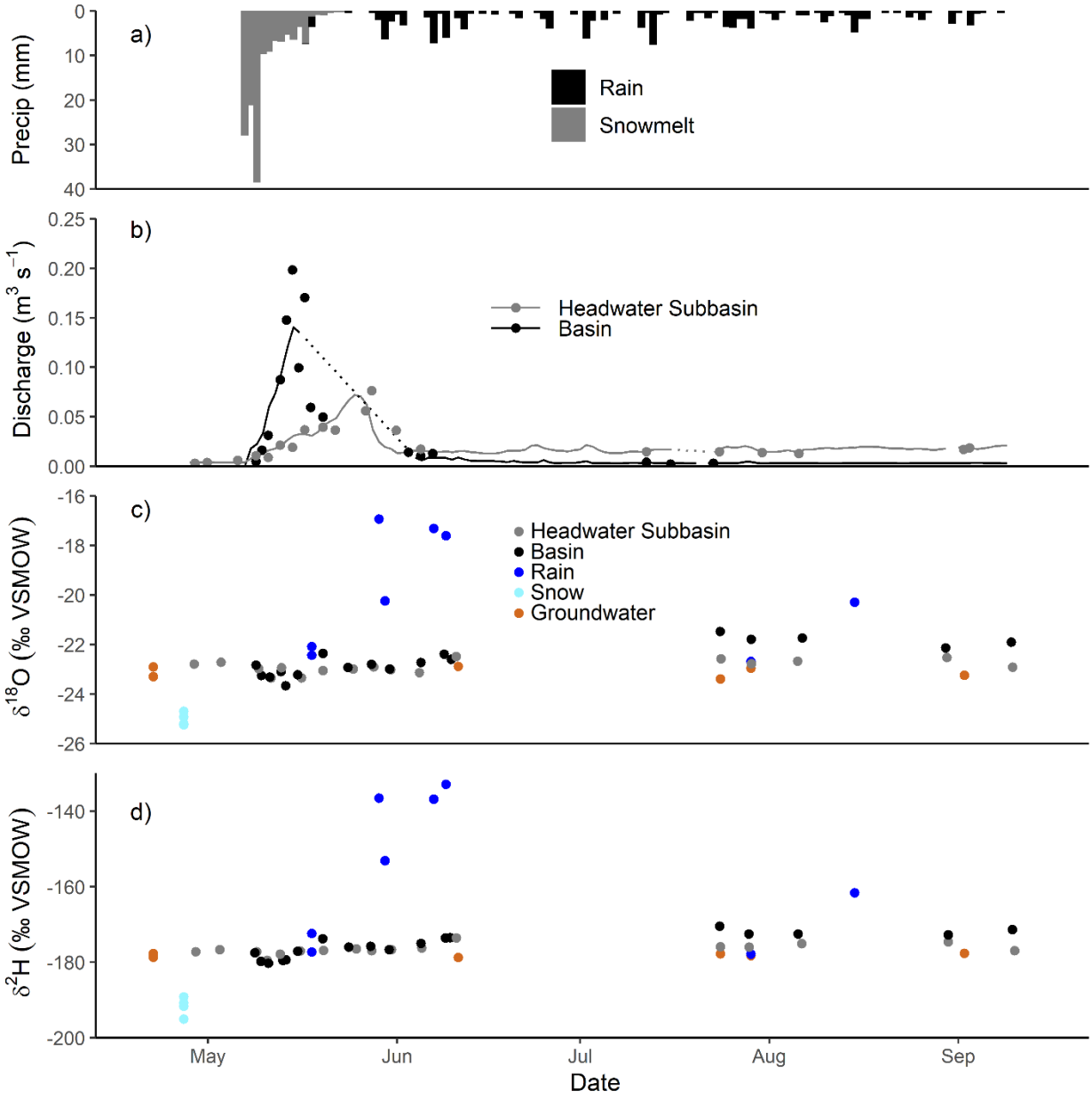

Figure 6-27: Time series of a) daily precipitation hyetograph; b) daily mean streamflow hydrographs; c) $\delta^{18}O$ of source water and stream water samples d) $\delta^{2}H$ of source water and stream water samples. $\delta^{18}O$ and $\delta^{2}H$ values are reported as deviations per mil (‰) of $^{18}O/^{16}O$ and $^{2}H/^{1}H$ ratios relative to Vienna Standard Mean Ocean Water (VSMOW), respectively. Hydrograph segments with solid lines when discrete observations (points) allowed for stage-discharge relationship to be used and dotted lines when linear interpolation was required (Appendix 4.4).

Table 6-9: $\delta^{18}O$ (‰ VSMOW) values applied as tracer concentration values in source water separation calculations using equation 4.5. C_P and C_E refer to $\delta^{18}O$ compositions of pre-event and event waters, respectively.

Event	Outlet	C_P	C_E	Comments
Freshet	Basin	-22.9	-25	CP average of 4x samples collected in channel before melt. CE average from 4x snow samples.
Freshet	Headwater Subbasin	-22.9	-25	CP average of 4x samples collected in channel before melt. CE average from 4x snow samples.
Early Summer	Basin	-22.7	-17.9	CP collected June 5. CE OIPC modelled. Alternative CE from samples collected -17.5.
Early Summer	Headwater Subbasin	-23.1	-17.9	CT collected after runoff complete (2019-06-11 14:00) and therefore not displayed in Figure 4.4b.
Late Summer	Basin	-21.5	-17.3	CP collected July 24. CE OIPC modelled. CE of rain samples (-22.7) within ±0.2 of CT.
Late Summer	Headwater Subbasin	-22.6	-17.3	CP collected July 24. CE OIPC modelled. CE of rain samples (-22.7) within ±0.2 of CT.

Table 6-10: Basin outlet source water separation uncertainty of event water contribution (Q_E) calculated for each daily time step included in the freshet runoff event. C_T and C_P uncertainties were based on the LWIA analytical errors (±0.2 ‰). C_E uncertainty was set relatively high (±3 ‰) to account for potential errors resulting from fractionation during snowmelt (Taylor *et al.*, 2002)

Date	Q_T ($m^3 s^{-1}$)	Q_P ($m^3 s^{-1}$)	Q_E ($m^3 s^{-1}$)	Q_E (%)	Uncertainty (%)	comments
2019-05-07	0.000	0.000	0.000	0		flow first observed
2019-05-08	0.018	0.018	0.000	0		
2019-05-09	0.023	0.023	0.000	0		C_T more enriched than C_P
2019-05-10	0.034	0.028	0.005	16	9	
2019-05-11	0.060	0.049	0.012	19	7	
2019-05-12	0.074	0.064	0.010	14	10	
2019-05-13	0.094	0.087	0.008	8	17	
2019-05-14	0.121	0.078	0.043	35	4	
2019-05-15	0.140	0.105	0.035	25	6	
2019-05-16	0.135	0.116	0.020	14	10	
2019-05-17	0.129	0.115	0.014	11	13	
2019-05-18	0.122	0.113	0.009	7	20	
2019-05-19	0.115	0.111	0.004	4	40	
2019-05-20	0.109	0.109	0.000	0		C_T more enriched than C_P
2019-05-21	0.102	0.102	0.000	0	960	
2019-05-22	0.095	0.095	0.000	0	480	
2019-05-23	0.089	0.088	0.000	0	320	
2019-05-24	0.082	0.082	0.001	1	240	
2019-05-25	0.075	0.075	0.000	0	320	
2019-05-26	0.069	0.069	0.000	0	480	
2019-05-27	0.062	0.062	0.000	0	960	
2019-05-28	0.055	0.055	0.000	0		C_T more enriched than C_P
2019-05-29	0.049	0.048	0.001	1	124	
2019-05-30	0.042	0.041	0.001	2	62	
2019-05-31	0.035	0.034	0.001	3	41	
2019-06-01	0.029	0.028	0.001	3	55	
2019-06-02	0.022	0.022	0.000	2	83	

Table 6-11: Headwater subbasin outlet source water separation uncertainty of event water contribution (Q_E) calculated for each daily time step included in the freshet runoff event and flow period prior to freshet beginning. C_T and C_P uncertainties were based on the LWIA analytical errors (±0.2 ‰). C_E uncertainty was set relatively high (±3 ‰) to account for potential errors resulting from fractionation during snowmelt (Taylor *et al.*, 2002)

Date	Q_T ($m^3 s^{-1}$)	Q_P ($m^3 s^{-1}$)	Q_E ($m^3 s^{-1}$)	Q_E (%)	Uncertainty (%)	comments
2019-05-07	0.004	0.004	0.000	1	171	first day of melt
2019-05-08	0.008	0.008	0.000	2	86	
2019-05-09	0.013	0.012	0.000	2	57	
2019-05-10	0.014	0.012	0.002	12	12	
2019-05-11	0.016	0.013	0.003	21	7	
2019-05-12	0.018	0.016	0.002	11	13	
2019-05-13	0.021	0.021	0.000	1	240	
2019-05-14	0.027	0.025	0.002	7	20	
2019-05-15	0.031	0.027	0.004	14	10	
2019-05-16	0.033	0.026	0.007	21	7	
2019-05-17	0.032	0.027	0.006	17	8	
2019-05-18	0.031	0.027	0.004	13	11	
2019-05-19	0.035	0.031	0.003	10	14	
2019-05-20	0.042	0.039	0.003	6	23	
2019-05-21	0.045	0.043	0.003	6	25	
2019-05-22	0.049	0.046	0.003	5	28	
2019-05-23	0.058	0.056	0.003	5	31	
2019-05-24	0.067	0.064	0.003	4	36	
2019-05-25	0.072	0.070	0.003	3	41	
2019-05-26	0.071	0.069	0.002	2	62	
2019-05-27	0.062	0.061	0.001	1	124	
2019-05-28	0.037	0.037	0.000	0		C_T more enriched than C_P
2019-05-29	0.025	0.024	0.000	2	88	
2019-05-30	0.019	0.019	0.001	3	44	
2019-05-31	0.018	0.017	0.001	5	29	
2019-06-01	0.013	0.013	0.001	5	29	
2019-06-02	0.014	0.013	0.001	5	29	